Synthesis, Characterisation and Properties of Flexible Metal-Organic Frameworks

Thesis submitted in accordance with the requirements of the University of Liverpool for the degree of Doctor in Philosophy

by

Catherine G. Perkins

August 2013

Abstract

In this thesis the synthesis, characterisation and analysis of new Metal-Organic Frameworks (MOFs) are presented.

Introduction: Chapter 1 includes an overview of recent literature focusing on the potential application of porous MOFs.

Synthetic and Experimental Techniques: Chapter 2 contains information regarding the synthesis of the organic ligand, tetrakis-(4-carboxyphenyl)-benzene (H_4TCPB) and solvothermal MOF synthesis. Characterisation techniques used in this thesis are also explained.

Mixed Carboxylate-Imidazole Based Metal-Organic Frameworks: In chapter 3, the synthesis of MOFs containing ligands with both imidazole and carboxylate functionality are presented. The MOFs produced are based on metal-carboxylate coordination networks with imidazole coordinated as a terminal, neutral ligand in all cases. An investigation into how reagent ratio and addition of base affects the product of reaction with the combination of Co(II), 1,3,5-benzene tricarboxylate and imidazole yields three different frameworks from the same three reagents. The main compound discussed has the formula $Co_3(BTB)_{1.5}(IM)_{1.35}(O)_{0.5}(OH)_{0.5}(H_2O)_{1.65}$·*guests* and is based on a novel Co_6 building unit which comprises neutral imidazole, oxo, hydroxo and carboxylate coordination. This Co_6 unit is the basis of a 2D tri-layer, stacked into a 3D porous arrangement via π···π stacking interactions between 1,3,5-benzene tribenzoate ligands. This material was characterised to be permanently porosity towards N_2, CO_2 and CH_4, however the material is sensitive to activation conditions, presumably due to the reliance on weak π···π stacking interactions between imidazole ligands to retain the void space.

A Cerium-Based Metal-Organic Framework: Structure, Sorption and Structural Transformations upon Desolvation: In chapter 4, a 3D framework based on Ce(III) and H_4TPCB with the formula Ce(HTCPB)·*guests* is presented. A variable temperature single crystal x-ray diffraction experiment allowed four structures to be determined from the same parent material: The as-made structure, the partially desolvated structure in which all channel and coordainted H_2O has been removed but coordinated EtOH remains, the fully desolvated structure and the structure following re-exposure of the desolvated phase to air. Powder x-ray diffraction confirms that the phase changes observed occur in both the single crystal and bulk crystalline phases. A gas cell experiment on the rearranged phase shows that the material can reversibly uptake Xe into the channels. This investigation highlights the structural stability and flexibility of **11**.

Ce(HTCPB) for Xylene Separation and Analysis of Uptake of Aromatic Guests: In chapter 5, Ce(HTCPB) is investigated for its potential in xylene separation and shows *para*-/*meta*-xylene (pX/mX) selectivity in line with the highest performing MOF and zeolite materials. Analysis of the *para*-, *meta*-, *ortho*-xylene (oX) and ethylbenzene (EB) loaded single crystal structures provides an insight into the preference of the material for pX over the other isomers. The framework relaxes favourably around the pX isomer, which forms C-H···π and C-H···O interactions with the channel walls, forming an almost perfect pX pocket. Such interactions are formed to a lesser extent with the other less streamlined guests. Single crystals of Ce(HTCPB) are also loaded with benzene and toluene in for comparison with the pX loaded structure.

A Series of Isostructural Lanthanide-Based MOFs for Xylene Separation and A Framework using a Smaller Lanthanide: In chapter 6, a series of compounds isostructural with Ce(HTPCB) are presented with the formula Ln(HTPCB), where Ln = La, Ce, Pr, Nd and Sm. The single crystal structures of the desolvated and rearranged phases were also determined to be isostructural with the corresponding Ce(HTCPB) phases. These compounds were investigated for their pX/mX selectivities, with Pr, Nd and Sm(HTCPB) producing selectivities around 50 % higher than any reported MOF or zeolite material. Analysis of the pX and mX loaded single crystal structures of this series of compounds provided an understanding of the trend in selectivity observed. Also in this chapter, combination of H_4TCPB with a smaller lanthanide, Yb, produced a new framework.

Acknowledgements

Firstly, I would like to thank my supervisor, Professor Matt Rosseinsky for advice and support throughout my PhD.

I would also like to thank Dr John Warren for help with crystallography and solving all the impossible single crystal structures! John was an amazing source of support and guidance throughout my PhD and provided the sarcastic humour of many synchrotron trips, to DLS and ALS.

I would like to thank Dr Kyriakos Stylianou for being a fantastic mentor and even better friend throughout my PhD and for a long time to come. He showed me many educational things, including the solvothermal shake dance!

I would also like to thank Dr Chris Ireland, again for being a good friend and sending me countless papers to read!

I would like to thank Dr Darren Bradshaw and Dr Alexandra Fateeva for their help and guidance with the work surrounding the on Co_6-MOF. I would also like to thank Dr Kim Jelfs and Dr Phil Chater for their help and support with work on the Ce-MOF.

I would like to thank Julia and Alec for putting up with me in the office and help and advice with experimental work and characterisation and the rest of the MJR research group.

I was also like to thank Jane Remmer for being a constant source of support throughout my PhD.

Finally I would like to thank my friends and family for their constant support outside of university.

Abbreviations

MOF(s): Metal-Organic Frameworks(s)

IRMOF(s): Isoreticular Metal-Organic Framework(s)

ZIF(s): Zeolitic Imidazolate Framework(s)

COF(s): Covalent Organic Framework(s)

SBU: Secondary Building Unit

PSM: Post-Synthetic Modification

SCXRD: Single-Crystal X-Ray Diffraction

SCSC: Single-Crystal-to-Single-Crystal

CIF: Crystallographic Information File

PXRD: Powder X-ray Diffracion

IGA: Intelligent Gravimetric Analyser

DR: Dubinin-Radushkevich

BET: Brauner-Emmett-Teller

Q_{st}: Isosteric Heat of Adsorption

PSD: Pore Size Distribution

TGA: Thermogravimetric Analysis

IR: Infra-Red

GC: Gas Chromatography

NMR: Nuclear Magnetic Resonance

Ln(III): Lanthanide^{3+} ion

1,4-BDC: 1,4-benzene dicarboxylic acid

1,3,5-BTC: 1,3,5-benzene tricarboxylic acid

1,3,5-BTB: 1,3,5-Benzene tribenzoic acid

H_4TCPB: 1,2,4,5-Tetrakis-(4-carboxyphenyl)-benzene

IM: Imidazole

N-MeIM: N-methyl imidazole

Py: Pyridine

DCM: Dichloromethane

EtOH: Ethanol

DMF: Dimethyl formamide

DEF: Diethyl formamide

ALS: Advanced Light Source, Berkeley Labs, CA, US

DLS: Diamond Light Source, Didcot, UK

pX: *Para*-xylene

mX: *Meta*-xylene

oX: *Ortho*-xylene

EB: Ethylbenzene

Tol: Toluene

Benz: Benzene

AB: Aminoborane

Bipy: 4,4'-Bipyridine

Asp: Aspartic Acid

En: Ethane diamine

Ox: Oxalate

List of Compounds

1 $Zn_3(1,4\text{-}BDC)_3(Im)_2$•DMF

2 $Co_3(1,4\text{-}BDC)_3(Im)_2$•DMF

3 Zn(3,5-pydc)(Im)•DMF

4 $Co(1,3,5\text{-}BTC)_2(DMF)_2$•DMF

5 $Co_3(BTC)_2(Im)_2(DMF)$•DMF

6 $Co_3(BTC)(Im)_3$

7 $Co_3(BTB)_{1.5}(Im)_{1.35}(O)_{0.5}(OH)_{0.5}(H_2O)_{1.65}$•$(EtOH)_{2.17}$·$(H_2O)_{7.87}$

8 $Co_7(O)_2(1,3,5\text{-}BTB)_4(NMeIM)_5(H_2O)_4$·DMF

9 $Co_3(1,3,5\text{-}BTB)(Py)_3(H_2O)_3$·$H_2O_9$

10 La(HTCPB)(EtOH)(H_2O)•(EtOH)(H_2O)

10D Desolvated La(HTCPB)

10R Rearranged La(HTCPB)

10P La(HTCPB) loaded with pX

10M La(HTCPB) loaded with mX

11 Ce(HTCPB)(EtOH)(H_2O)•(EtOH)(H_2O)

11S Partially desolvated **11**

11D Desolvated **11**

11R Rearranged **11D**

11PM Ce(HTCPB) loaded with pX and mX from a 1:1 mixture.

11P Ce(HTCPB) loaded with pX

11M Ce(HTCPB) loaded with mX

11O Ce(HTCPB) loaded with oX

11EB Ce(HTCPB) loaded with EB

11T Ce(HTCPB) loaded with Toluene

11B Ce(HTCPB) loaded with Benzene

11RP Rearranged Ce(HTCPB) loaded with pX

11RB Rearranged Ce(HTCPB) loaded with Benzene

11RXe Rearranged Ce(HTCPB) loaded with Xe

12 $Pr(HTCPB)(EtOH)(H_2O)\bullet(EtOH)(H_2O)$

12D Desolvated Pr(HTCPB)

12R Rearranged Pr(HCTPB)

12P Pr(HTCPB) loaded with pX

12M Pr(HTCPB) loaded with mX

13 $Nd(HTCPB)(EtOH)(H_2O)\bullet(EtOH)(H_2O)$

13D Desolvated Nd(HTCPB)

13R Rearranged Nd(HTCPB)

13P Nd(HTCPB) loaded with pX

13M Nd(HTCPB) loaded with mX

14 $Sm(HTCPB)(EtOH)(H_2O)\bullet(EtOH)(H_2O)$

14D Desolvated Sm(HTCPB)

14R Rearranged Sm(HTCPB)

14P Sm(HTCPB) loaded with pX

14M Sm(HTCPB) loaded with mX

15 $Yb_2(TCPB)(EtOH)(H_2O)\bullet(H_2O)$

Contents

Chapter 1

Introduction

1.1 General Introduction

Although the behaviour of molecules in the gas and liquid phase is well understood, it is not yet possible to predict how a compound will come together in the solid state. With the intention that it should one day be possible to design crystalline solids with specific properties, the field of crystal engineering develops the knowledge and understanding of the interactions present between the various building blocks that can be used. It is necessary to investigate both strong and weak interactions, as although the stronger interactions are most likely to direct assembly, the multitude of weaker interaction that exist between two molecules can also have a substantial effect on the overall crystal structure of a compound.

Metal-organic frameworks are materials that comprise metal ions and organic ligands, generally with multiple functionalities. These compounds can extend in one, two or three dimensions depending on the interactions present between their component species. Interactions may vary in strength, from the strongest coordination bonds between metal and ligand, through intermolecular interactions of differing strength such as hydrogen bonds, down to simple Van der Waals forces. A combination of all these effects determines the structure and topology of the framework material produced.

In this thesis, the synthesis of new porous MOFs has been explored and their potential applications investigated. In this chapter various porous materials and their properties are discussed with a particular emphasis on MOFs.

1.2 Porous Materials

Porous materials have been at the forefront of research and industrial processes for decades. They are divided into three main categories: Microporous, mesoporous and macroporous[1]:

(i) Pores smaller than 20 Å are known as microporous.
(ii) Pores exceeding 50 Å are known as macroporous.
(iii) Intermediate size pores of 20-50 Å are known as mesoporous.

Porous materials can be divided into three classifications: Organic porous material such as polymers, activated carbons and covalent-organic frameworks; inorganic porous materials such as zeolites and aluminosilicates; hybrid inorganic-organic materials or Metal-Organic Frameworks (MOFs). Porous materials are an important area of research for their applications in gas storage, molecular sieves and catalysis.

1.2.1 Inorganic Porous Materials

1.2.1.1 Zeolites

Zeolites are aluminosilicate materials with the general formula $Mx/n[x AlO_2.y SiO_2].zH_2O$, where M^{n+} is the exchangeable cation, $[x AlO_2.y SiO_2]^{x-}$ is the main anionic framework and zH_2O is the sorbate phase[2]. The structures are based on a continuous array of corner-sharing AlO_4 and SiO_4 tetrahedra, with the overall negative charge generated by Aluminium compensated for by cations such as Na^+, Mg^{2+}, Ca^{2+} and K^+ within the voids. The cations within zeolites are interchangeable, giving rise to different properties.

Natural zeolites occur as rock products from volcanic activity, however currently the majority of commercial zeolites are man-made, synthesised via hydrothermal sol-gel synthesis or high pressure solvothermal synthesis. The first zeolite was discovered by A. F. Crostedt in 1756, who found that when a rock of stillbite was heated quickly, it appeared to boil. This occurred as water trapped in the pores of the natural zeolitic rock began to escape as the rock was heated. This is where the term 'zeolite' originated: it literally means 'boil stone' translated from the the greek 'zein lithos' (ζειν λιθος). Research into synthetic molecular sieve zeolites was initiated by Union Carbide in 1948, who by 1959 had a patent granted for the synthesis, purification of synthetic zeolites A, X and Y (US2,882,243, molecular sieve absorbents) and their separation, purification and catalytic properties[3].

In the 1940's, synthetic zeolites were made by the hydrothermal crystallisation of alkali aluminosilicate gels at around 100 °C, ambient pressures and high pH. Zeolites with intermediate Si/Al ratios were produced using this method with over 20 topologies. Following this, higher Si/Al ratio zeolites were synthesised using a template approach, in which the aluminosilicate structure was grown around a quaternary ammonium salt template. This salt could then be washed away after synthesis, leaving a cavity with a specific size, shape and geometry, giving zeolites applications in areas such as catalysis and separations[4]. There are currently over 200 zeolite types, depending of the synthesis method and structure produced[5].

Zeolites have applications in many areas of industry today. They are used in water purification as they can remove toxic or unwanted contaminants. For example, they can soften hard water through ion exchange, remove ammonia from aquariums and remove radioactive contaminants from nuclear wastewater[6]. They are also used in the catalytic cracking of long hydrocarbon chains from the naptha fraction following fractional distillation of crude oil in the petrochemical industry, to yield the more valuable smaller branched and aromatic hydrocarbons. Currently Zeolite Y is used as it has a large number of active sites, high thermal stability (793 °C) and size selectivity

(channels have a pore diameter of 7.4 Å)[7]. Zeolites can also be used as detergents and this is close to being the largest single use for zeolites worldwide: Zeolites P, A and X are used[8].

1.2.1.2 Organic Porous Materials

Organic molecules pack together in the solid state via intermolecular interactions such as hydrogen bonds, π-π stacking interactions and van der Waals forces, generally in a close-packing arrangement to avoid free space, yielding a more stable 3D structure. However, examples have been shown to possess permanent porosity and these organic porous materials offer advantages over zeolites due to their solubility[9] and for this reason their potential porosity has been investigated. Organic porous materials can either be continuous organic polymers that in the solid state possess permanent porosity, or discrete organic molecules that crystallise with void spaces within the structure[10].

Porous Organic Polymers (POPs)

Porous organic polymers (POPs) are organic polymers, synthesised via condensation or addition reactions, but which crystallise with void spaces due to insufficient close-packing. POPs have been shown to have potential applications in gas storage and catalysis, with good processability.

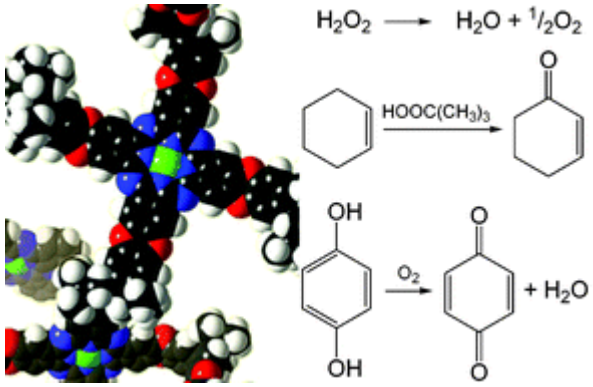

Figure 1: *Reactions catalysed by CoPc-PIM-A and FePorph-PIM. Figure taken from reference[11].*

An example of two POPs are HPOP-1 and HPOP-2, published by Chen *et al.*. A hexaphenylbenzene derivative was polymerised with either 1,4-benzene diborane via Suzuki coupling, or 1,4-diacetylyl benzene via Sonogashira coupling to yield HPOP-1 and HPOP-2 respectively. These polymers have BET surface areas of 1148 and 742 m^2/g respectively, measured using a N_2 isotherm at 77K and H_2 uptakes of 1.5 and 1.08 wt% respectively[12].

POPs have also been shown to have application in catalysis[13]. One example is a polymer synthesised by Mackintosh *et al.*. A spiro-linked cobalt phthalocyanine polymer (CoPc-PIM-A, PIM = Polymer of Intrinsic Microporosity) and a spiro-linked iron porphyrin network polymer (FePorph-PIM) were both synthesised and characterised to have different BET surface areas depending on the purity of the monomers and metal content. CoPc-PIM-A produced BET surfaces areas of between 120 and 612 m^2/g resulting from different synthesis methods and FePorph-PIM had a BET surface area of 866 m^2/g. All CoPc-PIM-A polymers produced were active catalysts in decomposition of hydrogen peroxide, cyclohexene oxidation by *t*-butylhydroperoxide and hydroquinone oxidation, significantly enhancing the rate of reaction compared to their low molar mass analogues. FePorph-PIM also enhanced the rate of reaction of hydroquinone oxidation. This work showed the potential of porous organic polymers is catalysis, due to their microporosity and incorporation of catalytically active units[11].

Discrete Porous Organic Compounds

To date there are over 50 porous organic materials reported that are based on discrete organic compounds[9].

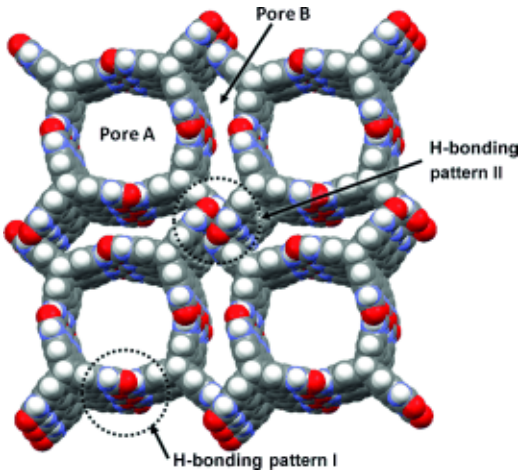

Figure 2: *View down 001 of the single crystal structure of TTBI. C gray, H white, O red, N blue. Figure taken from reference*[14].

Reaction of hexaammonium triptycene hexachloride with carbonyldiimidazole produced triptycenetrisbenzimidazolone (TTBI). There are four TTPI molecules per unit cell, which crystallise to form cylindrical 1D pores down the 001 axis with a diameter of 14.5 Å and hydrogen bonding between molecules (*Figure 2, pore A*). Additional smaller pores of 5.8 Å are created due to the packing of the molecules (*Figure 2*, *pore B*). The compound was calculated to have a

micropore volume of 1.02 cm^3/g with a pore size distribution of 7.8 Å. A N_2 isotherm showed the crystalline material achieves a Langmuir surface areas of 3020 m^2/g[14], a value which is comparable MOF-5, which has a Langmuir surface area of 2900 m^2/g . This shows that porous organic materials can be considered as potential alternatives to both zeolites and metal-organic frameworks.

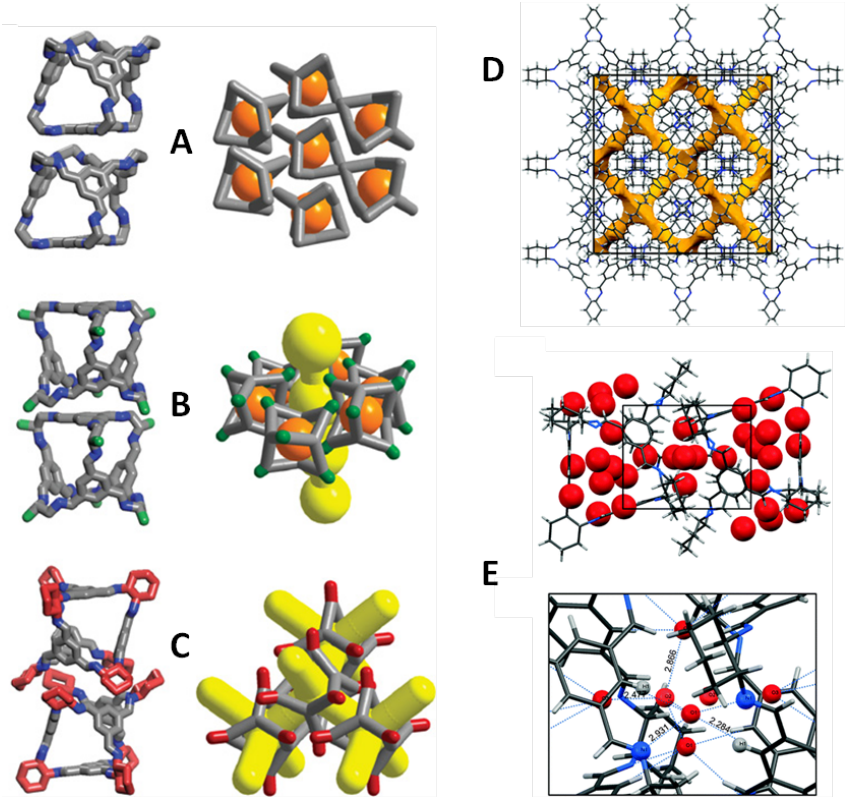

Figure 3: *Cage-cage packing of A: Cage-1; B: Cage-2; C: Cage-3. Isolated voids shown in orange, interconnected pores shown in yellow, methyl groups shown in green, cyclohexyl groups shown in red. Figure adapted from reference[15]. D: Crystal structure of CC3 showing diamondoid channel structure; E: Guest water molecules taken up by CC3, 12 per cage, with hydrogen bonding shown below. Figures adapted from reference[16].*

More recently, porous organic cages have been researched for their porosity. In 2009, the first examples of these compounds were published. Tozawa *et al.* published examples of three tetrahedral cages[15]: Cage-1 is synthesised by condensation of 1,3,5-triformylbenzene and1,2-ethylene diamine and crystallises from ethyl acetate; cage-2 by condensation of 1,3,5-triformylbenzene and 1,2-propylenediamine and crystallises from acetonitrile; cage-3 by the [4+6] cycloimmination reaction between 1,3,5-triformylbenzene and (R,R)-1,2-diaminocyclohexane and crystallised from chloroform.

Following crystallisation, the cages pack differently depending on the side groups present and this affects the compounds porosity. Cage-1 packs window-arene, meaning there is no potential porosity, only voids present within the cages (*Figure 3A*). Cage-2 packs in the same way, but the additional methyl groups means that there is a larger gap between cages which generates a small channel, producing undulating 1D porosity (*Figure 3B*). Cage-3 packs window-window, meaning there is permanent 3D porosity between cages (*Figure 3C*). The Langmuir surface areas of these compounds was measured using N_2 isotherms at 77 K, and showed surface areas of 40, 600 and 733 m^2/g respectively for cages-1-3 (BET surface areas of 533 and 730 m^2/g for cage-2 and -3 respectively). Cages-2 and -3 were also shown to taken up CH_4, CO_2 and H_2, whereas the effectively non-porous cage-1 only took up minimal amounts of the gasses. Due to the solvent processable nature of organic molecules in general, cage-1 was recrystallized from dichloromethane and *ortho*-xylene to yield a porous polymorph with a BET surface area of 550 m^2/g, which was determined to have similar packing to the original cage-1 by LeBail refinement, but with reduced symmetry. The authors comment on the use of this finding as a potential for on/off switching porosity between interconvertible polymorphs[15].

Hasell *et al.* from the same group also published work on a water-stable porous organic cage. The cage 'CC3' is synthesised via the cycloimmination of four 1,3,5-benzene trialdehydes and and six cyclohexane diamine molecules. The cages pack window-to-window, with a channel diameter of 5.8 Å, producing a diamondoid channel network (*Figure 3D*). Unlike the previously published examples (above), this cage is stable in boiling water for 4 hours and crystallographic analysis shows 12 guest water molecules are taken up per cage all of which are involved in hydrogen bonding between other guest water molecules and N-donor atoms from the imine lone pairs in the cage (*Figure 3E*). The CC3 structure takes up 20.1 wt% water at 95 % humidity, and the adsorption-desorption process was cycled three times to further highlight the stability of the material in moisture. Demonstrating the water stability of such discrete organic porous materials opens up the potential applications of such compounds in areas including drug delivery, separations and catalysis; areas in which they may not be applicable if they were not water stable[16].

Covalent Organic Frameworks (COFs)

Covalent Organic Frameworks (COFs) are materials that are constructed from robustly covalently bonded light elements including C, H, O, N and B and are sometimes referred to as 'organic zeolites'[17].

The first example of COFs was published by the group of Yaghi in 2005[18]. COF-1 ($(C_3H_2BO)_6{\cdot}(C_9H_{12})_1$) was synthesised via molecular dehydration, in which three phenylboronic

acid molecules combined in a second dehydration reaction to give the trigonal planar building block, boroxine anhydride. When combined with 1,4-benzene boronic acid, a 2D layered COF was formed with hexagonal 1D channels. In the synthesis of COF-5 ($C_9H_4BO_2$), phenylboronic acid was reacted with hexahydroxy triphenylene, to produce a larger trigonal planar building block, a triboronate ester. When combined with 1,4-benzene boronic acid, a 2D layered COF is formed with larger hexagonal 1D channels than COF-1 due to the larger building blocks used. COF-1 and COF-5 were shown to have thermal stability up to 600 °C and BET surface areas of 711 and 1590 m^2/g respectively by means of a reversible type-I and type-IV N_2 isotherms respectively at 77 K. Of the surface area of 711 m^2/g for COF-1, 587 m^2g (83 %) is a micropore contribution and 124 m^2/g (17 %) is a mesopore contribution, arising from mesopores between crystallites. This is also shown in the pore size distribution curves, which show peaks between 6-12 Å and also between 35-41 Å. For COF-5, the pore size distribution of 24-44 Å is consistent with 2D sheets with aligned hexagonal channels, but there is also a mesoporous contribution (23 %) between 5-20 Å, which the authors attribute to slipping of the hexagonal sheets within the structure[18].

Uribe-Romo *et al.* of the same research group synthesised COF-300, via the condensation of a tetrahedral building block, tetra-(4-anilyl)methane, with a linear linker, terephthaldehyde, to yield a diamondoid structure with diamondoid 3D channels, linked by imine bonds. COF-300 was shown to be stable up to 490 °C and to be insoluble in water. An Ar isotherm showed a BET surface area of 1360 m^2/g and a calculated pore volume of 0.72 cm^3/g with a pore size distribution calculated to be 7.2 Å[19]. This is another example of the 3D stable porous compounds that can be produced through covalent bonds.

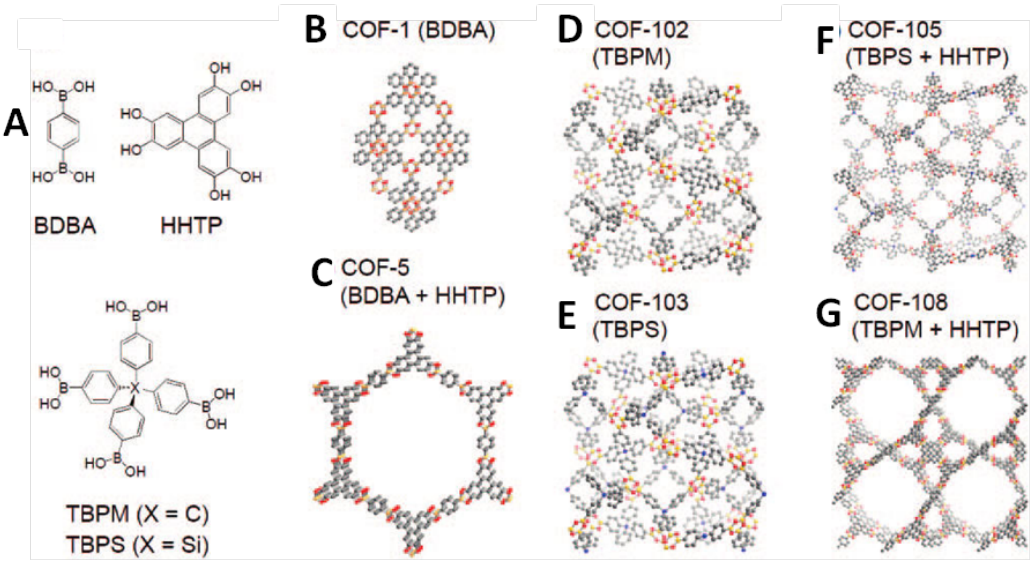

Figure 4: *A: Structures of building unit and crystal structures of B: COF-1; C: COF-5; D: COF-102; E: COF-103; F: COF-105 and G: COF-108. H atoms are omitted for clarity. C (grey), B (orange), O (red), Si (blue). Figure adapted from reference[20].*

COFs have been shown to have application in gas storage. Grand Cononical Monte Carlo (GCMC) simulations were used to simulate and describe H_2-host interactions in COFs -1, -5, 102, -103, 105, and -108 (*Figure 4*). COF-5 was firstly used to compare the experimental vs theortical values of H_2 uptake and came out in good agreement, with an experimental uptake of 3.3 wt% and a theoretical uptake of 3.4 wt % at 50 bar. H_2 uptake at 77 K for the other compounds was calculated as follows: COF-1, 3.8 wt% at 70 bar; COF-5, 3.4 wt% at 80 bar; COF-102, 8.8 wt% at 80 bar; COF-105, 10 wt% at 80 bar; COF-108, 10 wt% at 100 bar. The authors state that these values show that COF-105 and COF-108 outperform high achieving MOF materials in H_2 uptake, such as MOF-177 and MOF-5 with uptakes of 7.0 and 7.1 wt% respectively. Volumetric H_2 uptakes show that COF-1 is the best at 20 bar, but COF-105 is the best in the high pressure region, with an uptake of 40.4 g/L[20]. This is close to the goal put in place by DOE of 45 g/L and again is better than MOF-177 which has a volumetric uptake of 39.1 g/L[21].

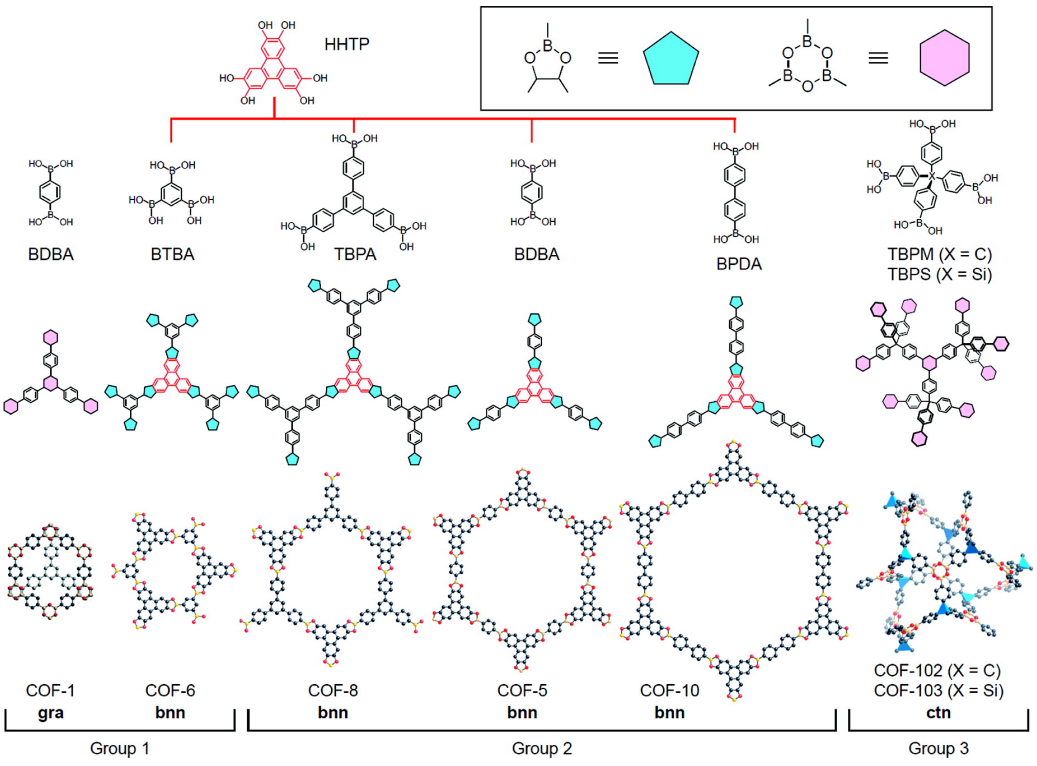

Figure 5: *Condensation reactions to form 2D COF-1, -5, -6, -8 and -10 and 3D COF-102 and -103. B (orange), O (red), C (black), atom X in COF-102 and -103 (blue tetrahedron). All hydrogen atoms are omitted for clarity. The topology and the group classification number are indicated for each COF. Figure and caption taken from reference*[22].

Furukawa and Yaghi published work on three groups of COFs in 2009, characterising them by their pore size and investigating their CH_4, CO_2 and H_2 uptakes[22] (*Figure 5*). COF-1 and COF-6

(group 1) are 2D structures with 1D channels and small pores of 9 Å. They have Langmuir surface areas of 970 and 980 m^2/g respectively, H_2 uptakes of 14.8 and 22.6 mg/g, CH_4 uptakes of 40 and 65 mg/g and CO_2 uptakes of 230 and 310 mg/g respectively. COF-5 COF-8 and COF-10 (group 2) are 2D structures with 1D channels and larger pores of 27, 16 and 32 Å respectively. They have Langmuir surface areas of 1990, 1400 and 2080 m^2/g respectively, H_2 uptakes of 35.8, 35.0 and 39.2 mg/g, CH_4 uptakes of 89, 87 and 80 mg/g and CO_2 uptakes of 870, 630 and 1010 mg/g respectively. COF-102 and COF-103 (group 3) are 3D structures with 3D porosity and pores of 12 Å. They have Langmuir surface areas of 4650 and 4630 m^2/g respectively, H_2 uptakes of 72.4 and 70.5mg/g, CH_4 uptakes of 187 and 175 mg/g and CO_2 uptakes of 1200 and 1900 mg/g respectively. The group 3 COFs are the highest performing and when compared to other porous materials are shown to have comparable Langmuir surface areas (MOF-177[21], MOF-5[23] with surface areas of 5640 and 4400 m^2/g), H_2 uptakes (MOF-177[21] and MOF-5[23] with H_2 uptakes 75.2 and 76.0 mg/g), CH_4 uptakes ((IRMOF-6[24] and MIL-101(Cr)[25] both with CH_4 uptakes of 160 mg/g) and CO_2 uptakes (MOF-177[26] and MOF-101(Cr)[25] with CO_2 uptakes of 1490 and 1760 mg/g) to the highest performing MOFs[22]. These COF-102 and COF-103 materials can be place in line with the highest performing porous material, with potential applications in gas storage.

1.2.1.3 Metal-Organic Frameworks (MOFs)

Metal-Organic Frameworks are materials which comprise metal centres and organic ligands with multiple coordinative functionalities. Metals are chosen for their coordination sphere and ligands are chosen for their coordination modes, directionality and functionality.

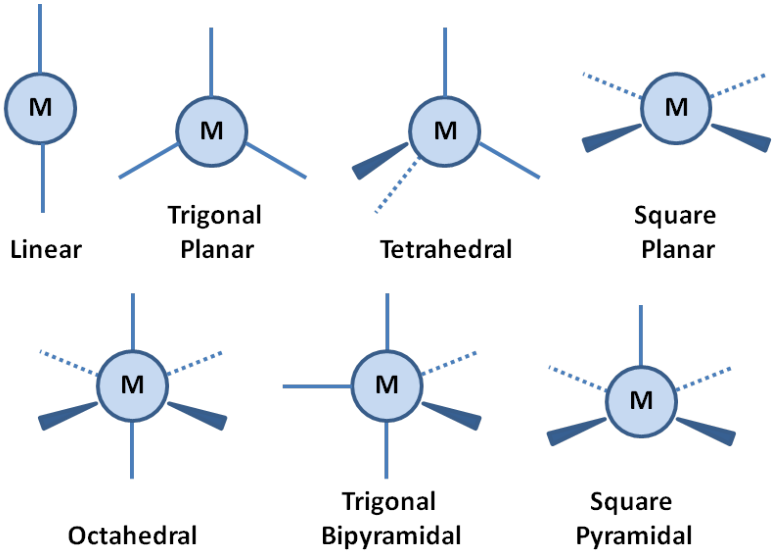

Figure 6: *Possible metal geometries when using d-block metals.*

In MOF synthesis, both metal centres and organic linkers are chosen for their specific coordination geometries. The d-block metal ions can allow access to different topology frameworks depending on their size, coordination number and coordination geometry. The coordination number of the d-block elements ranges from 2 to 6, with 2 producing linear compounds, 3 trigonal planar, 4 tetrahedral or square planar, 5 trigonal bipyramidal and 6 producing octahedral. Other shapes can also be accessed based on these parent shapes (*Figure 6*). In order to access higher coordination numbers, the lanthanides can be used. With lanthanides, the f-orbitals are used in metal-ligand coordination, which have a less restricted coordination geometry. This allows coordination numbers of 7-9 to be achieved, with no specific geometry around the metal centre.

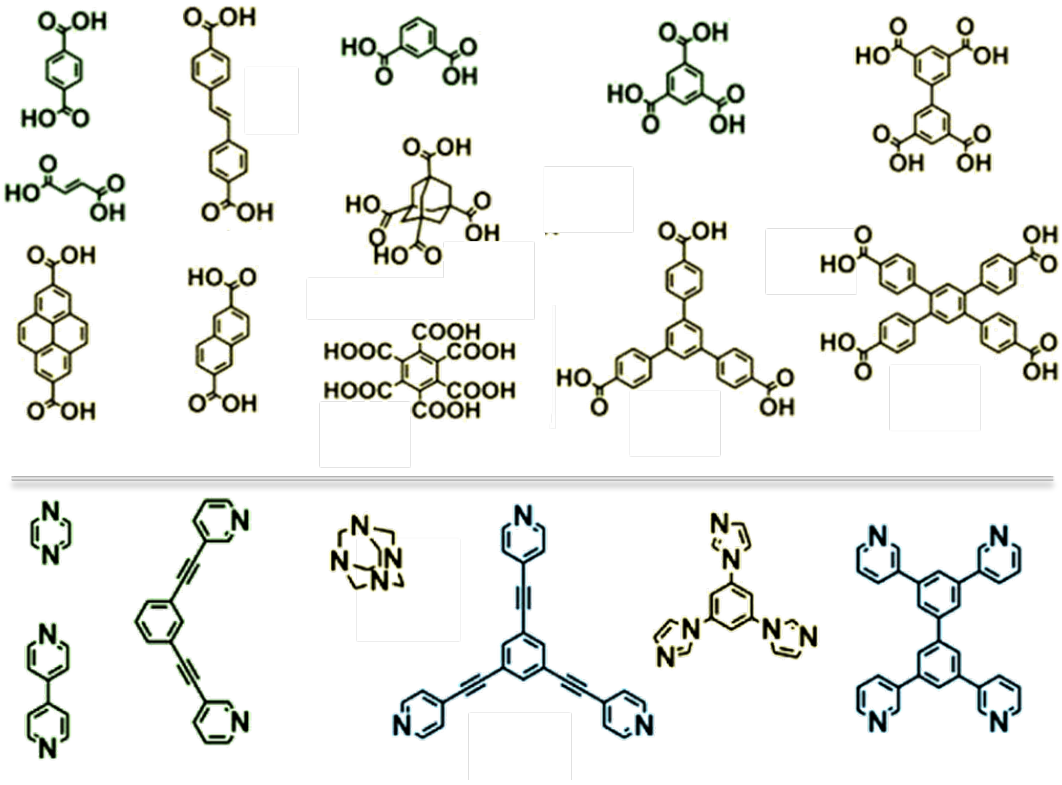

Figure 7: *Carboxylate-based (top) and N-based (bottom) ligands of varying geometry.*

The ligand chosen can be used to determine to dimensionality and pore chemistry of the framework produced (*Figure 7*). If a linker only has one coordination site, such as N in pyridine or the carboxylate group in benzoic acid, then only complexes can form with no 2D or 3D structure possible. However if a multifunctional linker is used in combination with a metal centre of specific geometry, multidimensional frameworks can form (*Figure 8*). Examples of multifunctional linkers are shown in *Figure 7*. For example, if tetrahedral Zn(II) is combined with the linear 1,4-benzene dicarboxylic acid, there is potential to form 2D or 3D frameworks. This is known as the 'node and spacer' approach and the first example of coordination framework synthesis using this technique

was published by Hoskins and Robson in 1990[27], who synthesised diamondoid networks by combining tetrahedral Zn(II) with linear CN^- and tetrahedral Cu(I) centres with tetrahedral 4,4',4'',4'''-tetracyanotetraphenylmethane linkers.

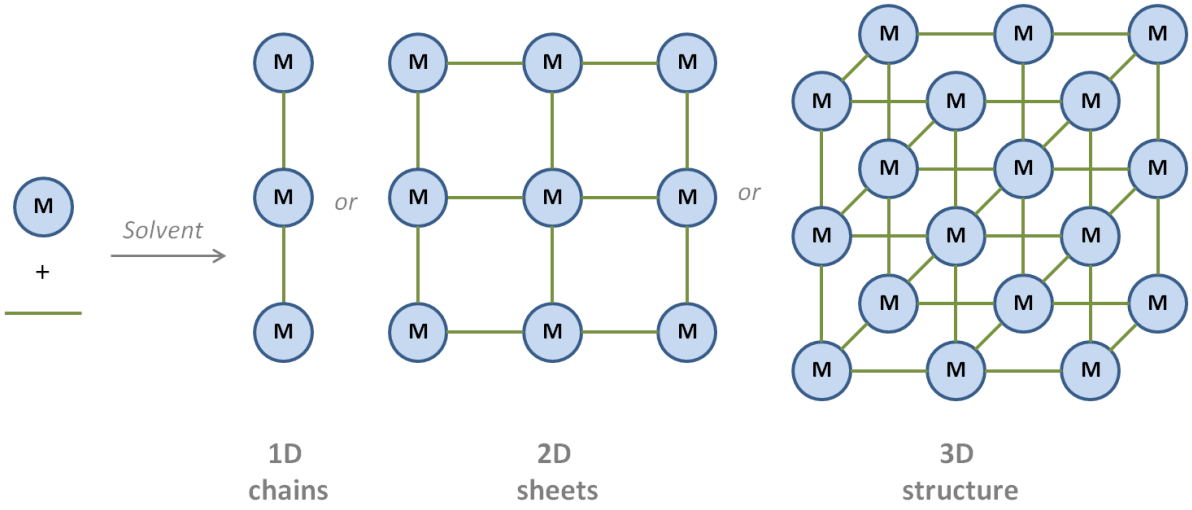

Figure 8: *Schematic of MOF synthesis process.*

Another useful tool in MOF synthesis is the use of Secondary Building Units (SBUs)[28-30]. SBUs are building blocks comprising a central metal ion and other atoms either from the atoms of the coordinating functional group of the linker or bridging atoms that link several metal ions, to produce a new geometry building block.

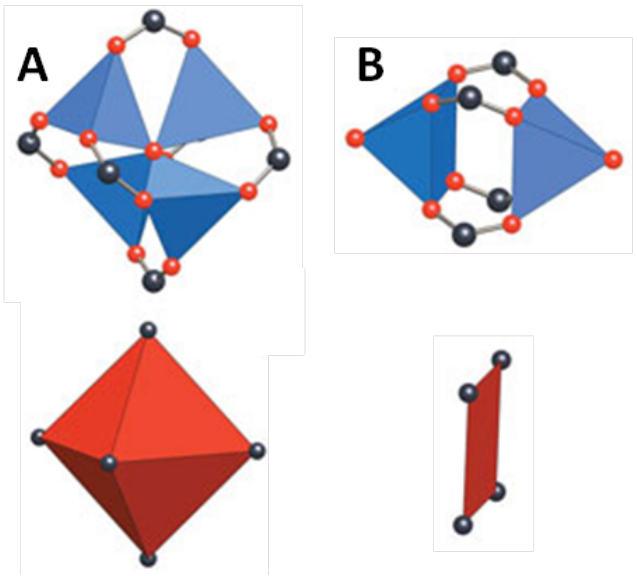

Figure 9: *Examples of common Secondary Building Units (SBUs) and the geometry they create. Figure adapted from reference*[31].

A common example of this is the $Zn_4O(CO_2)_6$ SBU used in the synthesis of the IRMOF series (*Figure 9C*): Four tetrahedral Zn(II) metal ions are bridged by a tetrahedral μ_4-O and the other three Zn-coordination sites are occupied by three O atoms from separate carboxylate functional groups of three separate linkers. This produces an octahedral building block which when bridged using the linear 1,4-BDC ligand, produces a cubic 3D framework[26]. Another common SBU is the paddlewheel[32-33], in which two metal centres are bridged by four (M)-O-C-O-(M) carboxylate bridges, creating a square planar arrangement around each of the two metal ions within the SBU (*Figure 9A*), such as is found in MOP-1 $(Cu_{24}(1,3\text{-BDC})_{24}(DMF)_{14}(H_2O)_{10})$[34] and MOF-101 $(Cu_2[o\text{-Br-}C_6H_3(CO_2)_2]_2$[35].

1.3 Terminology of Coordination Compounds

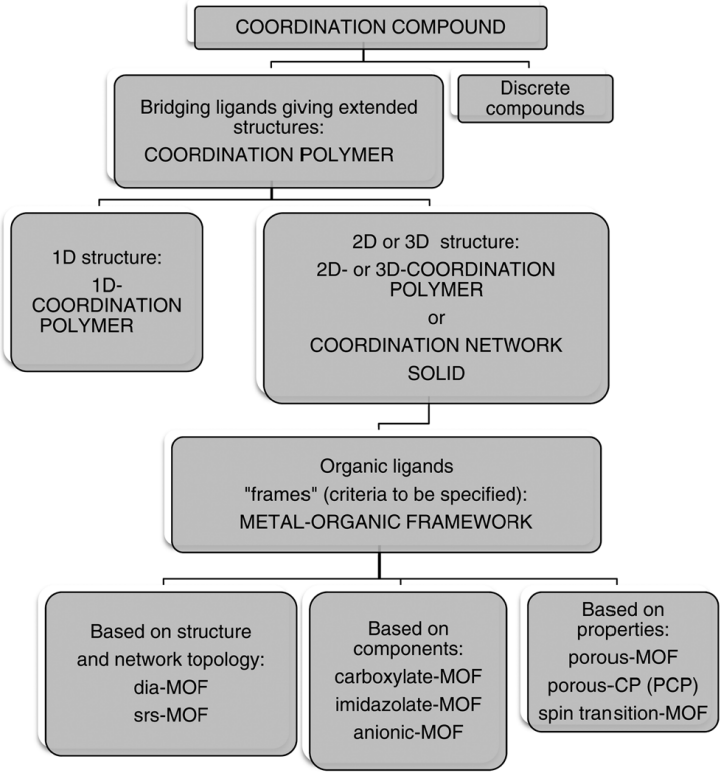

Figure 10: *Hierarchy of nomenclature for coordination compounds. Figure taken from reference*[36].

As a wealth of research being is being conducted in the area of 'Metal-Organic Frameworks', a recent publication has recommended systematic nomenclature for the description of metal-ligand coordination based materials. The need for such defined nomenclature arose after many journals

were published with different authors in different research areas using the same description for different types of framework, thus causing confusion[36].

The overall category of coordination compounds is first divided into two sections: coordination polymers (CPs) and discrete compounds. In this instance, the definition of a coordination compound is a compound in which 'bridging ligands give extended structures'. The term CP was first coined from the term 'polymer' which describes a material in which monomers are held together by covalent bonds[37]; hence a coordination polymer is a material in which structural units are held together by coordination bonds.

Coordination polymers are then broken down into two sections: 1D coordination polymers and 2/3D coordination polymers or coordination network solids. Where organic ligands are used in a coordination network solid, the material can be referred to as a metal-organic framework and can poses pre-text describing topology, components or properties of the MOF, such as dia-MOF, carboxylate-MOF and porous-MOF respectively. The MOF must have potential voids, however there is no demand for physical porosity measurements for the material to be called a MOF.

The terms stated here shall be used to describe the coordination compounds discussed in this thesis.

1.4 History of Metal-Organic Frameworks

Porous materials have been extensively researched for many decades. In the 1990's a 'new' class of porous materials was discovered in which the combination of multidentate organic bridging linkers and metal ions yielded framework materials with similar synthesis methods, topologies and properties to those of the well-known zeolites. Furthermore, these coordination compounds were shown to have tuneable properties offering access to a multitude of applications. This was the start of the rapidly expanding research area of MOFs.

The first examples of what would now be referred to as a coordination compounds were produced by E. A. Tomic in 1965, who synthesised 'coordination polymers' based on dihydroxynaphthalene-2,6-dicarboxylic acid combined with Zn(II), Ni(II), Al(III), and Fe(III), 2,3,6,7-naphthalenetetracarboxylic acid combined with Th(IV) and pyromellitic acid with Th(IV) and U(IV) in order to investigate their thermal stability[38]. Since then, research into coordination compounds has been increasing, with early papers on MOFs starting to emerge in the 1990's[39].

Early examples include Cu(tpp) and Cu(tcp) (where tpp = 5,10,15,20-tetra(4-pyridyl)-21H-23H-porphyrin and tcp = 5,10,15,20-tetra(4-cyanophenyl)-21H-23H-porphyrin), synthesised by Abrahams *et al.* in 1994. Both frameworks have PtS topology, arising from the use of a porphyrin-based linker as a square planar node and Cu(I) as a tetrahedral node[40].

In 1995, Venkataraman *et al.* synthesised ($[Ag(CPB)(CF_3SO_3)].2C_6H_6$ (where CPB = 1,3,5-tri(3-cyanophenylethynyl)benzene) which is a 2D coordination network based on trigonal pyramidal Ag centres with CPB coordinated via the $C\Xi N^-$ nitrogen, with benzene found in the channels. The authors comment on the 'zeolite-like behaviour' of the framework, as heating to remove the solvent from the channels yields a desolvated sample for single-crystal structure determination without loss of structural integrity[41].

This link from zeolites to MOFs has lead to the development of MOF materials with a variety of interesting structural properties and applications. The aim was to produce material similar to zeolites, but with more tuneable channel and pore sizes, introduction of metal centres for their catalytic properties and ability to enhance gas storage capabilities and functionalization of the organic linkers, again to access frameworks with different applications.

1.5 Porous MOFs

MOFs are of interest due to their wide range of tuneable properties[42]. Current research focuses on the synthesis of porous MOFs as they have applications in many areas of chemistry due to a combination of their robustness and void space, allowing access to metal centres. The specific geometry of metal centres alongside the possible functionalisation of the organic linkers makes porous MOFs extremely useful and gives them potential application in areas such as storage and separation, medicinal applications, catalysis and molecular sensors.

An interest in MOFs was initiated by the study of zeolite materials and their use. Zeolites are aluminosilicate microporous materials primarily used as molecular sieves, with very uniform pore structures, giving them the ability to sort molecules based on their size or geometry. MOFs offer an alternative method for molecular separation, with a more facile synthesis and more adaptable functionality. Frameworks of different topology with different pore sizes can be created to enhance the affinity of the material to one guest over another, thus making them capable of purifying one material by selectively taking up another. This can be extended to the resolution of two enantiomers from a racemic solution, through the use of a chirally selective MOF. Zeolite Y has the highest surface area reported of all aluminosilicate zeolites of 904 m^2/g. Much higher surface areas can be potentially achieved in MOFs, and with a greater possibility to control or alter that area by changing the size and shape of the organic linkers.

Another recent class of MOFs being investigated which mimic the structure of zeolites are zeolitic imidazolate frameworks (ZIFs). It has been shown that the topology of ZIFs synthesised using only imidazole with a tetrahedral metal centre such as Zn(II) or Co(II) is influenced strongly by the

conditions and ratio of imidazole used[43-44]. Porous ZIFs have attracted considerable attention due to their potential applications in areas such as gas storage[45-46] and separation[47]. They are of interest as they mimic the structure of common zeolites but offer a variety of new properties through the introduction of metal centres into the void spaces.

1.5.1 Properties and Applications of Porous MOFs

As a result of their general rigidity and open nature, porous MOFs have found application in many areas of chemistry. They have been found to catalyse different chemical reactions in place of conventional heterogeneous catalysts, store harmful of potentially useful gasses at volumes far beyond those which can be housed in an equivalent sized pressurised vessel and subsequently release those gasses in a much safer manner. As a result, MOFs have potential application in industry, at a large scale, however in order for transfer from lab-scale to industrial plant scale, much research into scalability, stability and cost effectiveness must be carried out.

1.5.1.1 Gas Storage

Storage of gasses is an important area of research as currently most gasses are stored in highly pressurised vessels. This is potentially unsafe if the vessels are not stored correctly and also limits the ability to use gasses as an alternate source of fuel. Gasses such as H_2 and CH_4 have high energy contents, but until they can be stored in a safer way, they cannot be used for their energy in areas such as transportation. Other potentially explosive gasses such as acetylene and toxic gasses such as carbon monoxide also are currently stored under pressure which is not ideal. MOFs offer a potential solution in this area, as they have been shown to have porosity towards a variety of different gasses. This porosity means that MOFs could be used to store gasses in a safer way, with the possibility of creating a way to use fuel gasses in transport. Research has shown that gas storage in MOFs is possible via host-guest and guest-guest interactions and can be optimised through introducing open metal sites into the frameworks, controlling interpenetration and incorporating functional groups onto the linkers[48].

1.5.1.1.1 Hydrogen Storage

Due to the imminent need for a non-petroleum fuel source in transport, the use of H_2 is being investigated as a potential alternative as it possesses an extremely high energy content. However, it is not yet possible to use in this area as it must be stored as either a pressurised gas, cryogenic

liquid or in chemical or physical combination with materials such a metal hydrides[49]. Although materials such as activated carbon and lithium hydride show huge H_2 uptake, their properties cannot be tailored to give them application in other areas of chemistry. MOFs however can be changed or altered for their potential application: Free metal sites can be introduced into the channels of porous materials by using metal-coordinating solvents in the synthesis in a 'template' approach which can be removed post-synthesis leaving the metal sites free for gas binding[50]. This gives MOFs an advantage over other materials, as the affinity of a framework for a particular gas can be altered by changing the metal centre.

The U.S. Department of Energy (DOE) target for hydrogen storage is 1.8 kg/kg (5.5 wt %) by 2017 at an operating temperature of 40-60 °C. There are many examples of MOFs being investigated for their H_2 uptake capabilities, but to date only a few come close to reaching this target[51].

MOF-177, synthesised by Yaghi *et al.*, is the best example of a candidate for H_2 storage in line with the DOE targets. It is a 3D framework based on $ZnO_4(CO_2)_6$ clusters connected via benzene-1,3,5-tribenzoate (1,3,5-BTB) molecules, giving a structure with the formula $Zn_4O(BTB)_2$. The topology is a (6,3)-coordinated net, with the octahedral $Zn(O)_4(CO_2)_6$ at the centre of a six-coordinated site to three 1,3,5-BTB molecules. The structure has extra-large pores that are able to uptake large amounts of guest molecules, including polycyclic organic guest molecules (Astrazon Orange R, Nile Red and Reichardt's dye), although is still considered to be microporous. The pore volume was calculated to be 1.59 cm^3/g using the Dubinin-Radushkevich equation, and the Langmuir surface area assuming monolayer coverage was estimated to be 4,500 m^2g^{-1} following N_2 uptake experiments on a fully evacuated framework at low pressures at which the material is fully saturated by N_2, which produced a type I reversible isotherm[52]. MOF-177 has since been investigated for its uptake capability of other gasses, namely O_2 and H_2. H_2 adsorption at 298 K and 10 MPa was found to be 0.62 wt%, which is one of the highest capacities for a framework material at ambient temperature that has been reported. The material was also shown to preferentially uptake oxygen over nitrogen, which highlights it for potential application in gas purification and separation. Water vapour isotherms showed that the framework could adsorb 10 wt% at 298 K, however it was not stable, meaning that MOF-177 could only be a candidate for gas storage under dry conditions at ambient temperature[53].

Tranchemontagne *et al.* have carried out an investigation looking into ways in which to enhance the H_2 uptake and storage ability of MOFs including using N-containing, B-containing and alkyne-containing frameworks and looking at how interpenetration affects the overall H_2 capacity[54]. Five new frameworks were synthesised; MOF-324, 325 and 326, IRMOF-61 and 62 (*Figure 11*).

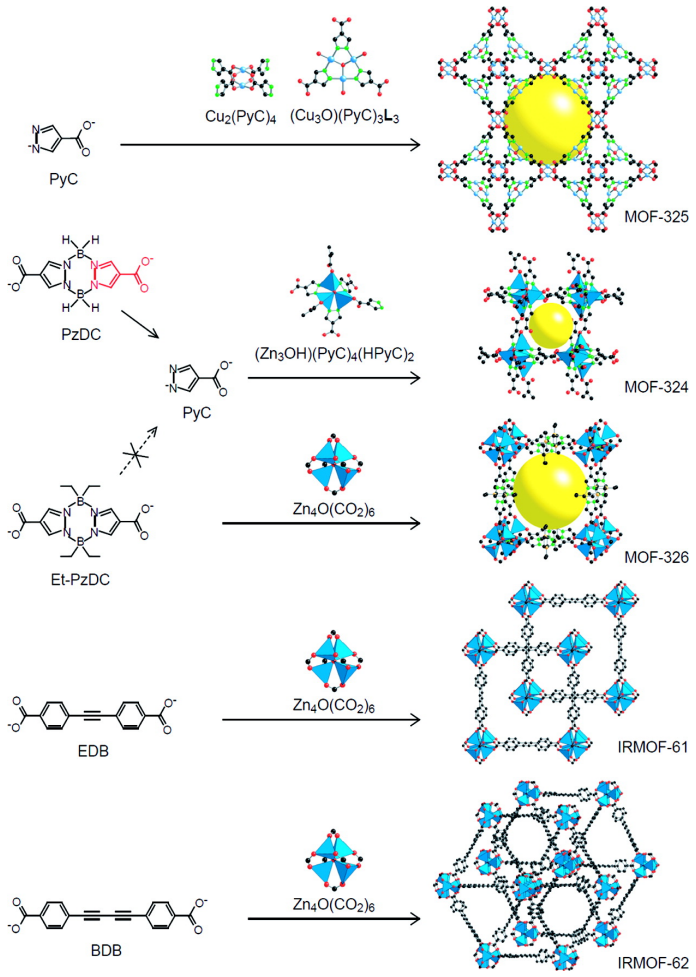

Figure 11: *Organic linkers used (left) in combination with SBUs (middle) producing new MOFs (right). Zn (blue polyhedron), Cu (blue), O (red), C (black), B (orange), N (green). Figure taken from reference*[54].

The frameworks were shown to have BET surface areas of 1600, <10, 1380, 1410 and 2420 m^2/g respectively by means of N_2 isotherms. The H_2 uptake capacity of MOFs-324, -326 and IRMOFs-61 and -62 were measured to be 21.0, 9.2, 10.7 and 17.2 mg/g respectively at 760 torr and 77 K. In comparison with other materials, the authors comment that the highest uptake observed with MOF-324 of 21 mg/g is lower than that of reported MOFs containing free metal centres such as MOF-505 and HKUST-1 with H_2 uptakes of 24 and 25 mg/g respectively, but higher than MOF-5 and MOF-177 with H_2 uptakes of 13 and 12 mg/g at low pressure.

MOF-324 and IRMOF-62 were also investigated for their H_2 storage capacity at high pressure, at 77K. The uptakes observed were 33 and 49 mg/g respectively at 77 K, which in this case is much lower than that of MOF-177 which has a H_2 capacity of 75 mg/g at high pressure due to its much larger surface area. The authors conclude that small-pore diameter MOFs such as MOF-324 show good H_2 uptake at 77 K and 760 torr, the polarisable ligands in MOF-326 enhance host-guest

interactions and interpenetrated structures such as IRMOF-61 and -62 as a result of using longer ligands produce controllable pore diameters which in the case of IRMOF-62 produces a framework with comparable H_2 uptake to MOF-177[54].

Another example of a MOF with high H_2 uptake capacity that reaches uptakes that exceed the DOE target is NOTT-122, synthesised by Yan *et al.*. The framework is based on Cu_2O_8 paddlewheels linked by 1,3,5-BTB ligands in 3D and is made up of three cages with internal diameters of 13, 13.9 and 20 Å. This produces a BET surface area of 3800 m^2/g and a total H_2 uptake of 10.0 wt% at 77 bar and 77 K, as a result of the high surface area and pore volume of the MOF[55].

1.5.1.1.2 Carbon Dioxide Storage

CO_2 capture can be enhanced by introducing free metal sites within the channels of the frameworks to which it can coordinate, or by introducing basic groups which attract the acidic gas. This is an area of interest in MOF chemistry as CO_2 capture and storage technology can potentially be employed to reduce emissions from CO_2 sources[56].

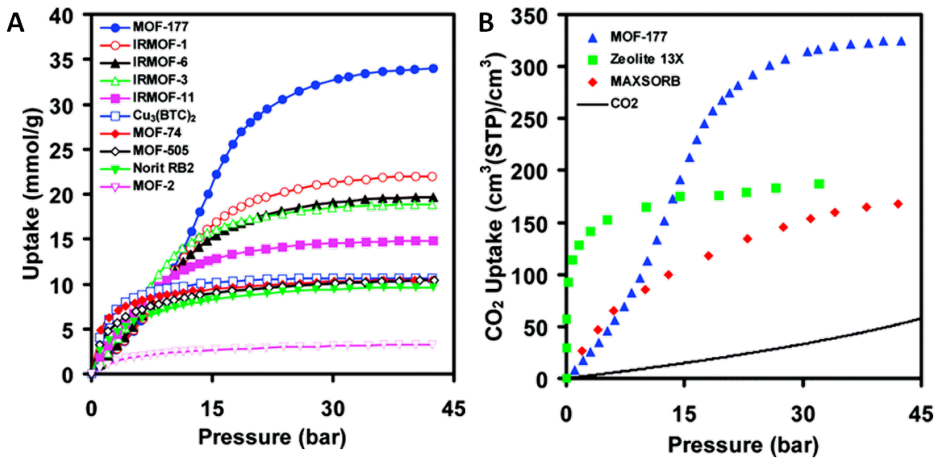

Figure 12: *A: Comparison of gravimetric CO_2 capacities for several MOFs (and an activated carbon as a reference) determined at ambient temperature and pressures up to 42 bar; B: Comparison of the volumetric CO_2 capacity of crystalline MOF-177 relative to zeolite 13X pellets, MAXSORB carbon powder, and pressurized CO_2. Figures taken from reference[26].*

There are many examples of MOFs with good CO_2 uptake capacity[44-45, 56-57]. Millward and Yaghi have selected MOFs that have exceptional CO_2 uptake capacity for discussion, once of which is MOF-177 (*Figure 12*). Today, CO_2 is generally removed from the flue exhausts of power plants by chilling and pressurising the exhaust or passing the fumes through an aqueous solution of amine. There are other methods of CO_2 removal that include chemisorption of the gas onto solid oxide surfaces, however none of these techniques are ideal. Within the paper it is noted that for an

effective adsorption material to have long term viability in CO_2 removal it must reversibly uptake CO_2 and be flexible to a point at which fine-tuning of the framework can be carried out to optimise uptake capacity[26].

MOF-177 can hold up to 33.5 mmol/g, which is far higher than the CO_2 capacity of other reported MOF/ZIF materials and activated carbons. It can hold 9 times more CO_2 in a container at 35 bar than in the same container without adsorbent and a comparable amount of CO_2 to other benchmark materials such as zeolite 13X (32 mmol/g)[58] and the powdered activated carbon MAXSORB (25 mmol/g)[59].

Two large cage ZIFs, ZIF-67[46] and -100[45] have also been shown to have very high CO_2 uptakes. One litre of ZIF-69 can hold 82.6 litres of CO_2 at 273 K and ZIF-100 can hold up to 28.2 litres CO_2 at 273 K (1.7 mmol/g) and 15.9 litres at 298 K. These values exceed the CO_2 capacity of granular BPL carbon[60], giving them potential application as an alternative solid medium for the storage of CO_2.

1.5.1.1.3 Methane Storage

One of the most well-known examples of MOFs is the IRMOF series, published by Eddoaudi *et al.* in 2002. Zn_4O building units linked by dicarboxylate linkers of varying lengths produced a series of MOFs with varying porosity.

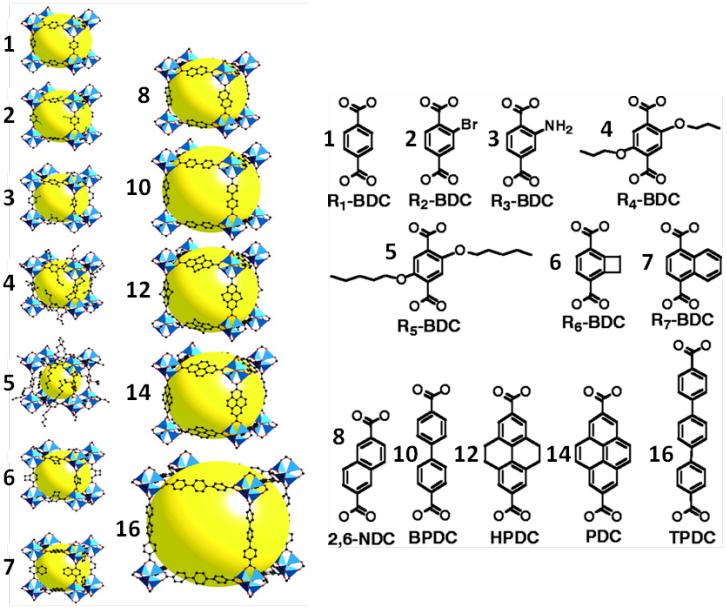

Figure 13: *Single crystal x-ray structures of the IRMOF series (left) with the ligands used for each (right). IRMOF1-8, 10, 2, 14 and 16 are non-interpenetrated and IRMOF 9, 11, 13 and 15 are doubly interpenetrated versions of 10, 12, 14 and 16 respectively. Zn (blue polyhedra), O (red), C (black), Br (green in 2), amino-groups (blue in 3). Figure adapted from reference[24].*

IRMOF-1 (MOF-5) through to IRMOF-16 all have the same cubic topology with pores ranging from 3.8- 28.8 Å in diameter. IRMOF-6 was investigated for storage of CH_4 due to an aperture size in line with the size of a potential CH_4 guest. A N_2 isotherm showed a Langmuir surface area of 2630 m^2/g. Following from this, its CH_4 uptake capacity at standard temperature and pressure was measured to be 240 cm^3 in the pressure range 0 to 42 atm, which is reported to be higher than zeolite 5A which has an uptake capacity of 87 cm^3[24]. CH_4 uptake experiments on IRMOF-1 and -3 showed lower uptakes of 135 and 120 cm^3 respectively and this difference was attributed to the hydrophobic nature of the channels in IRMOF-6.

1.5.1.1.4 Acetylene Storage

Acetylene is an alkyne with the formula C_2H_2 (H-CΞC-H) and is mainly used in welding and to produce ethylene in the production of polyethylene. It is a highly explosive gas and its storage under pressure can result in the exothermic formation of bi-products including benzene and vinylacetylene, which can cause explosions if stored at pressures over 2 atm[48]. This has initiated research into a low-pressure storage alternative, with MOFs being at the forefront.

A series of MOFs with the formula M_2(DHTP) where M=Co(II), Mn(II), Mg(II) and Zn(II) and DHTP = 2,5-dihydroxyterephthalate were synthesised by Xiang *et al.*. The MOFs show respective C_2H_2 uptakes of 230, 182, 167 and 150 cm^3/cm, which are comparable with the C_2H_2 uptake of HKUST-1 at 177 cm^3/cm, with Co_2(DHTP) being the highest reported C_2H_2 uptake to date, making it a good candidate for storage of the gas. This high uptake is attributed to the strong Co(II)$\cdots C_2\Xi H_2$ interactions that form at the vacant metal sites within the channels of the 3D framework[61].

1.5.1.1.5 Harmful Gasses

MOFs are also being investigated for their ability to absorb and capture toxic gasses. Currently, gasses such as SO_2, NH_3, NO NO_2, CO, CO_2, Et_2O and Cl_2 are removed by activated carbons[62], metal oxide impregnated activated carbons[63] and zeolites[64]. MOFs offer surface areas that far exceed those that can be achieved with activated carbons, with vacant metal sites available within the channels and pores.

Britt *et al.* investigated the dynamic adsorption capacity of several MOFs[65]: MOF-5, IRMOF-3, MOF-177, IRMOF-62, which are 3D frameworks based on the $Zn_4O(CO_2)_6$ SBU linked by terephtalic acid, 2-amino terephtalic acid, 1,3,5-benzene tribenzoate, and diacetylene-1,4-bis(4-

benzoic acid) respectively, MOF-199 which is a 3D structure based on a $Cu_2(CO_2)_4$ SBU linked via 1,3,5-benzene tricarboxylate and MOF-74 which is a structure based on 1D chains of $Zn_2O_2(CO_2)_2$ linked by 2,5-dihydroxy terepthalate. The dynamic absorption capacity was measured, which the authors defined as 'the quantity of a gas adsorbed by a material before the time at which the concentration of the gas in the effluent stream reaches an arbitrary "breakthrough" value, 5% of the feed concentration'. IRMOF-3, MOF-74 and MOF-199 were found to hugely outperform BPL carbon, with MOF-199 as an example taking up 59 times more NH_3 and 62 times more SO_2 due to the presence of open Cu sites within the channels. MOF-5 and MOF-177 did not perform as well as BPL carbon due to lack of ligand functionality, however introduction of the amino group into MOF-5 (IRMOF-3) enhanced the NH_3 and SO_2 uptake capacity 18-fold. IRMOF-62 was shown to take up Cl_2, however it was found to be poor in comparison to BPL carbon, possibly due to the reactive nature of the gas. This work demonstrates how MOFs can be used to combat potentially serious problems, with the uptake, capture and storage of harmful gasses from flue gas streams or other sources.

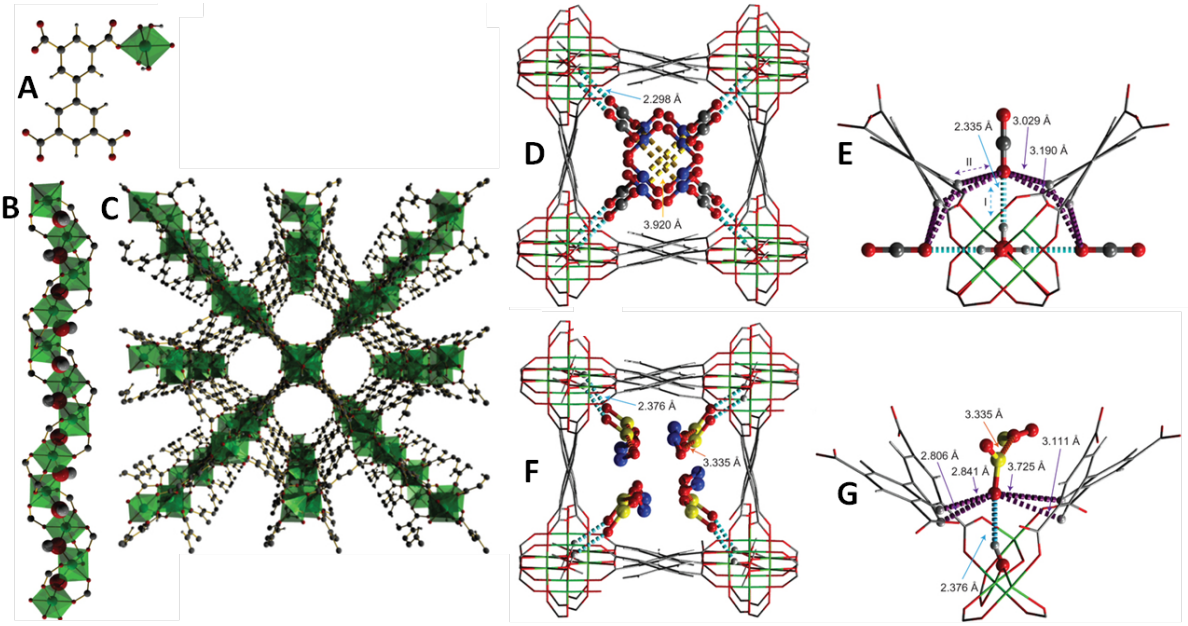

Figure 14: *NOTT-300. A: Coordination of L^{4-} to Al(III); B: Corner-sharing octahedral $[AlO_4(OH)_2]_\infty$ chain; C: 3D structure along the c-axis; D: Structure of NOTT-300·3.2CO_2. Two CO_2 molecules have grey and blue C atoms respectively. O=C=O···CO_2 dipole shown in yellow; E: Role of –OH and –CH groups in CO_2 binding within channels. Al-OH···CO_2 interaction in cyan, -CH···CO_2 interaction shown in purple; F: Structure of NOTT-300·4.0SO_2. Two SO_2 molecules have grey and blue S atoms respectivel; G: Role of –OH and –CH groups in SO2 binding. Al-OH···SO_2 interaction in cyan, -CH···SO_2 interaction shown in purple. Figures taken from reference* [66].

Selective uptake and capture of CO_2 and SO_2 was demonstrated by Yang *et al.* with the MOF, NOTT-300 ($[Al_2(OH)_2(C_{16}O_8H_6)]$)[66]. The structure of NOTT-300 contains chains of $[AlO_4(OH)_2]$ units linked by biphenyl-3,3′,5,5′-tetracarboxylic acid ligands into 3D, with 1D channels of

6.5 × 6.5 Å. The selectivity of the material towards these harmful gasses arises from interactions formed between CO_2 and SO_2 with the Al-OH groups present within the channels. These are accompanied by weak hydrogen bonds forming with the C-H groups of the benzene rings of the channel walls. The interactions that form are strong enough to selectively uptake and store the gasses but sufficiently weak for facile release. This makes NOTT-300 an ideal candidate for the selective uptake and economic release of these two harmful gasses.

The detection of harmful gasses is also an important area of research. Ag nanoparticles coated with the MOF $Cu_3(1,3,5\text{-}BTC)_3(H2O)_3$ (HKUST-1) have been shown to improve the sensing of CO_2 over the un-functionalised Ag nanoparticles, with a 14-fold signal enhancement[67] by Kreno *et al.*. A layer-by-layer method of MOF growth was employed in order to control the thickness of the MOF at the nanoparticle surface. As the MOF is selective to CO_2, it acts as a harmful gas 'recruiter', taking up CO_2 molecules preferentially over other atmospheric gasses and directing them towards the sensing Ag surface.

1.5.1.2 Separation

Separations are important industrially to isolate pure compounds for use in other syntheses or processes. Many compounds produced synthetically yield a combination of more than one product and in some cases it is difficult to obtain high purity yields experimentally.

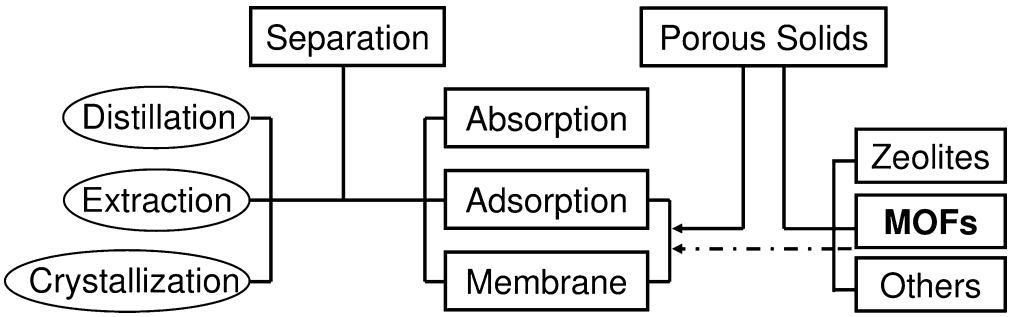

Figure 15: *Separation methods and applications of porous solids acting as the supporting medium in separations. Reference and caption taken from reference*[68].

Separation of compounds is achieved via methods including distillation, extraction and crystallisation, or using porous materials such as zeolites and MOFs, however between 90-95 % of industrial separations are currently carried out using distillation (*Figure 15*)[68]. Distillation relies in a difference in physical properties, mainly the boiling or melting point of the compounds to be

separated and therefore requires a lot of energy in many cases is an economically ineffective process. Sometimes, if the physical properties of two compounds are too similar, such as with *para*- and *meta*-xylene with respective boiling points of 138 and 139 ° respectively, distillation is not feasible and other methods of separation must be employed. A more economic route for separation is desired and MOFs are being investigated for their potential application in this area.

Separation using porous materials is achieved via adsorption or using membranes. Absorptive separation using MOFs relies on different adsorption and desorption behaviour of the compounds to be separated, for example, they may have different steric, kinetic or equilibrium effects. In absorptive separations, host regeneration is important in making the process more economical. Membrane separations involve a thin coating of the MOF of a support, producing a high surface area material. Such materials are lower in cost than bulk MOF separations, easy to process, reliable and are more economical than other methods. Membranes are most often used in gas separations[68].

MOFs offer an advantage over other methods of gas and liquid separation due to the tuneability of their pore size and surface chemistry, stability, flexibility, and more economical operating conditions. MOFs have tuneable pore sizes depending on the size and length of the linker used, so separations based on size exclusion are possible. Also, the pore chemistry can be altered by introducing functional groups which may favour one guest to be taken up over another.

1.5.1.2.1 Gas Separation

There are many examples of MOFs being used for gas separations. The most commonly reported gas separations are CO_2/CH_4 for the enrichment of natural gas. There is also a demand for CO_2 separation from a mixture of gasses; power plant flue gasses generally have a composition of 6.5:1:1 N_2:O_2:CO_2 and removal of CO_2 from this is essential for the reduction of greenhouse gas emissions[57, 69]. The DOE's goal was to have technology in place by 2012 that can achieve 90 % CO_2 capture and storage. MOFs are one of several technologies being investigated for this target as there have been many examples of MOFs that are capable of both storing large amounts of CO_2 and separating it from a mixture of other gasses[57]. Gas separation can be achieved through several effects including gating, the use functional groups within the pores to alter the pore chemistry, size dependant host-guest interactions and guest-guest interactions. The extent of separation is dependent on the strength of one or more of these effects.

Ideally, separation would be based on size exclusion; the MOFs should take up only one guest from a mixture and trap it within the pores. However, design of a MOF with channels small enough to separate CO_2 from a mixture is extremely challenging, so the 'size dependant' separation is

effectively kinetically controlled, as despite the fact that in most cases the pores of MOFs are larger than all gasses, the smaller CO_2 can pass through more quickly and easily, whereas diffusion of other larger gasses is more restricted[68].

CO_2 separation using a gating effect was demonstrated by Seo *et al.* with the framework $Cd_2(pzdc)_2(bhbpb)(H_2O)_2$, where pzdc = pyridine dicarboxylate and bhbpb = 2,5-bis(2-hydroxyethoxy)-1,4-bis(4-pyridyl)benzene). The framework is a 3D pillared network, with Cd-pzdc sheets linked via bhbpb ligands. The ethylene gycol pendent groups branching from the central aromatic ring of the linear bhbpb linker act as molecular gates, activated by the inclusion of guest (H_2O and MeOH). The gate is locked by a hydrogen bond and as a result, no N_2 or O_2 can be taken up by the framework, shown with adsorption isotherms, however as high partial pressures of CO_2, the gate can be opened allowing CO_2 to enter; the framework favours CO_2 over both N_2 and O_2 (*Figure 16A*)[70].

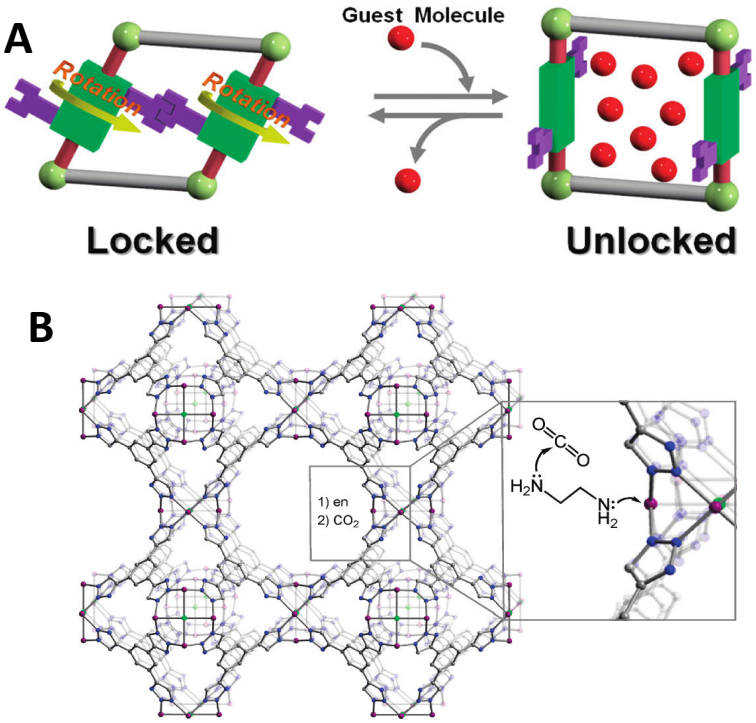

Figure 16: *A: Gating mechanism in $Cd_2(pzdc)_2(bhbpb)(H_2O)_2$. Figure taken from reference [70]; B: Structure and CO_2 uptake enhancement method in $H_3(Cu_4Cl)_3$-$(BTTri)_8$. Figure taken from reference[69].*

Also, CO_2 has quadrupole moment, which other gasses such as CH_4, H_2, N_2, Ar do not have. This can be taken advantage of, by modifying the pores and incorporating functional groups that with attract the polar CO_2 and hold it within the framework, whereas other guest gasses will pass through, not forming any strong host-guest interactions[68]. Demessence *et al.* published an anionic

MOF with the formula $[H_3(Cu_4Cl)_3\text{-}(BTTri)_8]$ where BTTri = 1,3,5-tris(1H-1,2,3-triazol-5-yl)benzene). The material is both air and water stable and is based on a square planar Cl-centered Cu_4Cl^{7+} units bridged by BTTri linkers into a 3D cubic sodalite-type structure. The framework has a BET surface area of 1770 m^2/g shown by a N_2 isotherm at 77K and the CO_2 adsorption isotherm shown a maximum uptake at 1 bar of 90 mmol/g, which is the highest maximum uptake reported. Following activation, the unsaturated Cu sites in the framework were modified by coordinating ethyldiamine (en), which coordinates to the metal centre via one -NH_2 group, with the other free in the channels. This improves the CO_2 uptake at low pressure (0.06 bar) from 0.277 mmol/g (0.92wt%) in the unmodified material to 0.366 mmol/g (1.6 wt%) in the en-modified material. This improvement is attributed to the interaction of polar CO_2 with the amine groups of the en ligand (*Figure 16B*). The MOF was also tested for CO_2/N_2 separation at 298 K and showed a maximum selectivity of 21:1 at 1 bar, which improved to 25:1 when using the en-modified framework[69].

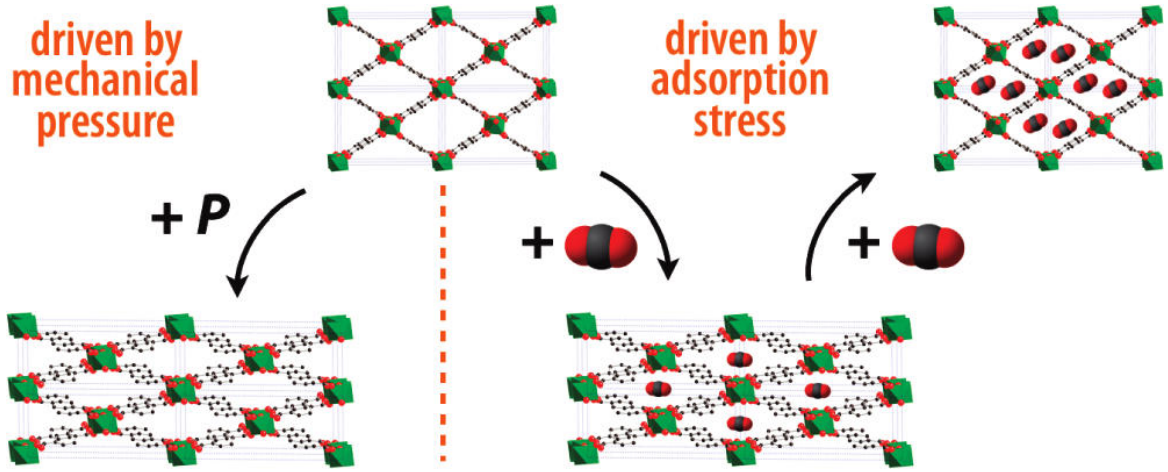

Figure 17: Breathing mechanism in MIL-53(Cr). Pressure induced narrowing of the channels and channel re-opening with the inclusion of CO_2.Figure taken from reference[71].

Size dependent host-guest interactions are most evident in flexible MOFs. When one guest interacts with the host framework it can pass through, but in altering the pore or channel shape it may hinder diffusion of another guest, thus separation of two guest compounds is achieved. An example of this behaviour is shown with MIL-53(Cr). At room temperature and pressure, MIL-53 is in its more stable open form. As CO_2 is taken up by the framework, it interacts with the pore walls, inducing a structural change from the open porous form to the closed form at low pressure (20 kPa). As the pressure of CO_2 is increased (0.4 MPa), the structure switched back to the open form, allowing a larger amount of CO_2 to be taken up. CH_4 does not have this effect on the framework as it does not interact with the channel walls in the same way. At low pressure, in the closed form CH_4 is unable to diffuse through the framework where CO_2 can, giving a potential selectivity for CO_2. When CO_2

and CH_4 are co-adsorbed, the pressure needed to induce the structural change from closed to open is greater, thus the CO_2/CH_4 selectivity decreases with increasing pressure[72].

ZIFs have also been shown to have a high CO_2 capacity. ZIF-20, based on $Zn(purinate)_2$ has a maximum pore aperture of 2.8 Å, smaller than most gasses (*Figure 18A-C*). However, using a gate-type mechanism, the purinate linkers swing open allowing the diffusion of gasses into the cavities. CO_2 and CH_4 uptake isotherms showed that the material takes up around 5 times more CO_2 than CH_4 due to host-guest interactions between the uncoordinated N-sites on the purinate linker with the polar CO_2. This was followed up by a breakthrough experiment which confirmed that ZIF-20 can separate CO_2 from a CH_4[73].

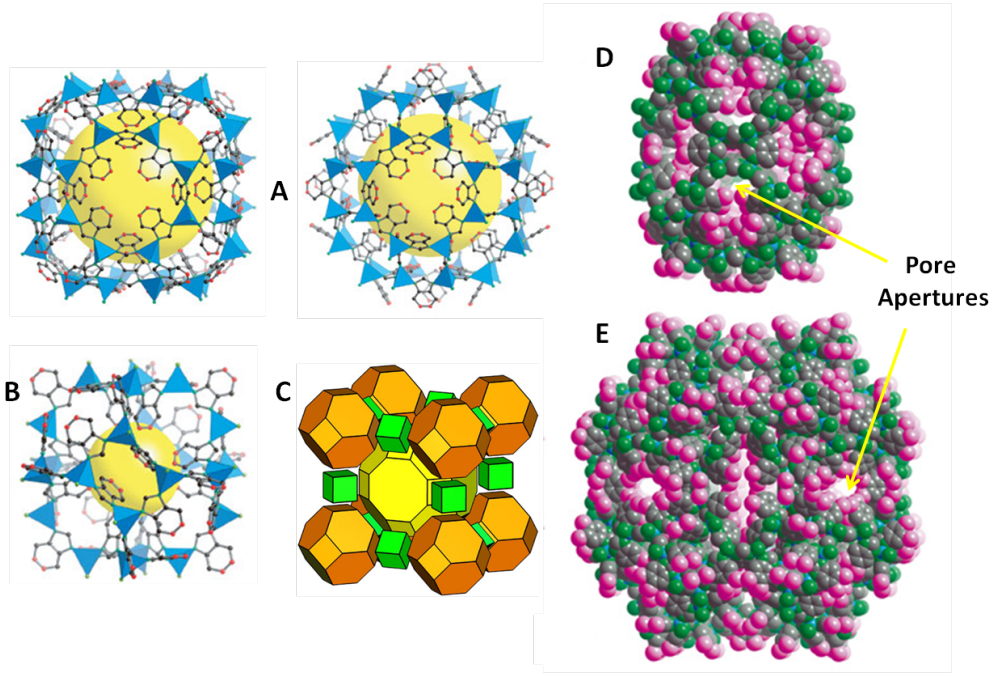

Figure 18: *A-C: Structure of ZIF-20. A: Two α-cages and B: Cube cage that all link to form C: The LTA topology structure. Figures taken from reference[73]; D: ZIF-95; E: ZIF-100.Figures taken from reference[45].*

ZIF-95 and -100 have been shown to separate CO_2 from N_2 with selectivities of 18:1 and 25:1 respectively and CO_2 from CO with selectivities of 11.5 and 17.5 respectively (*Figure 18D,E*). These high selectivities towards CO_2 are attributed to both ideal size pore apertures of 3.65 and 3.35 Å, similar in size to CO_2 (~3 Å), leading to huge cavities of 24.0 and 35.6 Å respectively, which act as CO_2 reservoirs, alongside strong quadrupolar interactions between CO_2 and the N-atoms that line the cavity walls[45].

Separation of similar boiling gaseous hydrocarbons is also an important area of research. Ethane/ethene and propane/propene mixtures are currently separated using cryogenic distillation,

however this is energy inefficient due to the low temperatures and high pressures required[74]. Geier *et al.* have used MOF-74 (CPO-27, [M_2(dobdc)] (dobdc^{4-} = 2,5-dioxido-1,4-benzenedicarboxylate), M = isostructural Zn(II), Co(II), Ni(II), Mg(II), Mn(II), Fe(II)) to selectively separate these two mixtures of hydrocarbons (*Figure 19A*)[75]. From gas sorption isotherms collected at 45 °C and 1 bar, the IAST selectivity was determined using the formula $S = [n_{alkene}/n_{alkane}] / [x_{alkene}/x_{alkane}]$ for each isostructural MOF over a range of compositions (*Figure 19C,D*).

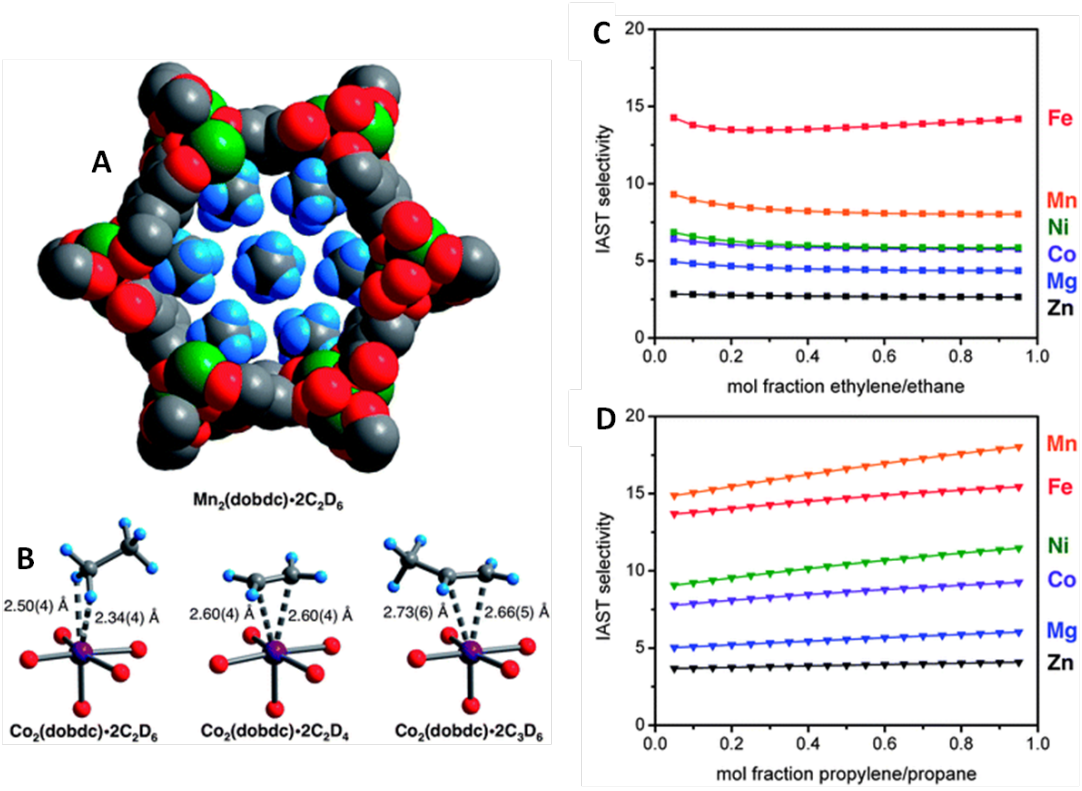

Figure 19: *A: Channel within structure of $Mn_2(dobdc)\cdot 2C_2D_6$ determined from neutron diffraction; B: First coordination sphere for Co in $Co_2(dobdc)$ when exposed to ethane, ethane and propene; C: IAST selectivity of MOF-74 analogues towards ethane/ethane mixtures; D: IAST selectivity of MOF-74 analogues towards propene/propane mixtures. Figures taken from reference*[75].

Overall the results show that the selectivity of the frameworks towards propene is generally higher than for ethene due to the increased polarizability of the guests. The propene/propane selectivity of the MOF-74 analogues increases with increasing propene content, whereas the ethane/ethane selectivity remains constant across all compositions. The highest selectivity observed for propene/propane is with the Mn analogue with a high of 18, and the highest observed for ethene/ethane is with the Fe analogue at 15. The selectivity towards the unsaturated hydrocarbons observed is due to the interactions that can form between the M^{2+} metal centre and the C=C double bond; interactions that cannot form in the case of saturated hydrocarbons (*Figure 19B*).

1.5.1.2.2 Liquid Separation

Liquid separation works on the same principles as gas separation. The separation of liquids can be achieved by either vapourising and subsequent separation as a vapour, or in the liquid phase. Vapour phase separation of liquids is generally achieved using gas chromatography (GC) and liquid phase via standard liquid chromatography.

Separation relies on size or shape exclusion and different host-guest interactions. The framework $(H_2dab)[Zn_2(ox)_3]_3$, where dab = diamino butane and ox = oxalate, was synthesised by Sadakiyo *et al.* and is based on 2D sheets of $Zn_2(ox)_3$ with H_2dab present in the voids between the 2D sheets as counter ions. The $–NH_3^+$ groups of the H_2dab molecules hydrogen bonds with the oxygens of the ox linkers, holding the guest in place. As there are hydrogen bonding sites in the interlayer space, the material absorbs protic solvents including H_2O, EtOH and MeOH but does not absorb H_2, N_2, MeCN, other non-polar solvents, or PrOH or BuOH. This work shows that both size exclusion and host-guest interactions play a part in the selectivity of the material; guests larger than EtOH cannot be taken up to to void size restrictions and guests that cannot form host-guest hydrogen bonds are also not taken up by the framework[76].

Xylenes have been separated by GC by Yan *et al.* with baseline resolution within 2 minutes. Isolation of pure xylenes is essential in industry, for example, *para*-xylene is used as a precursor in the synthesis of polyester[77]. Other xylene contaminants in this synthesis would yield an un-useable product. A capillary column was coated with MIL-101, a framework based on unsaturated Cr metal sites and the 1,4-BDC linker. A sample of mixed xylenes (*Para*-, *meta*-, *ortho*-xylene (pX, mX, oX) and ethylbenzene (EB)) were vapourised and passed through the column, with pX eluting first, followed by mX, then EB then oX. The selectivity observed is due to both pore-filling effects, host-guest interactions and polarity of the MIL-101 framework[78]. A similar effect was observed with MIL-47, in which the different C8 aromatics (pX, mX, oX and EB) packed differently within the pores due to steric effects and resuted in GC separation of the isomers, but with pX and mX eluting at the same time, followed by EB then oX. The linear pX molecule is able to enter in line with the channel perfectly and it can therefore leave easily, hence it is eluted first. The mX guest has slightly more steric hindrance within the channels but can tilt to accommodate this and so can enter and leave easily, eluting alongside pX. The larger steric ethyl groups on EB hinder progress through the channels, so it eluted after mX and pX and the largest isomer oX elutes last, as progress through the channels is greatly hindered due to its wider diameter[79].

The MOF Mn(1,4-BDC)(BNPO), where BNPO = 4,4′-bipyridine-N,N′-dioxide, was synthesised by Xu *et al.* and is based on infinite chains of MnO_6 octahedra bridged into 3D by the organic ligands. The framework was synthesised using DMF, so the structure has DMF present within the channels.

However, upon activation and DMF removal, the vacant structure has more closed channels, similar to the breathing effect observed with MIL-53[80]. Single crystals were loaded with benzene, toluene and chlorobenzene and analysis showed that all three aromatic compounds could be taken up into the channels in pairs, with two symmetry equivalent positions for each pair. When an equimolar mixture of toluene and benzene were exposed to the framework, only benzene was selectively taken up; no toluene could be found in the single crystal structure. A similar effect was observed when using an equimolar mixture of chlorobenzene and benzene, from which only chlorobenzene was taken up by the single crystals. The order of selectivity was explained by the host-guest and guest-guest interactions present. All three guests form parallel displaced π-π stacking interactions with one another. They also form T-shaped π-π interactions with the central aromatic ring of the 1,4-BDC linker, but whereas two symmetrical interactions are picked up for toluene and chlorobenzene, only one is present for benzene. Also, chlorobenzene picks up an additional C-H···Cl hydrogen bond which the other guests cannot, hence the selectivity trend is chlorobenzene>toluene>benzene[81].

Ortho-susbtituted aromatics have also been selectively separated using MIL-53. Alaerts *et al.* separated mixtures of xylenes and EB, ethyl toluenes and cymenes using batch liquid separation, poulse chromatography and breakthrough experiments[82]. With the xylenes, the batch experiments showed that the framework had a preference for oX over pX, mX and EB, with selectivities of 11:1 for oX:EB, 3.8:1 for oX:mX and 3.1:1 for oX:pX. This was followed by by pulse chromatography experiments which showed EB eluting first, followed by a mixed pX/mX peak, followed by oX. The preferred selectivity of MIL-53 for oX was confirmed by breakthrough experiments in which showed oX eluting a crystallite-filled column 20 minutes after EB and 9 minutes after mX. The selectivity is attributed to pore-filling effects, similar to those observed in the vapour phase separation of C8 isomers using MIL-101[83]. The same ortho-preferred selectivity was seen with the larger ethyltoluene and cymene guests: O-ethyltoluene is selectively absorbed in the liquid batch experiments over p- and m-ethyl toluene with selectivities of 5.5:1 and 4.7:1 respectively and o-cymene was selectively absorbed over p-cymene and m-cymene with selectivities of 7.1:1 and 4.6:1 respectively. In the breakthrough experiments, both o-ethyltoluene and o-cymene were eluted last, as seen with the xylenes. In all cases, pore-filling effects are responsible for the strong preference of MIL-53 towards ortho-substituted compounds. The methyl groups of the ortho-isomers are able to interact with the host-carboxylate groups, with the other isomers cannot.[82].

1.5.1.2.3 Stereoisomer Separation

Stereoisomers are compounds that have the same molecular formula and bond sequence, but a different 3D arrangement of atoms. This term includes *cis-trans* isomerism and chiral compounds.

Chiral Separation

Isolation of enantiomerically pure chiral compounds is challenging and therefore chiral separation is necessary. It is of great concern in the pharmaceutical industry, as in most cases a drug is only active in one of its chiral forms, and administration of the opposite enantiomer can have unwanted side effects. One famous example is the compound thalidomide ((*RS*)-2-(2,6-dioxopiperidin-3-yl)-1*H*-isoindole-1,3(2*H*)-dione) which highlights the how crucial such separations are: In the 1950's, expectant mothers were given a racemic mixture of the drug to combat morning sickness, however it was later discovered that only one enantiomer has these positive effects; the other caused thousands of children to either die early or be born with birth defects.

Currently, optically pure compounds are sythesised via isolation from natural resources, direct synthesis using homochiral reagents and synthesis using asymmetric catalysis[68]. The separation of racemic products is achieved by chromatography.

Recently, MOFs have been shown to have the ability to separate chiral compounds using batch liquid separation and are being researched as a potential alternative in chiral separations.

Chiral MOFs can be synthesised by:

(i) Synthesising a MOF using a chiral linker,
(ii) Synthesising a framework that crystallises in a chiral space group,
(iii) Introduce a chiral functional group into the pores of a MOF post-synthesis.

All of these methods will produce a framework with chiral pores that have the potential to separate chiral compounds.

An example of a MOF being used for chiral separation is $Ni_2(L\text{-asp})_2(bipy)$[84]. The framework was produced by first synthesising phase pure and enantiomerically pure Ni(L-asp) units, followed by solvothermal combination with the 4,4'-bipy linker, yielding a 3D framework with chiral channels. Careful control of the synthesis conditions was required to avoid conversion of L-aspartate to D-aspartate at high temperatures. The MOF was able to separate chiral diols in liquid batch experiments, in which a mixture of R- and S- enantiomers were exposed to the framework for 24 hours, after which time the framework was washed and the guest diols were extracted via

microdistillation for GC analysis. The R-enantiomer preferred over to S- in all cases, with the highest reported enantiomeric excess (e.e.) observed for the compounds with a 1,3- orientation of -OH groups branching from the carbon chain, with 2-methyl-2,4-pentane diol at 53.7 % and other high e.e. values of 24.5 and 17.9 % reported for 2,4-pentane diol and 1,3-butane diol. In this case, the MOF $Ni_2(L\text{-asp})_2(bipy)$ was synthesised using a chiral linker and crystallised in the chiral space group $P2_12_12$ with chiral channels that were able to separate chiral guests. In the paper the authors comment that the racemic version of the MOF, $Ni_2(DL\text{-asp})_2(bipy)$ was also synthesised, but crystallised in a non-chiral space group $P2_1/n$, with non-chiral channels and was unable to separate the same chiral compounds.

Cis-Trans Isomer Separation

Alkenes are the starting or intermediate materials in the synthesis of high performance polymers, insecticides and pesticides, however the separation of their similar boiling isomers is difficult and currently separation is achieved via costly crystallisation or cryogenic distillation. Zeolites have been shown to have application in the absorptive separation of *cis*- and *trans*- alkenes based on size exclusion, where the bulkier *cis*-isomer cannot enter the channels. Alaerts *et al.* carried out absorptive separations of alkenes using $Cu_3(1,3,5\text{-BTC})_2$ which was able to take up and contain the guest due to interaction of the C=C double bond with the open Cu(II) metal sites in the channels. In batch experiments using butene, *cis*-but-2-ene was preferred to *trans*-but-2-ene with a selectivity of 1.9:1 and the same preference for the *cis*-isomer was also observed with pent-2-ene isomers. This preference for the *cis*-isomer in both cases was attributed to the fact that within the framework, the Cu(II) metal centres are held in a plane by four O atoms. The *cis*-isomers will be able to approach the place with less seric hindrance than the trans-isomers, hence selectivity is observed[85].

Maes *et al.* used MIL-96 to separate *cis*- and *trans*- piperidines. MIL-96 has the formula $Al_2O(OH)_{18}(H_2O)_3(Al_2(OH)_4)[1,3,5\text{-BTC}]_6\cdot 24H_2O$, first synthesised by Loiseau et al.[86] and is a 3D framework based on a honeycomb lattice of $Al_4(OH)_2$ and $Al_2(OH)_4$ octahedra, linked via 1,3,5-BTC molecules, Al-μ_3-O clusters isolated within the channels, linked to the main framework by the 1,3,5-BTC ligands. The structure contains an A and two B cages at 417 and 635 $Å^3$ respectively. The cages can take up 2 *trans*-piperidines per cage, but only around 0.5 *cis*-piperidines due to steric effects. This leads to a selectivity for the *trans*-isomer at 3.7:1 at low concentration, increasing to 9.5:1 at high concentrations. This increase in selectivity is due to the diffusion through the narrow cavity windows and enhanced packing of the *trans*-isomer within the cages with increasing concentration which cannot be achieved for the bulkier *cis*-isomer. When

compared to zeolite 5A, which has selectivities of 3.8-4.3, this work shows how separation can be achieved via size exclusion and enhanced using MOFs with available metal sites[87].

1.5.1.3 Catalysis

Introduction of metal centres into porous materials gives them potential applications in catalysis. In MOFs, metal sites may be solvated after synthesis, but activation will give rise to metals with available coordination sites. These Lewis acidic vacant metal sites are present within the channels and can act as catalytic sites in many organic or photochemical reactions.

Li *et al.* synthesised MOF-based catalysts to speed up the rate of H_2 release from ammonium borane (NH_3BH_3, AB). Safe storage of H_2 is essential it is to be used as a fuel in transportation[88]. AB is stable in air and has a high H_2 capacity of 19.6 wt% making it an ideal candidate for research into its application for H_2 storage[89], however unless carried out at temperatures over 100 °C or catalysed[90], the dehyrogenation of this material is slow.

Two novel MOFcats (MOF catalysts) were synthesised from microporous MOFs with catalytic Ni^0 sites; MOF1 ([Ni(4,4'-bipy)][HBTC], 4,4-bipy = 4,4'-bipyridine) and MOF2 ([Ni(pyz)][$Ni(CN)_4$], pyz = pyrazine). MOFcat1 and MOFcat2 have lowered the dehdrogenation activation energy of AB and significantly increased the H_2 release rates at temperatures below 90 °C[91]. At 80 °C, MOFcat1 and MOFcat2 release $H_{2\,at}$ 7.5 wt% in 2 hours and 6.0 wt% in 40 minutes respectively and at 90 °C, release 7.0 wt% in 40 minutes and 6.0 wt% in 20 minutes respectively.

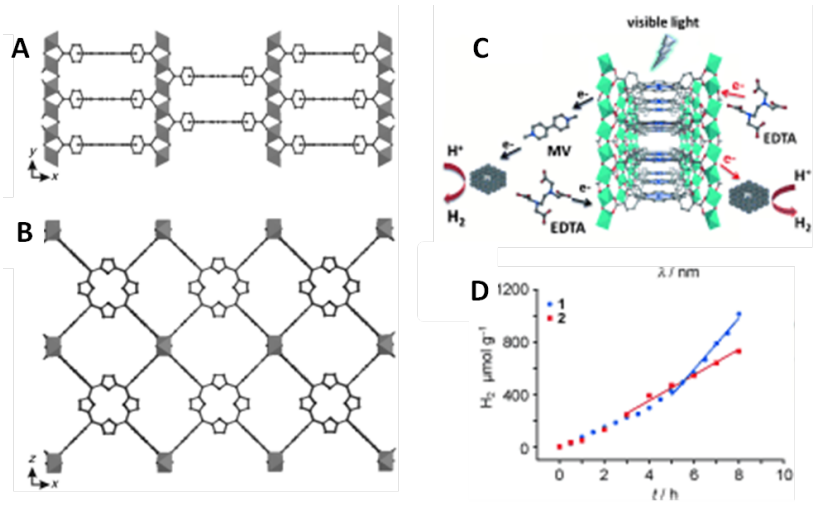

Figure 20: *Crystal structure of Al-PMOF viewed down A: 100 and B: 001 directions; C: Schematic representation for the photocatalytic reactions. Left: Reaction involving Al-PMOF, methyl viologen, colloidal Pt and sacrificial EDTA; Right: Reaction involving Al-PMOF, colloidal Pt and sacrificial EDTA, where EDTA = Ethylenediaminetetraacetic acid; D: Photocatalytic evolution of H_2 from H_2O by 1. Free-base Al-PMOF (blue) and 2. ZnAl-PMOF. Figures adapted from reference[92]*

In catalysis, a reagent is used to speed up a chemical reaction, remaining chemically unchanged itself. Photocatlaysis involves the use of a light-activated catalyst, which once activated can also speed up a chemical process.

Another method by which H_2 can be obtained is via the H_2O splitting process. Recent work in MOF synthesis has produced a number of examples of MOFs capable of this reaction[93].

One example of a MOF-photocatalyst in the H_2O splitting reactions was shown by Fateeva e*t al.*. Porphyrin complexes are well known as photo catalysts; The group synthesised a water-stable 3D porphyrin based Al-containing MOF (Al-PMOF)[92], with 3D porosity. Elliptical pores of 6 × 11 Å run along the 010 direction connected by 5 Å rectangular pores running along the 100 and 001 directions (*Figure 20B*). Modification of the Al-PMOF with addition of Zn(II) ions to the free base sites produced ZnAl-PMOF. The authors demonstrated that the ZnAl-PMOF was an active photocatalyst, producing 200 μmol of H_2 per hour per gram under visible radiation with 0.1% efficiency, illustrating one of the first visible light photocatalytic MOFs.

1.5.1.4 Sensors

MOFs are good candidates for sensors as they combine permanent porosity with vacant metal sites and allow choice of metal and ligand combination depending on the characteristic properties required. Fluorescent MOFs can absorb guests into their pores to alter emission, by changing intensity or altering wavelength of emission. The fluorescent behaviour of a MOF can result from ligand-based or metal-based fluorescence. The use of highly conjugated aromatic ligands may produce intraligand emission, ligand-metal (LMCT) or metal-ligand (MLCT) charge transfer. Metal-based emission generally results from incorporation of a lanthanide metal centre, which have characteristic luminescent properties (*Figure 21*). Lanthinide (III) ions (Ln(III)) have well defined energy levels which are specific and characteristic to each individual Ln(III). Laporte-forbidden f-f emissions range from the visible to near-IR region of the spectrum depending on the Ln(III) ion, with a different colour emission for each. For example, Tm(III) emits in the blue, Dy(III) in yellow, Tb(III) in green, Sm(III) in orange, Eu(III) in red and near-IR for Yb(III), Nd(III) and Er(III)[94]. As these f-f transitions are forbidden, the excited states have long lifetimes, however the Ln(III) ions themselves have low absorption coefficients.

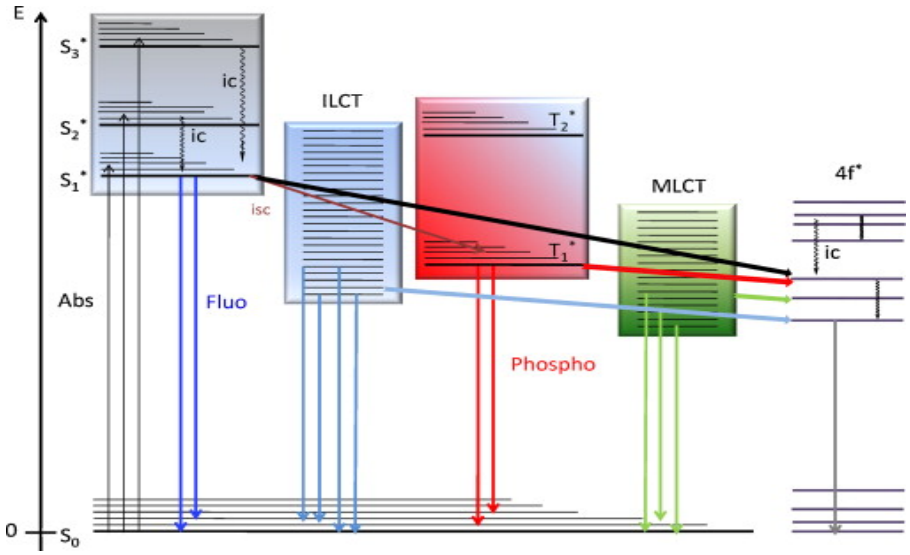

Figure 21: *Schematic representation of the photophysical processes that can occur in the antenna sensitization of a lanthanide luminescence (S: singlet state, T: triplet state, Abs: absorption, ic: internal conversion, Fluo: fluorescence, Phospho: phosphorescence, isc: intersystem crossing, ILCT: IntraLigand Charge Transfer, MLCT: metal-to-ligand charge transfer). Figure taken from reference*[94].

MOFs have been researched for their luminescent properties as they offer the opportunity to fine-tune the luminescent behaviour of the metal Ln ion as both ligand chemistry and trapped guest can alter their emission. There are many examples of Ln-MOFs produced through combination of lanthanide salts with carboxylate ligands in hydro(solvo)thermal synthesis using DMF, EtOH and acetonitrile as solvents[95].

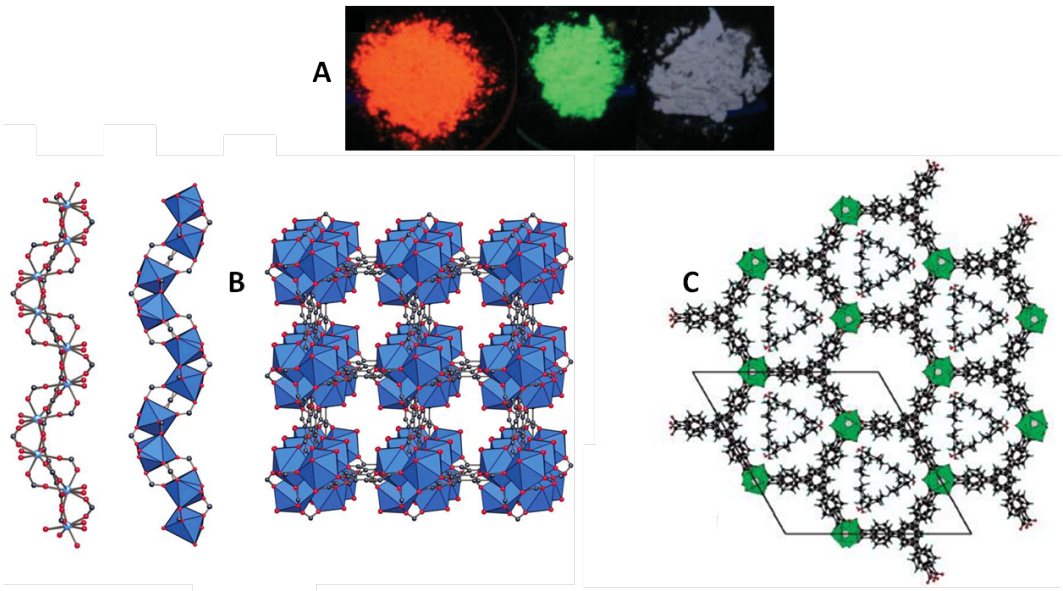

Figure 22: *A: MIL-78(Y, Eu) (red), MIL-78(Y, Tb) (green) and MIL-78(Y, Dy) (blue). Figure taken from reference*[96]*; B: Structure of MIL-76. Tb-carboxylate SBU (left) and 3D structure (right) Figure taken from reference*[97]*; C: MIL-103(Tb) 3D structure. Figure taken from reference*[98].

MIL-78(Y, Eu) has the formula $Y_{1-x}Eu_x$(1,3,5-BTC) (x ~ 0.024) and is a highly luminescent Y-doped 3D Ln-MOF. The framework has high thermal stability and emits in the red under UV irradiation. Tb(III) and Dy(III) analogues, MIL-78(Y, Tb) and MIL-78(Y, Dy) have also been synthesised and emit in the green and blue respectively under UV irradiation (*Figure 22A*)[96].
Another example is MIL-76(Tb) with the formula (Tb(1,3,5-BTC)$(H_2O)_{1.5}$·(DMF), synthesised by Rosi *et al.*. The 7-coordinate Tb(III) has six carboxylate oxygens from the 1,3,5-BTC ligand and one terminal H_2O coordinated, which forms Tb-carboxylate rod SBUs, held in 3D by bridging 1,3,5-BTC ligands. Following activation at 200 °C, MOF-76(Tb) has an N_2 Langmuir surface area of 334 m^2/g (*Figure 22B*)[97]. Devic *et al.* have since extended the linker and synthesised a new 3D framework based on 1,3,5-BTB with the formula Tb(1,3,5-BTB)(H_2O)·2$(C_6H_{12}O)$ (MIL-103). MIL-103(Tb) has a Langmuir surface area of between ranging from 1030 to 1330 m^2/g depending on the sample used (*Figure 22C*)[98].

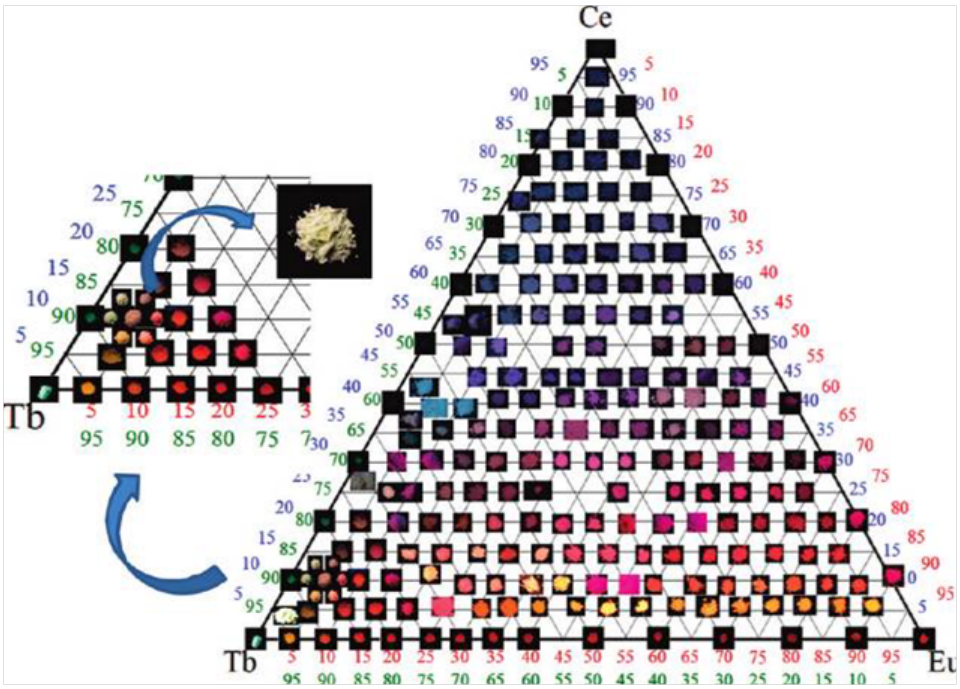

*Figure 23: Photographs of the luminescence of the compounds with general formula [(Ce_2-x-y*Eu*x*Tb*y*)($C_8H_4O_4$)$_3$(H_2O)$_4$]∞ with* x + *y* ≤ *2 under UV Irradiation. Figure and caption taken from reference*[99].

Mixed Ln-MOFs have also been shown to have interesting properties. Tb(III) emits in the green, Ce(III) emits in the blue and Eu(III) emits in the red region of the visible spectrum. Kerbellec *et al.* have synthesised a range of Ln-MOFs with the general formula [(Ce_2-*x*-*y*Eu*x*Tb*y*)($C_8H_4O_4$)$_3$(H_2O)$_4$]∞ with *x* + y ≤ 2. Varying the relative amounts of Ce:Tb:Eu results in a wide range of frameworks with a variety of luminescent properties, producing a range of colours (*Figure 23*)[99].

MOFs can be used as sensors in two ways: The MOF itself reacts to external stimuli or the response is guest dependant[100]. Many MOFs produce optical responses depending on solvent coordination to the metal centre or guest inclusion; depending on the coordination environment. For example, the desolvation of HKUST-1 induces a colour change from turquoise to dark blue and subsequent reexposure to air regenerates the turquoise colour[101]. ZIF-8 films have been used to produce a Fabry-Pérot device. Layers of different thickness lead to colouration of the originally colourless ZIF-8 films when grown on a silicon surface due to optical interference. Upon exposure to propane gas shifts the colour of the film and is sensitive to propane partial pressure[102].

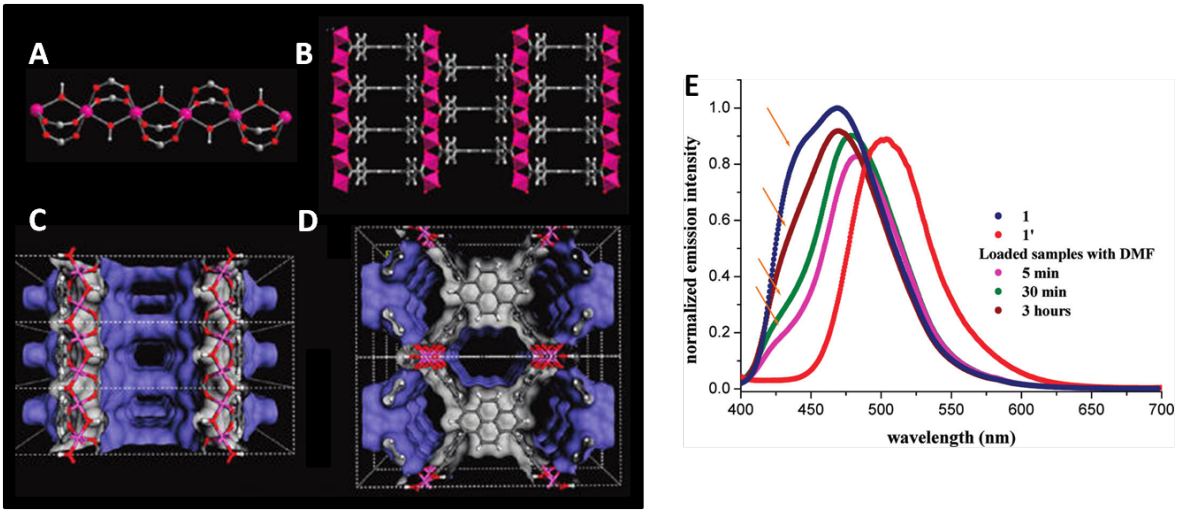

Figure 24: *A: 1D $InO_4(OH)_2$ chains in 1 viewed along the [010] direction; B: View of the structure of 1 along [001], showing the infinite chains of $InO_4(OH)_2$ units (pink octahedra) connected via the TBAPy ligand (In, pink; C, gray;H, white; O, red); Connolly surface representations with a probe radius of 1 Å of the 3D non-interpenetrated structure of 1 viewed along the C: 001 and D: 010 directions (gray is outside the surface, and blue is inside the surface); E: Effect of DMF molecules on the fluorescence characteristics of $In_2(OH)_2$(TBAPy). Figure adapted from reference[103].*

Stylianou *et al.* have synthesised a 3D fluorescent MOF based on the 1,3,6,8-tetrakis(p-benzoic acid)pyrene (TBAPy) ligand combined with an In(III) metal centre. The structure is based on In-carboxylate chains linked by TBAPy ligands. The framework has the formula $[In_2(OH)_2(TBAPy)]\cdot guests$, has a BET surface area of 1189 m^2/g and displays ligand-based fluorescence that is guest-dependant (*Figure 24*). DMF is present in the channels after synthesis and this improves the fluorescence by achieving the spatial separation of the TBAPy ligands in this structure and so avoiding self-quenching. Substitution with toluene results is π-π stacking between the guest toluene and TBAPy ligands which quenches the materials florescence. When non- polar molecules such as dioxane enter the channels, the weaker host-guest interactions quench the emission more effectively[103].

1.5.1.5 Post-Synthetic Modification

Post-Synthetic mModification (PSM) of MOFs is a useful tool as it allows access to structures that would not usually form under standard MOF forming conditions, with modified ligands that may be extremely difficult to synthesise using standard organic chemistry techniques. These frameworks can be designed for their potential applications and extends the possibilities of MOFs, by introducing chemical functionality or catalytic metal sites into the pores of a pre-formed MOF.

Functionality can be introduced in the initial synthesis in structures such as IRMOF-3, in which an amino group has been added to the 1,4-BDC ligand (as used in the synthesis of IRMOF-1), producing an isostructural framework but with added functionality[24].

PSM is used where this technique cannot be employed. There are three types of PSM characterised by the chemical bond(s) that are broken during the PSM approach[104]:

(i) Covalent PSM
(ii) Dative PSM
(iii) Post-synthetic Deprotection (PSD)

In covalent PSM, the MOF is modified heterogeneously using a reagent to form a new covalent bond, generally at the organic linker. In dative PSM, a dative bond is formed heterogeneously between a reagent and some part of the MOF, generally a metal-reagent dative bond. PSD involves bond cleavage within a MOF, for example, deprotection of an ester functionality to become a carboxylate or alcohol group[104].

Today there are many examples of MOFs that have been post-synthetically modified to produce frameworks with new applications compared to their parent materials. An example of the use of covalent and dative PSM was shown by Ingleson *et al.*, in which IRMOF-3 (2-amino functionalised 1,4-BDC linker) was modified using salicylaldehyde to form the modified IRMOF-3sal. This Schiff base functional group was able to bind $V(O)(acac)_2$ (acac = acetylacentoate) within the channels of the framework, producing IRMOF-3Vsal (*Figure 25A*). These steps show that introducing a strong metal chelator into the pores of the framework does not damage the structural integrity of the material and yields a 3D porous framework with metal sites available in the channels as additional functionality; a framework that could not have been produced in a one-step solvothermal reaction.

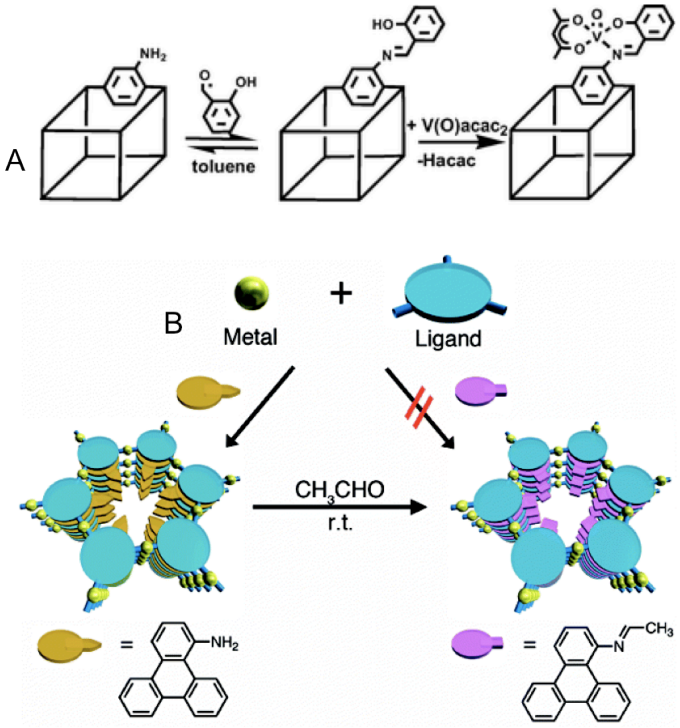

Figure 25: *A: PSM of IRMOF-3 to produce Schiff base functionality on 1,4-BDC linker with the ability to bind catalytic metal sites. Figure taken from*[105]*; B: PSM of trapped guest in the pores of a MOF, resulting in the formation of a framework that could not be produced under the same solvothermal conditions as the parent material. Figure taken from*[106].

As the material contains free metal sites in the pores, it was investigated for its catalytic properties. In the oxidation reaction of cyclohexene with ^{t}BuOOH, the MOF showed 40 % conversion. This demonstrated the usefulness of PSM and how it can be used to produce MOFs with applications in many areas of chemistry[105].

Guest molecules in the pores of MOFs can also be used for PSM. Haneda *et al.* synthesized a 3D framework based on Zn(II) and 1-aminotriphenylene linkers with trapped 1-aminotriphenylene guest molecules in the channels of the MOF, held in place by π···π stacking interactions[106]. Reaction with EtOH resulted in a chemical reaction with the amino group of the trapped guest molecules, producing an unstable imine within the pores (*Figure 25B*). The resulting framework could not be synthesised under similar solvothermal conditions and the process was monitored by single crystal x-ray diffraction. This highlights the stability of the framework, as through the making of new covalent bond under reaction conditions, the structural integrity of the single crystals was not affected.

The physical properties of MOFs can be enhanced by changing the pore chemistry using PSM. Wang *et al.* showed that the H_2 uptake capacity of IRMOF-3 and UMCM-1-NH_2; frameworks

based on Zn(II) and 2-NH_2-1,4-BDC, could be enhanced by modifying with anhydrides[107]. New frameworks IRMOF-3-AMPh and UMCM-1-AMPh were isolated from the parent framework by carrying out PSM using benzoic anhydride which reacted at the amino group in the channels to form the resulting MOFs. The H_2 uptake capacity increased from 1.51 and 1.35 wt % respectively for IRMOF-3 and UMCM-1-NH_2 to 1.73 and 1.54 wt % respectively for IRMOF-3-AMPh and UMCM-1-AMPh, due to the enhanced interaction of H_2 with the phenyl groups of the modified host.

1.5.1.6 Medicinal Applications

Recently, MOFs have started to be investigated for potential application in drug delivery[108]. There are several strict regulations that must be followed for substances to be used *in vivo*: their efficacy, toxicology, ease of reproducibility and manufacture and their stability[109]. In 2010, Horcajada *et al.* published work showing that the iron carboxylate MOFs MIL88A (butane-dioic acid), MIL-88Bt (tetramethyl terepthalate) and MIL-100 (benzene tribenzaote) were non-toxic under biological conditions and produced no negative side effects when administered at a rate of 220 mg/g[110], opening the door for the investigation of MOFs as drug delivery agents.

In general, MOFs are investigated for high stability, as low thermal or moisture stability may reduce its potential applications in gas storage, catalysis and separation. However for medicinal applications, an element of instability is required. If slow degradation can be achieved with non-toxic consequences, MOFs can be used as nano encapsulators, taking up large quantities of a drug and releasing it slowly over a given period of time with MOF degradation.

An amino functionalised MIL-101(Fe) was synthesised by Taylor-Pashow *et al.* and has been shown to release the anti cancer drug Cisplatin ($[Pt(NH_3)_2(Cl)_2]$) slowly over 3 days with a payload of 12.8 wt % in a phosphate-buffered saline (PBS) buffer at 37 °C[111]. The host framework was post-synthetically modified by reaction of the activated cisplatin precursor, ethoxysuccinato-cisplatin (ESCP), at the amino group of the functionalised benzene tribenzoate lignad with 40.2 % functionalisation. Slow degradation of the drug to iron oxide allowed the slow release of the cisplatin drug.

Another example of drug slow release is shown with the MOFs Ni and Co-CPO-27. NO is essential as a vasodilator in the human body, however the administration of large quantities can cause organ damage. For this reason, slow release is vital to avoid any negative side effects.

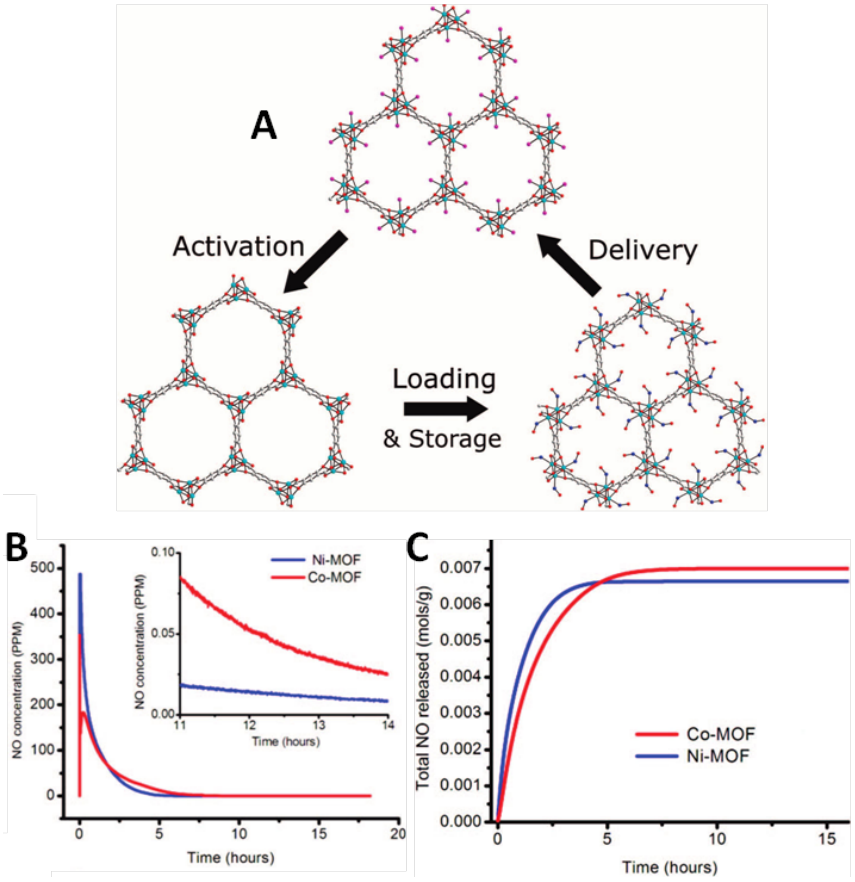

Figure 26: *A: NO loading and storage in M-CPO-27; B: NO concentration released over time; C: Total NO released over time. Figures taken from reference*[112].

Activated Co- and Ni-CPO-27 take up 7.0 mmol NO/g of MOF, with one NO chemisorbed coordinated at each unsaturated metal site in the pores and the remaining NO physisorbed to the channel walls. The NO loaded material can be stored for up to 20 weeks, after which time NO can be released by H_2O substitution as efficiently as it can immediately after NO uptake. When exposed to moisture, the physisorbed NO is released quickly within the first two minutes, but the chemisorbed NO is realeased much more slowly, with the materials still releasing NO after 14 hours (*Figure 26*)[112].

1.6 Conclusions

Over the last 20 years, MOFs have proved to be real alternatives to other porous materials in gas capture and storage, separation of liquids and cases, catalysts, drug delivery agents and molecular sensors. Research into design, improving stability and tuneability is all aiming towards the goal of structure prediction for application centred MOF design.

1.7 Project Overview

The aim of this research project was to synthesise new porous stable 3D MOFs with applications in storage and separation. Solvothermal techniques were used using different reagents, concentrations and solvent systems to produce different frameworks with new interesting structural features.

In chapter 3, the synthesis of frameworks comprising both imidazole and carboxylate coordination are investigated. The main feature is a framework based on novel Co_6 building units connected by 1,3,5-BTB ligands which propagate 2D tri-layeres. This material was shown to be porous to N_2, CO_2 and CH_4 depending on the activation conditions employed, highlighting the importance of investigating all possible activation conditions.

In chapter 4, a 3D MOF based on Ce(III) and H_4TCPB is introduced, Ce(HTCPB)·*guests*. The material can be fully desolvated in the single crystal phase with a partially desolvated stable intermediate also isolated. The structure of a rearranged framework can be determined following exposure of the material to air. All four phases can be isolated in both the single crystal and bulk phases, highlighting the stability of the material.

In chapter 5, Ce(HTCPB) is used to selectively sorb xylene and ethylbenzene isomers. The single crystal structures of the C_8-loaded structures are determined and used to explain the selectivity observed, with the high pX/mX and pX/oX selectivities obtained being the key separations under investigation in xylene separation, comparable with the highest values reported for MOF and zeolite materials.

In chapter 6, a series of frameworks isostructural with Ce(HTCPB) are presented with the formula Ln(HTCPB), where Ln = La, Ce, Pr, Nd and Sm. They are tested for pX/mX separation and Pr(HTCPB) displays a pX/mX selectivity around 50 % higher than any other material reported to date. The unit cell volume of the desolvated frameworks decreases in line with the lanthanide contraction. The synthesis of a framework based on H_4TCPB and a smaller lanthanide, Yb, is also discussed, which shows a different as-made structure, demonstrating that the size of the metal centre in important in structure formation.

For convenience, CIFs for the single crystal structures presented are provided in the additional information sections at the end of the chapter in which the material is discussed.

1.8 References

[1] D. H. Everett, *Pure Appl. Chem.* **1971**, *31*, 579.

[2] W. M. Meier, *Pure Appl. Chem.* **1986**, *10*.

[3] D. W. Breck, W. G. Eversole, R. M. Milton, *J. Am. Chem. Soc.* **1956**, *78*, 2338-2339.

[4] E. M. Flanigen, R. W. Broach, S. T. Wilson., *Zeolites in Industrial Separation and Catalysis*, WILEY-VCH, **2010**.

[5] http://www.iza-structure.org/databases. Accessed 08.08.2013.

[6] A. Shoumkova, *Australian Institute of High Energetic Materials (ABN: 68 126 426 917)* **2011**.

[7] A. Corma, *Zeolites in Oil Refining and Petrochemistry, Kluwer Academic* **1992**.

[8] Association of Detergent Zeolite Producers, *Zeolites for Detergents - As Nature Intended* **2000**, *European Chemical Industry Council (ECIC)*.

[9] M. Mastalerz, *Chem.-Eur. J.* **2012**, *18*, 10082-10091.

[10] N. B. McKeown, P. M. Budd, *Chem. Soc. Rev.* **2006**, *35*, 675-683.

[11] H. J. Mackintosh, P. M. Budd, N. B. McKeown, *J. Mater. Chem.* **2008**, *18*, 573-578.

[12] Q. Chen, M. Luo, T. Wang, J. X. Wang, D. Zhou, Y. Han, C. S. Zhang, C. G. Yan, B. H. Han, *Macromolecules* **2011**, *44*, 5573-5577.

[13] P. Kaur, J. T. Hupp, S. T. Nguyen, *ACS Catal.* **2011**, *1*, 819-835.

[14] M. Mastalerz, I. M. Oppel, *Angew. Chem. Int. Ed.* **2012**, *51*, 5252-5255.

[15] T. Tozawa, J. T. A. Jones, S. I. Swamy, S. Jiang, D. J. Adams, S. Shakespeare, R. Clowes, D. Bradshaw, T. Hasell, S. Y. Chong, C. Tang, S. Thompson, J. Parker, A. Trewin, J. Bacsa, A. M. Z. Slawin, A. Steiner, A. I. Cooper, *Nat. Mater.* **2009**, *8*, 973-978.

[16] T. Hasell, M. Schmidtmann, C. A. Stone, M. W. Smith, A. I. Cooper, *Chem. Commun.* **2012**, *48*, 4689-4691.

[17] S. Y. Ding, W. Wang, *Chem. Soc. Rev.* **2013**, *42*, 548-568.

[18] A. P. Cote, A. I. Benin, N. W. Ockwig, M. O'Keeffe, A. J. Matzger, O. M. Yaghi, *Science* **2005**, *310*, 1166-1170.

[19] F. J. Uribe-Romo, J. R. Hunt, H. Furukawa, C. Klock, M. O'Keeffe, O. M. Yaghi, *J. Am. Chem. Soc.* **2009**, *131*, 4570.

[20] S. S. Han, H. Furukawa, O. M. Yaghi, W. A. Goddard, *J. Am. Chem. Soc.* **2008**, *130*, 11580.

[21] A. G. Wong-Foy, A. J. Matzger, O. M. Yaghi, *J. Am. Chem. Soc.* **2006**, *128*, 3494-3495.

[22] H. Furukawa, O. M. Yaghi, *J. Am. Chem. Soc.* **2009**, *131*, 8875-8883.

[23] S. S. Kaye, A. Dailly, O. M. Yaghi, J. R. Long, *J. Am. Chem. Soc.* **2007**, *129*, 14176.

[24] M. Eddaoudi, J. Kim, N. Rosi, D. Vodak, J. Wachter, M. O'Keeffe, O. M. Yaghi, *Science* **2002**, *295*, 469-472.

[25] P. L. Llewellyn, S. Bourrelly, C. Serre, A. Vimont, M. Daturi, L. Hamon, G. De Weireld, J. S. Chang, D. Y. Hong, Y. K. Hwang, S. H. Jhung, G. Ferey, *Langmuir* **2008**, *24*, 7245-7250.

[26] A. R. Millward, O. M. Yaghi, *J. Am. Chem. Soc.* **2005**, *127*, 17998-17999.

[27] B. F. Hoskins, R. Robson, *J. Am. Chem. Soc.* **1990**, *112*, 1546-1554.

[28] M. Eddaoudi, D. B. Moler, H. L. Li, B. L. Chen, T. M. Reineke, M. O'Keeffe, O. M. Yaghi, *Acc. Chem. Res.* **2001**, *34*, 319-330.

[29] J. Kim, B. L. Chen, T. M. Reineke, H. L. Li, M. Eddaoudi, D. B. Moler, M. O'Keeffe, O. M. Yaghi, *J. Am. Chem. Soc.* **2001**, *123*, 8239-8247.

[30] S. L. Qiu, G. S. Zhu, *Coord. Chem. Rev.* **2009**, *253*, 2891-2911.

[31] O. M. Yaghi, M. O'Keeffe, N. W. Ockwig, H. K. Chae, M. Eddaoudi, J. Kim, *Nature* **2003**, *423*, 705-714.

[32] F. N. Dai, H. Y. He, D. L. Gao, F. Ye, X. L. Qiu, D. F. Sun, *CrysEngComm* **2009**, *11*, 2516-2522.

[33] S. I. Vagin, A. K. Ott, B. Rieger, *Chem. Ing. Tech.* **2007**, *79*, 767-780.

[34] M. Eddaoudi, J. Kim, J. B. Wachter, H. K. Chae, M. O'Keeffe, O. M. Yaghi, *J. Am. Chem. Soc.* **2001**, *123*, 4368-4369.

[35] M. Eddaoudi, J. Kim, M. O'Keeffe, O. M. Yaghi, *J. Am. Chem. Soc.* **2002**, *124*, 376-377.

[36] S. R. Batten, N. R. Champness, X. M. Chen, J. Garcia-Martinez, S. Kitagawa, L. Ohrstrom, M. O'Keeffe, M. P. Suh, J. Reedijk, *CrystEngComm* **2012**, *14*, 3001-3004.

[37] A. J. Ihde, *The Development of Modern Chemistry*, Dover Publications, New York, **1984**.

[38] E. A. Tomic, *J. Appl. Polym. Sci.* **1965**, *9*, 3745.

[39] S. L. James, *Chem. Soc. Rev.* **2003**, *32*, 276-288.

[40] B. F. Abrahams, B. F. Hoskins, D. M. Michail, R. Robson, *Nature* **1994**, *369*, 727-729.

[41] D. Venkataraman, G. B. Gardner, S. Lee, J. S. Moore, *J. Am. Chem. Soc.* **1995**, *117*, 11600-11601.

[42] G. Ferey, *Chem. Soc. Rev.* **2008**, *37*, 191-214.

[43] K. S. Park, Z. Ni, A. P. Cote, J. Y. Choi, R. D. Huang, F. J. Uribe-Romo, H. K. Chae, M. O'Keeffe, O. M. Yaghi, *P. Natl. Acad. Sci. USA* **2006**, *103*, 10186-10191.

[44] R. Banerjee, H. Furukawa, D. Britt, C. Knobler, M. O'Keeffe, O. M. Yaghi, *J. Am. Chem. Soc.* **2009**, *131*, 3875.

[45] B. Wang, A. P. Cote, H. Furukawa, M. O'Keeffe, O. M. Yaghi, *Nature* **2008**, *453*, 207-U206.

[46] R. Banerjee, A. Phan, B. Wang, C. Knobler, H. Furukawa, M. O'Keeffe, O. M. Yaghi, *Science* **2008**, *319*, 939-943.

[47] H. Bux, F. Y. Liang, Y. S. Li, J. Cravillon, M. Wiebcke, J. Caro, *J. Am. Chem. Soc.* **2009**, *131*, 16000.

[48] R. B. Getman, Y. S. Bae, C. E. Wilmer, R. Q. Snurr, *Chem. Rev.* **2012**, *112*, 703-723.

[49] B. Sakintuna, F. Lamari-Darkrim, M. Hirscher, *Int. J. Hydrogen Energy* **2007**, *32*, 1121-1140.

[50] M. Dinca, J. R. Long, *Angew.Chem. Int. Ed.* **2008**, *47*, 6766-6779.

[51] *Department of Energy (D.O.E)*, *Multi-Year Research, Development and Demonstration Plan*, http://www1.eere.energy.gov/hydrogenandfuelcells/mypp/pdfs/storage.pdf. Accessed 08.08.2013.

[52] H. K. Chae, D. Y. Siberio-Perez, J. Kim, Y. Go, M. Eddaoudi, A. J. Matzger, M. O'Keeffe, O. M. Yaghi, *Nature* **2004**, *427*, 523-527.

[53] Y. Li, R. T. Yang, *Langmuir* **2007**, *23*, 12937-12944.

[54] D. J. Tranchemontagne, K. S. Park, H. Furukawa, J. Eckert, C. B. Knobler, O. M. Yaghi, *J. Phys. Chem. C* **2012**, *116*, 13143-13151.

[55] Y. Yan, X. Lin, S. H. Yang, A. J. Blake, A. Dailly, N. R. Champness, P. Hubberstey, M. Schroder, *Chem. Commun.* **2009**, 1025-1027.

[56] D. M. D'Alessandro, B. Smit, J. R. Long, *Angew. Chem. Int. Ed.* **2010**, *49*, 6058-6082.

[57] J. D. Figueroa, T. Fout, S. Plasynski, H. McIlvried, R. D. Srivastava, *Int. J. Greenh. Gas Con.* **2008**, *2*, 9-20.

[58] S. Cavenati, C. A. Grande, A. E. Rodrigues, *J. Chem. Eng. Data* **2004**, *49*, 1095-1101.

[59] S. Himeno, T. Komatsu, S. Fujita, *J. Chem. Eng. Data* **2005**, *50*, 369-376.

[60] S. Sircar, T. C. Golden, M. B. Rao, *Carbon* **1996**, *34*, 1-12.

[61] S. C. Xiang, W. Zhou, Z. J. Zhang, M. A. Green, Y. Liu, B. L. Chen, *Angew. Chem. Int. Ed.* **2010**, *49*, 4615-4618.

[62] G. Skodras, I. Diamantopoulou, P. Natas, A. Palladas, G. P. Sakellaropoulos, *Energy Fuel* **2005**, *19*, 2317-2327.

[63] J. V. Romero, J. W. H. Smith, B. M. Sullivan, L. Macdonald, L. M. Croll, J. R. Dahn, *ACS Comb. Sci.* **2013**, *15*, 101-110.

[64] G. W. Peterson, C. J. Karwacki, W. B. Feaver, J. A. Rossin, *Ind. Eng. Chem. Res.* **2008**, *47*, 185-191.

[65] D. Britt, D. Tranchemontagne, O. M. Yaghi, *P. Natl. Acad. Sci. USA* **2008**, *105*, 11623-11627.

[66] S. H. Yang, J. L. Sun, A. J. Ramirez-Cuesta, S. K. Callear, W. I. F. David, D. P. Anderson, R. Newby, A. J. Blake, J. E. Parker, C. C. Tang, M. Schroder, *Nat. Chem.* **2012**, *4*, 887-894.

[67] L. E. Kreno, J. T. Hupp, R. P. Van Duyne, *Anal. Chem.* **2010**, *82*, 8042-8046.

[68] J. R. Li, J. Sculley, H. C. Zhou, *Chem. Rev.* **2012**, *112*, 869-932.

[69] A. Demessence, D. M. D'Alessandro, M. L. Foo, J. R. Long, *J. Am. Chem. Soc.* **2009**, *131*, 8784.

[70] J. Seo, R. Matsuda, H. Sakamoto, C. Bonneau, S. Kitagawa, *J. Am. Chem. Soc.* **2009**, *131*, 12792-12800.

[71] A. V. Neimark, F. X. Coudert, C. Triguero, A. Boutin, A. H. Fuchs, I. Beurroies, R. Denoyel, *Langmuir* **2011**, *27*, 4734-4741.

[72] L. Hamon, P. L. Llewellyn, T. Devic, A. Ghoufi, G. Clet, V. Guillerm, G. D. Pirngruber, G. Maurin, C. Serre, G. Driver, W. van Beek, E. Jolimaitre, A. Vimont, M. Daturi, G. Ferey, *J. Am. Chem. Soc.* **2009**, *131*, 17490-17499.

[73] H. Hayashi, A. P. Cote, H. Furukawa, M. O'Keeffe, O. M. Yaghi, *Nat. Mater.* **2007**, *6*, 501-506.

[74] R. B. Eldridge, *Ind. Eng. Chem. Res.* **1993**, *32*, 2208-2212.

[75] S. J. Geier, J. A. Mason, E. D. Bloch, W. L. Queen, M. R. Hudson, C. M. Brown, J. R. Long, *Chem. Sci.* **2013**, *4*, 2054-2061.

[76] M. Sadakiyo, T. Yamada, H. Kitagawa, *J. Am. Chem. Soc.* **2011**, *133*, 11050-11053.

[77] M. Minceva, A. E. Rodrigues, *AlChE J.* **2007**, *53*, 138-149.

[78] Z. Y. Gu, X. P. Yan, *Angew. Chem. Int. Ed.* **2010**, *49*, 1477-1480.

[79] V. Finsy, H. Verelst, L. Alaerts, D. De Vos, P. A. Jacobs, G. V. Baron, J. F. M. Denayer, *J. Am. Chem. Soc.* **2008**, *130*, 7110–7118.

[80] C. Serre, F. Millange, C. Thouvenot, M. Nogues, G. Marsolier, D. Louer, G. Ferey, *J. Am. Chem. Soc.* **2002**, *124*, 13519-13526.

[81] G. H. Xu, X. G. Zhang, P. Guo, C. L. Pan, H. J. Zhang, C. Wang, *J. Am. Chem. Soc.* **2010**, *132*, 3656.

[82] L. Alaerts, M. Maes, L. Giebeler, P. A. Jacobs, J. A. Martens, J. F. M. Denayer, C. E. A. Kirschhock, D. E. De Vos, *J. Am. Chem. Soc.* **2008**, *130*, 14170-14178.

[83] T. Y. Yan, *Ind. Eng. Chem. Res.* **1989**, *28*, 572-576.

[84] R. Vaidhyanathan, D. Bradshaw, J. N. Rebilly, J. P. Barrio, J. A. Gould, N. G. Berry, M. J. Rosseinsky, *Angew. Chem. Int. Edit.* **2006**, *45*, 6495-6499.

[85] L. Alaerts, M. Maes, M. A. van der Veen, P. A. Jacobs, D. E. De Vos, *PCCP* **2009**, *11*, 2903-2911.

[86] T. Loiseau, L. Lecroq, C. Volkringer, J. Marrot, G. Ferey, M. Haouas, F. Taulelle, S. Bourrelly, P. L. Llewellyn, M. Latroche, *J. Am. Chem. Soc.* **2006**, *128*, 10223-10230.

[87] M. Maes, L. Alaerts, F. Vermoortele, R. Ameloot, S. Couck, V. Finsy, J. F. M. Denayer, D. E. De Vos, *J. Am. Chem. Soc.* **2010**, *132*, 2284-2292.

[88] L. Schlapbach, A. Zuttel, *Nature* **2001**, *414*, 353-358.

[89] B. Peng, J. Chen, *Energy Environ. Sci.* **2008**, *1*, 479-483.

[90] M. C. Denney, V. Pons, T. J. Hebden, D. M. Heinekey, K. I. Goldberg, *J. Am. Chem. Soc.* **2006**, *128*, 12048-12049.

[91] Y. Q. Li, P. Song, J. Zheng, X. G. Li, *Chem.-Eur. J.* **2010**, *16*, 10887-10892.

[92] A. Fateeva, P. A. Chater, C. P. Ireland, A. A. Tahir, Y. Z. Khimyak, P. V. Wiper, J. R. Darwent, M. J. Rosseinsky, *Angew. Chem. Int. Ed.* **2012**, *51*, 7440-7444.

[93] J. L. Wang, C. Wang, W. B. Lin, *ACS Catal.* **2012**, *2*, 2630-2640.

[94] A. D'Aleo, F. Pointillart, L. Ouahab, C. Andraud, O. Maury, *Coord. Chem. Rev.* **2012**, *256*, 1604-1620.

[95] M. D. Allendorf, C. A. Bauer, R. K. Bhakta, R. J. T. Houk, *Chem. Soc. Rev.* **2009**, *38*, 1330-1352.

[96] C. Serre, F. Millange, C. Thouvenot, N. Gardant, F. Pelle, G. Ferey, *J. Mater. Chem.* **2004**, *14*, 1540-1543.

[97] N. L. Rosi, J. Kim, M. Eddaoudi, B. L. Chen, M. O'Keeffe, O. M. Yaghi, *J. Am. Chem. Soc.* **2005**, *127*, 1504-1518.

[98] T. Devic, C. Serre, N. Audebrand, J. Marrot, G. Ferey, *J. Am. Chem. Soc.* **2005**, *127*, 12788-12789.

[99] N. Kerbellec, D. Kustaryono, V. Haquin, M. Etienne, C. Daiguebonne, O. Guillou, *Inorg. Chem.* **2009**, *48*, 2837-2843.

[100] B. Liu, *J. Mater. Chem.* **2012**, *22*, 10094-10101.

[101] S. S. Y. Chui, S. M. F. Lo, J. P. H. Charmant, A. G. Orpen, I. D. Williams, *Science* **1999**, *283*, 1148-1150.

[102] G. Lu, J. T. Hupp, *J. Am. Chem. Soc.* **2010**, *132*, 7832.

[103] K. C. Stylianou, R. Heck, S. Y. Chong, J. Bacsa, J. T. A. Jones, Y. Z. Khimyak, D. Bradshaw, M. J. Rosseinsky, *J. Am. Chem. Soc.* **2010**, *132*, 4119-4130.

[104] S. M. Cohen, *Chem. Rev.* **2012**, *112*, 970-1000.

[105] M. J. Ingleson, J. P. Barrio, J. B. Guilbaud, Y. Z. Khimyak, M. J. Rosseinsky, *Chem. Commun.* **2008**, 2680-2682.

[106] T. Haneda, M. Kawano, T. Kawamichi, M. Fujita, *J. Am. Chem. Soc.* **2008**, *130*, 1578.

[107] Z. Q. Wang, K. K. Tanabe, S. M. Cohen, *Chem.-Eur. J.* **2010**, *16*, 212-217.

[108] P. Horcajada, R. Gref, T. Baati, P. K. Allan, G. Maurin, P. Couvreur, G. Ferey, R. E. Morris, C. Serre, *Chem. Rev.* **2012**, *112*, 1232-1268.

[109] A. C. McKinlay, R. E. Morris, P. Horcajada, G. Ferey, R. Gref, P. Couvreur, C. Serre, *Angew. Chem. Int. Ed.* **2010**, *49*, 6260-6266.

[110] P. Horcajada, T. Chalati, C. Serre, B. Gillet, C. Sebrie, T. Baati, J. F. Eubank, D. Heurtaux, P. Clayette, C. Kreuz, J. S. Chang, Y. K. Hwang, V. Marsaud, P. N. Bories, L. Cynober, S. Gil, G. Ferey, P. Couvreur, R. Gref, *Nat. Mater.* **2010**, *9*, 172-178.

[111] K. M. L. Taylor-Pashow, J. Della Rocca, Z. G. Xie, S. Tran, W. B. Lin, *J. Am. Chem. Soc.* **2009**, *131*, 14261.

[112] A. C. McKinlay, B. Xiao, D. S. Wragg, P. S. Wheatley, I. L. Megson, R. E. Morris, *J. Am. Chem. Soc.* **2008**, *130*, 10440-10444.

Chapter 2

Synthetic and Experimental Techniques

2.1 Overview

In this chapter, the synthetic techniques, instrumentation, data collection and analysis methods for all work carried out in this thesis will be discussed. The characterisation of these compounds was carried out using single-crystal x-ray diffraction (SCXRD), powder x-ray diffraction (PXRD), thermogravimetric analysis (TGA), elemental microanalysis, Infra-red spectroscopy (IR), nuclear magnetic resonance spectroscopy (NMR) and gas sorption isotherms.

The synthetic techniques used to synthesise both the organic organic ligands and MOFs presented in this thesis are discussed in this chapter. Organic synthesis was used to produce the ligand 1,2,4,5-tetrakis(4-carboxyphenyl)benzene (H_4TCPB), which was used to synthesise compounds **10**-**14** and all related structures.

Solvothermal synthesis was used to produce all MOFs **1**-**14** in this thesis and their 3D structure was determined by single crystal x-ray structure analysis. MOF chemistry requires careful selection and combination of metal salts and organic linker ligands in specific solvent mixtures, heating to a particular temperature at which the desired compound will form, careful cooling to ensure single crystals are formed for structure determination and phase pure samples are achieved but using the correct stoichiometry and reaction conditions. This complicated set of criteria must be adhered to in order to isolate phase pure crystalline MOF material for its analysis and potential applications.

Characterisation of MOFs is necessary to determine the 3D structure, phase purity and potential applications. First and foremost the material must be phase pure, so any data obtained can be considered accurate for every sample. All compounds were determined to be phase pure by PXRD, TGA and elemental microanalysis. Gas sorption isotherms (N_2, CO_2, CH_4, Ar and H_2O) were collected for compounds **8** and **11** for BET surface area analysis, Dubinin-Radushkevitz pore volume analysis, isosteric heats of adsorption (Q_{st}) and the pore side distribution (PSD).

2.2 Experimental Methods

2.2.1 Synthesis

2.2.1.1 Organic Synthesis of Tetrakis(4-carboxyphenyl)benzene Ligand (H_4TCPB)

Reagents and solvents for the synthesis of the H_4TCPB ligand used for the synthesis of compounds **10**-**15** were purchased from Sigma-Aldrich and used without further purification.

The following reaction was run 6 times in parallel using a Radley's Carousel and all 6 reactions were combined for the work-up and isolation:

1,2,4,5-Tetrabromobenzene (3.15 g, 8 mmol), p-tolylboronic acid (6.53 g, 48 mmol) and potassium carbonate (8.85 g, 64 mmol) were charged to a round-bottomed flask followed by toluene (120 mL), MeOH (40 mL) and deionised H_2O (32 mL). N_2 was bubbled through the reaction mixture for 5 minutes and then tetrakis(triphenylphospine) palladium(0) was charged and the mixture was heated at reflux under a N_2 atmosphere for 4 days. The six biphasic reaction mixtures were cooled to ambient temperature, combined and the layers separated. The organic layer was washed with 1M HCl (250 ml), water (2 x 250 ml), dried over $MgSO_4$ and filtered. The filtrate was concentrated on a rotary evaporator until approximately 50 ml of solvent remained. The suspension was diluted with 50 ml of acetone and filtered to afford 16.0 g of crude material. The solid was dissolved in hot toluene, a small amount of insoluble material was removed by filtration and the filtrate was concentrated to a volume of 50 ml. The suspension was allowed to cool to ambient temperature and the solid was collected by filtration. The cake was washed with toluene (10 mL) and dried under vacuum to afford 14.5 g (69 % yield) 1,2,4,5-tetra-p-tolyl-benzene as a white solid. ^{1}H NMR ($CDCl_3$): 7.47 (2H, s, Ar-H), 7.12 (8H, d, Ar-H), 7.04 (8H, d, Ar-H), 2.32 (12H, s, 4 x CH_3). This was then oxidised using a reported oxidation step to yield the final product of 1,2,4,5-tetra(4-carboxyphenyl)-benzene[1]:

1,2,4,5-tetra-p-tolyl-benzene (1.5 g) was charged to a 45 ml capacity Teflon liner followed by H_2O (16.2 ml) and 70 % HNO_3 (6.3 ml). The suspension was sealed in a solvothermal vessel and heated to 180 °C at a rate of 4 °C/min. The reaction was held at 180 °C for 24 hours then cooled to 25 °C. The suspension was filtered, washed with water and dried briefly under suction. 12.8 g of crude solid was dissolved in hot THF (400 mL). The hot solution was filtered to remove some insoluble material and the filtrate was transferred to a rotary evaporator and concentrated to ~100 mL. Chloroform (100 ml) was then charged to the flask and the suspension was filtered. The cake was washed with chloroform and dried under suction to afford 9.33 g of material. The above purification was repeated again to afford 7.72 g of 1,2,4,5-tetra(4-carboxyphenyl)-benzene which was characterised to be phase pure by ^{1}H NMR: ^{1}H NMR (DMSO): 13.00 (4H, br s, 4 x COOH), 7.85 (8H, d, 8 x ArH), 7.58 (2H, s, 2 x ArH), 7.37 (8H, d, 8 x ArH).

2.2.1.2 Hydrothermal/Solvothermal Synthesis

Hydrothermal synthesis is a method in which reagents and aqueous solvents or solvent mixtures are sealed in a hydrothermal autoclave reactor (*Figure 1A,B*) meaning they can react at elevated

temperatures up to 250 °C and pressures up to 150 bar to form chemical compounds. Solvothermal synthesis is carried out in exactly the same way, except other organic solvents can be used.

Reagents and solvents are added to a Teflon liner, which is then sealed in a stainless steel autoclave (*Figure 1*). The reaction is then heated to a dwell temperature at a chosen rate and is then held at that temperature for a set period of time until it is cooled back to room temperature, again at a pre-determined rate. As the reaction is carried out in a sealed reactor, it can be heated to temperatures above the boiling point of the solvents used (although this is not always necessary), which allows high pressures to be achieved within the vessel. Due to the number of variables involved in hydro(solvo)thermal synthesis, including solvent(s) used, heating schemes and reagent ratios and concentrations used, precise control over the particle size, phase purity, crystallinity and yield can be optimised.

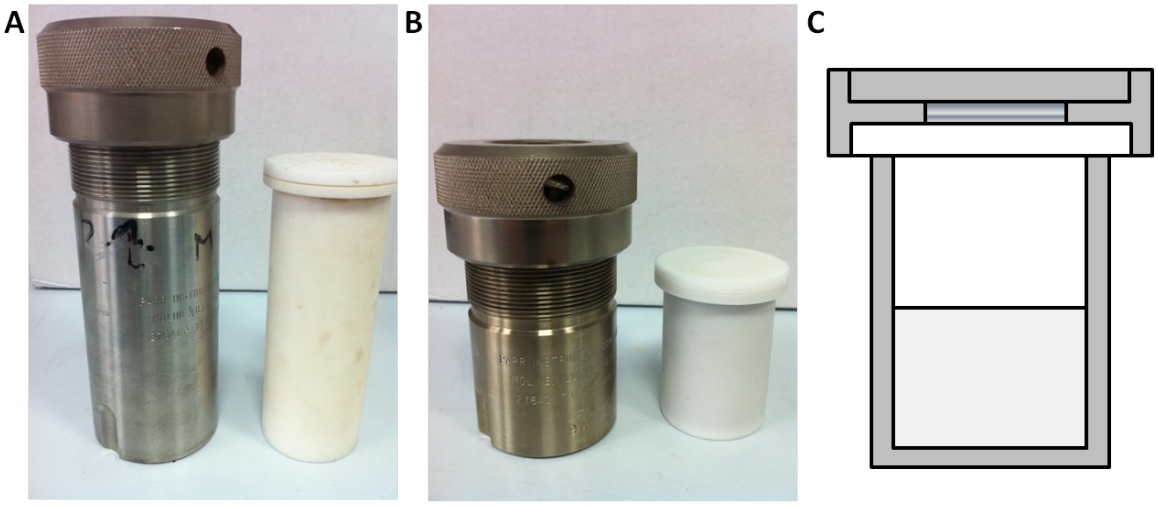

Figure 1: *Solvo(Hydro)thermal teflon liners and stainless steel autoclaves. A: 40 ml reactor; B: 20 ml reactor; C: Schematic of a teflon liner inside a stainless steel reactor.*

The main reason for employing hydro(solvo)thermal synthesis is the ability to carry out a reaction at temperatures above the boiling point of the solvents used, thus at pressures above 1 atm[2-3]. Hydro(Solvo)thermal synthesis relies on the solvating capabilities of solvents under the reaction conditions. Reagents are often dissolved in the solvent mixture, after which point, nucleation initiates crystal growth. Hydro(Solvo)thermal methods are widely used, especially in the synthesis of crystalline materials and have been shown to form many materials. Examples include the synthesis of the carbon allotrope graphene, which has been produced using solvothermal methods by combining EtOH and Na and heating to 220 °C for 72 hours, yielding phase pure crystalline product[4]. There are also many examples of solvothermal methods being used to produce

nanoparticles such as Ohtani *et. al.* who synthesised tantalum oxide nanoparticles for photo-generation of hydrogen, by combining tantalum pentabutoxide in toluene and water, yielding a more thermostable product than that which could be produced under atmospheric conditions. Careful control of synthesis conditions allowed Muramatsu *et. al.* to synthesise highly crystalline cubic Indium-Tin-oxide nanoparticles with a narrow size distribution for use in electrodes[5].

MOFs can be synthesised via many methods such as solvent layering[6] techniques, microwave synthesis[7-9] and slow evaporation of solvents[10], however the most common method of MOF synthesis uses solvothermal chemistry. Stainless steel autoclaves are often used to achieve higher temperatures, however MOFs can be synthesised at lower temperatures in which case borosilicate glass vials can be used (at temperatures less than 120 °C). The use of borosilicate glass vials allows for a higher turnover of reactions, exploring more conditions at one time. In each MOF synthesis, there are many variables. These include metal salt used (nitrates, sulphates, oxides, halides etc.), organic ligands(s), ratio of reagents chosen, solvent(s), ratio of solvents chosen, concentration, ramp rate, dwell temperature, dwell time and cooling rate. The ideal outcome is the formation of single crystals for structure analysis and second to that is highly crystalline powder from which the structure can be determined by Rietveld analysis following PXRD data collection. The high number of variables means that there are many reactions that need to be tried to finally reach the desired phase pure product in the morphology required.

The synthesis conditions for the MOFs discussed in this thesis are described in each chapter.

2.2.2 X-Ray Diffraction

The human eye can determine the size and shape of an object at the macroscopic level. Light rays of varying wavelengths are reflected from the surface of an object in different directions and the lens of the eye is able to bring these rays back together and convert them in a way which allows the brain to comprehend what the object is and how far away it is. In a similar way, x-ray diffraction is used to analyse materials at the microscopic level, down at the atomic scale.

The process of x-ray diffraction uses a fixed wavelength of light and measures the intensity variation and scattering direction following diffraction off the atoms within the sample: it effectively looks at the scattering of monochromatic radiation. The term ‘diffraction’ is the variation in intensity as a result of interference from regions of electron density. This allows a picture of the structure of a material to be built up from atom and bond positions.

A perfect crystal will have no defects but in reality all materials have a number of defects, however structural analysis of a single crystal will provide an average of atom positions, so the structure can

still be determined and any defects will be ignored. Within a crystal particle, there is long range order with the repeating units described in 3D by a unit cell.

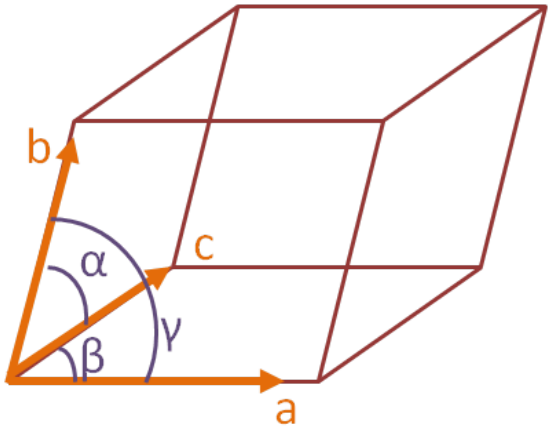

Figure 2: *Unit cell, defined by cell lengths (a, b, c) and angles (α, β, γ).*

The unit cell is described by three axis dimensions (a,b,c) and three angles (α,β,γ), known as the unit cell parameters (*Figure 2*). This unit cell will repeat periodically throughout the crystal lattice. The point at the origin of the unit cell is known as the lattice point and the arrangement of this in 3D alongside any structural motifs provided by the structure gives rise to translational symmetry. There are seven possible crystal systems depending on the unit cell parameters, shown in table 1.

Table 1: *The seven crystal systems with their corresponding unit cell parameters:*

Crystal System	Unit Cell Dimensions	Minimum Symmetry Elements
Triclinic	$a \neq b \neq c$ $\alpha \neq \beta \neq \gamma$	None
Monoclinic	$a \neq b \neq c$ $\alpha = \gamma = 90\,° \neq \beta$	**One** C2 axis or mirror plane
Orthorombic	$a \neq b \neq c$ $\alpha = \beta = \gamma = 90\,°$	**Three** C2 axis or mirror planes
Tetragonal	$a = b \neq c$ $\alpha = \beta = \gamma = 90\,°$	**One** C4 axis
Trigonal	$a = b = c$ $\alpha = \beta = \gamma \neq 90\,°$	**One** C3 axis
Hexagonal	$a = b \neq c$ $\alpha = \beta = 90\,°, \gamma = 120\,°$	**One** C6 axis
Cubic	$a = b = c$ $\alpha = \beta = \gamma = 90\,°$	**Four** C3 axis

Within each of these crystal systems, there are potentially up to four lattice types: Primitive (P) in which the lattice points are on the vertices of the unit cell only, Body-centered (I) in which the lattice points are found at all 8 vertices and one at the centre, face-centered (F), in which lattice points are found at each vertex and in the centre of each face and side centred (A,B,C) in which lattice points are found at each vertex and only one face. If a lattice point is on a vertice, only ¼ of the point is in the unit cell, as 4 unit cells join at one vertex. If a lattice point is found at a face, ½ of the point is found in the unit cell, as each face is shared by two unit cells. These lattice types are referred to as Bravais lattices. The crystal system and lattice type can also be present alongside other symmetry elements including inversion centres, screw axis, mirror planes and glide planes and altogether this leads to a space group determination, which fully describes the crystal structure symmetry (Table 1). In total there are 230 possible space groups[11].

2.2.2.1 Single-Crystal X-Ray Diffraction (SCXRD)

The determination of the crystal structure gives insight into how a material comes together in the solid state, inclusive of the position of the atoms and the strength of bonding present between those atoms. The term 'structure' describes the specific position of atoms and bonds within a 3D array, the determination of which can be used to not only describe a material, but also predict and analyse its reactivity of potential applications[12].

It is in fact the electrons within the atom that scatter the x-rays, which allows an electron density map to be generated, where the clusters of electron density represent atoms. For example, a carbon atom has 12 electrons whereas an oxygen atom has 8; these two elements will be distinguishable from the electron density map, taking into account any atomic vibrations and distortion of electron density within bonds.

$$\boldsymbol{\lambda = 2d_{hkl}sin\theta}$$

Equation 1: *Bragg Equation, where λ = the wavelength or path length of the x-ray, d = the distance between 2 atoms at coordinated h,k,l, and θ = the scattering angle hence 2sinθ is the angle between the incident and diffracted x-ray.*

The reciprocal lattice generated through diffraction is described in terms on hkl, which relate to the x,y,z (a,b,c) coordinates of the atoms within the single crystal in real space. Each diffraction point, or reflection as it is more commonly known, has a specific hkl coordinate, which allows the reciprocal 3D structure to be generated. The angle at which an x-rays are diffracted off adjacent atoms in a plane determines whether or not the waves produced are constructive or destructive.

Only when a diffracted x-ray satisfies Bragg's Law (Bragg Equation) will it produce constructive interference and appear as a reflection in the diffraction pattern (*Equation 1*).

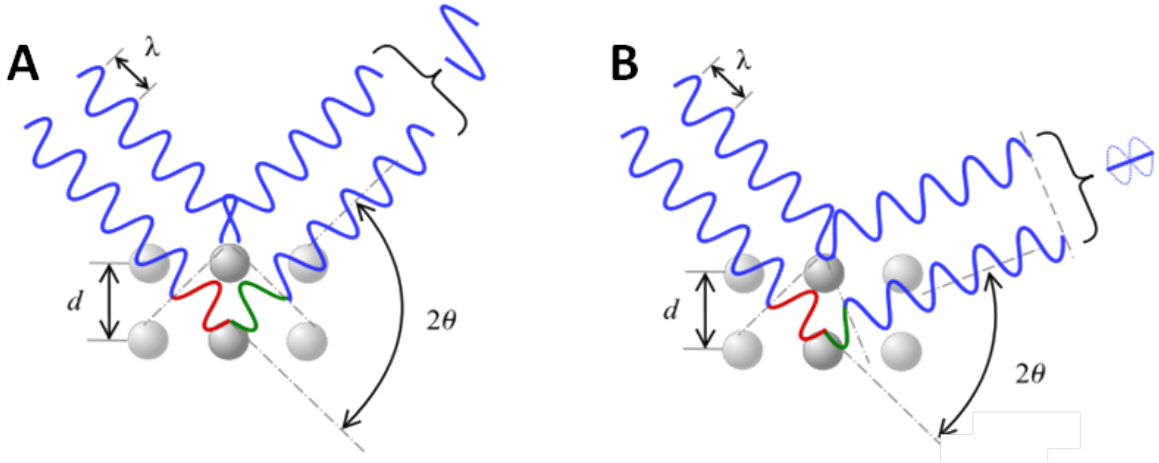

Figure 3: *Bragg's Law. Angle of 2θ determines whether the diffracted x-rays produced from two adjacent atoms are A: constructive; or B: Destructive. Figure adapted from reference*[6].

For two adjacent points or atoms, two separate waves will arrive at each point with the same phase. The diffracted waves will only undergo constructive interference if the path difference, d, is equal to an integer value of the wavelength, λ (*Figure 3*). This results in each generated reflection having an associated lattice plane (h,k,l) that occurs at an angle of 2θ, depending on the interplanar spacing d(h,k,l).

The conversion of scattered x-rays into an electron density map is complex. The amplitude of each scattered x-ray is recorded as a relative intensity against all other scattered x-rays from the single crystal. At this stage, the phases of all x-rays are lost, hereby creating the 'phase problem'. There are structure solution methods, which later deal with the phase problem in order for the single crystal structure to be determined (Patterson method[13], Direct Methods[14] and charge flipping[15]).

2.2.2.2 Data Collection

The method of single crystal data collection is as follows:

1. Select a suitable crystal using a microscope. The crystal should ideally be between 50-250 µm (however this is not always possible) and should extinguish under polarised light.
2. A matrix is run consisting of around 20 frames at different orientations for indexing (unit cell determination).

3. Once the unit cell has been reduced, the full data collection method is set up for the collection of intensity data.
4. The raw data is integrated against the unit cell.
5. The structure is solved using Direct methods, the Patterson method or charge flipping[12].
6. Once all atoms have been identified the structure model is refined against the data and the refinement value, R_f (R-factor) gives an indication as to how well the model fits the data. Ideally this number should be lower than 5 %.
7. Once refined, the structure can be completed and a crystallographic information file (CIF) generated for submission to the Cambridge Crystallographic Data Centre (CCDC).

Single crystal data collections for compounds **1-7** were carried out using a Bruker Smart diffractometer with Cu Kα radiation. Single crystals were isolated from the mother liquor and onto a glass fibre, which were then transferred to the goniometer under N_2 gas stream at 150 K. The data was processed using Smart software. Scaling and absorption correction was undertaken using SADABS 2008/4. The final structures were solved using Direct methods in Olex2[16-17] and refined using ShelXL[18] in Olex2. All data sets could not be finalised due to insufficient data and resolution from very small single crystals, however the structure was determined from the data and PXRD analysis was used to determine phase purity of the MOFs.

Single crystals of **7**, **8**, **9** and all Ln(HTCPB)·*guests* compounds (**10-14**, **10D-14D**, **10R-14R**, **11S**, **10D-14D**, **10R-14R**, **10P-14P**, **10M-14M**, **11O**, **11EB**, **11PM**, **11T**, **11B**, **11RP**, **11R'P** and **11RB**) were isolated from hydrothermal synthesis and mounted in Fomblin inert oil onto a two stage capillary fibre. Single crystal data collections for compounds were carried out using a Rigaku AFC12K goniometer with Mo Kα radiation from a Rigaku 007-HF Molybdenum rotating anode microfocus X-ray source and collected using Saturn 724+ CCD detector. Environmental control was achieved using a nitrogen stream from a Oxford Cryosystem 700+ Cryostream[19].
In this thesis, all single crystal data collection, structure determination and analysis was carried out with the assistance of Dr John Warren at the University of Liverpool[20].

2.2.2.3 Data Processing

Compounds 1-3: The data were intergrated using APEXII[21] and absorption correction was carried out using SADABS[22]. The structure was determined and refined using ShelXL[18] and finalised using Olex2[17].

Compounds 7-9: The data were integrated using FS_Process[23] with absorption and scaling correction carried out using SADABS[22]. The structure was solved in Olex2[17] using direct methods and ShelXL[18] respectively.

Compounds 10, 10D, 10R, 10P, 10M, 12, 12D, 12R, 12P, 12M, 13, 13D, 13R, 13P, 13M, 14, 14D, 14R, 14P, 14M: The data were integrated using FS_Process[23] with absorption and scaling correction carried out using SADABS[22]. The structure was solved in Olex2[17] using direct methods and ShelXL[18] respectively.

Compound 11, 11S, 11D, 11R, 11P, 11M, 11PM, 11O, 11EB, 11T, 11B, 11RP, 11R'P, 11RB: The data was integrated and reduced using FS_Process[23] with absorption and scaling correction being undertaken with the program ABSCOR[24]. Using Olex2[17] the structure was solved with the olex2.solve structure solution program[16] using Charge Flipping and refined with the ShelXL_ifc refinement package[18] using Least Squares minimisation.

2.2.2.4 Powder X-Ray Diffraction (PXRD)

PXRD works through the same principles as SCXRD, however in this case the sample consists of multiple small crystallites instead of one large single crystal. For this reason a 3D diffraction pattern cannot be generated, only a 2D diffraction pattern (*Figure 4*).

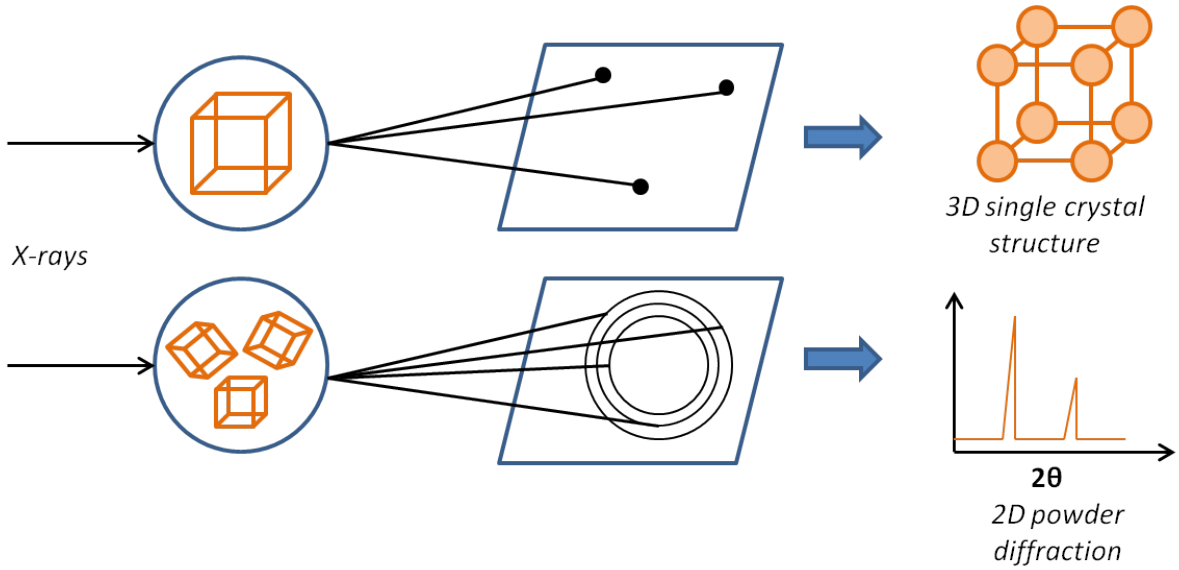

Figure 4: *Single crystal x-ray diffraction and powder x-ray diffraction techniques.*

Whereas in single crystal x-ray diffraction, one crystal produces spots in the diffraction pattern, multiple crystallites produces multiple spots at the same 2θ value, which generated rings in the diffraction pattern. This is translated into a 2D output in the form of a graph, from which information about the atom positions can be determined. These can be indexed and refined against the structural model provided from the single crystal data, allowing the phase purity of the bullk material to be determined.

2.2.2.5 Data Collection

PXRD of compounds **1-5, 7** and **8** and all PXRD data on the isolation of bulk phases **11**, **11S** and **11R** were collected using a PAnalytical diffractometer, using Co Kα radiation in reflection geometry. Samples were ground with a pestle and mortar and were then transferred to a zero-background holder.

PXRD profiles of **1-5, 7** and **8** were indexed to the single crystal structure unit cell using CheckCell and determined to be phase pure. Compound **8** was characterised to be phase pure via Rietveld refinement against the single crystal structure using Topaz by Alec McLennan at the University of Liverpool[25].

X-ray Powder Diffraction (PXRD) data for compounds **8**, **11** and variable temperature study on **8, 11** were collected in transmission geometry on station I11, Diamond Light Source using synchrotron radiation at a wavelength of 0.825054 Å. Data analysis was carried out by Dr Phil Chater at the University of Liverpool[26].

X-ray powder diffraction data of **8** following gas sorption measurements were collected using a Bruker D8 Advance diffractometer with Mo Kα radiation and Lynxeye detector in transmission geometry.

PXRD data on the reversibility of phases **11D-11R-11D** were collected in transmission geometry from sample-loaded 0.5 mm spinning capillaries using a STOE Stadi-P diffractometer with Cu Kα radiation.

PXRD data on xylene loaded **11**: **11D**; **11PM** after 1 minute, 10 minutes, 24 hours and 7 days and all Ln(HTCPB) compounds where Ln = La (**10**), Ce (**11**), Pr (**12**), Nd (**13**), Sm (**14**) and Eu (**15**) were collected using a Bruker diffractometer with Cu Kα radiation in transmission geometry in a 0.5 mm spinning capillary. Data for the time dependence experiments (**11PM** after 1 minute, 10 minutes, 24 hours and 7 days) was analysed by Dr Phil Chater at the University of Liverpool[26].

All data (except variable temperature) were collected at room temperature.

2.2.3 Thermogravimetric Analysis (TGA)

TGA is used to determine the overall thermal stability of solid materials, including MOFs and to investigate structural properties of the material. The technique monitors the weight change with with increasing temperature, starting with the loss of volatile solvents followed by the loss of higher boiling components.

A sample of around 5-10 mg is heated slowly and the mass is recorded at each temperature over time, producing a graph of % weight loss against time. In the case of MOFs, an initial weight loss corresponding to the loss of guest solvent molecules is seen, followed by the loss of any coordinated guests. A subsequent plateau shows the stability of the material, after which a sharp weight loss is seen with the breakdown of the framework. The final reading at the highest temperature corresponds to the mass of the remaining metal oxide and can be used to confirm the phase purity of the material. This technique has an accuracy of ±0.001 mg and can therefore be used in conjunction with elemental microanalysis to calculate the exact composition of a material.

TGA of compounds **1-3, 7, 10-14** were carried out under a carrier gas atmosphere of air using a TA instrument SDT Q600. Samples were heated at 2 °C /min up to 600 ºC and then cooled back down to room temperature.

2.2.4 Elemental Microanalysis

Elemental microanalysis is used to accurately measure the ratio elements within a compound. Generally, C, H and N are the three elements measured as the majority of organic compounds contain them, however other elements can be measured including O, S, F, Cl, Br and some others. If the compound contains C and H alone, the values measured should add up to 100 % exactly, if not, this implies there are other contaminants present.

For MOFs, CHN analysis is a useful tool in determining the phase purity of a material once the structure has been determined. The single crystal structure will provide a metal:ligand combination and the expected ratio of C H and N from the ligand and any guest solvent can be calculated from TGA. The values measured from elemental analysis should match these predicted ratios if the material is phase pure.

Elemental analyses (C, H and N) were obtained using a Thermo EA1112 Flash CHNS-O Analyzer.

2.2.5 Gravimetric Gas Sorption

Gas sorption isotherms are measured to estimate the pore size and surface area of a material. Knowledge of the surface area can provide an insight into potential applications. Gravimetric gas sorption methods involve changing the partial pressure of the adsorbate and monitoring the change in mass of the sample.

The process of collecting an isotherm involves firstly activating the material. Then, from a vacuum, the sample is exposed to a vapour guest with increasing pressure, and the % weight uptake is measured against partial pressure of the vapour. Guests can either be chemisorbed or physisorbed onto a channel or external surface, but gas sorption isotherms rely on the physisorption of guests, with their uptake and removal giving insight into the porosity of the material.

The six isotherm types shown in Figure 5 and depending on porosity, channel/pore shape and the nature of any host-guest and guest-guest interactions, different isotherm graphs will be produced. The profile of an isotherm provides information about the pore size, shape and internal surface chemistry.

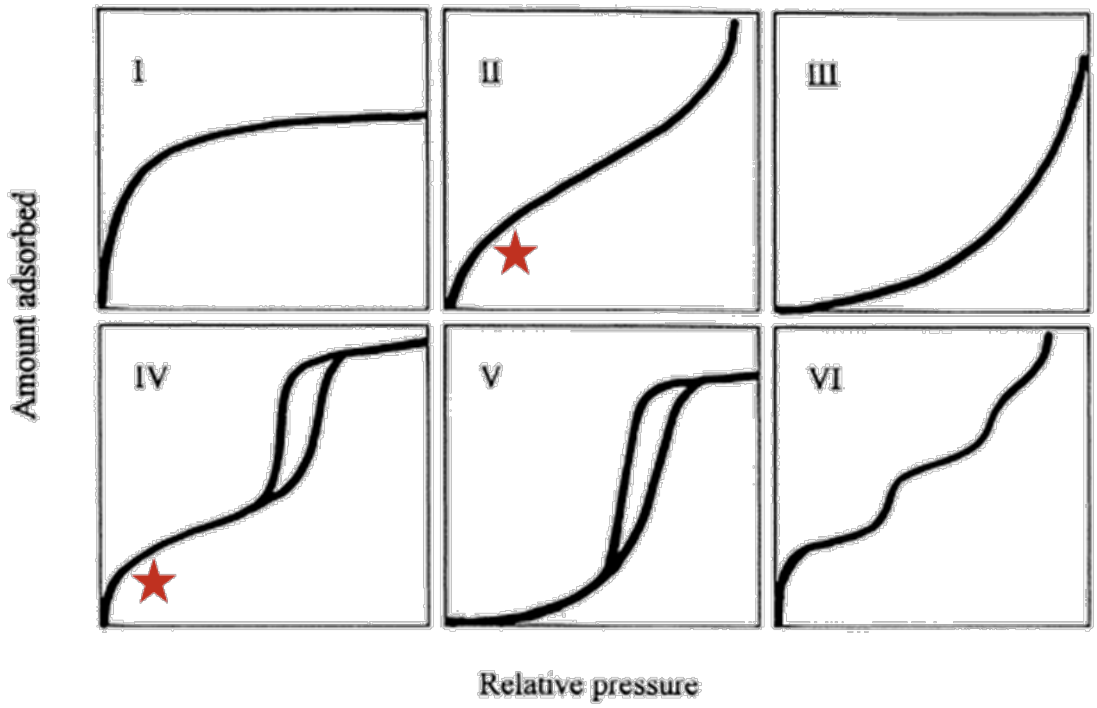

Figure 5: Isotherm measurement graphs observed for different material types. The star in II and IV represents the point at which monolayer coverage is achieved. Figure adapted from reference[27].

A reversible type I isotherm is characteristic of microporous materials with the maximum uptake controlled by the total accessible micropore volume. These material generally have small external

surface areas, such as zeolites, activated carbons and many MOFs. Reversible Type II isotherms are concave to the x-axis and are characteristic of macroporous or non-porous materials. In Figure 5, the red star on the type II isotherm represents the point at which monolayer coverage is achieved, after which, multilayer coverage begins. Reversible type III isotherms are not common and are convex to the x-axis. Within material exhibiting such isotherms, guest-guest interactions play an important role. Type IV isotherms are characteristic of mesoposous materials. Again the star in Figure 5 represents the point at which monolayer coverage is achieved after which multilayer coverage commences. The hysteresis loop in type IV isotherms result from capillary condensation of the guest vapour within the pores, which occurs below the saturation vapour pressure the pure liquid guest. Type V isotherms are uncommon, as type III, with their convex shape, but are obtained with some guests due to guest-guest interactions. Type VI isotherms occur with the step by step multilayer adsorption of guests onto non-porous surfaces. Each step height represents the monolayer capacity of the material[28].

Information in addition to the porosity type of the framework can be extracted from a gas sorption isotherm; the Brunauer–Emmett–Teller (BET) surface area for determination of the surface area, pore volume and isosteric heat of adsorption (Q_{st}).

2.2.5.1 BET Surface Area Determination

The BET surface area is one of the most common methods of surface area determination. Is assumes that the adsorbed mono-layers of guest taken up are in dynamic equilibrium with the vapour under measurement.

$$\frac{\boldsymbol{p}}{\boldsymbol{V(p^0 - p)}} = \frac{\boldsymbol{1}}{\boldsymbol{V_m C}} + \frac{\boldsymbol{C-1}}{\boldsymbol{V_m C}} \cdot \frac{\boldsymbol{p}}{\boldsymbol{p}}$$

Equation 1: *Linear BET equation. V = amount of adsorbent, p/p^0 = relative pressure, Vm = monolayer capacity, C = constant*[28].

From equation 1, V_m is determined. This is achieved by plotting the linear curve of $p/V(p^0-p) = f(p/p^0)$. The surface area can then be calculated using equation 2.

$$\boldsymbol{A_s = V_m N_a A_X}$$

Equation 2: *Surface area determination. A_s = surface area of adsorbent, N_a = Avagadro's number, A_x = cross sectional area of adsorbate*[28].

The BET model assumes adsorption of a gas onto a flat surface, but in MOFs this does not occur; adsorption in MOFs takes place at vacant metal centres and at the channel walls within the void spaces and in some cases occurs as a pore-filling mechanism rather than layer-by-layer. However, despite the fact the BET model cannot fully describe the physisorption in MOFs, it is often used to measure the surface area of these materials[29-32]. In the low pressure region, it is able to reproduce the isotherm shapes expected for the different pore systems. For this reason, the points corresponding to the initial uptake in the adsorption branch of the isotherm between p/p^0 = 0.2-2 mbar are plotted as p/p^0 against $p(n(p-p^0)$ for BET surface area determination. In this thesis, the BET surface area for the compounds discussed was calculated using the Hiden software for BET surface area analysis.

2.2.5.2 Pore Volume Determination

The pore volume of a MOF can be calculated using the Dubinin-Radushkevich (DR) equation[33]. Once calculated from the isotherm, the pore volume can be compared to that determined from single crystal structure of a MOF. This provides information into the extent of desolvation, phase purity and stability of the material.

$$\mathbf{logV} = \boldsymbol{logV_0} - \frac{\boldsymbol{RT}}{\boldsymbol{\beta E_0}} + \left(\mathbf{log}\frac{\mathbf{p^0}}{\mathbf{p}}\right)^{\mathbf{2}}$$

Equation 3: *The Dubinin-Radushkevich equation for pore volume determination[33]. V = volume adsorbed at equilibrium, V_0 = micropore capacity, p_0 = saturation vapour pressure at temperature T, p = equilibrium pressure, β= affinity of gas under analysis relative to p_0, R = gas constant, E_0 = activation energy.*

In order to calculate the pore volume, the adsorption branch of a CO_2 isotherm collected at 195 K is used and plotted using equation 3. This allows for the determination of the pore volume of a material.

2.2.5.3 Isosteric Heat of Adsorption

The isosteric heat of adsorption (Q_{st}) is used to quantify the strength of interaction between the host porous solid and the adsorbed vapours in an isotherm measurement. The Q_{st} can be calculated once isotherms have been collected on the same material at different temperatures. For example, if CO_2

isotherms have been collected at 298 K and 273 K, the data can be used together to calculate the affinity of that material for CO_2.

In this thesis, all Q_{st} presented was calculated using a virial-type method (*Equation 4,5*), using the adsorption branches of CO_2 and CH_4 isotherms collected at 298 K and 273 K[34].

$$\mathbf{ln}P = \mathbf{ln}N + \frac{1}{T}\sum_{i=0}^{m} a_i N^i + \sum_{i=0}^{n} b_i N^i$$

Equation 4: *Virial-type equation for determination of virial coefficients. P = pressure of adsorption at temperatures T, N – amount adsorbed, a_i, b_i = virial coefficients, m,n = number of coefficients needed to describe the isotherm[34].*

$$\mathbf{Q_{st}} = -R\sum_{i=0}^{m} a^i N^i$$

Equation 5: *Equation for determination of Qst. R = gas constant, N – amount adsorbed, a_i = virial coefficient[34].*

The virial coefficients, a_0 to a_m were calculated using equation 4 and were then used to determine the Q_{st} using equation 5. In this thesis, the Q_{st} for the MOFs discussed were calculated using these equations.

2.2.5.4 Gas Sorption Measurements

CO_2 and CH_4 gas sorption isotherms on all samples were measured using the Intelligent Gravimetric Analyser (IGA) from Hiden. Samples were washed with and appropriate solvent and left to air dry prior to use and were then outgassed at 100 °C under dynamic vacuum (10^{-5} mbar) until constant mass loss was reached.

For the Brunauer-Emmett-Teller (BET) surface area measurement, the samples were cooled to 195 K by means of a Dewar vessel containing dry ice. The isotherms were measured to an absolute CO_2 pressure of 1 bar. For measurements at 273 K and 298 K, the samples were cooled using a Dewar vessel containing ice and water respectively. The samples in these cases were measured to a CO_2 pressure of 10 bar.

2.2.6 Volumetric Gas Sorption

The method of collecting a gas sorption isotherm using volumetric methods is based on monitoring the drop in adsorbate pressure in a system of known volume. The data collected is plotted as %wt uptake against unit mass or volume of adsorbate and the results obtained allow the adsorption capacity of the system to be determined[35].

As the BET is calculated from the initial points in the adsorption branch of an isotherm, '5-point' BET measurements can be perfomed volumetrically for BET surface area determination, in which only the first five points of the adsorption branch are collected. N_2 BET measurements on compound **8** were carried out volumetrically using a Quantochrome Nova 4200 Surface Area Analyser. A fresh washed and air dried sample of **8** was used to collect a five point BET measurement. Data were collected at 77 K, cooled in liquid N_2, in the range of pressure $0.05 \leq P/P_0 \leq 0.3$.

2.2.7 Ultra-Violet-Visible Spectroscopy

Ultra Violet Visible (UV/vis) Spectroscopy is used to measure electron transitions within a compound. Electronic transitions are affected by how the ligands and metal centre interact upon coordination; the ligand field and the geometry of the metal centre. This technique can provide useful information into how a ligand is coordinated and was used to identify the wavelength of maximum absorbance of compound **11** in Chapter 4 of this thesis.

A UV/vis spectra was collected in a solid state holder at room temperature on a Perkin–Elmer Lambda 650S UV/vis spectrometer equipped with Labsphere integrating over the spectral range 190-900 nm using $BaSO_4$ reflectance standards.

2.2.8 Fluorescence Spectroscopy

Fluorescence excitation and emission spectra were collected at room temperature on a Perkin–Elmer LS 55 fluorescence spectrometer with a scan speed of 10 nm/min. Fluorescent measurements were performed on samples (as-made **11**, free H_4TCPB ligand and $Ce(NO_3)_3.6H_2O$) in a solid state holder.

2.3 References

[1] O. K. Farha, J. T. Hupp, *Acc. Chem. Res.* **2010**, *43*, 1166-1175.

[2] A. Rabenau, *Angew. Chem. Int. Ed.* **1985**, *24*, 1026-1040.

[3] R. I. Walton, *Chem. Soc. Rev.* **2002**, *31*, 230-238.

[4] M. Choucair, P. Thordarson, J. A. Stride, *Nat. Nanotech.* **2009**, *4*, 30-33.

[5] T. Sasaki, Y. Endo, M. Nakaya, K. Kanie, A. Nagatomi, K. Tanoue, R. Nakamura, A. Muramatsu, *J. Mater. Chem.* **2010**, *20*, 8153-8157.

[6] P. Smart, A. Bejarano-Villafuerte, R. M. Hendry, L. Brammer, *CrystEngComm* **2013**, *15*, 3160-3167.

[7] J. S. Lee, S. B. Halligudi, N. H. Jang, D. W. Hwang, J. S. Chang, Y. K. Hwang, *Bull. Korean Chem. Soc.* **2010**, *31*, 1489-1495.

[8] J. Y. Choi, J. Kim, S. H. Jhung, H. K. Kim, J. S. Chang, H. K. Chae, *Bull. Korean Chem. Soc.* **2006**, *27*, 1523-1524.

[9] H. Bux, F. Y. Liang, Y. S. Li, J. Cravillon, M. Wiebcke, J. Caro, *J. Am. Chem. Soc.* **2009**, *131*, 16000.

[10] L. Brammer, G. M. Espallargas, H. Adams, *CrystEngComm* **2003**, *5*, 343-345.

[11] T. Hahn, *International Tables for Crystallography, Vol. A*, **2006**.

[12] W. Clegg, *Crystal Structure Determination*, Oxford University Press, New York, United States, **1998**.

[13] A. L. Patterson, *Phys. Rev.* **1934**, *46*, 0372-0376.

[14] M. M. Woolfson, *Rep. Prog. Phys.* **1971**, *34*, 369.

[15] C. Dumas, A. van der Lee, *Acta Crystallogr. D* **2008**, *64*, 864-873.

[16] L. J. Bourhis, O. V. Dolomanov, R. J. Gildea, J. A. K. Howard, H. Puschmann, *olex2.solve* **2011**.

[17] O. V. Dolomanov, L. J. Bourhis, R. J. Gildea, J. A. K. Howard, H. Puschmann, *J. Appl. Crystallogr.* **2009**, *42*, 339-341.

[18] G. Sheldrick, *Acta Crystallographica Section A* **2008**, *64*, 112-122.

[19] J. Cosier, A. M. Glazer, *J. Appl. Crystallogr.* **1986**, *19*, 105-107.

[20] *Data Processing carried out by Dr. John Warren at the University of Liverpool.*

[21] Bruker, *APEXII 2010* **2010**.

[22] Bruker, *SADABS* **2008**.

[23] Rigaku, **2001**, FS_process.

[24] T. Higashi, *ABSCOR* **2001**.

[25] *Data processing carried out by Alec McLennan at the University of Liverpool.*

[26] *Analysis carried out by Dr. Phil Chater at the University of Liverpool.*

[27] M. D. Donohue, G. L. Aranovich, *Adv. Colloid Interfac.* **1998**, *76*, 137-152.

[28] K. S. W. Sing, D. H. Everett, R. A. W. Haul, L. Moscou, R. A. Pierotti, J. Rouquerol, T. Siemieniewska, *Pure Appl. Chem.* **1985**, *57*, 603-619.

[29] F. J. Uribe-Romo, J. R. Hunt, H. Furukawa, C. Klock, M. O'Keeffe, O. M. Yaghi, *J. Am. Chem. Soc.* **2009**, *131*, 4570.

[30] D. J. Tranchemontagne, K. S. Park, H. Furukawa, J. Eckert, C. B. Knobler, O. M. Yaghi, *J. Phys. Chem. C* **2012**, *116*, 13143-13151.

[31] Y. Yan, X. Lin, S. H. Yang, A. J. Blake, A. Dailly, N. R. Champness, P. Hubberstey, M. Schroder, *Chem. Commun.* **2009**, 1025-1027.

[32] A. Demessence, D. M. D'Alessandro, M. L. Foo, J. R. Long, *J. Am. Chem. Soc.* **2009**, *131*, 8784.

[33] Y. K. Tovbin, *Russ. Chem. Bull.* **1998**, *47*, 637-643.

[34] S. A. Al-Muhtaseb, J. A. Ritter, *Ind. Eng. Chem. Res.* **1998**, *37*, 684-696.

[35] R. E. Morris, P. S. Wheatley, *Angew. Chem. Int. Ed.* **2008**, *47*, 4966-4981.

Chapter 3

Mixed Carboxylate-Imidazole Based Metal-Organic Frameworks

3.1 Introduction

Coordination compounds can extend in one, two, or three dimensions depending on the interactions present between their component species. Interactions may vary in strength, from the strongest coordination bonds between metal and ligand, through intermolecular interactions of varied strength such as hydrogen bonds. MOFs (3D coordination compounds with potential porosity) are of interest due to their wide range of tuneable properties. Current research focuses on the synthesis of porous MOFs, with multiple or multifunctional linkers, as they have potential applications in many areas of chemistry due to a combination of their robustness and void space allowing access to metal centres, such as storage[1-2] and separation[3-4], medical applications[5], non-linear optics, catalysis[6] and molecular sensors[7].

There have been many reported examples of carboxylate MOFs with high thermal stabilities and high gas uptake and storage capabilities. Polynuclear metal clusters have more recently been used as secondary building units (SBUs) in MOF synthesis as they can enhance the stability of a framework whilst adding interesting structural characteristics and dimensionality, such as MOF-5, in which octahedral Zn_4O clusters propagate a 3D framework with high thermal stability and permanent porosity[8] and MIL-101, where trivalent metal clusters afford high chemical stability[9]. Selection of the appropriate metal and ligand combination alongside the judicious choice of synthetic conditions all play a role in the formation of metal clusters within a MOF, slight deviations from which can result in the formation of an entirely different framework[10].

There are many examples of cluster-containing frameworks based on the 1,3,5-benzenetribenzoate (1,3,5-BTB) ligand[11]. MOF-177 contains an ZnO_4 SBU similar to that found in MOF-5, but in this case the ZnO_4 building units are held in 3D by 1,3,5-BTB ligands, creating a large pore microporous framework with a Langmuir surface area assuming monolayer coverage of N_2 of 4500 m^2/g[4]. Jia *et. al.* present two isostructural MOFs (cationic JUC-101 and anionic JUC-102) which contain $Ni_3(\mu_3\text{-}OH)O_{12}$ clusters linked by 1,3,5-BTB ligands. JUC-101 has a measured BET surface area of 3742 m^2/g and has been shown to absorb 4.18 wt% of H_2 at 30 atm and 77 K. The corresponding JUC-102 can absorb cationic dye molecules[12].

Zeolitic imidazolate frameworks (ZIFs) are a recent class of MOFs. They are of interest as they mimic the structure of common zeolites but offer a variety of new properties through the introduction of metal centres into the void spaces. Imidazole (IM) is a useful linker ligand as it can lose a proton to form a ditopic imidazolate ($C_3N_2H_3^-$), so when combined with metal salts forms networks with the formula $M(IM)_2$, propagated by tetrahedral MN_4 clusters. ZIFs are of interest as the angle that the M - IM - M unit creates mimics that of the Si - O – Si bond angle of 145 ° present in many common zeolites (*Figure 1*). The ability to incorporate metal ions and organic ligands into

a zeolite structure is desired as the resulting structures would possess pores containing a large amount of transition metal sites. The electronic and steric properties of these sites can be altered using various functionalised organic ligands.

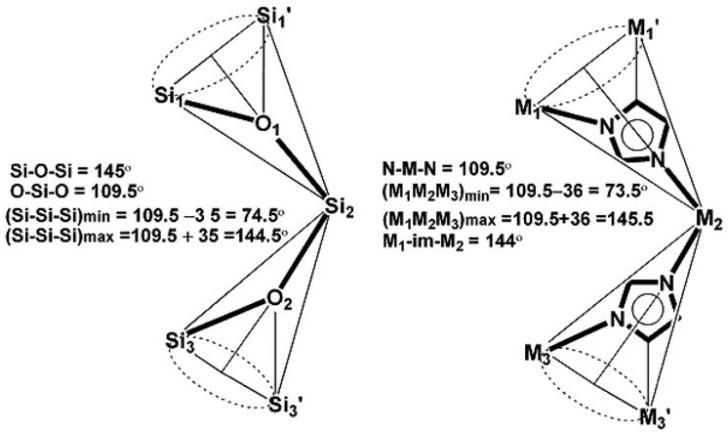

Figure 1: *Schematic display of the flexibility of the T-T-T angles in silicates and zinc (or cobalt) imidazolate polymers (T = Si/Al; only three neighbouring T-atoms are selected for clarity). Figure adapted from reference*[13].

In the synthesis of common Si or Al based zeolites, organic amines play a major role in obtaining the correct structure through structure direction, templation[14] and gel-pH altering or buffering[15]. So far in the solvothermal or non-solvothermal synthesis of metal-imidazolates no amine has been found to have a templating effect, whereas organic solvents such as DMF (N,N-dimethylformamide), DEF (N,N-diethylformamide) or NMP (N-methylpyrrolidone) have a strong solvating effect and play the role of a template or structure-directing agents[13].

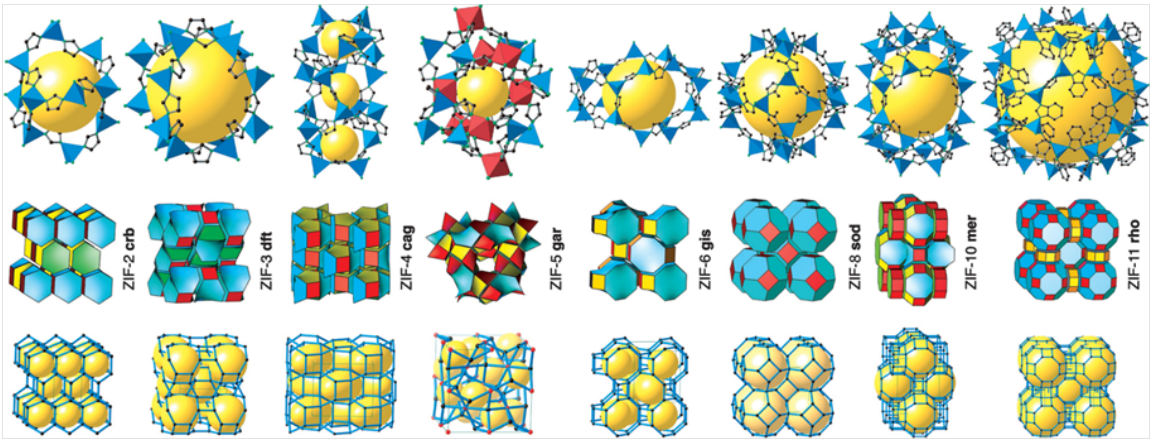

Figure 2: *Single-crystal structures for ZIF's: ZnN_4 tetrahedra in blue, InN_6 octahedra in red (ZIF-5). H atoms are omitted for clarity. Figure taken from reference*[16].

For the purpose of replicating zeolitic frameworks, ZIFs have been synthesised using modified IM ligands combined with metal salts (Zn(II) and Co(II)). Park *et. al.* have synthesised a range of ZIFs (ZIFs 1-12) containing Zn(II) and Co(II) (based on aluminosilicate zeolites) and a mixed metal ZIF containing Zn(II) and In(III) (based on a garnet network) together with various IMs (*Figure 2*)[16]. Two compounds in particular, $Zn(MeIM)_2$ (ZIF-8) and $Zn(PhIM)_2$ (ZIF-11) have demonstrated high thermal stability up to 550 °C and chemical stability in boiling alkaline, water and organic solvents. All ZIFs were synthesised by combining metal nitrate salts with an IM-type linker in an amide solvent (DMF or DEF) followed by heating to temperatures between 85 °C and 150 °C for 24 hours. The ZIF precipitated after 48-96 hours from solution[16]. The synthesis of ZIF-8 ($Zn(2\text{-}mIM)_2$; mIM = methylimidazolate) has since been modified by Bux *et. al.* by replacing DMF with pure MeOH as it can later by removed from the crystal much more easily[17]. This framework was investigated for the production of membranes with molecular sieving properties.

Generally, amide solvents such as DMF or DEF are chosen as solvents in the solvothermal synthesis of ZIFs for their high boiling points, as lower boiling solvents result in precipitation of reactants over reagents. All ZIFs to date have been synthesised using IM-based ligands only and several examples are to be discussed: Banerjee *et. al.* have synthesised a range of twenty-five ZIFs using high throughput methods for applications in CO_2 capture. Three ZIFs in particular, Zn(bIM)(nIM) (ZIF-68), Zn(cbIM)(nIM) (ZIF-69) and $Zn(IM)_{1.13}(nIM)_{0.87}$ show high thermal stability up to 330 °C and chemical stability in refluxing organic and aqueous media[18]. A range of pore diameters was also achieved by Yaghi *et. al.* between 3.8 Å (using IM) to 13.1 Å (using nitrobenzimidazole), while all ZIFs maintained a GME topology (GME = zeolite code for gmelinite. All ZIFs produced showed thermal stability up to 300 °C, demonstrated by heating in an atmosphere of N_2 and chemical stability, demonstrated by boiling in benzene, methanol and water for 7 days, after which time all ZIFs retained their structures[19]. ZIFs with 'colossal cages' have been synthesised by Wang *et. al.* for the storage of large quantities of CO_2; ZIFs as 'carbon dioxide reservoirs'. Within this paper, the synthesis of the porous ZIF-95 ($Zn(cbIM)_2$; cbIM = 5-chlorobenzimidazole) was achieved by combining $Zn(NO_3)_2.4H_2O$ with cbIM in DMF and water and heating the solution to 120 ˚C. The framework contains two giant elliptical cages measuring 25.1×14.3 Å and 30.1×20.0 Å. ZIF-100 ($Zn_{20}(cbIM)_{39}(OH)$) was synthesised using the same conditions, but with precise control of the amount of water added, and with the added use of $Zn(O_3SCF_3)_2$[20]. ZIF-95 and ZIF-100 have respective BET surface areas of 1,050 m^2/g and 595 m^2/g, measured using a N_2 isotherm, however, slow gas diffusion was observed. This was attributed to the largest pore aperture of 3.65 Å and 3.35 Å respectively in ZIF-95 and ZIF-100, hence why these materials are good candidates for CO_2 storage.

There are over 180 zeolite topologies and to date only 20 have been successfully replicated in MOFs[21]. Draznieks *et. al.* have used DFT (Density Functional Theory) to model the structure of ten hypothetical porous ZIFs which are based upon different zeolitic topologies not yet seen in other materials. The energy of aluminosilicate zeolites increases with density and the authors demonstrate that the same is true for ZIFs[22]. The idea is to model the stability of frameworks with zeolitic topologies which can then be used as synthesis targets. This has been achieved by Rodriguez-Albelo and co-workers, who have designed and simulated a new family of MOFs based on ε-type Keggin polyoxometalates (POMs) as building units and benzene-1,4-dicarboxylate (1,4-BDC). These new materials are referred to as Z-POMOFs and the authors have gone on to synthesise these frameworks following their simulation[23]. This work was inspired by the synthesis of ZIF-60, a large-pore framework which possesses LTA topology and suggests that there may be other viable large-pore ZIFs.

In general, in order to increase the pore size of a framework, the intuitive choice is to use a longer linker between metal sites; longer/larger linker equals greater distance between metal sites equals larger channel space. However the problem in achieving this is that increasing linker size often results in interpenetration of the framework. This is shown with the IRMOF (isoreticular MOF) series[8]. IRMOFs 1-16 use linkers of increasing length: 1-7 include functionalised 1,4-BDC; 8 uses the longer 2,6-NDC; 10 uses 1,4-biphenyl dicarboxylate (1,4-(4,4')BPDC); 12 uses protonated 1,4-pyrene dicarboxylate (1,4-HPDC); 14 uses 1,4-PDC; 16 uses 1,4-(4,4')triphenyl dicarboxylate (1,4-TPDC). When the shorter linkers are used (IRMOFs 1-8), non-interpenetrated frameworks are produced, however under similar conditions, using longer linkers (IRMOFs 10, 12, 14, 16) produces doubly interpenetrated networks. In order to achieve the non-interpenetrated counterparts (IRMOFs 9, 11, 13 and 15 respectively), the synthesis conditions must be changed to a more dilute reaction mixture and the synthesis must be carried out with care. There are ways to avoid interpenetration, including the use of linkers with sterically hindering functional groups[24] that blocks the ability of the framework to interpenetrate, specific control of temperature or concentration[25] of reaction and employing the template effect[26].

In order to increase pore size and improve structural stability, the use of mixed ligands in MOF synthesis has been shown to be effective. Combination of two or more functional groups or linkers within a MOF can enhance its stability or alter its properties and also reduces interpenetration. Klein *et. al.* combine 2,6-napthalene dicarboxylate (2,6-NDC) and 1,3,5-BTB in the synthesis of the MOF DUT-6 (*Figure 3A*). The secondary 2,6-NDC linker stabilises the open framework, linking the $Zn_4O_6^+$ clusters. DUT-6 is a 3D mesoporous framework which is stable up to 380 °C, with a total solvent accessible volume of 21,902 $Å^3$ (79.2% of the cell volume) and a hydrogen adsorption capacity of 666 cm^3g^{-1} at 50 bar (5.64 wt%), which is one of the highest reported for

MOFs[27]. The framework contains a similar paddlewheel SBU to the $Cu_4O_6^+$ SBU linked by 1,3,5-BTB ligands in MOF-14[28], however whereas MOF-14 is interpenetrated, the additional cross-linked provided by 2,6-NDC between clusters enhances the stability of the framework and removes interpenetration.

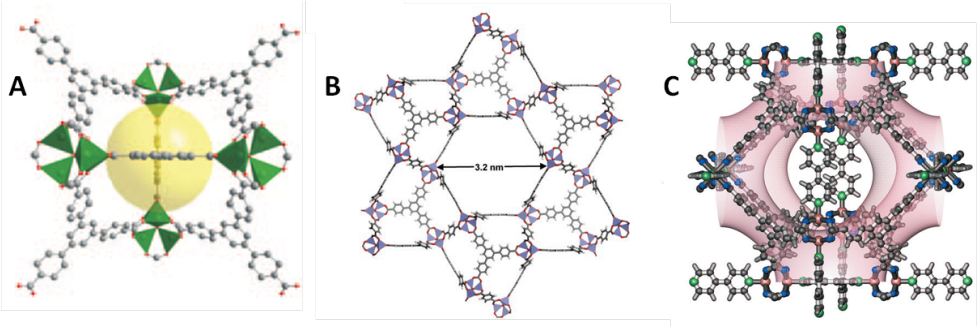

Figure 3: *Representation of A: DUT-6[27]; B: UCMC-1[29] and C: DUT-23[30]. Figure adapted from references.*

Further examples of 3D porous non-interpenetrated MOFs using multiple linkers include UMCM-1[29] which comprises 1,3,5-BTB, 1,4-BDC linking Zn_4O clusters producing a mesoporous framework with a BET surface area of 4160 m^2g^{-1} (*Figure 3B*) and the series of isomorphic DUT-23 compounds (Zn, Cu, Ni, Co) in which the 4,4'-bipy linker was inserted into a Zn(1,3,5-BTB) framework between paddlewheel units to avoid interpenetration and yield porous 3D frameworks (*Figure 3C*). The DUT-23 (Zn, Cu, Co) compounds have BET surface areas of 4340, 4730, 4850 m^2g^{-1} respectively[30].

In this chapter are reported the syntheses, structure determination and characterisation of coordination compounds containing both IM and various carboxylic acid ligands, in which the carboxylates form the 2D or 3D frameworks with IM coordinated as a terminal neutral ligand in all cases. Attempts to deprotonate IM to induce ZIF connectivity within these frameworks by increasing the IM concentration and adding base were unsuccessful, however changing the conditions in this way allowed access to three new 2D frameworks, in which IM is coordinated as a terminal neutral ligand and involved in hydrogen bonding with the adjacent 2D layer in each case.

The synthesis of a porous 2D MOF based on a novel Co_6 cluster which exhibits good thermal stability and permanent porosity is also discussed. Metal-carboxylate coordination between Co(II) and 1,3,5-BTB forms the backbone of 2D sheets, between which IM is responsible for hydrogen bonding and π-π stacking with the next sheet to extend the framework into three dimensions. The framework has variable porosity depending on the activation conditions used. Changing the secondary linker (IM (**7**), py (**8**), N-MeIM (**9**)) changes the structure obtained and highlights the need for hydrogen bonding from this ligand to stabilise structural motifs present in **7**.

3.2 Experimental

Full synthetic methods for the synthesis of compounds **1-9** in this chapter are discussed in this section. General methods are given for compounds **1-6** and **7-9** separately in sections 3.2.1 and 3.2.2 respectively.

3.2.1 Synthesis of Compounds 1-6:

A mixture of $M(NO_3)_2.xH_2O$, carboxylic acid, and IM, were added to a 12 ml borosilicate glass vial, to which DMF (6 ml) was then added and the vial was sealed. The solution was sonicated for 15 minutes, allowing all reagents to dissolve. This was then heated to 120 °C at a rate of 2°C/min and held at that temperature for 48 hours and then cooled at 0.2 °C/min back down to room temperature:

Zn_3(1,4-BDC)$_3$(Im)$_2$·DMF (**1**): $Zn(NO_3)_2.6H_2O$ (8.94 mg, 0.3 mmol), 1,4-BDC (4.98 mg, 0.3 mmol) and IM (1.36 mg, 0.2 mmol) were used. Large colourless block single crystals were formed. The formula of **1** was calculated to be $Zn_{1.5}$(1,4-BDC)$_{1.5}$(Im)·0.8DMF·H_2O from elemental microanalysis: Calculated: C 43.79, H 3.62, N 7.97; Theory: C 43.75, H 3.63, N 8.02.

Co_3(1,4-BDC)$_3$(Im)$_2$·DMF (**2**): $Co(NO_3)_2.6H_2O$ (8.88 mg, 0.3 mmol), 1,4-BDC (4.98 mg, 0.3 mmol) and IM (1.36 mg, 0.2 mmol) were used. Large purple block single crystals were formed. The formula of **2** was calculated to be $Co_{1.5}$(1,4-BDC)$_{1.5}$(Im)·DMF·0.6H_2O from elemental microanalysis: Calculated: C 44.409, H 3.721, N 8.507; Theory: C 44.43, H 3.77, N 8.64.

Zn(3,5-pydc)(Im)·DMF (**3**): $Zn(NO_3)_2.6H_2O$ (12.8 mg, 0.6 mmol), 3,4-pydc (10 mg, 0.6 mmol) and IM (4.08 mg, 0.6 mmol) were used. Large colourless block single crystals were formed. The formula of **3** was calculated to be Zn(3,5-pydc)(Im)·0.9DMF·0.3H_2O from elemental microanalysis: Calculated: C 40.932, H 3.705, N 12.316; Theory: C 41.25, H 3.79, N 12.77.

Co(1,3,5-BTC)$_2$(DMF)$_2$·DMF (**4**): $Co(NO_3)_2.6H_2O$ (29.1 mg, 0.1 mmol), 1,3,5-BTC (21.0 mg, 0.1 mmol) and IM (6.8 mg, 0.1 mmol) were used in the ratio 1:1:1. Large pink hexagonal single crystals were formed.

Co_3(BTC)$_2$(Im)$_2$(DMF)·DMF (**5**): $Co(NO_3)_2.6H_2O$ (29.1 mg, 0.1 mmol), 1,3,5-BTC (21.0 mg, 0.1 mmol) and IM (20.4 mg, 0.3 mmol) in the ratio 1:1:3. Large purple needle single crystals were formed.

Co_3(BTC)(Im)$_3$ (**6**): $Co(NO_3)_2.6H_2O$ (29.1 mg, 0.1 mmol), 1,3,5-BTC (21.0 mg, 0.1 mmol) and IM (20.4 mg, 0.3 mmol) were used in the ratio 1:1:3 with the addition of 1 drop of 1M NaOH. Large purple needle single crystals were formed.

3.2.2 Synthesis of Compounds 7-9:

A mixture of $CoCO_3$, 1.3.5-benzene tribenzoate (1,3,5-BTB) and an N-based ligand (IM, Py, NMeIM) were added to a solution of EtOH (3 ml) and H_2O (3 ml) in a 12 ml borosilicate glass vial which was sealed and left to sonicate for 15 minutes after which time a pale purple suspension had formed. This was then heated to 100 °C for 36 hours at a rate of 2 °C/minute, and then cooled back down to room temperature at 0.2°C/ minute.

Co_3(1,3,5-BTB)$_{1.67}$(IM)$_{1.36}$(O)·(EtOH)$_{2.17}$·(H_2O)$_{7.87}$ (7): $CoCO_3$ (2.71 mg, 2.2 mmol), 1,3,5-BTB (10 mg, 2.2 mmol) and IM (4.65 mg, 6.6 mmol) used in a 1:1:3 ratio. The product was isolated in the form of purple block single crystals which were washed with EtOH and H_2O and left to air dry. The formula of **8** was calculated to be $Co_3(H_3BTB)_{1.67}(IM)_{1.36}(O)\cdot(EtOH)_{2.17}\cdot(H_2O)_{7.87}$ from CHN microanalysis: Calculated: C 51,22, H 4.76, N 3.06; Theory: C 51.22, H 4.56, N 3.05.

$Co_7(O)_2$(1,3,5-BTB)$_4$(NMeIM)$_5$(H_2O)$_4$·DMF (8): $CoCO_3$ (2.71 mg, 2.2 mmol), 1,3,5-BTB (10 mg, 2.2 mmol) and MeIM (4.9 mg, 6.6 mmol) used in a 1:1:3 ratio. The product was isolated in the form of small dark purple single crystals.

Co_3(1,3,5-BTB)(Py)$_3$(H_2O)$_3$·H_2O_9 (9): $CoCO_3$ (2.71 mg, 2.2 mmol), 1,3,5-BTB (10 mg, 2.2 mmol) and pyridine (Py) (5.0 mg, 6.6 mmol) used in a 1:1:3 ratio. The product was isolated in the form of purple needle single crystals.

3.2.3 Single Crystal Data Collection and Analysis

In this chapter, data for the single crystal structure solution of **1**, **2**, **3**, **7**, **8** and **9** was collected from the Rigaku Rotating Anode Diffractometer at the University of Liverpool. The structures were solved and refined using Olex2[31-32]. All structure solution and refinement was carried out with the assistance of Dr John Warren.

3.2.4 Powder X-Ray Diffraction and Analysis

Powder X-ray diffraction (PXRD) data from of **1**, **2** and **3** was collected in reflection geometry using a PanAnalytical Diffractometer with Co Kα radiation and were confirmed to by phase pure by indexing to the single crystal unit cell using Chekcell[33]. PXRD data and variable temperature data of **7** was collected in transmission geometry in a sealed 0.5 mm capillary, collected at station I11 at Diamond Light Source (DLS), Didcot, UK. Le Bail fit of **7** was carried out by Dr Phil Chater at the University of Liverpool.

3.3 Results and Discussion

3.3.1 Imidazole-Based Coordination Polymers

An initial set of experiments were set up with the intention of producing frameworks comprising both carboxylate and ZIF functionality. Literature precedent for the formation of carboxylate-based and ZIF frameworks individually showed DMF as the generally used as a solvent, however only Zn- and Co-based ZIFs had been synthesised at this time[16]. This lead to the decision to use Zn(II) and Co(II) as the metal salts, alongside a variety of carboxylate linkers: 1,4-Benzenedicarboxylate (1,4-BDC), 1,3,5-benzene tricarboxylate (1,3,5-BTC) and 3,5-pyridine dicarboxylate (3,5-pydc) and imidazole (IM), in DMF.

We found that the combination of carboxylic acids with IM under standard MOF/ZIF conditions produces M-carboxylate coordination frameworks in which IM is coordinated as a terminal neutral ligand. The structures isolated from the initial experiments were $Zn_3(1,4\text{-BDC})_3(IM)_2$ (**1**), $Co_3(1,4\text{-BDC})_3(IM)_2$ (**2**) and Zn(3,5-pydc)(IM).DMF (**3**).

Compounds **1** and **2** are isostructrual and were synthesised by combining $M(NO_3)_3.6H_2O$ (0.3 mmol, where M=Zn and Co respectively), 1,4-BDC (0.3 mmol) and IM (0.2 mmol) in DMF, followed by heating to 120 °C for 48 hours. Their structure is a framework in which Zn/Co(II) metal centres and bridging 1,4-BDC ligands create a 2D coordination network. IM is coordinated to M(II) as a terminal, neutral ligand and forms hydrogen bonds between the 2D layers, creating a 3D network. They both crystallise in a monoclinic $P2_1/n$ space with **1** having unit cell dimensions of a=14.7415 Å, b=9.4766 Å, c=15.4246 Å, α=γ=90 ° and β=104.290 ° and **2** with unit cell dimensions of a=14.7040 Å, b= 9.6419 Å, c=15.5050 Å, α=γ=90 ° and β=106.258 ° respectively. Compound **2** is used for structure description:

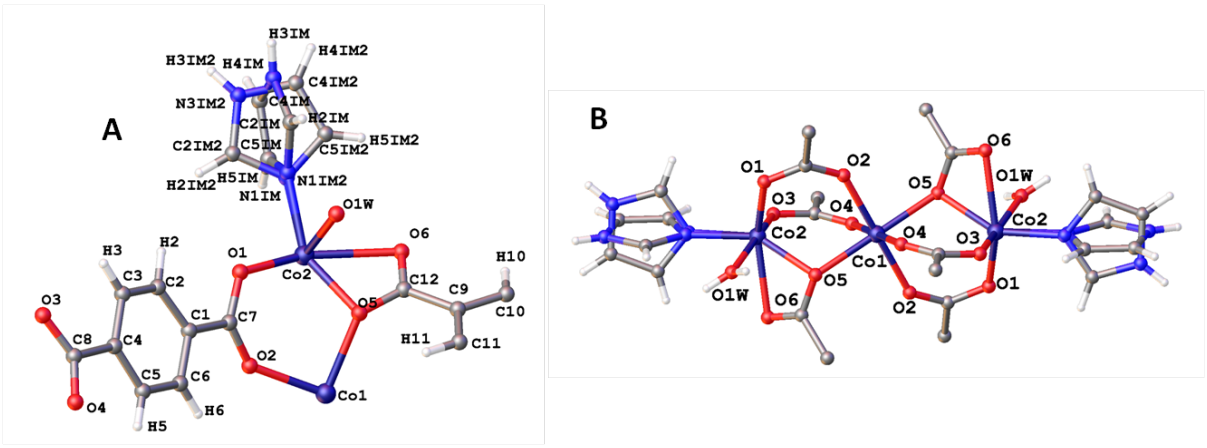

Figure 4: *A: Asymmetric unit in **1** and **2** (**2** used as example); B: Co_3 unit in **2**. Co (purple), C (grey), N (blue), O (red), H (white). Imidazole is disordered over two positions, shown in both figures.*

The asymmetric unit of **2** contains two Co, one and a half 1,4-BDC molecules, one coordinated disordered IM and one coordinated H_2O (*Figure 4A*). Co1 is octahedral and sits on an inversion centre and its coordination sphere is filled by two symmetry equivalent carboxylate oxygens; O4 and O2 and μ_2-O5. Co2 is 5-coordinate and its coordination sphere is filled by carboxylate oxygens O1, O3, O6 and μ_2-O5, H_2O (O1W) and disordered IM (N1IM1/2). Co1 and Co2 are connected via two carboxylate bridges; (Co2)-O3-C8-O4-(Co1) and (Co2)-O1-C7-O2-(Co1) and one μ_2-O bidentate bridge. As Co1 sits on an inversion centre which forms a Co_3O_{12} building unit, with H_2O and IM coordinated as terminal neutral ligands at either end of the linear unit (*Figure 4B*).

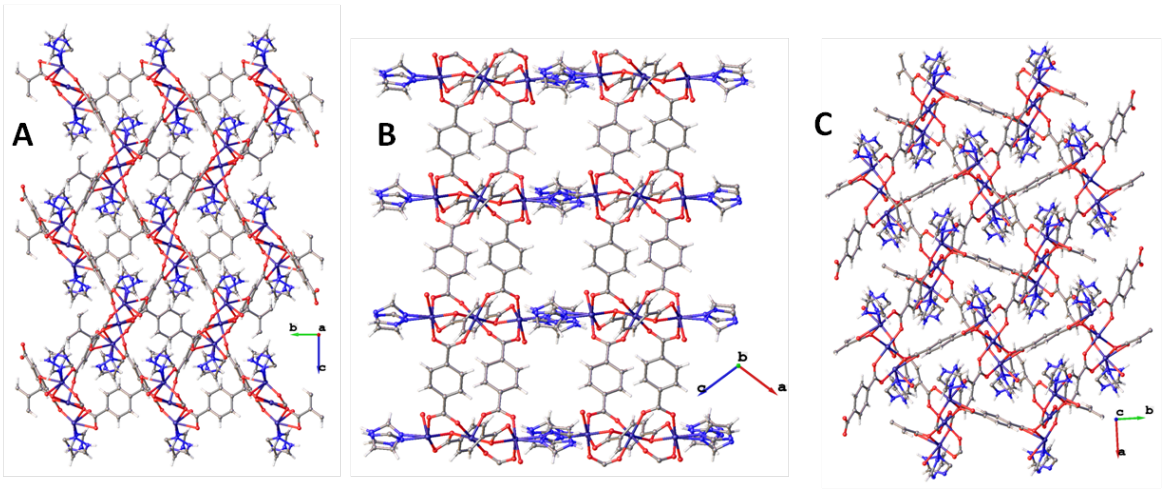

Figure 5: *Packing of* ***2****. A: View down 100; B: View down 010; C: View down 001.*

The Co_3O_{12} building unit lies horizontally and propagates the 2D layers with IM coordinated at the ends of the linear unit. These IMs hydrogen bond to carboxylate oxygens of the adjacent 2D layer (*Figure 5B*) with an H33···O2 distance of 2.140 Å and an N33-H33···O2 angle of 158.764 °. The phase purity of **1** and **2** was confirmed using PXRD (*Figure 6A*), TGA (*Figure 4B,C*) and CHN microanalysis (*Section 3.2.1*). For **1** and **2** respectively, initial TGA weight losses of 23.7 % and 21.05 % were observed which correspond to the loss of solvent from the frameworks. Compound **1** was found to be stable up to 350 °C, whereas **2** was stable up to 300 °C, after which point a drop in mass relating to the loss of organic matter was seen leaving the final ZnO (for **1**) and CoO (for **2**). Weight loss and final weight percentages match well with the theoretical formula of the frameworks including guest solvent in comparison with CHN microanalysis.

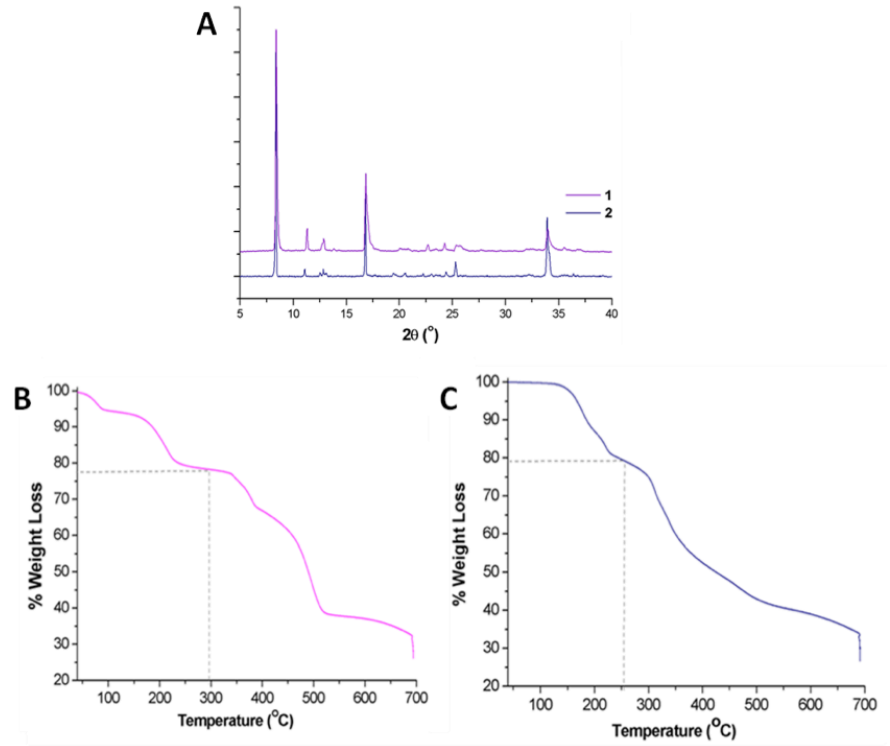

Figure 6: *A: PXRD profiles of isostructural **1** and **2**; B: TGA profile of **1**; C: TGA profile of **2**. Grey dotted lines represent temperature at which guest solvent has been removed.*

Compound **3** was synthesised by combining $Zn(NO_3)_3.6H_2O$ (0.6 mmol), 1,4-BDC (0.6 mmol) and IM (0.6 mmol) in DMF followed by heating to 120 °C for 48 hours. **3** crystallises in the orthorhombic space group Pbca (R = 3.2 %) with unit cell dimensions a=11.6602, b=13.8053, c=19.1435 and α = β = γ = 90. One DMF molecule, disordered over two positions, is present within the voids of the structure.

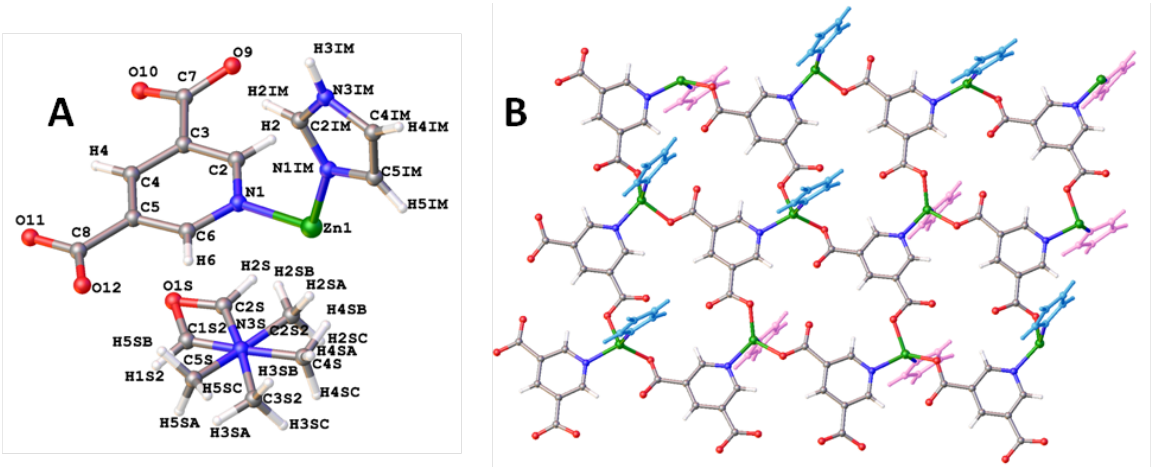

Figure 7: *A: Asymmetric unit in **3** with atom numbering shown. B: 1D sheets in **3**, showing imidazole coordinated above (blue) and below (pink) in the order two up two down. Zn (green), C (grey), N (blue), O (red), H (white).*

The asymmetric unit of **3** (*Figure 7A*) contains one Zn(II), one coordinated 3,5-pydc and one IM, with one disordered DMF molecule present in the void space (either part of the two-part disorder refines to 50 % occupancy). Zn is tetrahedral and is coordinated to N1IM of IM, pyridine N1 and carboxylate O9 and O12 of 3,5-pydc.

The structure consists of 2D sheets of Zn(II) and 3,5-pydc, with IM coordinated up or down from the a,c-plane on alternate Zn(II) centres in the order two up, two down (*Figure 7B*). Each 3,5-pydc molecule is coordinated to three different Zn(II) centres via the pyridine nitrogen and two monodentate carboxylate oxygens. C-O···H-N hydrogen bonding is present between the non-coordinated carboxylate oxygen O10 with the imidazole N-H of the adjacent 2D sheet with a distance of 1.879 Å at a N3IM-H3IM···O10/11 angle of 151.325 °, which creates the structure shown (*Figure 8A*).

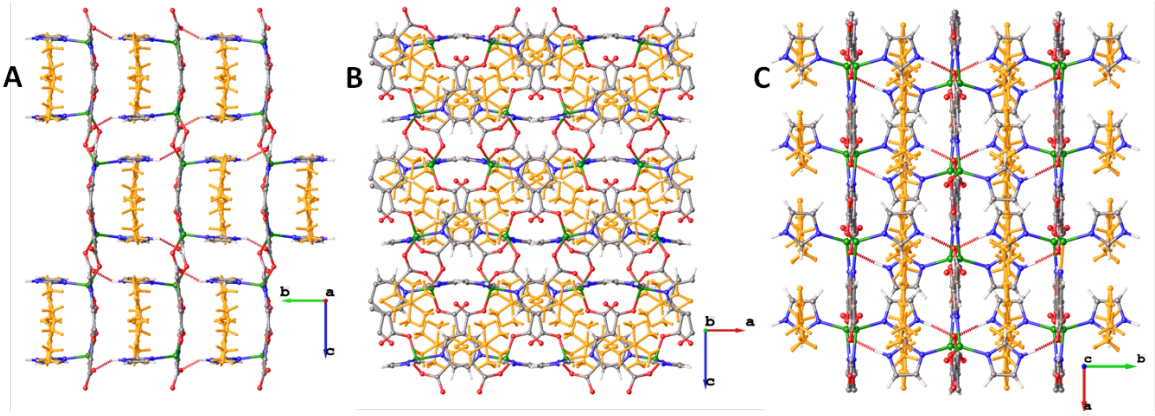

Figure 8: *Single crystal structure of **3**. Packing down A: 100; B: 010 and C: 001. Channel DMF shown in orange.*

PXRD shows the phase purity of the material (*Figure 9A*). TGA shows an initial weight loss of 20 % which corresponds to the guest DMF and H_2O molecules and shows the material is stable to around 200 °C, but undergoes constant degradation with heating (*Figure 9B*).

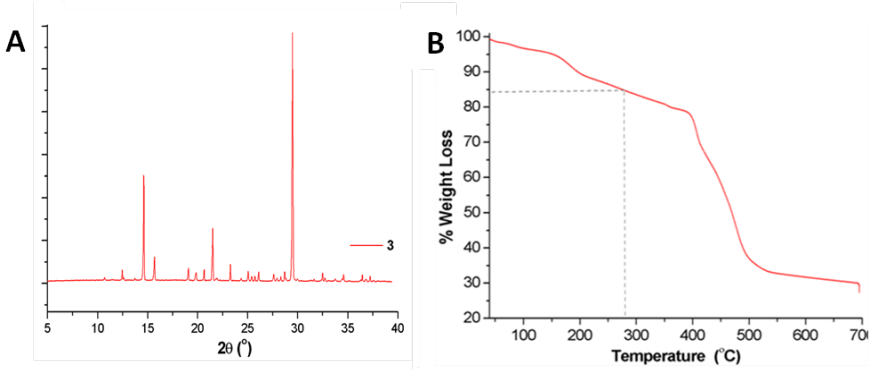

Figure 9: *A: PXRD profile of **3**; B: TGA profile of **3**. Grey dotted lines represent temperature at which guest solvent has been removed.*

3.3.2 The Influence of Base and Imidazole Concentration on Metal-Organic Frameworks based on Benzene-1,3,5-Tricarboxylate

In part 3.3.1, the synthesis of mixed IM/carboxylate frameworks in which IM is coordinated as a terminal neutral ligand was discussed. In this section, an investigation into whether the IM can be deprotonated and coordinate with ZIF connectivity alongside carboxylate coordination within the same MOF is discussed.

For this investigation, Co(II) was chosen to be the metal centre for two reasons: Firstly, it is one of the two metals shown to form ZIF type frameworks (Zn and Co) and secondly, due to its changing colour with different coordination environments, it is immediately clear if there is any difference in Co coordination in the product formed.

1,3,5-BTC was chosen as the carboxylate ligand to use alongside IM as it is a commercially available ligand that can be acquired at a low cost for extensive research in this area. It was thought that the angles between the carboxylate groups in these molecules of 120 ° would be more likely to form a less strained framework in which imidazole is theoretically coordinating from both nitrogen sites, with an M-N-M angle of 109.5 °.

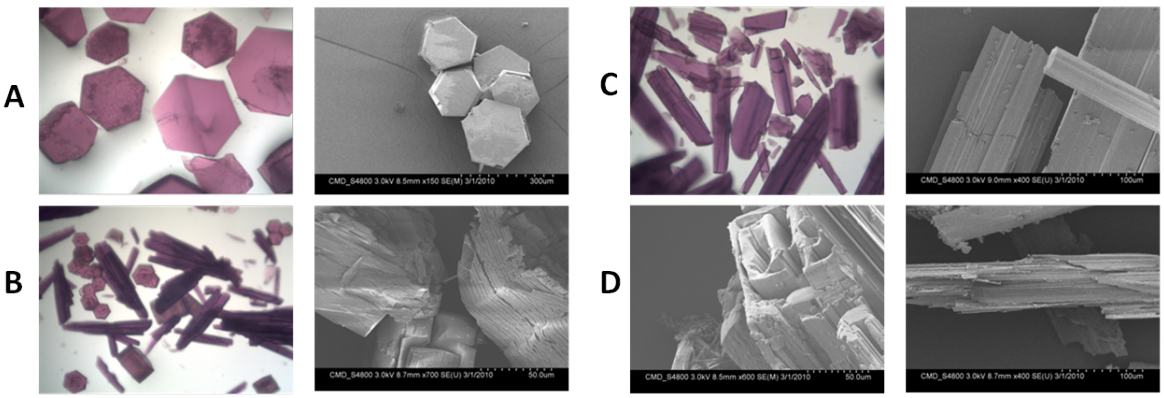

Figure 10: *OM and SEM images of reaction products when using $Co(NO_3)_2.6H_2O$, 1,3,5-BTC and IM in the ratio A: 1:1:1 yielding **4**; B: 1:1:2 yielding a mixture of **4** and **5**; C: 1:1:3 yielding **5** and D: 1:1:3 with base yielding **6**.*

Within this study the molar ratio of Co(II):1,3,5-BTC:Im was altered from 1:1:1 through to 1:1:6 in DMF, and the products analysed for MOF formation and ZIF coordination. In the case where a 1:1:1 molar ratio was used, this implies that for every Co(II) there were six potential coordination sites from 1,3,5-BTC oxygens and two from IM nitrogens, meaning theoretically there is less chance of an IM containing framework forming, however with increasing IM concentration, the chance of IM inclusion into the framework increases. SEM and OM images of the products formed

when a 1:1:1 ratio of reagents is used show large pink hexagonal single crystals are formed. With increasing the ratio to 1:1:2, the same pink hexagonal single crystals are seen alongside a new phase, which is present in the forms of long purple needle shaped crystals. Upon increasing this ratio again up to 1:1:3, we can see only the presence of the purple needle crystals, and this is the same product seen for ratios up to 1:1:6.

Structural analysis of both pink and purple crystals show two different frameworks. The pink hexagonal crystals have the formula $Co(1,3,5\text{-}BTC)_2(DMF)_2.DMF$ (**4**) and have no IM present within the structure. Within the asymmetric unit of **4**, there are six octahedral Co(II) metal centres (Co1-6), six 1,3,5-BTC(L1-6) and twelve DMF molecules (S1-12) (*Figure 11*).

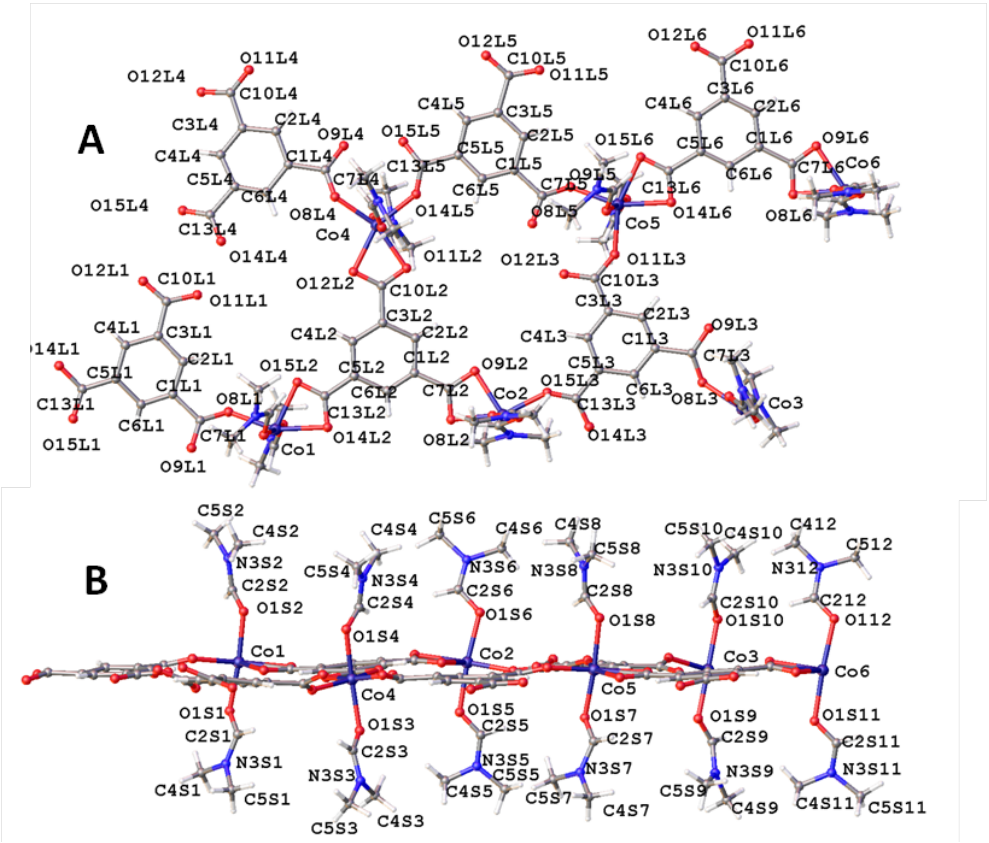

Figure 11: *Asymmetric unit in **4** with atom numbering scheme. A: Co and 1,3,5-BTC numbered; B: Co and DMF numbered. Co (purple), C (grey), N (blue), O (red), H (white).*

The coordination sphere of octahedral Co2 is filled by bidentate carboxylate coordination from O9L2 and O9L2, monodentate carboxylate coordination from O15L3 and O12L5, and O1S5 and O1S6 from two DMF molecules (*Figure 12B*). The coordination sphere of octahedral Co3 is filled by bidentate carboxylate coordination from O12L6 and O11L6, monodentate carboxylate coordination from O15L1 and O8L3, and O1S10 and O1S9 from two DMF molecules (*Figure 12C*).

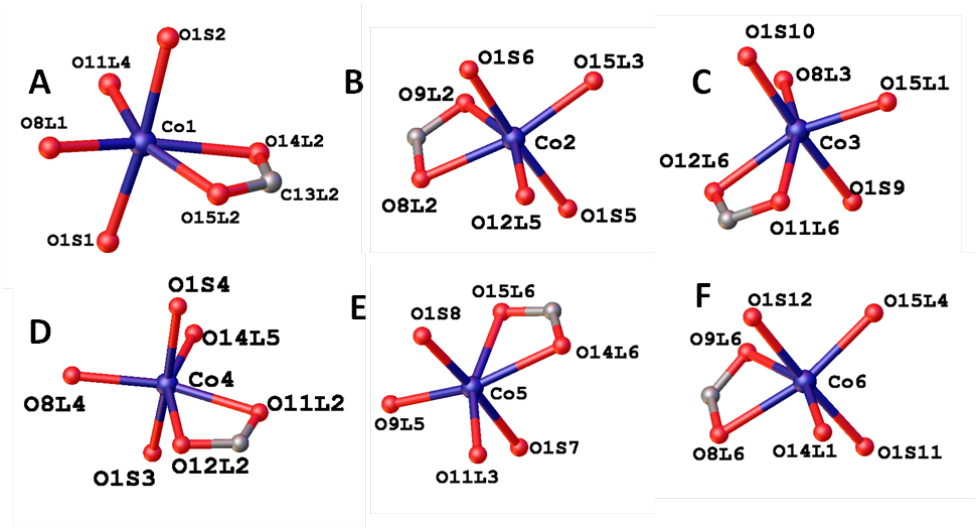

Figure 12: *Coordination sphere of Co(II) in* ***4****: A: Co1; B: Co2; C: Co3; D: Co4; E: Co5 and F: Co6.*

The coordination sphere of octahedral Co4 is filled by bidentate carboxylate coordination from O11L2 and O12L2, monodentate carboxylate coordination from O14L5 and O8L4, and O1S4 and O1S3 from two DMF molecules (*Figure 12D*). The coordination sphere of octahedral Co5 is filled by bidentate carboxylate coordination from O15L6 and O14L6, monodentate carboxylate coordination from O9L5 and O11L3, and O1S11 and O1S12from two DMF molecules (*Figure* **12***E*). The coordination sphere of octahedral Co6 is filled by bidentate carboxylate coordination from O8L6 and O9L6, monodentate carboxylate coordination from O15L4 and O14L1, and O1S11 and O1S12 from two DMF molecules (*Figure 12F*).

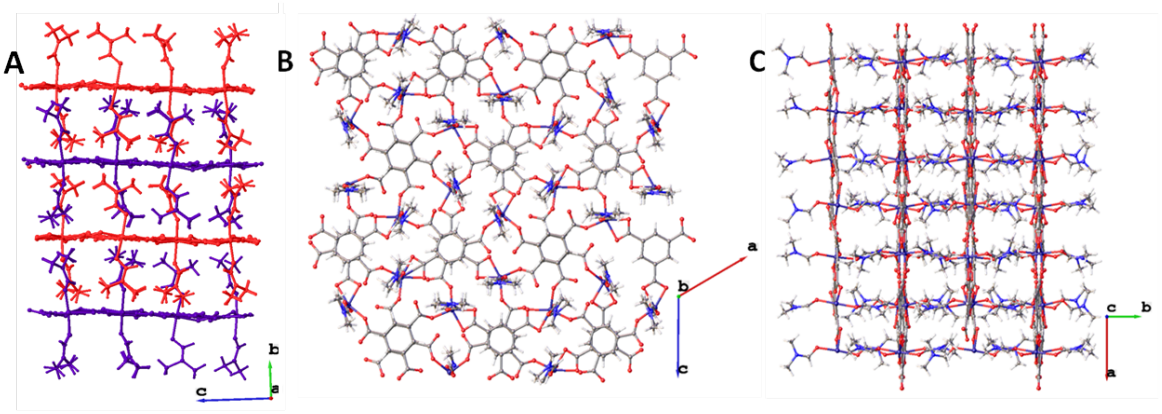

Figure 13: *Single crystal structure of* ***4****. Packing down A: 100; B: 010 and C: 001.*

The structure is based on 2D sheets of Co(1,3,5-BTC)$_2$ with two DMF molecules coordinated to each Co(II) oriented into the interlayer space; one up one down (*Figure 13*).

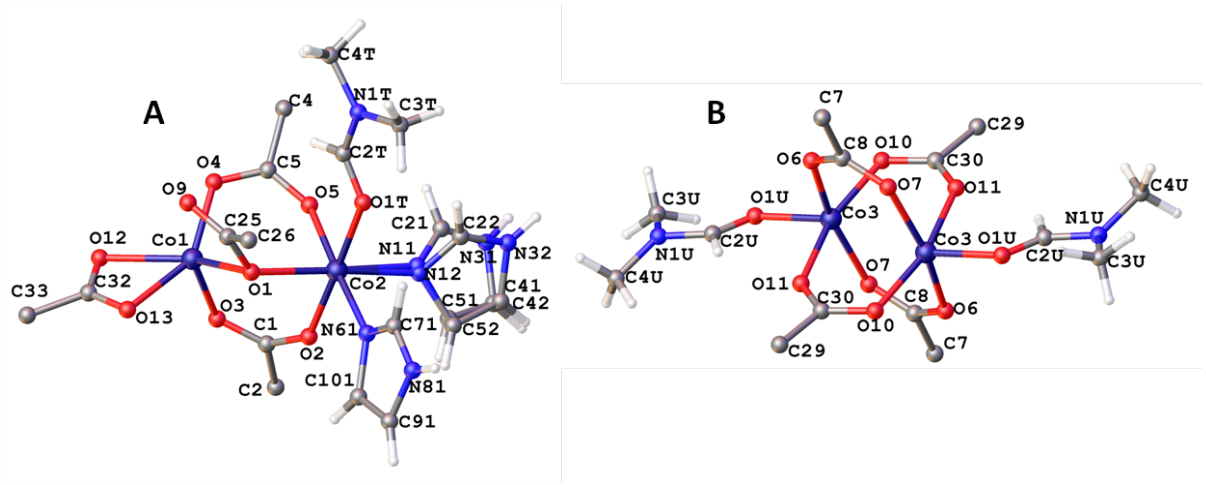

Figure 14: *Coordination environments of A: Co1 and Co2 and B: Co3 in* ***5****. Co (purple), O (red), C (grey), H (white). Co (purple), C (grey), N (blue), O (red), H (white).*

The purple needle crystals have the formula $Co_3(1,3,5\text{-BTC})_2(Im)_2(DMF)_2.DMF$ (**5**). Increasing the concentration of IM in the reaction mixture inevitably forces IM into the product structure. In **6**, IM is coordinated as a terminal neutral ligand, bonded to Co(II) via only one N.

Three different Co(II) geometries are present in **5**: A Co_2O_8 paddlewheel is formed by four 1,3,5 BTC carboxylates (Co3), a pentahedral (Co1) and an octahedral (Co2). Pentahedral Co1 is coordinated to by O12 and O13 of a bidentate carboxylate, O3 and O4 from independent carboxylates that bridge between Co1 and Co2 and a bridging carboxylate μ2-O1, which also bridges between Co1 and 2 (*Figure 14A*). The coordination sphere of Co2 is filled by O5 and O2 of independent bridging carboxylates, bridging carboxylate μ2-O1, N11/12 and N61 of coordinated IM and O1T or coordinated DMF. Co1 and Co2 are connected by two bridging carboxylates, (Co1)-O4-C5-O5-(Co2) and (Co1)-O3-C1-O2-(Co2), and μ2-O1.

Two symmetry equivalent Co3 atoms make up the Co_2O_8 paddlewheel (*Figure 14B*). The two Co3 centres are bridged by two symmetry equivalent carboxylate bridges; (Co3)-O7-C8-O6-(Co3) and (Co3)-O10-C30-O11-(Co3) with two equivalent DMF molecules coordinating to each Co3 via O1U, completing the square pyramidal geometry Co3, forming the Co_2O_8 paddlewheel.

The 3D structure of **5** is propagated by Co_2O_8 paddlewheels (*Figure 14A*) and C_2O_5 building units (*Figure 14B*), connected via fully deprotonated 1,3,5-BTC ligands. The structure has potential porosity along the 100 direction, but this was not confirmed experimentally as phase pure sample could not be isolated.

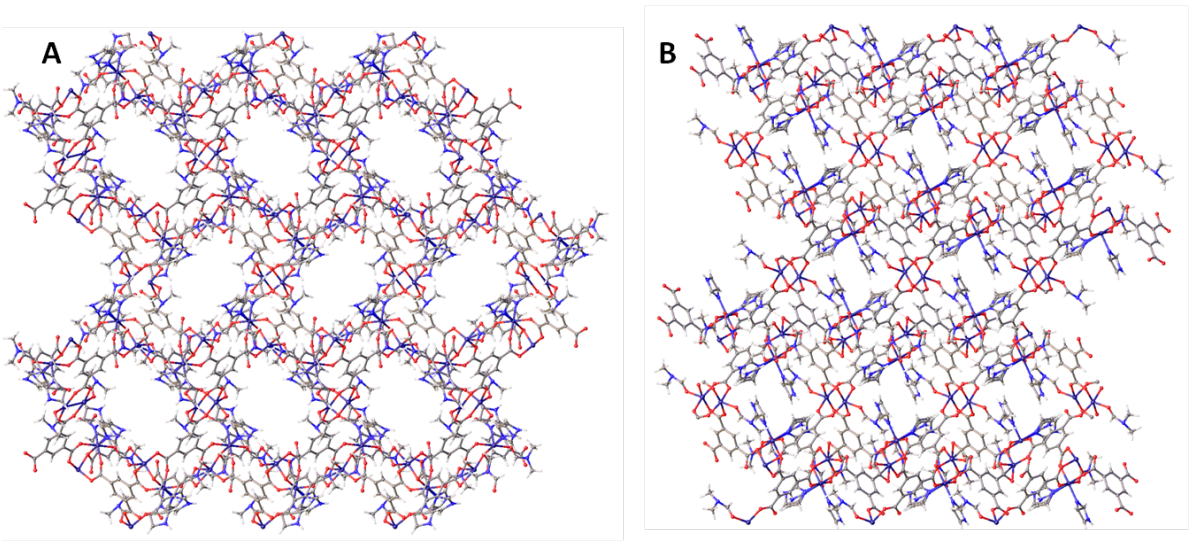

Figure 15: *Packing down A: 100 and B: 010 of* ***5****. Un-resolvable solvent electron density in channels along 100 not shown for clarity.*

In attempt to deprotonate the other N site of IM in order to encourage ZIF formation, base (1M $NaOH_{(aq)}$) was added to the reaction mixture in which a molar ratio of 1:1:3 of Co(II), 1,3,5-BTC and IM was used. The product formed in this case had a very similar appearance to **5** in the form of purple single crystals as seen in the SEM.

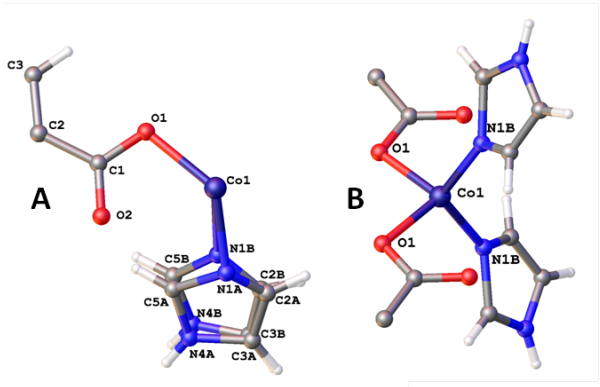

Figure 16: *A: Asymmetric unit in* ***6****; B: Co coordination environment. Co (purple), C (grey), N (blue), O (red), H (white).*

However, determination of the single crystal structure showed a new phase, **6**, which has the formula Co_3(1,3,5-BTC)$(IM)_3$. The structure of **6** contains 2D sheets in which tetrahedral Co(II) is bound to two of the three fully deprotonated 1,3,5-BTC carboxylates and two IM molecules. The IMs on adjacent Co(II) atoms point upwards or downwards respectively propagating the 2D layers. Each upward pointing IM is involved with hydrogen bonding from a downward facing IM of the next 2D sheet and vice versa, forming a 3D network held in place by C-H···O hydrogen bonding

from both parts of the disordered imidazole: C3A-H3A···O1 at 1.997 Å at an angle of 172.684 ° and C3B-H3B···O1 at 1.949 Å at an angle of 168.547 ° (*Figure 17*). IM is coordinated to Co(II) as a terminal neutral ligand again in this case, but addition of base has caused the deprotonation of all carboxylate groups present on the 1,3,5-BTC molecule, which in turn has resulted in the formation of a framework which is different in structure to **5**.

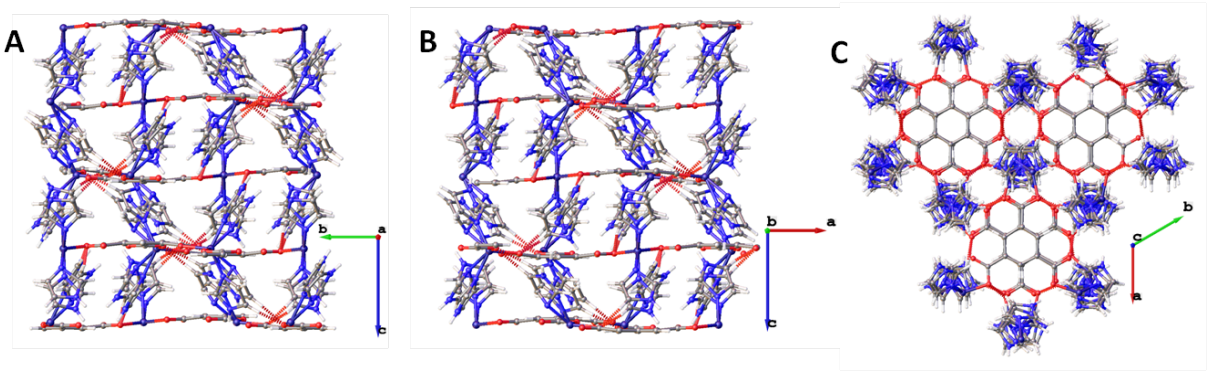

Figure 17: *Packing down A: 100; B: 010 and C: 001 in* ***6****. N-H···O Hydrogen bonding shown as red dotted line in A and B.*

Addition of more base to the reactions resulted in the same product, up to a point at which an amorphous product was formed, presumably due to the very basic nature of the reaction mixture which would break down any MOF formed. Adding base to reactions which had a higher IM concentration resulted also in phase pure **6**, again up to a point at which an amorphous product was formed.

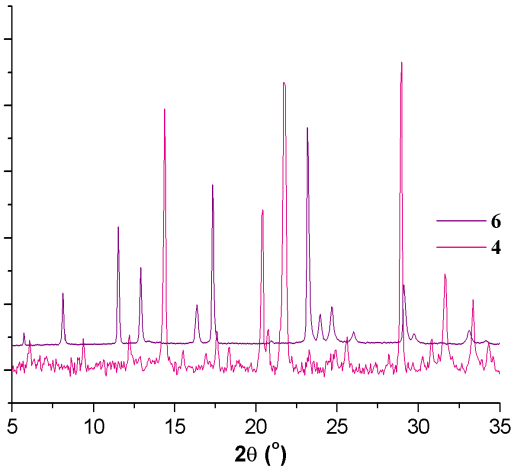

Figure 18: *PXRD profiles of* ***4*** *and* ***6****.*

Compounds **4** and **6** were synthesised phase pure, shown by PXRD (*Figure 18*), however compound **5** could not be isolated phase pure.

3.3.3 A Porous Layered Metal-Organic Framework From $\pi - \pi$-Stacking of Layers Based on a Co_6 Building Unit[34]

Compound **7** was synthesised by combining $CoCO_3$ (2.2 mmol), 1,3,5-BTB (2.2 mmol) and IM (6.6 mmol) used in a 1:1:3 ratio in EtOH and H_2O in a sealed borosilicate glass vial and heating to 100 °C for 36 hours. The product was isolated in the form of purple block single crystals shown by OM and SEM images (*Figure 19*), which were washed with EtOH and H_2O and left to air dry.

Single crystals of **7** were collected from the mother liquor of reaction by vacuum filtration and left to air dry. Subsequent characterization by single crystal X-ray diffraction shows **7** crystallizes in a monoclinic crystal system with space group C2/c (R_1 = 7.61 %) and unit cell dimensions *a*=17.133(3) Å, *b*=30.205(6) Å, *c*=20.953(4) Å, *β*=92.78(3)° and V=10830(4) $Å^3$ (*Figure 20*).

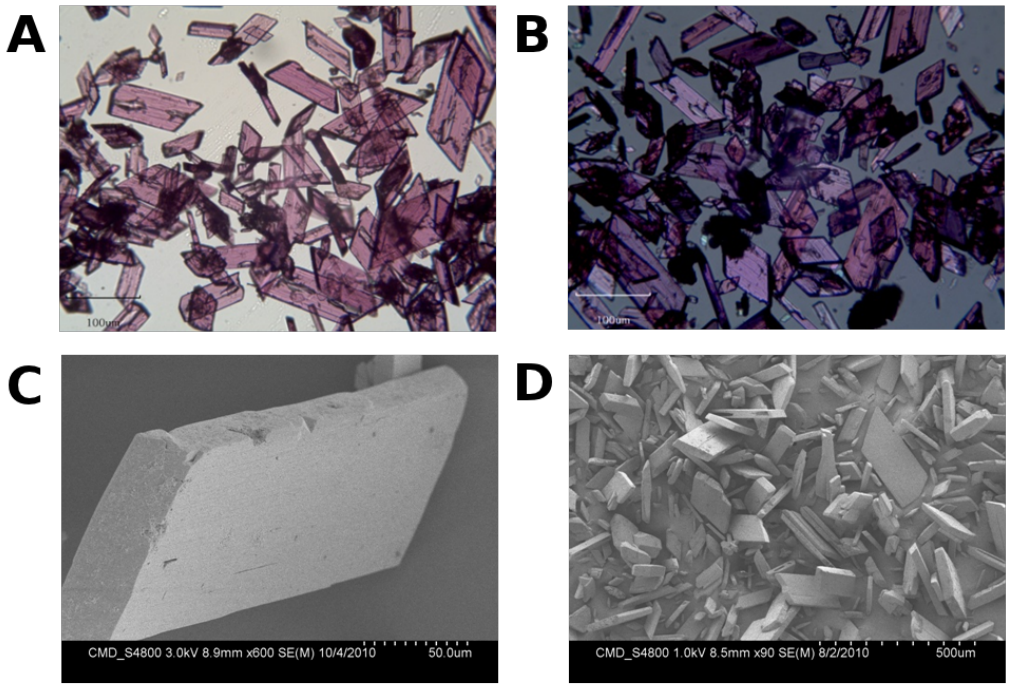

Figure 19: *Optical Microscope images of A: 7 and B: 7 with 90 ° polarisation and Scanning Electron Microscope images of C: A single crystal of 7 and D: Bulk sample of 7. Figure adapted from reference[34].*

Compound **7** is a 2D coordination framework containing a Co_6 unit constructed from two symmetry equivalent $Co_3(\mu_3\text{-}O(H))$ motifs, each of which consists of two crystallographically independent octahedral Co and one tetrahedral Co atoms linked via the fully deprotonated carboxylate groups of three 1,3,5-BTB molecules.

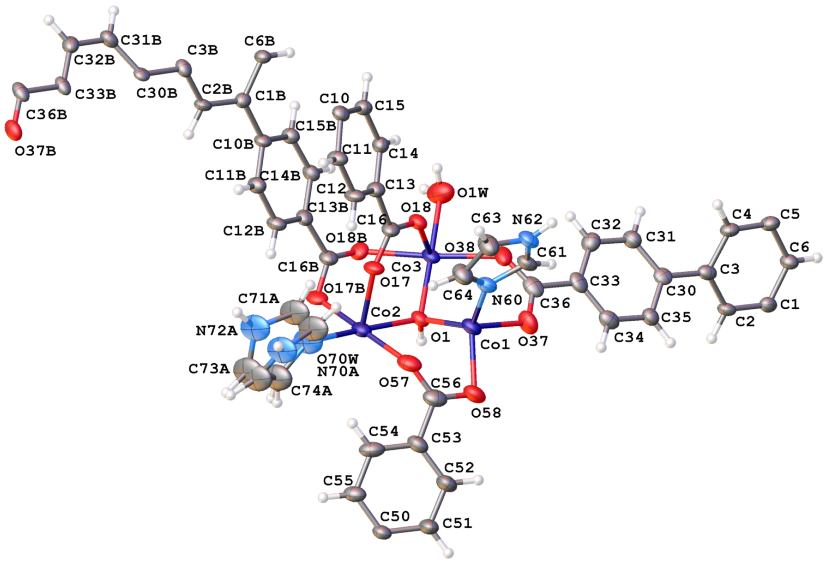

Figure 20: *Asymmetric unit of 7 showing atom numbering scheme and thermal ellipsoids. Co (purple), C (grey), N (blue), O (red), H (white). Figure taken from reference*[34].

These Co_6 units propagate 2D sheets running perpendicular to the *c*-axis. Two IM molecules are coordinated in the axial positions of the Co_6 unit at Co1 oriented between adjacent 2D sheets and are involved in N-H···O hydrogen bonding between IM and carboxylate oxygen of the adjacent layer (N62-H62···O18 d=2.847 Å). π-π stacking of IMs (centroid-centroid distance: 3.968 Å, shift distance 2.231 Å) links the structure into a 3D non-covalent network. The crystal structure has 1D channels which run along the *c*-axis, with solvent and IM occupying the Co sites present within the channels; H_2O (100 % occupancy) is coordinated to Co3 and the vacant site at Co2 is filled by disordered water (65 % occupancy) and imidazole (35 % occupancy). Each layer is offset by approximately 7.88 Å derived from a centroid placed at the centre of the channel window.

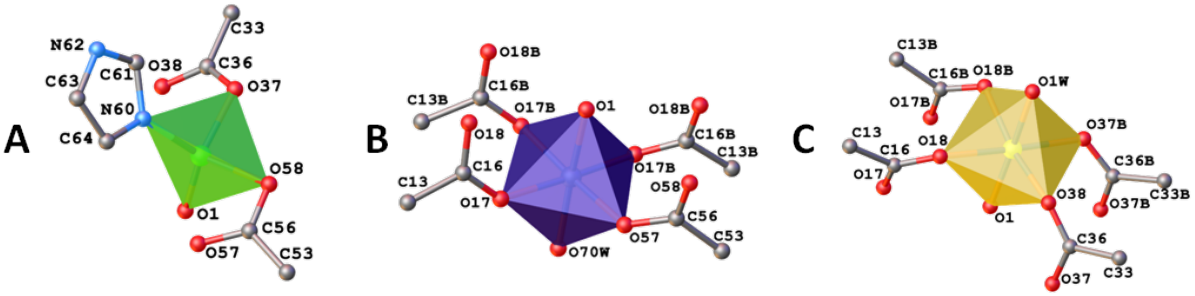

Figure 21: *Cobalt coordination environments in 7. A: Co1; B: Co2 and; C: Co3, with atom numbering around the different Ce coordination environments shown. Figure adapted from reference*[34].

A more detailed inspection of the single crystal structure allows us to identify that within the asymmetric unit of **7**, there are three crystallographically unique Co centres; tetrahedral Co1,

octahedral Co2 and octahedral Co3 (*Figure 21*), all corner shared through a μ_3-O17B(H) atom. The Co_6 unit is generated from this Co_3 unit through symmetry giving Co_6, initiated with two edge sharing octahedral at the inversion centre (Co2), both linked to separate octahedral Co3 and tetrahedral Co1. The Co_6 unit is rectangular in shape, with Co1 at what shall be referred to as the 'axial' positions, at the furthest point from the inversion centre. IM is bound to Co1 as a terminal neutral ligand, and has a protonated N62-H62, which points away from the inversion centre. This N-H is involved in hydrogen bonding with the adjacent 2D layer (*Figure 22A*).

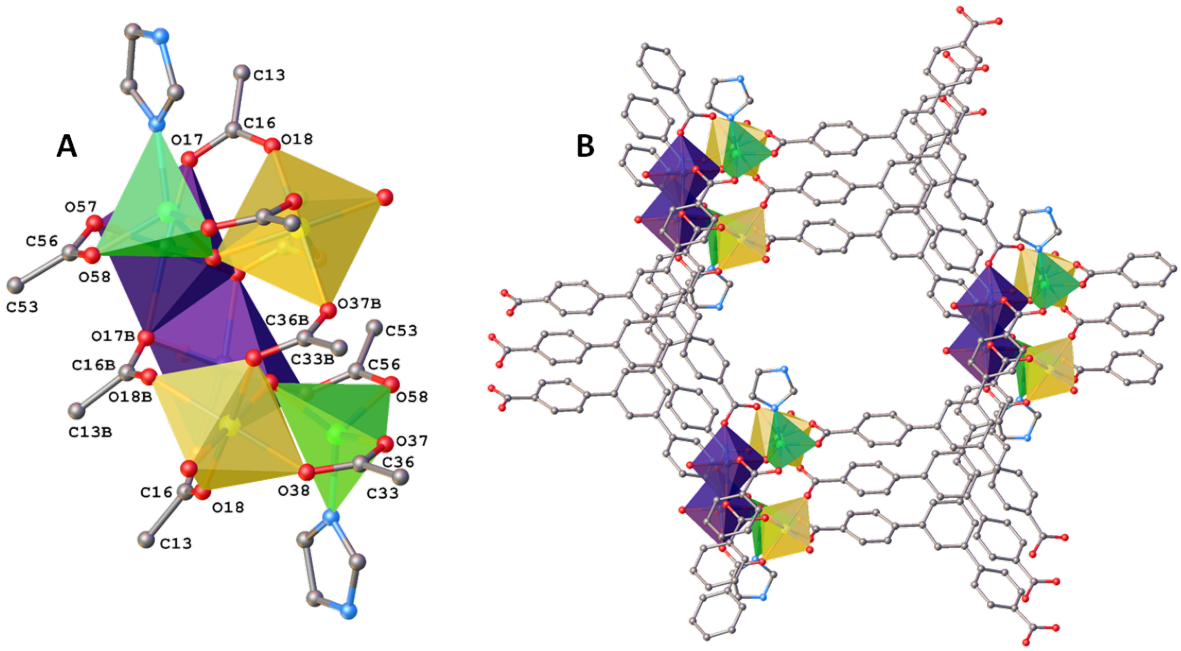

Figure 22: *A: Coordination of Co1 (green) Co2 (purple) and Co3 (yellow) within the Co_6 building unit in 7; B: Co_6 units perpendicular to 2D layers propagated by 1,3,5-BTB ligands. IM coordinated to Co_6 at axial positions, pointing between the 2D layers. Hydrogen atoms omitted for clarity. Figure adapted from reference[34].*

Although there are examples in the literature of mixed tetrahedral and octahedral clusters, this is the first example where there are both a tetrahedral and two crystallographically independent octahedral environments (Reported: AZENAU[35], BOYBOH[36], DOYWIY[37]).

The two edge sharing octahedra (Co2) are bridged by the 1,3,5-BTB carboxylate ligand oxygen (O17B) in a μ_2-O form. The coordination sphere of Co2 (*Figure 21A*) is completed via Co-O bonds to two different carboxylate groups (O17, O57), the disordered (50:50) μ_3-O/ μ_3-OH bridging O1 and, trans to that, a disordered IM/ H_2O moiety (35:65 occupancy) which point into the channel space at a slight angle to the *a*/*c* plane.

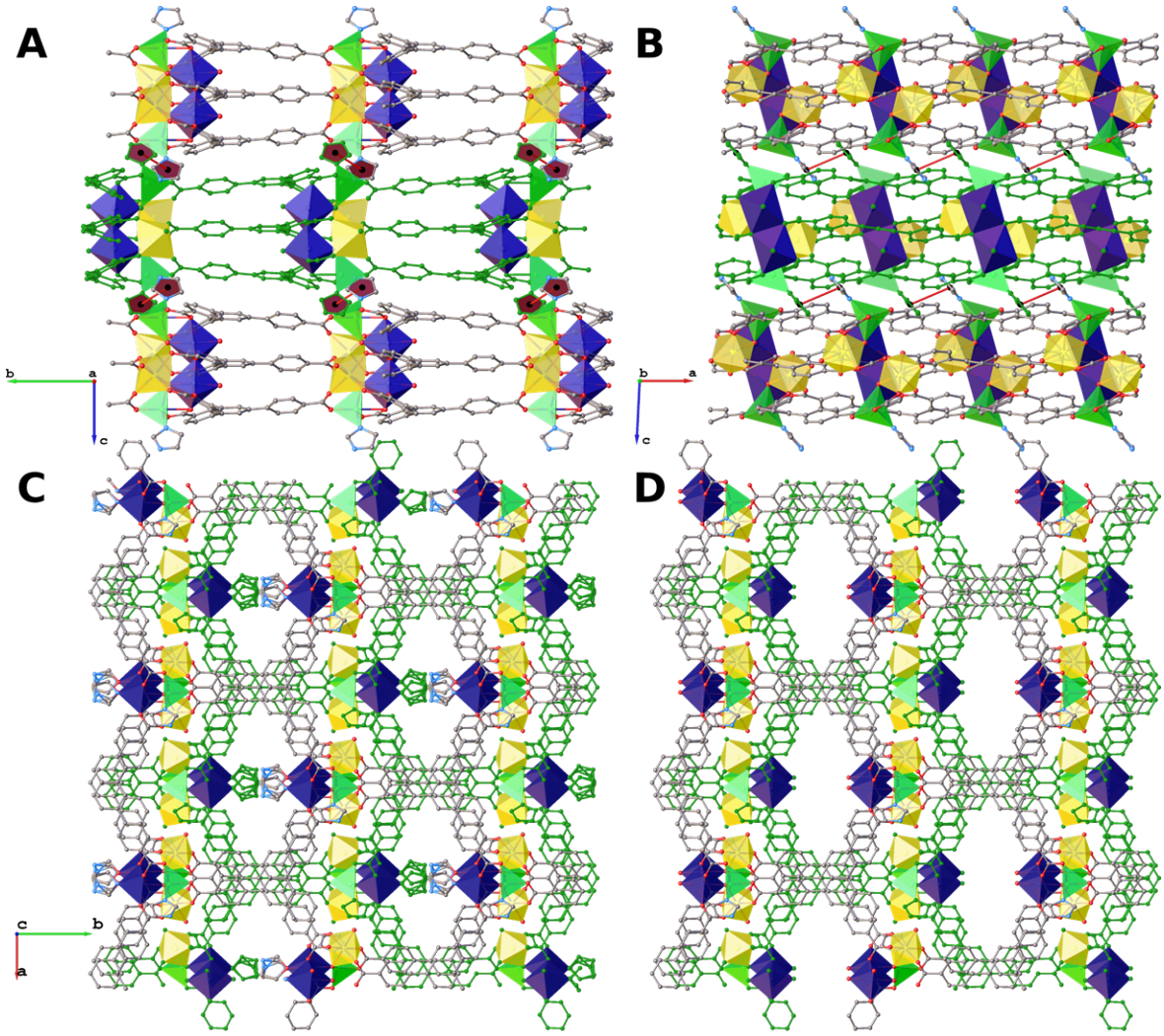

Figure 23: *Packing of 7 along A: 100; B: 010; C: 001 with disordered IM coordinated to Co2 shown; D: 001 with disordered IM not shown. Grey and green used to show packing of 2D layers. Hydrogen atoms omitted for clarity. Figure taken from reference*[34].

The disorder allows for some vacant Co2 sites to be accessible on removal of the 65 % bound water. O1 provides for a corner sharing point between the second octahedral Co centre Co3 (*Figure 21C*) and the tetrahedral Co1 (*Figure 21A*). The Co3 coordination sphere also includes an H_2O moiety directed into the channel space again at a slight angle to the *a*/*c* plane and results in an accessible (via the channel space) vacant Co site on full desolvation. The coordination sphere is completed through 4 bridging carboxylate η^1-O- η^1-O ligands each binding to a second Co centre. The final crystallographically unique Co centre caps the Co_6 unit via a fully occupied IM moiety and two η^1-O carboxylate bridges. The coordination mode of each 1,3,5-BTB can be considered as two η^1-O and one η^1- μ_2-O, thus each 1,3,5-BTB carboxylate oxygen is found to bond to at least one different Co centre. This is coupled to a twist from the central aryl ring of the pendant aromatic rings of between 25.704 - 34.428°, providing a propeller like motif based around each cluster and propagated through each 1,3,5-BTB tri-layer. This novel cluster motif could be driven by the

synergy between the π-π stacking of the 1,3,5-BTB ligands and the Co···Co through space separations found in the cluster, which form into a tri-layer with a range of π-π distances ranging from 3.506 to 3.787 Å (*Figure 23A,B*) with the central aromatic ring offset by 1.519 Å centroid-centroid.

These symmetry generated Co_6 clusters joined by fully deprotonated 1,3,5-BTB tri-layers propagate on the application of symmetry to form 2D sheets running parallel to the a/*b*-plane perpendicular to the *c*-axis (*Figure 23A,B*). The IM ligands coordinated to Co1 are seen to be coordinated in the axial positions of the cluster and form a weak hydrogen bond through N62-H62···O18 to the neighbouring 2D sheet. This coupled to a tentative IM-IM π-π interaction (*Figure 23B*) acts to anchor each 2D sheet to the next, propagating the structure into three dimensions. Disordered solvent shown as excess residual electron density was located within the channel space. This was determined potentially to be EtOH and H_2O and was removed through the application of dynamic squeezing based on a 1.2 Å probe and 0.2 Å grid set[31, 38].

Removal of the coordinated and guest solvent EtOH and H_2O molecules leaves a host structure with a 1D channel parallel to the *c*-axis (*Figure 23C,D*). The solvent accessible volume calculated from Olex2 (CalcSolv 1.2 Å probe, grid step 0.2 Å) is 3855.6 $Å^3$ per unit cell (35.6 % of the unit cell volume)[31]. Following the removal of channel solvent and the 1.65 coordinated H_2O molecules per asymmetric unit, the framework can be penetrated by a spherical probe radius of 0.7 Å, 0.7 Å and 1.5 Å down the *a*, *b* and *c*-axes respectively, with the largest spherical void being 7.6 Å in diameter, giving a packing index of 51.42 % (disordered IM retained in calculation, removal gives larger calculated values).

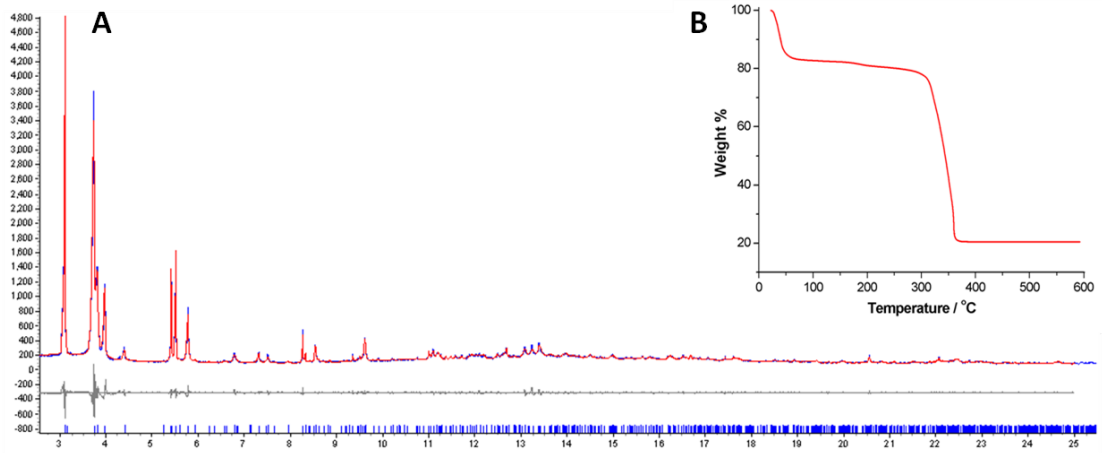

Figure 24: *PXRD profile of 7 collected in transmission geometry in a 0.5 mm capillary, collected at station I11 at Diamond Light Source Le Bail fit of 7 gives refined cell parameters of monoclinic C2/c, a = 17.185(3), b = 30.321(6), c = 21.505(10) Å, β = 85.690(23) °, with fit indicators of Rwp = 4.884 % and χ2 = 3.12; B: TGA profile of 7.*

Table 1: *CHN Microanalysis for* ***7*** *and* ***7D****:*

Formula	Theory (%)	Found (%)
$Co_3(H_3BTB)_{1.67}(IM)_{1.36}(O)\cdot(EtOH)_{2.17}\cdot(H_2O)_{7.87}$ (**7**)	**C:** 51.22 **H:** 4.76 **N:** 3.06	**C:** 51.22 **H:** 4.56 **N:** 3.05
$Co_3(H_3BTB)_{1.67}(IM)_{1.36}(O)$ (**7D**)	**C:** 58.30 **H:**3.04 **N:** 3.78	**C:** 59.59 **H:** 2.80 **N:** 3.89
$Co_3(H_3BTB)_{1.67}(IM)_{1.36}(O)\cdot(H_2O)_{3.33}$ (**7D**+air)	**C:** 55.04 **H:** 3.49 **N:** 3.49	**C:** 55.03 **H:** 3.49 **N:** 3.57

The phase purity of **7** was been confirmed by PXRD (*Figure 24A*), TGA (*Figure 24B*), and CHN microanalysis (*section 3.2.2, Table 1*). A. CHN microanalysis gives a composition for **7** of $Co_3(BTB)_{1.5}(IM)_{1.35}(O)_{0.5}(OH)_{0.5}(H_2O)_{1.65}\cdot 6.23H_2O\cdot 2.17EtOH$ (*Table 1*). The coordinated and guest EtOH and H_2O solvent molecules correspond to 19.80 % of the mass of **7**, which is in good agreement with the observed TGA initial mass loss of 20.01 % (coordinated IM is not lost during desolvation). The final mass percentage of 19.57 % corresponds to 3 equivalents of CoO after heating at 700 °C.

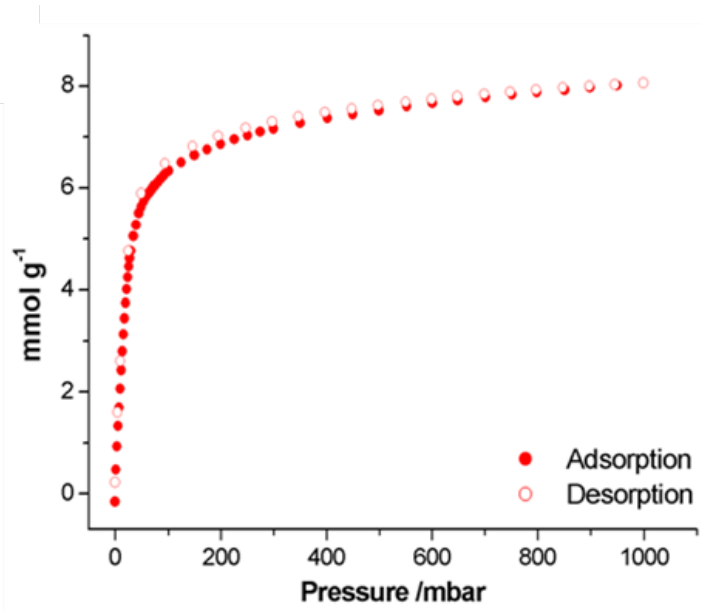

Figure 25: *CO_2 isotherm of* ***7*** *collected at 195 K following activation at 100 °C and 10^{-5} mbar overnight.*

The material was found to be permanently porous to CO_2 by means of an isotherm measured at 195 K and 1 bar, using activation conditions of 100 °C under 10^{-5} mbar overnight. An initial weight

loss of 20.68 % was observed with the loss of coordinated and guest EtOH and H_2O to give **7D**, which is comparable with the solvent loss observed in the TGA data. The type I CO_2 isotherm produced is characteristic of microporous materials[39]. The BET model applied over $p/p_0 = 0.02\text{-}0.17$ gives a surface area of 552(4) m^2/g, and is in agreement with the expected BET surface area of 525.61 m^2g^{-1} calculated using Olex2BET with CO_2 probe (3.996 Å). The Dubinin-Radushkevich[40] (DR) pore volume of **7** calculated from the CO_2 adsorption branch was calculated to be 0.342 cm^3g^{-1} compared with a pore volume of 0.299 cm^3g^{-1} determined from the rigid single crystal structure, following the removal of all guest (EtOH and H_2O) and bound H_2O molecules from Co2 and Co3. The discrepancy seen between experimental and calculated pore volume of **7D** is attributed to structural changes which occur upon desolvation, which are observed from PXRD (*Figure 27*).

The activation method of **7** was found to be crucial in accessing the available porosity of the material without causing framework collapse. When **7** is outgassed using conditions of 60 and 100 °C under dynamic vacuum (10^{-5} mbar), the BET surface area observed is 552 m^2g^{-1} (*Figure 25*), while at the higher activation temperature of 150 °C, producing **7D'**, the BET surface area is 360 m^2g^{-1} (*Figure 28D*). This is an important observation as the initial weight loss due to guest and coordinated solvent is comparable (20.1 % at 100 °C and 20.6 % at 150 °C), thus indicating that the observed reduction in porosity is due to thermally-induced framework collapse.

Purple **7** is outgassed at 100 °C under dynamic vacuum (10^{-5} mbar) overnight to yield violet **7D** which is consistent with a change in the coordination environment of the Co(II) cations upon desolvation and structural changes observed by PXRD. This is also in agreement with that shown by TGA data, with the loss of coordinated solvent molecules. The same colour change from purple to violet was observed in the 150 °C activated sample, revealing that the coordination environment of Co(II) changes as with the lower activation temperature of 100 °C. The PXRD profile of **7D'** is less crystalline than that of **7D**, confirming structural damage upon activation at high temperature.

Heating of a single crystal of **7** on a diffractometer using a nitrogen flow for temperature control showed the same colour change from purple to violet (*Figure 26*). Unfortunately single crystal structure determination of the desolvated phase **7D** was not possible as the crystal did not diffract with sufficient resolution for structure solution. However, images of the crystal during this experiment allowed for the colour change to be observed in a stepwise manner.

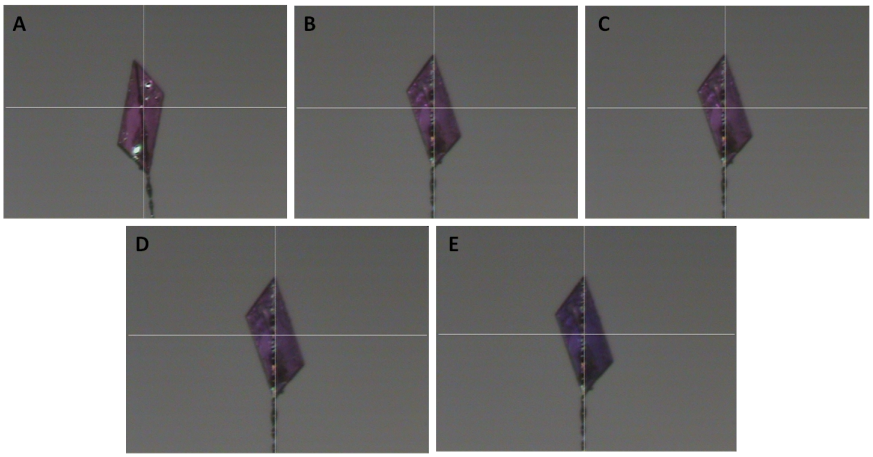

Figure 26: *A single crystal of* ***7*** *during the single crystal variable temperature experiment. A: 100 K; B: 300 K; C: 320 K; D: 240 K; E: 350 K.*

In order to further explore the effect of temperature on **7**, variable temperature PXRD carried out in a sealed capillary shows that the **7** is stable up to 90 °C at which point the coordinated and guest EtOH and H_2O molecules are removed, yielding **7D**. In the temperature range of 90 – 150 °C, **7D** is stable after which the framework starts to collapse, seen from the broadening of the reflection peaks, **7D'** (*Figure 27*)[41]. The initial sample was purple in colour and changed to violet after heating. This observation is consistent with TGA data and the difference in BET surface area between samples activated at 100 and 150 °C. Heating of a single crystal using a nitrogen stream for temperature control also shows this colour change (*Figure 26*).

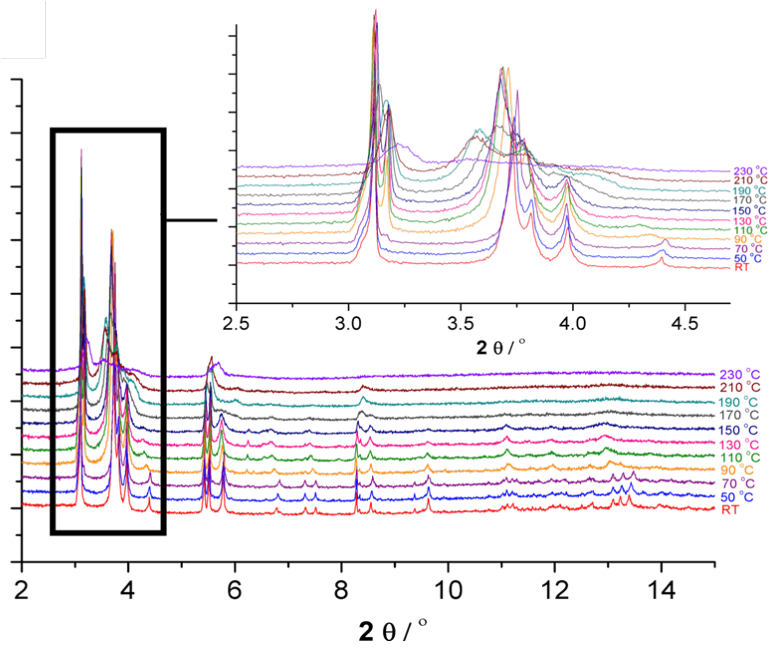

Figure 27: *Variable Temperature PXRD experiment to determine the point at which* ***7*** *becomes desolvated (****7D****) and subsequently decomposes.*

7D was found to be essentially non-porous to N_2 using the same activation method as used for CO_2. The activation procedure **7** was then optimised in order to determine the N_2 porosity of the material. Recently published results show the use of liquid and supercritical CO_2 as an alternative way to remove guest molecules without causing framework collapse, which is often seen upon heating under vacuum[42]. This method dictates that the as-made MOF should be firstly submerged in EtOH to fill the pores. This EtOH is then exchanged with liquid CO_2 and then rinsed with supercritical CO_2. The first attempt using this method afforded no porosity towards N_2 (BET surface area of 9 m^2/g was obtained). The CO_2-washed compound was then submitted to a stepwise activation procedure; overnight heating at 120°C (heating rate 1°C/ minute), followed by 2 hours heating at 10^{-5} mbar at the same temperature. The subsequent BET measurement gave the expected 500 m^2g^{-1}surface area. The same stepwise thermal activation without the initial step of using supercritical CO_2 yielded a BET surface area of 360 m^2g^{-1}, and direct activation under vacuum at 100°C gives almost no porosity towards N_2 (40 m^2/g)[43]. From these data, it is clear that that the activation procedure is crucial in accessing all the available porosity of **7**.

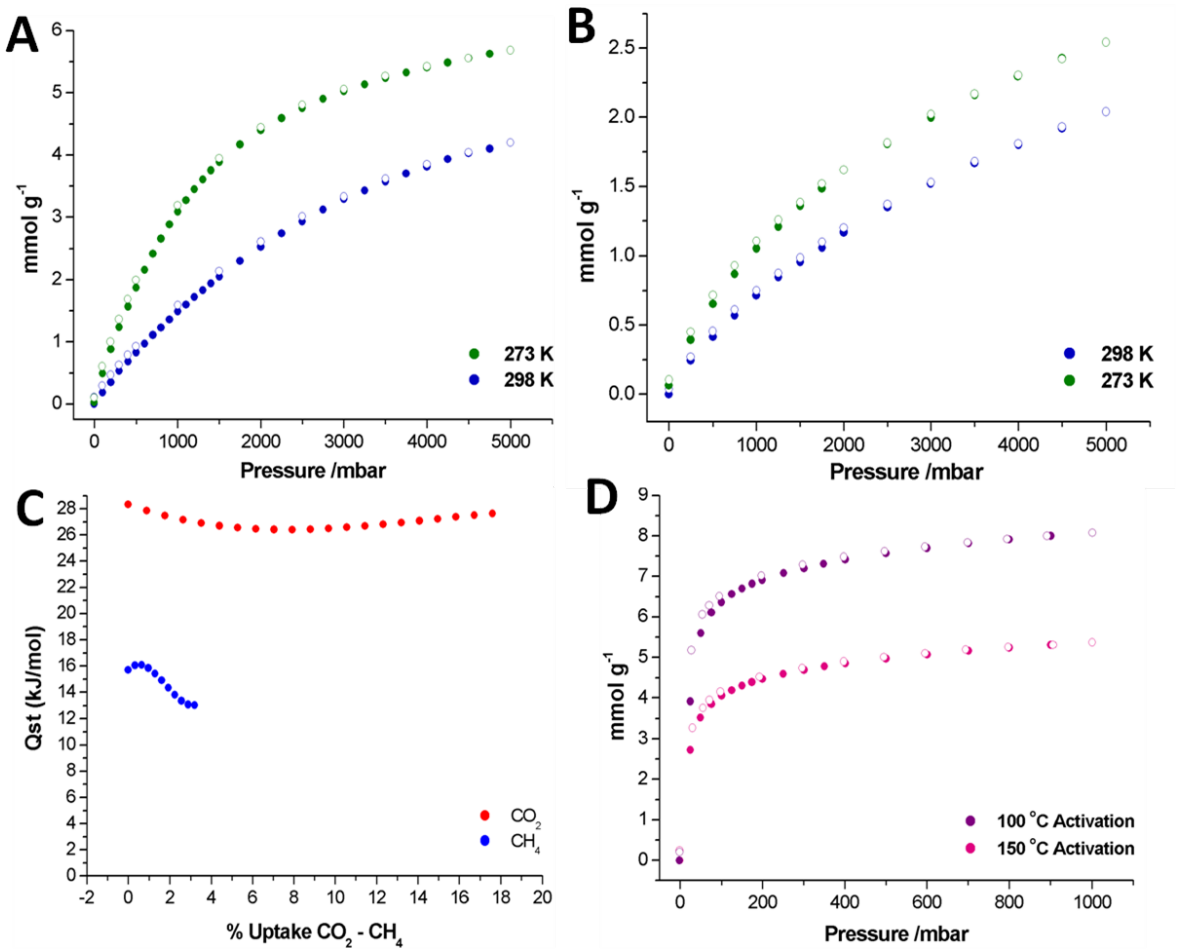

Figure 28: *A: CO_2 and B: CH_4 isotherms carried out on 7 at 298 K and 273 K for determination of C: Isosteric heats of absorption of the gasses; D: CO_2 isotherms collected on **8** at 195 K following activation at 100 and 150 °C.*

CO_2 and CH_4 isotherms were collected at 273 K and 298 K (*Figure 28A,B respectively*). Isosteric heats of adsorption (Q_{st}) for CO_2 and CH_4 were derived from a virial-type expression fitted to the adsorption branches of the isotherms measured at 273 K and 298 (*Figure 28C*). The strength of interaction between **7D** and CO_2 is not greatly affected by the loading, as the Q_{st} for CO_2 at zero coverage is 28.3 kJmol^{-1} with a slight decrease to 27.8 kJmol^{-1} at maximum loading. A larger decrease is seen in the Q_{st} for CH_4, which falls from 15.5 kJmol^{-1} at zero coverage to 13.0 kJmol^{-1} at high loadings.

3.3.4 Frameworks based on Cobalt (II) and 1,3,5-BTB

3.3.4.1 $Co_7(O)_2(1,3,5\text{-}BTB)_4(NMeIM)_5(H_2O)_4\cdot DMF$

In part 3.2.3, the framework $Co_3(1,3,5\text{-}BTB)_{1.5}(Im)_{1.35}(O)_{0.5}(OH)_{0.5}(H_2O)_{1.65}$·*guests* (**7**) was discussed. Following on from this, attempts were made to produce isostructural frameworks with different end group ligands present in place of IM. This was necessary to reinforce the argument that the inter-layer intermolecular N-H···O and π-π stacking interactions present between imidazole and the adjacent 2D layer within **8** were for a large part responsible for the formation of the framework.

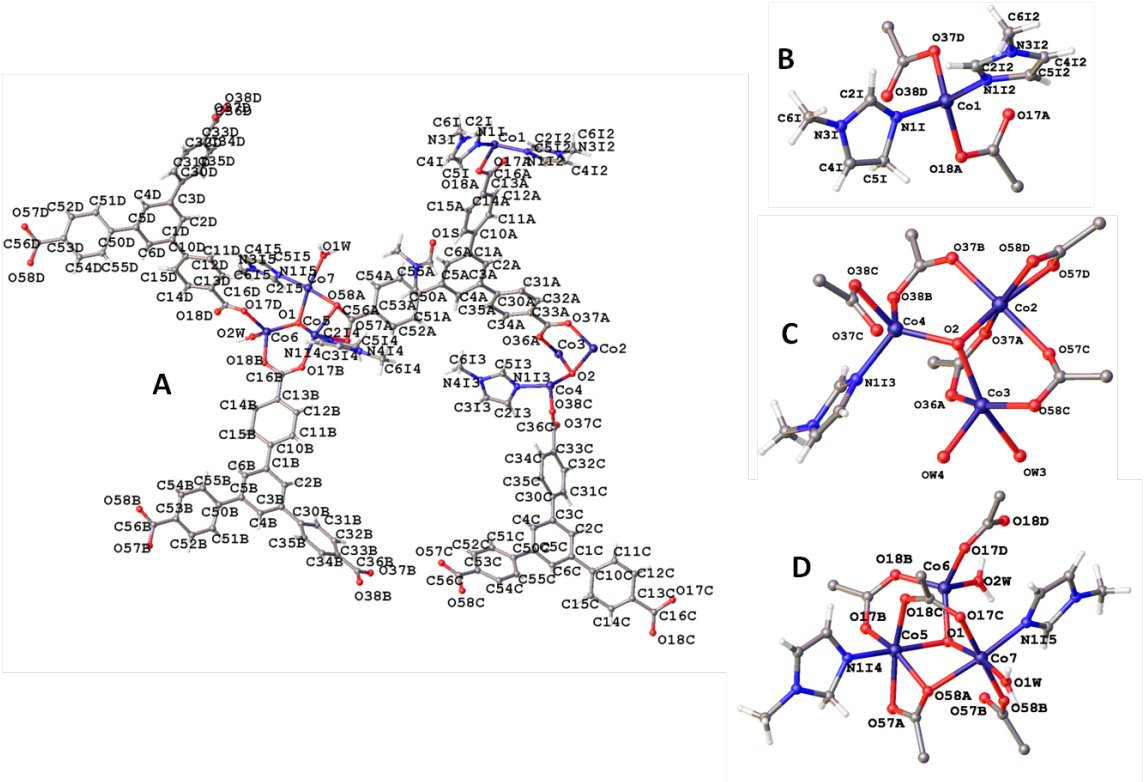

Figure 29: *Single crystal structure of **8**. A: Asymmetric unit with atom numbering; Coordination environment of B: Co1; C: Co2-4 and D: Co5-7. Co (purple), C (grey), N (blue), O (red), H (white).*

Compound **8,** $Co_7(O)_2(1,3,5\text{-BTB})_4(NMeIM)_5(H_2O)_4 \cdot DMF$, can be synthesised by combining $CoCO_3$, 1,3,5-BTB and IM in either $EtOH/H_2O$ or DMF/H_2O, however synthesis with DMF/H_2O produces single crystals suitable for x-ray diffraction. The reagents were mixed together and then heated to 120 °C for 48 hours, followed by slow cooling back down to room temperature. When 8 is synthesised in DMF/H_2O, large purple single crystals were produced with plate morphology.

8 is a complex 3D structure that crystallises in a monoclinic C2/c space group with unit cell dimensions of a=17.133(3) Å, b=30.205(6) Å, c=20.953(4) Å, α,γ=90.00 °, β=92.78(3) ° with a unit cell volume of 14110 $Å^3$. Within the formula unit there are seven unique Co atoms (three octahedral, three tetrahedral and one square based pyramid), four 1,3,5-BTB (numbered A-D) and five IM molecules coordinated as terminal neutral ligands (numbered I-I5), one guest DMF win the void space and four coordinated H_2O molecules (*Figure 29A*).

Co1 is tetrahedral and coordinated to two carboxylate oxygens (O18A , O37D) from 1,3,5-BTB 1 and 3, rings 1 and 3 respectively) and two IM molecules (N1I, N1I2) (*Figure 29B*).

Co2, 3 and 4 are connected via a μ_3-O2. Co2 and Co3 are bridged by a (Co2)-O37A-C33A-O36A-(Co3) carboxylate on ring 3 of 1,3,5-BTB molecule A. Co2 and Co4 are bridged by a (Co2)-O37B-C33B-O38B-(Co4) carboxylate from ring 3 of BTB molecule B. Co2 and Co3 are bridged by a (Co2)-O57B-C53B-O58B-(Co3) carboxylate from ring 5 of 1,3,5-BTB molecule D. The coordination sphere of square pyramidal Co3 is filled by carboxylate O36A, O58C, OW3, OW4 coordinated solvent H_2O molecules and the μ_3-O2. The coordination sphere of tetrahedral Co4 is filled by carboxylate O38C, O38B, μ_3-O2 and N1I3 of the coordinated IM molecule 3 (*Figure 29C*).

Co5, 6 and 7 are connected via a μ_3-O1. Co5 and Co6 are bridged by a (Co5)-O17B-C13B-O18B-(Co6) carboxylate on ring 1 of BTB molecule B. Co5 and Co7 are bridged by a (Co5)-O18C-C13C-O17C-(Co7) carboxylate on ring 1 of 1,3,5-BTB molecule C and a μ_2-O58A from ring 5 of 1,3,5-BTB molecule A. Co6 and Co7 are not bridged by carboxylates. The coordination sphere of octahedral Co5 is filled by carboxylate O17B, O18C, O57A and bidentate μ_2-O58A which also bonds to Co7, N1I4 from IM molecule 4 and μ_3-O1. The coordination sphere of tetrahedral Co6 is filled by solvent H_2O molecule O2W, carboxylate oxygen O18B and O17D and the μ_3-O1. The coordination sphere of octahedral Co7 is filled by solvent H_2O molecule O1W, carboxylate O58B, O17C, μ_2-O58A which also bridge to Co5, N1I5 from IM molecule 5 and the μ_3-O1 (*Figure 29C*).

The individual tetrahedral Co1 and two μ_3-O Co_3 clusters (Co2-4 and Co5-7) are held in a 3D coordination network by the 1,3,5-BTB ligands, with DMF free within the channels (*Figure 30*).

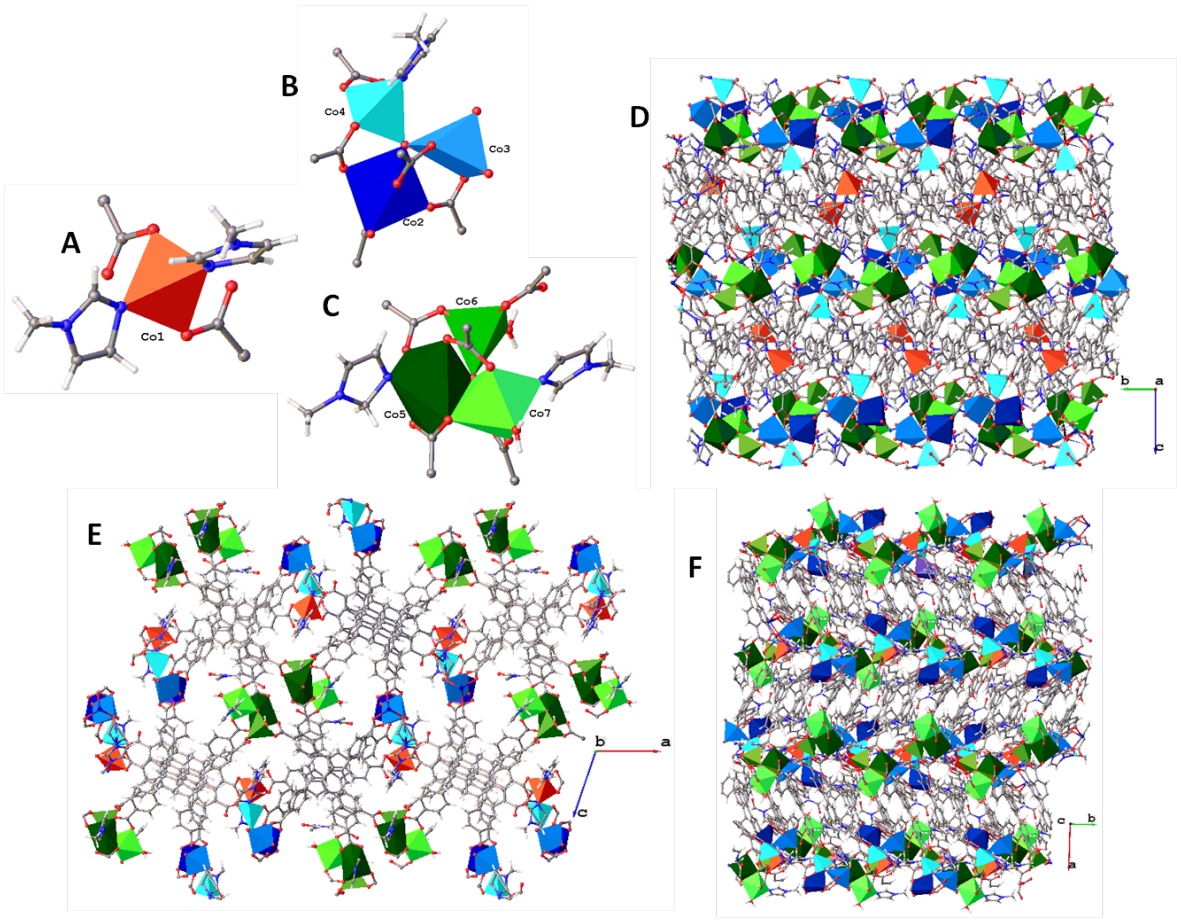

Figure 30: *Single crystal structure of* ***8****. Polyhedra colouring scheme for A: Co1; B: Co2-4 and C: Co5-7; D: Packing view down 100; E: View down 010 and F: View down 001.*

The framework has potential 1D porosity in the 010 direction following the removal of guest DMF and coordinated H_2O molecules. The framework can be penetrated by a spherical probe radius of 1.0, 1.4 and 0.6 Å down the a, b and c-axes respectively, with a largest spherical void with a radius of 3.2 Å. The structure is 28.7 % porous, meaning that of the unit cell volume of 14110 $Å^3$, 4046.3 $Å^3$ is solvent accessible volume.

The structure of **7** and **8** is completely different. Whereas **7** is a 2D framework containing a carboxylate and μ_3-O(H) bridged Co_6 building unit, **8** is a 3D framework with two carboxylate and μ_3-O bridged Co_3 units and an individual tetrahedral Co unit. The aim was to determine whether combination of Co, 1,3,5-BTB and N-MeIM under the same conditions would form the same framework as when combined with IM, or whether the free protonated N-H site of IM was needed to hydrogen bond within the structure in the formation of **7**. Under the same synthesis conditions of EtOH and H_2O, the presence of the addition methyl group on N-MeIM completely changes the product formed.

The framework was characterized to be phase pure by PXRD (*Figure 31*).

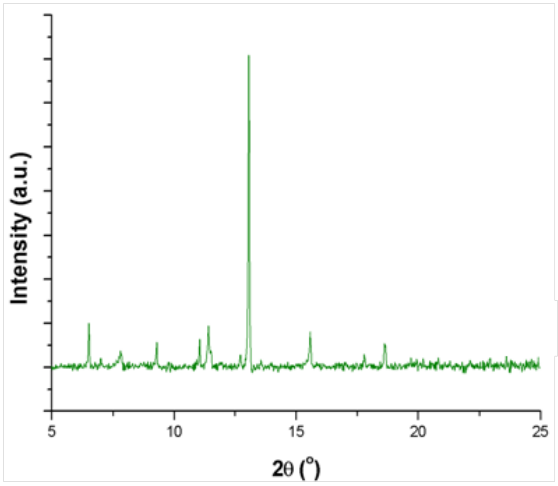

Figure 31: *PXRD profile of* ***8****.*

3.2.4.2 $Co_3(1,3,5\text{-BTB})(Py)_3(H_2O)_3{\cdot}H_2O_9$

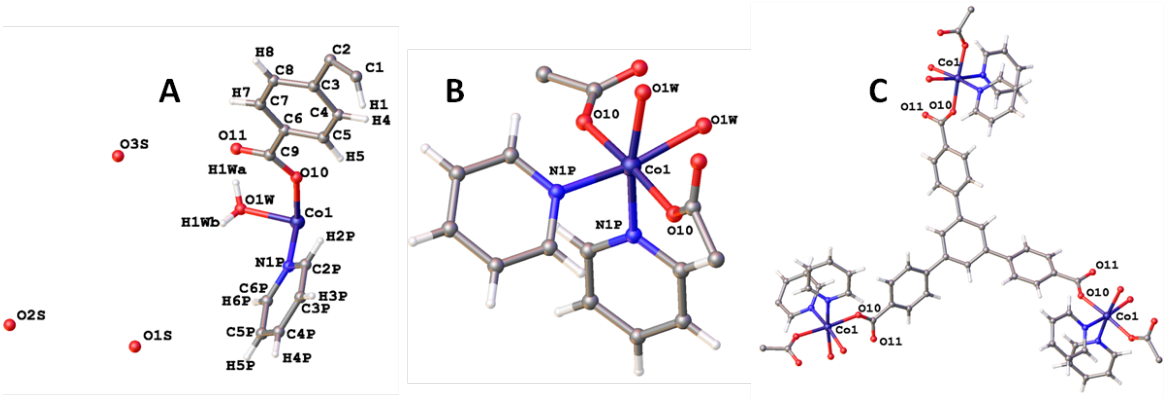

Figure 32: *A: Asymmetric unit in* ***9*** *with atom numbering shown; B: Co coordination environment in* ***9****; C: 1,3,5-BTB coordination modes in* ***9****. Co (purple), C (grey), N (blue), O (red), H (white).*

Compound **9** was synthesised by combining $CoCO_3$, 1,3,5-BTB and Py in EtOH and H_2O and heating to 120 °C for 48 hours. **9** crystallises in a trigonal P-3_1c space group with unit cell dimensions of a=18.747(2) Å, b=18.747(2) Å, c=14.786(2) Å, α=β=90 °, γ=120 ° and a unit cell volume of 4500 $Å^3$. The asymmetric unit contains 1/3 1,3,5-BTB molecules, one pyridine (Py), one coordinated H_2O and three guest H_2O molecules (*Figure 32A*): This gives the unit cell contents of $Co_3(1,3,5\text{-BTB})(Py)_3(H_2O)_3{\cdot}H_2O_9$. Each Co1 is octahedral with the coordination sphere being filled by two Py, two H_2O and two carboxylate oxygens (O10) from the 1,3,5-BTB ligand (*Figure 32B*). The ligand carboxyates all coordinated to Co1 via O10 with monodentate coordination, forming 2D sheets (*Figure 32C*).

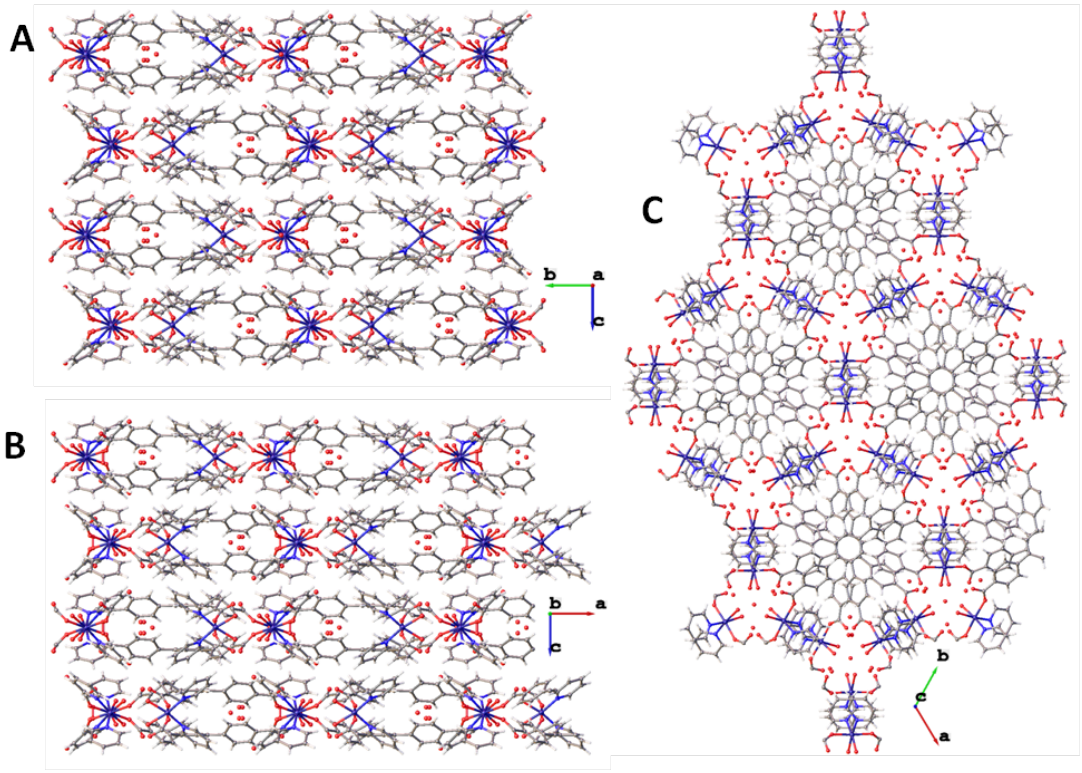

Figure 33: *Packing in* ***9****. View down A: 100; B: 010 and C: 001.*

Only Van der Waals interactions present between the 2D layers in **9**; the layers close pack. Guest H_2O is present in a potential channel down the 001 axis (*Figure 33C*). The 2D layers contains three interpenetrated Co(1,3,5-BTB)$(Py)_3(H_2O)_3$ sheets (*Figure 34*), that lie at 90 ° to each other in adjacent layers. Figure 34B shows one 2D layer down the 001 direction with void space that occupies guest H_2O in the single crystal structure and Figure 33C shows the packing of 2D layers, with the potential channel reduced in size due to rotation of adjacent close packing layers.

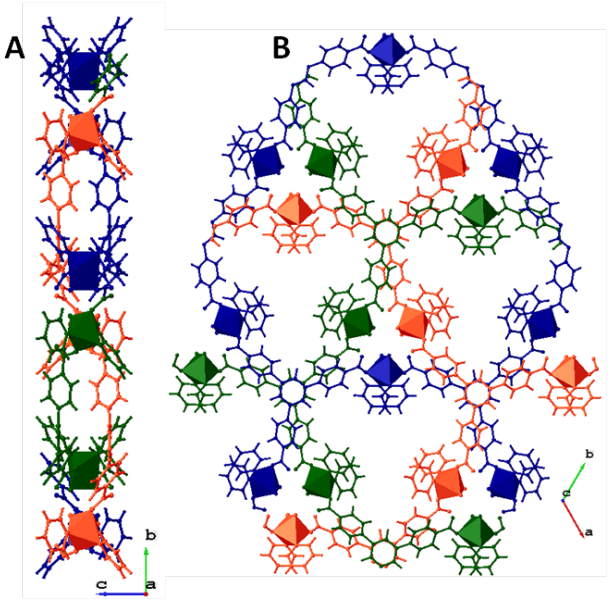

***Figure 34**: Triply interpenetrated Co(1,3,5-BTB)(Py)$_3$(H$_2$O)$_3$ sheets in 2D layers of **9**.Channel H$_2$O removed for clarity.*

Substitution of IM with Py in the synthesis of **7** to **9** again produces a completely different framework, with no Co_6 building unit. Py as N-MeIM has no donation group for hydrogen bonding as does IM in **7**, with the protonated N-H site. This means that N-MeIM and Py can only coordinate as terminal capping ligands and cannot propagate the framework via intermolecular interactions, which is seen in both the structures of **8** and **9** respectively.

3.4 Conclusions

In this chapter, the combination of IM and carboxylate linkers using the standard ZIF-forming conditions using DMF as a solvent yields 2D or 3D coordination networks in which carboxylate ligands connect metal centres and IM remains protonated and is coordinated as a terminal neutral ligand.

Altering the conditions by increasing the relative ratio of IM in the reaction mixture and adding base in attempt to encourage IM deprotonation still does not cause ZIF coordination: IM still coordinates as a terminal neutral ligand in **6**. However, the more basic nature of the reaction mixture in **7** means more or the carboxylate linker is deprotonated which causes a change in coordination to the metal centre, thus changing the structure isolated.

A novel Co_6 cluster is formed through combination of neutral IM, oxo, hydroxo and carboxylate coordination and is the basis of a 2D layer, stacked into a 3D porous arrangement via synergic π···π stacking interactions. This allows the development of permanent porosity towards N_2, CO_2 and CH_4, however the material is sensitive to activation conditions, presumably due to the reliance on weak IM-IM π···π stacking to retain the void space[34].

Maintaining the use of 1,3,5-BTB and Co(II) in the synthesis, but changing the second ligand from IM in **7** to N-MeIM in **8** and Py in **9** produces two completely different frameworks. Substitution of –H with –Me in **8** removes the possibility of hydrogen bonds forming from IM within the framework. This hydrogen bonding in **7** alongside π···π stacking between IM at terminal ends of the Co_6 building unit hold the 2D layers in place, producing a 3D network. In **8**, the N-MeIM is not involved in any intermolecular interactions with another part of the framework: the 3D structure is produced entirely from carboxylate coordination. In **9** there is only one donor atom in Py (N), meaning it can only coordinate as a terminal ligand and again is not involved in any intermolecular interactions with other atoms in the framework.

3.5 References

[1] M. Fischer, F. Hoffmann, M. Froba, *ChemPhysChem* **2010**, *11*, 2220-2229.

[2] S. C. Xiang, W. Zhou, Z. J. Zhang, M. A. Green, Y. Liu, B. L. Chen, *Angew. Chem. Int. Ed.* **2010**, *49*, 4615-4618.

[3] K. C. Stylianou, J. E. Warren, S. Y. Chong, J. Rabone, J. Bacsa, D. Bradshaw, M. J. Rosseinsky, *Chem. Commun.* **2011**, *47*, 3389-3391.

[4] H. K. Chae, D. Y. Siberio-Perez, J. Kim, Y. Go, M. Eddaoudi, A. J. Matzger, M. O'Keeffe, O. M. Yaghi, *Nature* **2004**, *427*, 523-527.

[5] A. C. McKinlay, R. E. Morris, P. Horcajada, G. Ferey, R. Gref, P. Couvreur, C. Serre, *Angew. Chem. Int. Ed.* **2010**, *49*, 6260-6266.

[6] L. F. Yang, S. Kinoshita, T. Yamada, S. Kanda, H. Kitagawa, M. Tokunaga, T. Ishimoto, T. Ogura, R. Nagumo, A. Miyamoto, M. Koyama, *Angew. Chem. Int. Ed.* **2010**, *49*, 5348-5351.

[7] K. C. Stylianou, R. Heck, S. Y. Chong, J. Bacsa, J. T. A. Jones, Y. Z. Khimyak, D. Bradshaw, M. J. Rosseinsky, *J. Am. Chem. Soc.* **2010**, *132*, 4119-4130.

[8] M. Eddaoudi, J. Kim, N. Rosi, D. Vodak, J. Wachter, M. O'Keeffe, O. M. Yaghi, *Science* **2002**, *295*, 469-472.

[9] G. Ferey, C. Mellot-Draznieks, C. Serre, F. Millange, J. Dutour, S. Surble, I. Margiolaki, *Science* **2005**, *309*, 2040-2042.

[10] M. Eddaoudi, D. B. Moler, H. L. Li, B. L. Chen, T. M. Reineke, M. O'Keeffe, O. M. Yaghi, *Acc. Chem. Res.* **2001**, *34*, 319-330.

[11] K. Gedrich, I. Senkovska, N. Klein, U. Stoeck, A. Henschel, M. R. Lohe, I. A. Baburin, U. Mueller, S. Kaskel, *Angew. Chem. Int. Ed.* **2010**, *49*, 8489-8492.

[12] J. H. Jia, X. Lin, C. Wilson, A. J. Blake, N. R. Champness, P. Hubberstey, G. Walker, E. J. Cussen, M. Schroder, *Chem. Commun.* **2007**, 840-842.

[13] Y. Q. Tian, Y. M. Zhao, Z. X. Chen, G. N. Zhang, L. H. Weng, D. Y. Zhao, *Chem.-Eur. J.* **2007**, *13*, 4146-4154.

[14] S. Mintova, 1 V. Valtchev, I. Kanev, *Mol. Eng.* **1995**, *4*, 369.

[15] K. Egeblad, C. H. Christensen, M. Kustova, C. H. Christensen, *Chem. Mater.* **2008**, *20*, 946-960.

[16] K. S. Park, Z. Ni, A. P. Cote, J. Y. Choi, R. D. Huang, F. J. Uribe-Romo, H. K. Chae, M. O'Keeffe, O. M. Yaghi, *P. Natl. Acad. Sci. USA* **2006**, *103*, 10186-10191.

[17] H. Bux, F. Y. Liang, Y. S. Li, J. Cravillon, M. Wiebcke, J. Caro, *J. Am. Chem. Soc.* **2009**, *131*, 16000.

[18] R. Banerjee, A. Phan, B. Wang, C. Knobler, H. Furukawa, M. O'Keeffe, O. M. Yaghi, *Science* **2008**, *319*, 939-943.

[19] R. Banerjee, H. Furukawa, D. Britt, C. Knobler, M. O'Keeffe, O. M. Yaghi, *J. Am. Chem. Soc.* **2009**, *131*, 3875.

[20] B. Wang, A. P. Cote, H. Furukawa, M. O'Keeffe, O. M. Yaghi, *Nature* **2008**, *453*, 207-U206.

[21] *http://www.iza-structure.org/databases*. Accessed 08.08.2013.

[22] D. W. Lewis, A. R. Ruiz-Salvador, A. Gomez, L. M. Rodriguez-Albelo, F. X. Coudert, B. Slater, A. K. Cheetham, C. Mellot-Draznieks, *CrystEngComm* **2009**, *11*, 2272-2276.

[23] L. M. Rodriguez-Albelo, A. R. Ruiz-Salvador, A. Sampieri, D. W. Lewis, A. Gomez, B. Nohra, P. Mialane, J. Marrot, F. Secheresse, C. Mellot-Draznieks, R. N. Biboum, B. Keita, L. Nadjo, A. Dolbecq, *J. Am. Chem. Soc.* **2009**, *131*, 16078-16087.

[24] O. K. Farha, C. D. Malliakas, M. G. Kanatzidis, J. T. Hupp, *J. Am. Chem. Soc.* **2010**, *132*, 950.

[25] S. Bureekaew, H. Sato, R. Matsuda, Y. Kubota, R. Hirose, J. Kim, K. Kato, M. Takata, S. Kitagawa, *Angew. Chem. Int. Ed.* **2010**, *49*, 7660-7664.

[26] S. Q. Ma, D. F. Sun, M. Ambrogio, J. A. Fillinger, S. Parkin, H. C. Zhou, *J. Am. Chem. Soc.* **2007**, *129*, 1858.

[27] N. Klein, I. Senkovska, K. Gedrich, U. Stoeck, A. Henschel, U. Mueller, S. Kaskel, *Angew. Chem. Int. Ed.* **2009**, *48*, 9954-9957.

[28] B. L. Chen, M. Eddaoudi, S. T. Hyde, M. O'Keeffe, O. M. Yaghi, *Science* **2001**, *291*, 1021-1023.

[29] K. Koh, A. G. Wong-Foy, A. J. Matzger, *Angew. Chem. Int. Ed.* **2008**, *47*, 677-680.

[30] N. Klein, I. Senkovska, I. A. Baburin, R. Grunker, U. Stoeck, M. Schlichtenmayer, B. Streppel, U. Mueller, S. Leoni, M. Hirscher, S. Kaskel, *Chem.-Eur. J.* **2011**, *17*, 13007-13016.

[31] O. V. Dolomanov, L. J. Bourhis, R. J. Gildea, J. A. K. Howard, H. Puschmann, *J. Appl. Crystallogr.* **2009**, *42*, 339-341.

[32] L. J. Bourhis, O. V. Dolomanov, R. J. Gildea, J. A. K. Howard, H. Puschmann, *olex2.solve* **2011**.

[33] *IUCr* **2010**, *ChekCell*.

[34] C. G. Perkins, J. E. Warren, A. Fateeva, K. C. Stylianou, A. McLennan, K. Jelfs, D. Bradshaw, M. J. Rosseinsky, *Micropor. Mesopor. Mater.* **2012**, *157*, 24-32.

[35] Z. P. Zubreichuk, T. O. Denisova, V. A. Knizhnikov, S. E. Nefedov, *Russ. Chem. Bull.* **2004**, *53*, 1770-1772.

[36] L. E. Jones, C. A. Kilner, M. A. Halcrow, *Chem.-Eur. J.* **2009**, *15*, 4667-4675.

[37] G. X. Liu, L. F. Huang, X. J. Kong, R. Y. Huang, H. Xu, *Inorg. Chim. Acta* **2009**, *362*, 1755-1760.

[38] *Data Processing carried out by Dr. John Warren at the University of Liverpool*.

[39] Jean Rouquerol, Françoise Rouquerol, K. S. W. Sing, *Adsorption by Powders and Porous Solids: Principles*, Academic Press, London, **1999**.

[40] Y. K. Tovbin, *Russ. Chem. Bull.* **1998**, *47*, 637-643.

[41] *Analysis carried out by Dr. Phil Chater at the University of Liverpool.*

[42] A. P. Nelson, O. K. Farha, K. L. Mulfort, J. T. Hupp, *J. Am. Chem. Soc.* **2009**, *131*, 458.

[43] *Supercritical CO_2 activation and volumetric BET measurements carried out by Dr Alexandra Fateeva at the University of Liverpool.*

3.6 Additional Information

Table 2: *Crystal data and structure refinement parameters for compounds **1**, **2** and **3**:*

Sample Code	1	2	3
Empirical formula	$C_{7.5}H_5\ Zn_{0.75}NO_{3.2}$	$C_{7.25}H_5Co_{0.75}N_{1.25}O_{3.125}$	$C_{26}H_{31}\ Zn_2N_8O_{10}$
Formula weight	208.85	203.82	746.3
Temperature/K	100	100	423.3
Crystal system	monoclinic	monoclinic	orthorhombic
Space group	$P2_1/n$	$P2_1/n$	Pbca
a/Å	14.741(3)	14.8323(6)	11.660(3)
b/Å	9.477(2)	9.6102(4)	13.805(3)
c/Å	15.425(3)	15.5373(10)	19.143(3)
α/°	90	90.00	90
β/°	104.290(3)	106.345(8)	90
γ/°	90	90.00	90
Volume/Å^3	2088.1(8)	2125.20(18)	3081.6(10)
Z	4	4	4
ρcalcmg/mm^3	1.329	0.637	1.609
m/mm^{-1}	1.765	0.606	2.513
F(000)	839	410.0	1532
Crystal size/mm^3	0.25 × 0.13 × 0.08	0.21 × 0.22 × 0.16	0.21 × 0.06 × 0.05
2Θ range for data collection	5.08 to 55.06°	6.16 to 54.96°	9.24 to 179.42°
Index ranges	-15 ≤ h ≤ 18, -12 ≤ k ≤ 11, -17 ≤ l ≤ 19	-19 ≤ h ≤ 18, -12 ≤ k ≤ 12, -20 ≤ l ≤ 18	-15 ≤ h ≤ 15, -17 ≤ k ≤ 14, -24 ≤ l ≤ 24
Reflections collected	11998	34888	53962
Independent reflections	4686[R(int) = 0.0352]	4841[R(int) = 0.0899]	3503[R(int) = 0.0618]
Data/restraints/ parameters	4686/55/246	4841/0/210	3503/0/244
Goodness-of-fit on F2	1.091	1.453	1.056
Final R indexes [I>=2σ (I)]	R_1 = 0.0681, wR_2 = 0.1975	R_1 = 0.1240, wR_2 = 0.3627	R_1 = 0.0324, wR_2 = 0.1204
Final R indexes [all data]	R_1 = 0.0898, wR_2 = 0.2116	R_1 = 0.1495, wR_2 = 0.3810	R_1 = 0.0344, wR_2 = 0.1236
Largest diff. peak/hole / e Å^{-3}	1.90/-0.63	2.37/-1.01	1.04/-0.3

Table 3: *Crystal data and structure refinement parameters for compounds **7**, **8** and **9**:*

Sample Code	7	8	9
Empirical formula	$C_{44.58}H_{30.44}Co_3N_{2.72}O_{11.65}$	$C_{65}H_{48}Co_{3.5}N_{5.3}O_{14.7}$	$C_{28}H_{20}CoN_2O_{8.8}$
Formula weight	966.71	1344.21	292.29
Temperature/K	373.1(10)	100	100
Crystal system	monoclinic	monoclinic	trigonal
Space group	C2/c	$P2_1/n$	P-31c
a/Å	17.133(3)	30.3202(5)	18.747(2)
b/Å	30.205(6)	14.7164(2)	18.747(2)
c/Å	20.953(4)	33.393(2)	14.786(2)
α/°	90.00	90.00	90.00
β/°	92.78(3)	108.742(8)	90.00
γ/°	90.00	90.00	120.00
Volume/Å^3	10830(4)	14110.0(9)	4500.3(9)
Z	8	8	12
ρcalcmg/mm^3	1.186	1.266	1.294
m/mm^{-1}	0.96	0.873	0.623
F(000)	3926	5495.0	1798.0
Crystal size/mm^3	0.2 × 0.2 × 0.2	0.15 × 0.06 × 0.03	0.8 × 0.11 × 0.02
2Θ range for data collection	1.94 to 54.36°	6.06 to 54.98°	3.72 to 49.4°
Index ranges	$-21 \le h \le 15$, $-38 \le k \le 38$, $-26 \le l \le 26$	$-28 \le h \le 39$, $-19 \le k \le 19$, $-43 \le l \le 43$	$-22 \le h \le 22$, $-13 \le k \le 22$, $-17 \le l \le 15$
Reflections collected	84214	222819	21547
Independent reflections	10671[R(int) = 0.0974]	32294[R(int) = 0.1552]	2546[R(int) = 0.0534]
Data/restraints/ parameters	10671/238/611	32294/0/1435	2546/0/168
Goodness-of-fit on F2	1.064	1.164	2.452
Final R indexes [I>=2σ (I)]	$R_1 = 0.0761$, $wR_2 = 0.2352$	$R_1 = 0.1272$, $wR_2 = 0.3523$	$R_1 = 0.1944$, $wR_2 = 0.5434$
Final R indexes [all data]	$R_1 = 0.1007$, $wR_2 = 0.2516$	$R_1 = 0.2242$, $wR_2 = 0.4035$	$R_1 = 0.2471$, $wR_2 = 0.5897$
Largest diff. peak/hole / e Å^{-3}	1.080/-1.459	4.80/-1.27	1.54/-1.45

CIFs could not be finalised for compounds **4**, **5** and **6** due to poor quality data.

Chapter 4

A Cerium-Based Metal-Organic Framework: Structure, Sorption and Structural Transformations upon Desolvation

4.1 Introduction

Lanthanides (Ln) can be used in MOF synthesis due to the large coordination sphere and unrestricted coordination geometry offered by the 4f orbitals, giving them a more flexible coordination sphere than the d-block elements. This allows for the production of a large range of MOF topologies with interesting structural properties[1-2]. However, it is more difficult to control Ln coordination, hence why Ln coordination compounds are less studied their d-block counterparts, which have common geometries of 2, 3, 4 and 6 coordinate. The d-block metals can be chosen for their specific coordination geometry, whereas the unpredictable coordination modes of Ln mean they cannot be used in the same way and structure prediction is difficult[3]. Lanthanide MOFs in general have low densities with high specific surface areas and thermal stabilities, making them ideal candidates for applications in areas such as catalysis[4-5], molecular recognition[6] due to their characteristic luminescent properties[7], separation[8] and gas storage[9]. The unpaired electrons present in lanthanide ions can also give rise to characteristic optical[10] and magnetic[11] properties.

Ma *et. al.* combined 4,4',4''-s-triazine-2,4,6-triyl-tribenzoate (TATB) with Ln to produce a series of isostructural frameworks (where Ln = Yb, Dy, Er, Y) with the formula $Ln(\mu_4\text{-}H_2O)(TATB)(SO_4)_2.xH_2O.y$DMSO (PCN-17). The structures are based on a square planar $Ln(\mu_4\text{-}H_2O)$ secondary building units (SBU) linked in 3D by the TATB ligands. A decrease in unit cell volume is observed in line with the lanthanide contraction: Dy>Y>Er>Yb and the structures are all stable up to 500-550 °C with BET surface areas of 738, 606, 814 and 820 m_2/g respectively for PCN-17(Dy, Y, Er, Yb). These materials are also shown to be selective to H_2 over CO and N_2, meaning they have potential applications in gas separations, for example, with H_2 separation from Co in fuel cells[7].

A series of isostructual chiral Ln-tricarboxylates with the formula $Ln(1,3,5\text{-}BTB)(H_2O)$.guests (MIL-103, where Ln = La-Ho, Y) were synthesised through combination of Ln and 1,3,5-BTB in a biphasic reaction using cyclohexanol and H_2O. The single crystal structures show a decrease in a- and c- unit cell parameters in line with the lanthanide contraction, a similar effect to that observed in the earlier example of the PCN-17 series. These frameworks are all stable to between 250-400 °C and have BET surface areas of around 700 m^2/g[12-13].

The 8-coordinate 3D structure $Yb(CTC)(DMF).(H_2O)_2$ (JUC-57, where CTC = cis, cis-1,3,5-cyclohexane tricarboxylic acid) was synthesised by Zhao *et. al.*. The framework contains a 3D channel network with dimensions of 11.8 x 6.9 Å and exhibits an antiferromagnetic interaction between Yb^{3+} centres[1].

One final example are a series of Ln-terepthalates, synthesised by McMullen *et al.*. Five frameworks with the formula $Ln_2(1,4\text{-}BDC)(H2O)_x$ were synthesised, where Ln = Er and Yb with a

coordination number of 8. Control of the amount of H_2O, *x*, in these compounds determined the structure produced: When less H_2O was present (x = 2), the frameworks produced are 3D. When more H_2O is added (x = 4), the structure becomes 2D and when the most H_2O is added (x = 6), the structure produced contains 1D chains[14].

All these examples show the various coordination modes than can be produced when using Ln as the metal central in MOF synthesis and the structures produced are porous and have interesting properties and potential applications.

Research into the production of stable MOFs is key if such materials are to have applications in areas such as gas storage, separation and catalysis, as stability is their one downfall when being compared to zeolites; heat, pressure and water stability are often investigated for their effects on the structure of MOFs. For example, MOF-177 completely loses its crystallinity upon immersion into water and in air the crystallinity reduces over a 5 week period with a change in structure from hexagonal to orthogonal[15]. As MOF-177 is a promising candidate for H_2 storage at 7.5 wt % at 77K and 70 bar[16], it is essential to understand its stability.

The 3D structures of the majority of MOFs are initially determined by single crystal x-ray diffraction (SCXRD), but following heating, activation or any other reaction, it may no longer be possible to determine the single crystal structure due to a reduction in crystallinity. In these cases, further characterisation is carried out using powder x-ray diffraction (PXRD) (which again may not be possible if the MOF has lost all structural integrity). There are examples where structural transformations are observed using single crystal diffraction, but these are uncommon. Most single-crystal-to-single-crystal (SCSC) transformations involve 'breathing' compounds in which the structure expands and contracts with guest uptake and loss[17], however reports of SCSC transformations in which chemical bonds are broken or made are few and far between[18]. This is one of the greatest challenges of solid state chemistry, as knowledge of the structure at all stages of a reaction is essential in order to understand the properties and potential application of a material, however in the majority of cases, deterioration in structural integrity is observed during a reaction[19].

Liu *et. al.* synthesised two enantiomeric Dy compounds and were able to investigate the SCSC transformations with release and absorption of different solvents, which they say is essential to understand the different physical ferroelectric, magnetic, and NLO properties[20]. In 2012, the SCSC transformation of a Cu-MOF with iodine release was reported in which the authors highlight how rare it is to have the ability to determine the 3D structure through a framework structural transition in which chemical bonds are broken and made[21]. Retention of the single crystal phase allows a clear understanding of the structure-property relationships of a material.

The first example of a SCSC transition with a Ln MOF was shown be Jia et. al., who synthesised a 3D porous framework with the formula $Ln_2(3,5\text{-Pydc})_3(DMF)_2$, where Ln = Er (**A**) or Y (**B**). Heating caused removal of DMF from the materials and the single crystal structures of the desolvated phases, **C** and **D** for Er and Y respectively, were determined. **C** and **D** were shown to have BET surface areas of 427 and 626 m^2/g respectively.

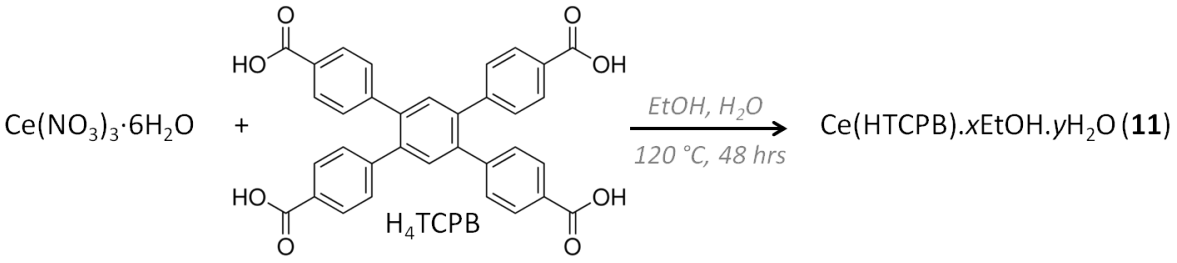

Figure 1: *Reaction scheme for synthesis of compound* ***11****. H_4TCPB = Tetrakis(4-carboxyphenyl)benzene ligand.*

In this chapter, the synthesis of a 3D neutral framework is discussed; solvothermal reaction of $Ce(NO_3)_3.6H_2O$ with the 1,2,4,5-tetracarboxyphenyl benzene (H_4TCPB) ligand (*Figure 1*) produces a framework with the formula Ce(HTCPB).*guests* (**11**). H_4TCPB is a commercially available ligand which has been used synthesise MOFs with large porosity and structural stability[22]. The rotational flexibility of the carboxyphenyl groups allows the ligand to form three dimensional frameworks, and there are examples of this ligand being used to form stable 3D frameworks with gas storage[22] and separation capabilities[23].

Bae *et. al.* showed that combination of $Zn(NO_3)_2.xH_2O$ with H_4TCPB in DMF followed by heating to 80 °C for 24 hours yielded phase pure Zn(TCPB)(DMF).DMF_x; a 3D non-interpenetrated framework. Removal of DMF from the framework by heating to 150 °C for 24 hours produced the desolvated material, which has a BET surface area of 800 m^2/g. The desolvated material was modified by soaking in py-CF_3, producing Zn(TCPB)(py-CF_3)$_2$ and this shows a high N_2/CO_2 selectivity of 42 at atmospheric pressure[24].

The H_4TCPB ligand has also been used in combination with a secondary linker to form 2D M-TCPB sheets between which linear linkers are used to bridge the sheets into a 3D framework. Frameworks with the formula Zn_2(Lbp)(Lta) where (Lbp = bipyridyl of varying length and Lta – tetraacid) were synthesized by combining the two linkers with $Zn(NO_3)_2.6H_2O$ in DMF and heating to 80 °C for 24 hours. However, the frameworks produced with 2-fold interpenetrated, so the H_4TCPB ligand was modified by adding –Br at the 3- and 6-positions of the central aromatic ring. This produces non-interpenetrated frameworks with larger BET surface areas. For example

the two frameworks Zn_2(4,4'-bipy)(TCPB) and Zn_2(4'4-bipy)(Br_2TCPB) had BET surface areas of 535 and 980 m^2/g respectively[25].

The H_4TCPB ligand has also been used in combination with a secondary linker to produce MOFs for post-synthetic modification (PSM). Within the group of Hupp, combination of H_4TCPB with modified 4,4'-bipy linkers produce two frameworks with pores large enough to accommodate the click reaction intermediate[26] and metal-alkoxide formation[27].

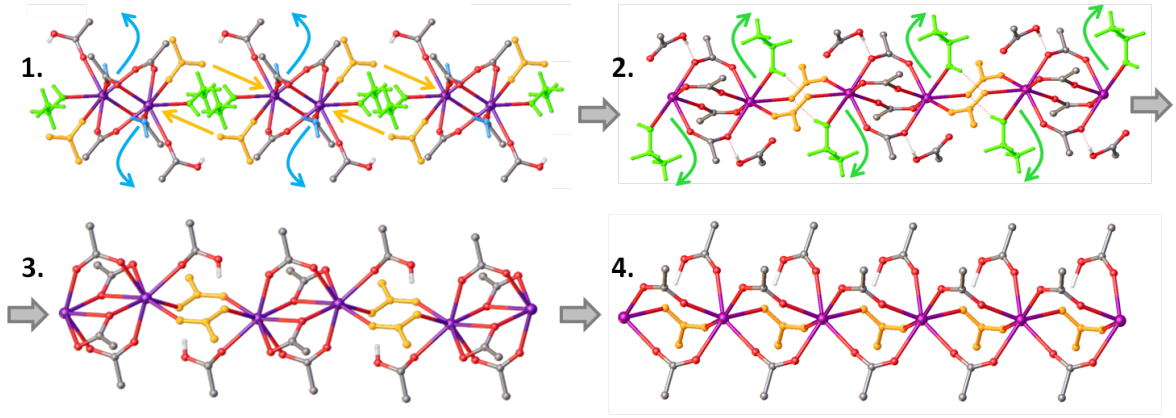

Figure 2: *Ce coordination environment during single-crystal-to-single-crystal transformations during the desolvation and rearrangement of* ***11****, showing which bonds are broken and made. 1. =* ***11****, 2. =* ***11S****, 3. =* ***11D*** *and 4. =* ***11R****.*

The aim was to investigate the desolvation procedure of **11** and if possible to determine the desolvated structure of the material. The four step SCSC structural changes of **11** during desolvation were investigated by means of a single crystal variable temperature experiment, which allowed the fully desolvated structure of **11** (**11D**) to be determined. This study also showed that desolvation proceeds *via* a stable intermediate (**11S**) known as the EtOH-solvate. Following desolvation, exposure of **11D** to the air causes a further structural change with the coordination of atmospheric H_2O, producing a new rehydrated/rearranged structure (**11R)** (*Figure 2*, *3*). Re-heating of **11R** shows that the single crystal structure can revert back to **11D** with the removal of H_2O. Compounds **11**, **11S** and **11R** are stable in air, shown by both single crystal and powder x-ray diffraction, however compound **11D** is only stable under N_2 in both the bulk powder and single crystal phases.

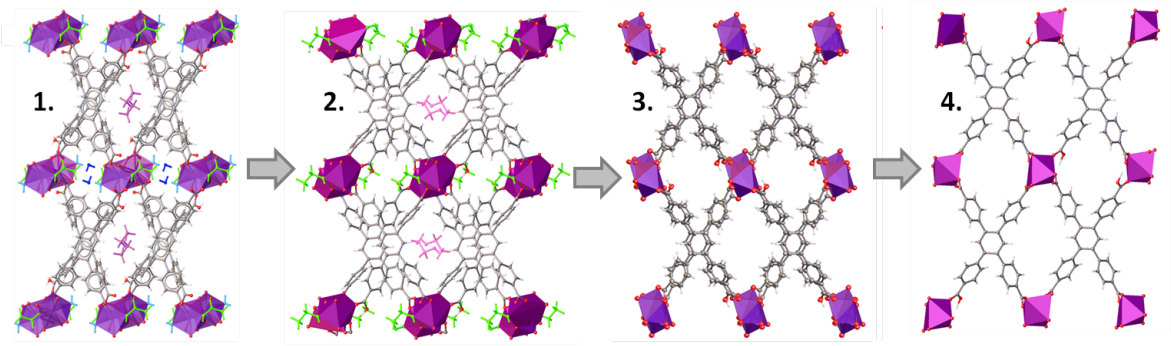

Figure 3: *View down 100 during the single-crystal-to-single-crystal transformations through the desolvation and rearrangement of* ***11****, showing which bonds are broken and made. 1. =* ***11****, 2. =* ***11S****, 3. =* ***11D*** *and 4. =* ***11R****.*

The fact that single crystals of **11** remain stable and diffract with good resolution throughout a variable temperature experiment to yield the fully desolvated structure **11D**, structural change to **11R** upon exposure to air and subsequent structure reversal back to **11D** with heating demonstrates the high flexibility and stability of these crystals.

Armed with the knowledge of the desolvated solvent free framework **11D**, it is possible to predict potential applications for this MOF.

4.2 Experimental

4.2.1 MOF Synthesis

An initial set of experiments were carried out in which the ratio and concentration of $Ce(NO_3)_3 \cdot 6H_2O$ and H_4TCPB, temperature to which the reaction was heated solvothermally, time at which the reaction was allowed to dwell at its reaction temperature, cooling rate and solvent combination and ratio (DMF, EtOH, H_2O, MeOH) were varied. When DMF was used alone or in combination with other solvents the reaction yielded amorphous material, however when using EtOH /H_2O mixtures, the product was more crystalline. Substitution of EtOH with MeOH in these reactions also yielded amorphous material.

Single crystals of compound **11** were finally synthesised by combining $Ce(NO_3)_3 \cdot 6H_2O$ (25.0 mg, 0.036 mmol) and H_4TCPB (10 mg, 0.018 mmol) in EtOH (3 mL) and H_2O (3 mL) in a sealed 12 mL borosilicate glass vial. An excess of $Ce(NO_3)_3 \cdot 6H_2O$ was used to ensure a high yield. The mixture was heated to 120 °C for 48 hours, followed by slow cooling at 0.2 °C/min back down to room. A scaled-up method (method B) at 3x scale was carried out to produce larger amounts of material for analysis.

4.2.2 Single Crystal Data Collection and Analysis

In this chapter, data for the single crystal structure solution of **11**, **11D**, **11D** and **1R** was collected from the Rigaku Rotating Anode Diffractometer at the University of Liverpool. The structures were solved and refined using Olex2[28-29]. All structure solution and refinement was carried out with the assistance of Dr John Warren.

4.2.3 Powder X-Ray Diffraction and Analysis

Powder X-ray diffraction (PXRD) data of **11**, **11S**, **11D** and **11R** was collected in transmission geometry using Bruker D8 Advance with Cu Kα radiation in a sealed 0.5mm capillary and indexed to the single crystal unit cell to confirm phase purity. Variable temperature data on **11** was collected at station I11 at Diamond Light Source (DLS), Didcot, UK. LeBail analysis of **11** and the variable temperature PXRD profiles was carried out by Dr Phil Chater at the University of Liverpool.

4.3 Results and Discussion

4.3.1 Single Crystal X-ray Diffraction

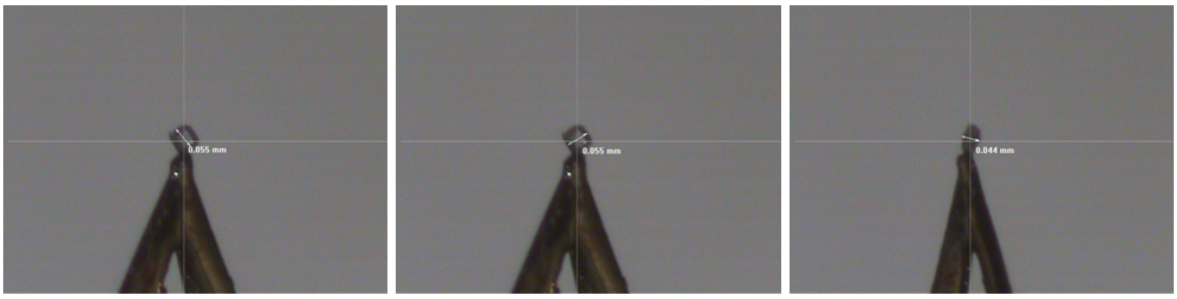

Figure 4: *Pictures of the crystal taken on the diffractometer displaying the crystal measurements.*

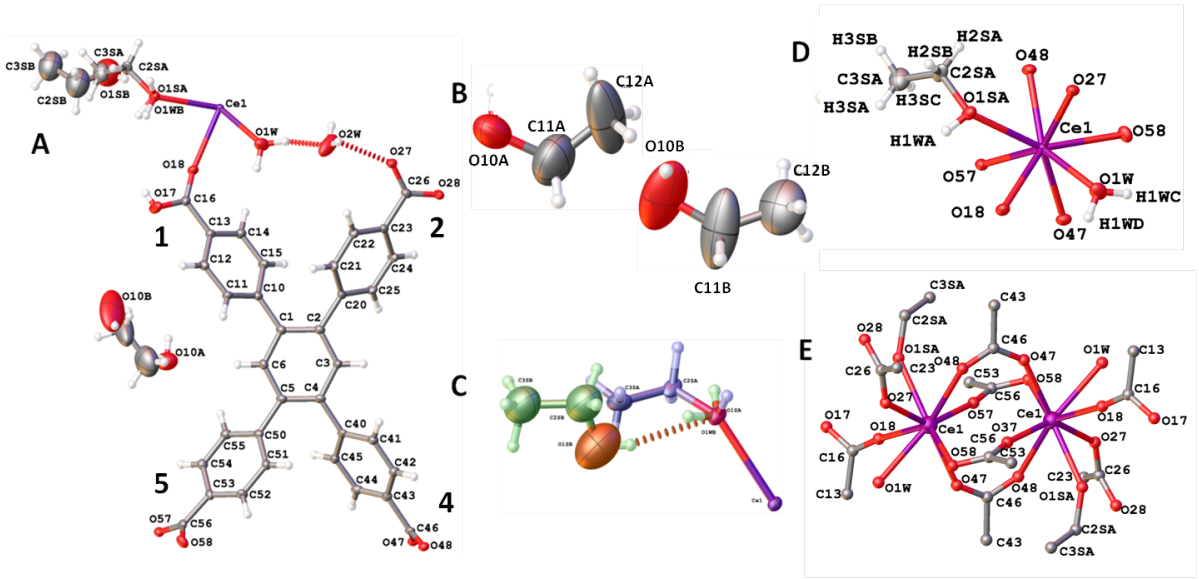

Figure 5: *Single Crystal Structure of **11**. A: Asymmetric unit with ring numbering shown; B: Both PART 1 and PART 2 of disordered channel EtOH; C: PART -1, PART 1 and PART 2 disorder in coordinated EtOH, channel EtOH and associated H_2O. Hydrogen bonding shown as red dotted line; D: Ce coordination single disordered component shown for C.*

A single crystal of **11** (0.055 × 0.055 × 0.044 mm) (*Figure 4*), was chosen for single crystal structure determination. **11** is a 3D neutral framework with potential 2D porosity following removal of the coordinated guest and channel EtOH and H_2O solvent molecules from the structure. **11** has unit cell dimensions of a = 10.5783(1) Å, b = 10.4271(1) Å, c = 16.9210(11) Å, α=83.158(6) °, β= 6.314(5) °, γ=70.023(5) ° and V=1702.797 $Å^3$. Within the asymmetric unit of **11**, there is one Ce(III), one HTCPB ligand, one disordered EtOH, one H_2O and Ce-coordinated EtOH and H_2O, which are both disordered with the channel EtOH.

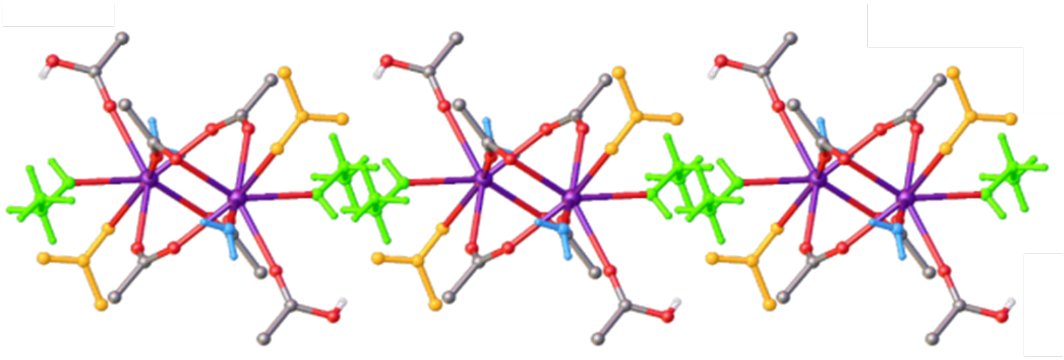

Figure 6: *Coordination environment of Ce in* ***11****.Coordinated EtOH and* H_2O *shown in green and cyan respectively. Monodentate non-protonated carboxylate on ring 2, that forms a bridge between* Ce_2 *dimers during desolvation (shown later) in orange.*

Compound **11** comprises of one Ce(III) and one mono-protonated HTCPB ligand in the asymmetric unit giving the framework an overall neutral charge. The ring numbering scheme of the HTCPB ligand is shown in Figure 5A: Ring 1 stems from C1 of the HTCPB central aromatic ring and possess the protonated carboxylate; ring 2 is adjacent to ring 1, branching from C2 of the central aromatic ring; rings 4 and 5 stem from C4 and C5 of the central aromatic ring respectively. The asymmetric O18-C16-O17 bond distances of carboxylate 1 of 1.224 Å and 1.303 Å respectively show that the ligand is protonated at this site. The Ce metal is 8 coordinate (for all compounds the Ce radius is set at 1.68 Å to remove C-Ce bonds) with the coordination sphere being occupied by one disordered EtOH/H_2O (O1SA, O1WB) site and one fully occupied H_2O (O1W) site. The remainder of the coordination sphere is filled with carboxylate oxygen atoms O18 (ring 1), O27 (ring 2), O47 and O48 (ring 4), O57 and O58 (ring 5) (*Figure 5D*). When grown this produces a Ce_2 dimer bridged by two of the four carboxylates groups of the ligand from O4x and O5x (where X = 7 or 8) (*Figure 6E*). These Ce_2 dimers are held in place hydrogen bonding between both of the two monodentate carboxylates from rings 1 and 2 and coordinated EtOH (*Figure 7*).

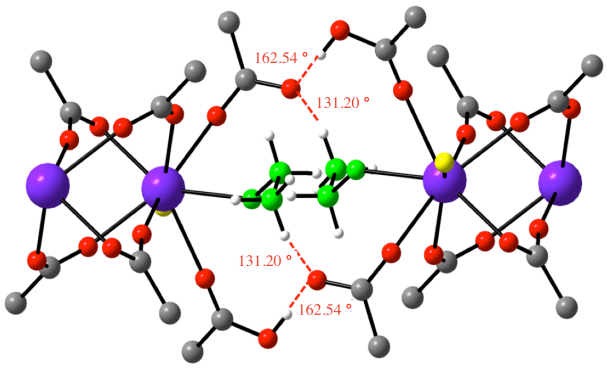

Figure 7: *Hydrogen bonding pocket within* ***11*** *between non-protonated and protonated monodentate carboxylates and Ce-coordinated EtOH.*

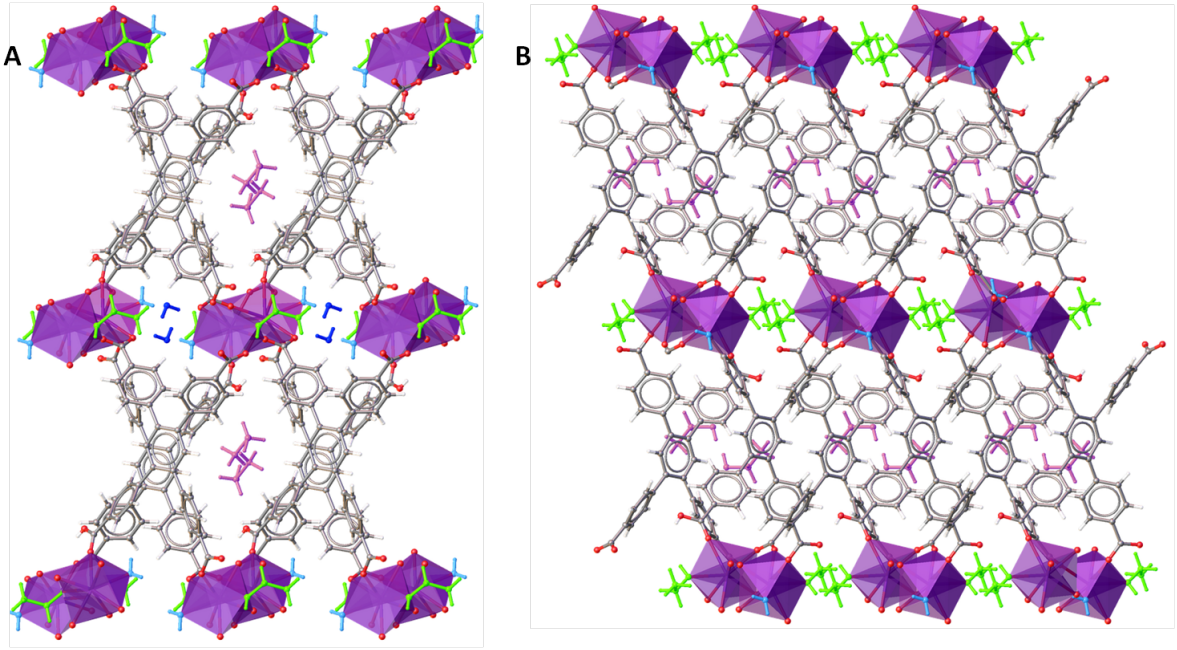

Figure 8: *View down A: 100 and B: 010 of as synthesized **11**. Ce (purple), oxygen (red), carbon (grey), hydrogen (white), coordinated EtOH and H_2O (green and cyan respectively), channel EtOH and H_2O (magenta and dark blue respectively).*

On packing we find two channels which run parallel with the 100 direction and a third which runs parallel to the 010 direction (*Figure 8*). Channel 1 is the largest and is found to be host to the disordered EtOH split over two positions. The smaller channel 2 intersects channel 3 at the Ce_2 dimer and hosts a hydrogen bonded H_2O (O1W) molecule within the Ce dimer layers. The Ce-bound disordered EtOH/H_2O and free EtOH are located within channel 2, orthogonal to channel 3. Overall, **11** is a 3D framework with potential 2D porosity, with bound and free solvent occupying the void space.

The crystal structure of **11** contains three unbound partial guest EtOH molecules. Two located in channel 1 with shared common carbon atoms. The third EtOH is found in channel 2 (O1SB, C2SB, C3SB) and is disordered with the Ce bound EtOH (O1SA, C2SA, C3SA) which is also disordered with a bound H_2O molecule (O1WB).

The 3D structure is based on isolated Ce_2 dimers which are held in a 3D structure by the HTCPB ligand. Each Ce_2 dimer is bridged by four (Ce-)O-C-O(-Ce) bidentate bridges (*Figure 5E*), filling four of the eight sites in the coordination sphere of Ce(III). Two monodentate carboxylates are also coordinated each Ce; one protonated and one non-protonated at the axial positions of the Ce_2 dimer, which alongside the EtOH/H_2O (O1SA, O1WB) and O1W brings the coordination to 8.
Of the four carboxylate groups belonging to each HTCPB ligand, two (from rings 1 and 2) coordinate to Ce *via* monodentate coordination the third and fourth (from rings 4 and 5) coordinate

to two symmetry equivalent Ce *via* a bidentate carboxylate bridges. This leaves a framework containing Ce_2 dimers linked in three dimensions *via* HTCPB ligands.

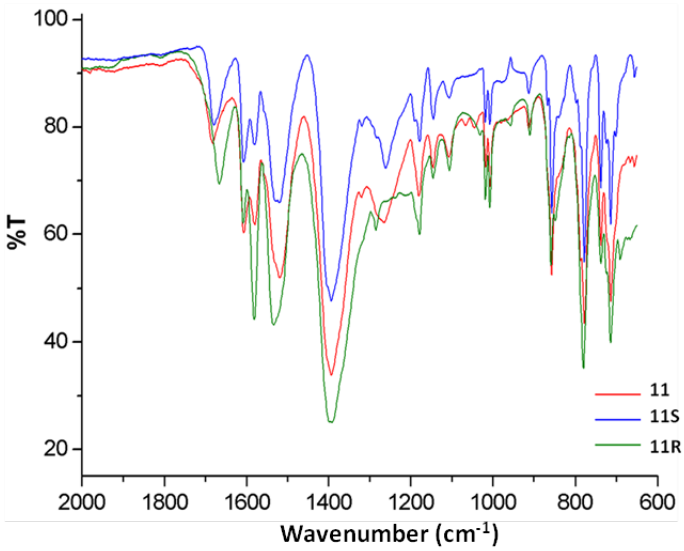

Figure 9: *IR spectra of **11**, **11S** and **11R** showing presence of C=O carbonyl (~1690 cm^{-1}), several conjugated C-O environments (1620-1550 cm^{-1}) and C-O single bond (1400 cm^{-1}), highlighting the presence of a protonated carboxylic acid group within the structure.*

As mentioned, one of the monodentate carboxylate groups is protonated (carboxylate 1) which can be seen from the asymmetric (Ce-)O17-C16-O18(-H) bond lengths of 1.233 Å and 1.303 Å respectively in comparison with the more uniform (Ce-)O28-C26-O27 bond lengths of 1.265Å and 1.271 Å respectively, seen in the non-protonated carboxylate group 2.

It is expected that C=O will have a shorter bond length than C-O, whereas conjugated C-O bonds will have lengths somewhere intermediate to the C=O and C-O. IR spectra show these three different C-O environments are present in the structure of **11** (and **11S**, **11R**, discussed later) which further confirms the protonation of one carboxylate (*Figure 9*). The spectrum shows that there are three carboxylate bonding environments in the material with characteristic carboxylate frequencies including a C=O carbonyl carboxylate peak at 1684 cm^{-1}, conjugated C-O peaks between 1607-1521 cm^{-1} and a C-O single bond peak at 1258 cm^{-1}, which indicates the presence of both protonated (O=C(R)-OH) and non-protonated (conjugated O-C(R)-O^-) carboxylate groups within the MOF *(Figure 9)*. The protonated monodentate carboxylate therefore interacts with Ce *via* the lone pair of the carbonyl oxygen (Ce-O18=C-O17H). This is also highlighted in the hydrogen bonded pocket within the structure, in which the protonated and non-protonated carboxylate groups from two separate ligands interact with one another within the 3D structure and also interact with OH of the Ce-coordinated EtOH (*Figure 7*).

Following the removal of channel solvent and the coordinated H_2O and EtOH molecules in the asymmetric unit, the frameworks can be penetrated by spherical probes with radii of 1.4, 0.9 and 0.5 Å down the a-, b-, and c-axis respectively, with a largest spherical void of 4.4 Å and a total solvent accessible volume of 505.9 $Å^3$ (calculated using Olex2[28]).

Upon standing at room temperature in air, single crystals of **11** which have been removed from their mother liquor and left on a glass slide for any residual solvent to evaporate over a period of 7 days have been found to be stable in air. Structural analysis of a single crystal from this sample showed that during this time, some of the coordinated EtOH had started to exchange with H_2O from the air, whilst retaining the same parent structure. However, synthesis in pure H_2O yielded an amorphous product, showing both EtOH and H_2O are required for the synthesis of this crystalline MOF. Attempt to synthesise **11** using MeOH/H_2O and MeOH/EtOH also yielded amorphous product, indicating that both EtOH and H_2O are important for structure formation.

4.3.2 Phase Purity

The phase purity of as-grown **11** was confirmed by powder X-ray diffraction (PXRD) (*Figure 13*), thermogravimetric analysis (TGA) (*Figure 14B*), and CH microanalysis (*Table 1*).

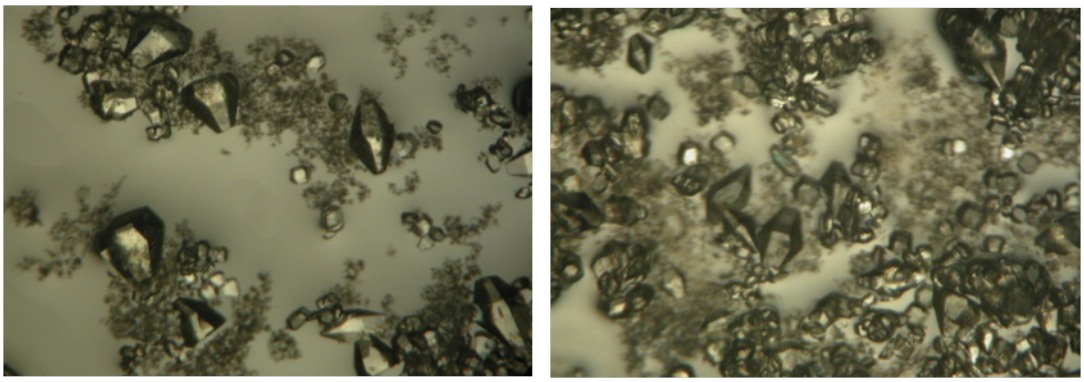

Figure 10: *Optical microscope images of single crystals of* ***11*** *at 11.25x magnification.*

Optical microscope (OM) images of **11** show the large colourless single crystals, which were later used for single crystal x-ray diffraction (*Figure 10*). Scanning electron microscope (SEM) images of **11** show the same single crystals formed *via* synthesis method A of around 50 μm (*Figure 11*). SEM images of **11** produced *via* synthesis method B show a more polycrystalline sample with a larger particle size distribution of between 2 and 20 μm (*Figure 12*).

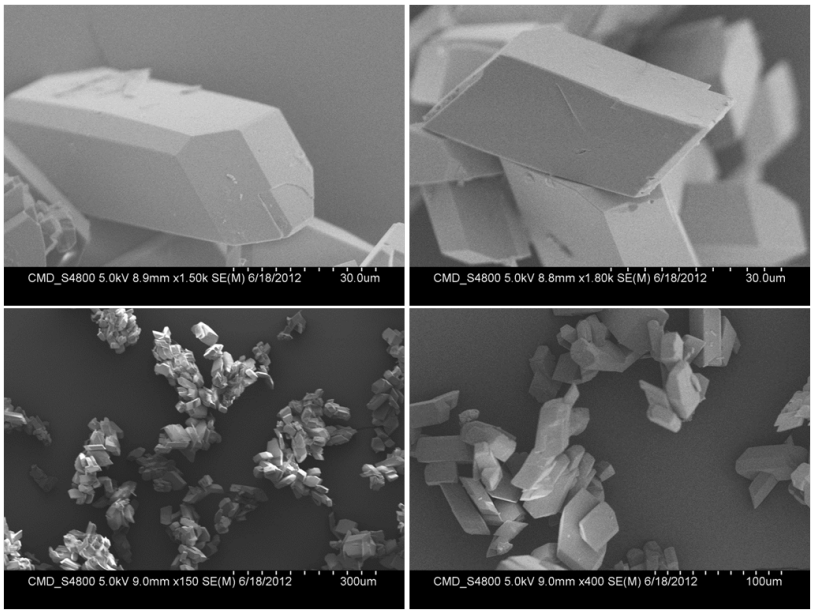

Figure 11: *SEM images of sample of single crystals of* ***11*** *with particle size of ca. 50 µm. Sample prepared using synthesis method A and used for single crystal experiments.*

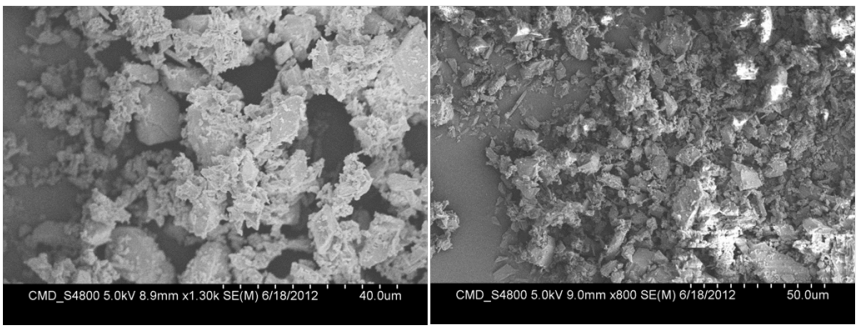

Figure 12: *SEM images showing a polycrystalline sample of* ***11*** *with particle size of ca. 2-20 µm following a scaled up synthesis. Sample prepared using method B and used for liquid sorption experiments.*

Samples prepared by both method A and B were shown to be phase pure by PXRD, however it is clear that different synthesis conditions yield products of different size and morphology (*Figure 14A*).

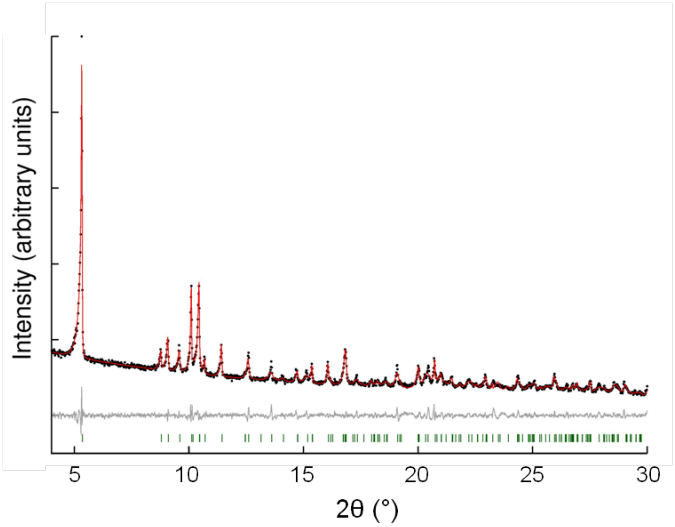

Figure 13: *PXRD profile of **11**. Final observed (black), calculated (red) and difference (grey) X-ray powder diffraction profile measured in transmission geometry using Bruker D8 Advance with Cu Kα radiation in a sealed 0.5mm capillary for the Le Bail refinement of **11** (R_{wp} = 4.511 %, R_{exp} = 2.940 %, R_p = 3.360 %, χ^2 = 2.353; a = 10.81826(97), b = 10.65732(70), c = 16.96384(152) Å, α = 76.92450(49), β = 83.27133(65), γ = 68.36294 (48), V = 1769.64575. (P_{-1}). Reflection positions are marked.*

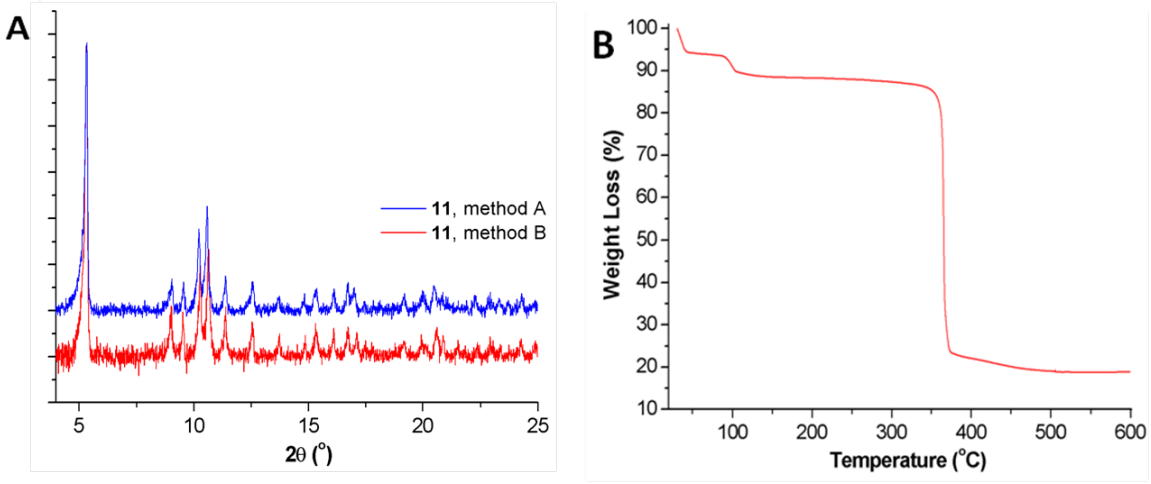

Figure 14: *A: PXRD profiles of **11** synthesized via method A (red) and method B (blue). Both index to be phase pure. Data collected in transmission geometry using Cu Kα radiation; B: TGA profile of **11**.*

TGA of **11** shows a weight change of 9.8 % observed for the loss of the guest and coordinated EtOH and H_2O molecules before reaching a plateau at 120 °C which is in good agreement with the values calculated from microanalysis of 9.7 % total solvent. The final mass percentage of 20.1 % corresponds to 1 equivalent of CeO_2 after heating at 600 °*C* (*Figure 14B*).

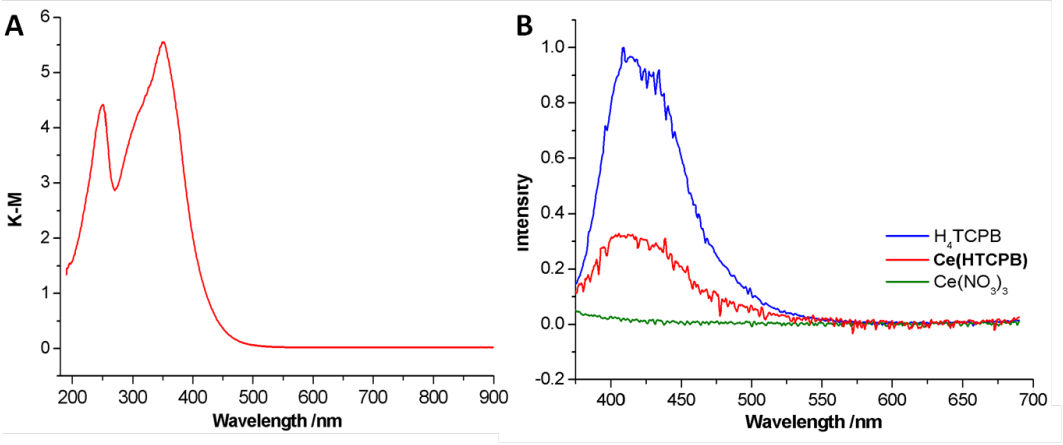

Figure 15: *A: UV-vis spectrum showing adsorption at 260 and 350 nm; B: Fluorescence spectra showing ligand-based fluorescence which is quenched upon coordination to the Ce (measurement taken following excitation at 350 nm).*

A UV-visible spectrum shows absorption at 260 and 350 nm. Following excitation at 350 nm, **11** displays ligand based fluorescence which is quenched upon coordination to the metal, however no metal to ligand charge transfer is observed (*Figure 15*).

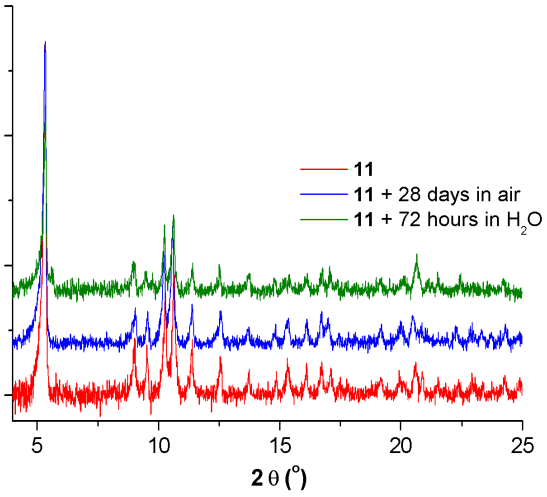

Figure 16: *PXRD profiles showing the stability of **11** in air and H_2O.*

Compound **11** is stable in air and moisture (*Figure 16*): A sample of **11** was synthesised, filtered and left in a glass vial for 28 days, after which time the PXRD was measured and showed no loss of crystallinity. The same is observed for single crystals of **11**; when a sample of single crystals are left on a slide in air for up to 7 days, the same resolution in diffraction is observed for SCXRD. Stability to air also implies a stability to moisture, so in order to demonstrate the stability of **11** in H_2O, a sample was left in H_2O for 72 hours after which time the PXRD again was measured and shows no loss of structural integrity.

4.3.3 Structural Changes upon Desolvation of Ce(HTCPB)

4.3.3.1 Single-Crystal Variable Temperature Experiment

In order to analyse the desolvation process of **11**, a single crystal was chosen, mounted on a glass fibre and a full sphere of data was collected at 50 K temperature intervals between 100 K and 250 K, and then continued with 10 K temperature intervals up to 340 K. When a shift in unit cell parameters was observed, the crystal was cooled to 100 K for a data collection so all data sets were comparable.

Table 1: *Unit cell dimensions and R factor during single crystal variable temperature experiment.*

Ce(HTCPB)	Unit Cell Dimensions			Unit Cell Volume (Å^3)	R_1 (%)
	a (Å) α (°)	b (Å) β (°)	c (Å) γ (°)		
11	10.5783(1) 83.158(6)	10.4271(1) 76.314(5)	16.9210(11) 70.023(5)	1702.80(1)	5.17
11S	9.5629(7) 87.067(2)	11.5520(8) 86.910(2)	15.0214(10) 81.372(3)	1636.70(2)	6.17
11D	9.2989(11) 93.756(5)	11.4163(13) 90.263(6)	15.2492(17) 93.814(6)	1611.70(3)	8.32
11R	5.0714(9) 109.850(9)	18.4520(3) 90.950(10)	19.5430(4) 94.481(9)	1713.10(5)	8.98

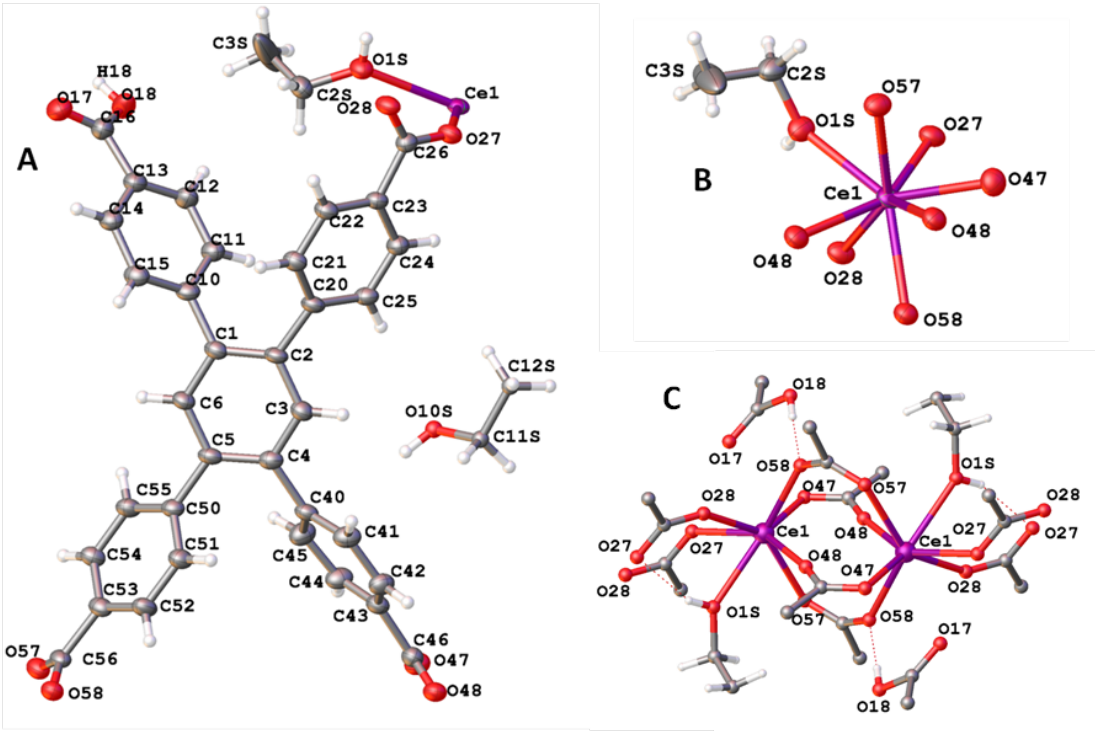

Figure 17: *Single Crystal Structure of **11S**. A: Asymmetric unit; B: Ce coordination; C: Ce dimer with bridging carboxylate and EtOH coordination shown. Ce (purple), O (red) C (grey), H (white).*

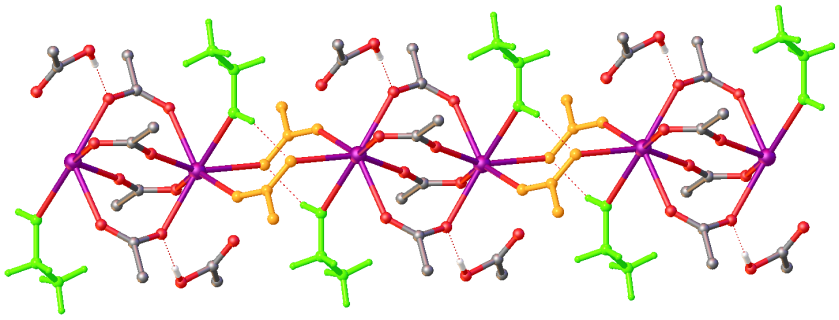

Figure 18: *Coordination environment of Ce in* ***11S****. Coordinated EtOH shown in green. Monodentate non-protonated carboxylate on ring 2 has formed a bridge between the* Ce_2 *dimers present in* ***11*** *in the first step of desolvation in which* H_2O *has been lost, leading to this intermediate* ***11S*** *in which the protonated carboxylate of ring 1 has become detached from Ce.*

The first structural transition from the ground state (**11**) occurred at 320 K, forming a new structure which is referred to as the EtOH solvate, **11S**. This change firstly sees the loss of coordinated H_2O from the structure (*Figure 2,1.-2.*). The second change involves the formation of a bidentate carboxylate bridge between the originally isolated Ce_2 dimers forming Ce-carboxylate chains propagating parallel to the a-axis (*Figure 17B)*. The non-coordinated O68 atom of the non-protonated monodentate carboxylate 2 unit on ring 2 coordinated to each Ce bonds to Ce in the adjacent Ce_2 dimer, meaning where there was originally no connectivity between Ce_2 in **11**, there are now two bidentate carboxylate bridges present; Ce-O67/O67'-C66/C66'-O68/O68'-Ce' (' denotes symmetry generated element) (*Figure 18, shown in orange*).

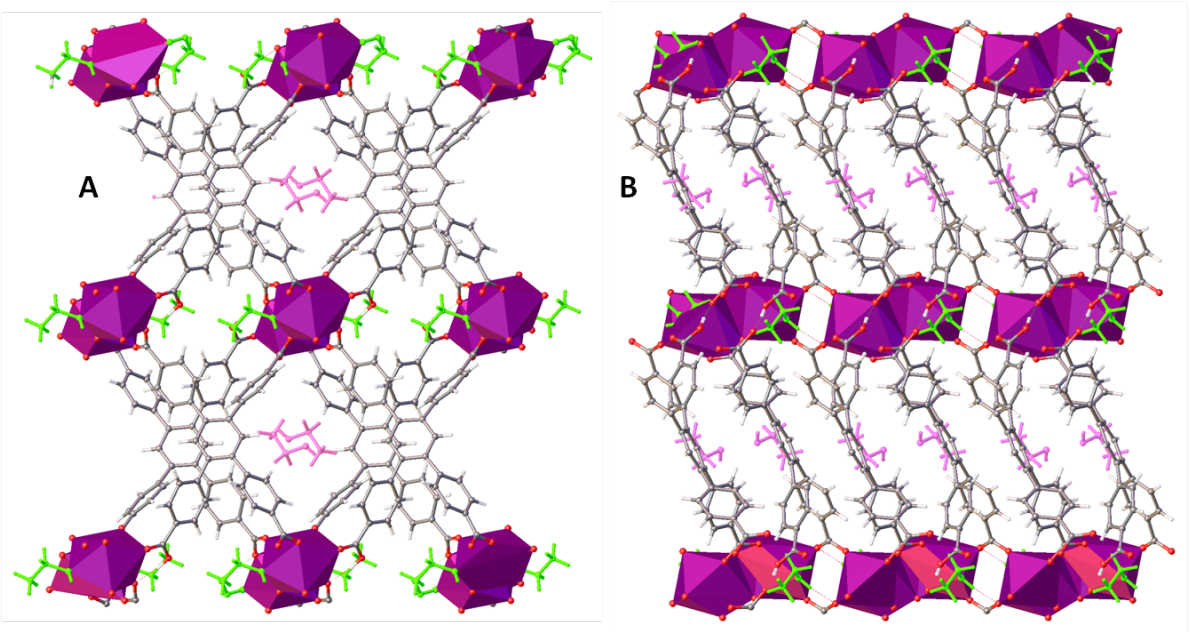

Figure 19: *View down A: 100 and B: 010 of intermediate* ***11S****. Ce (purple), oxygen (red), carbon (grey), hydrogen (white), coordinated EtOH (bright green), channel EtOH (magenta).*

Between the Ce_2 dimers in **11**, two EtOH molecules are coordinated, oriented into a channel down the b-axis, creating channel 3 with potential porosity following solvent romoval in **11**. However on forming the two carboxylate bridges between dimers, this third channel is closed and the overall structural now has the potential to have 1D porosity down the a-axis (guest EtOH still present, so not yet characterised as porous). This shift in structure is needed to accomodate the formation of the carboxylate bridges and causes the protonated monodentate carboxylate that in **11** is bound to the lanthanide *via* the lone pair on O17, to detach from the metal leaving it free within the channels (*Figure 18, 19, 20*).

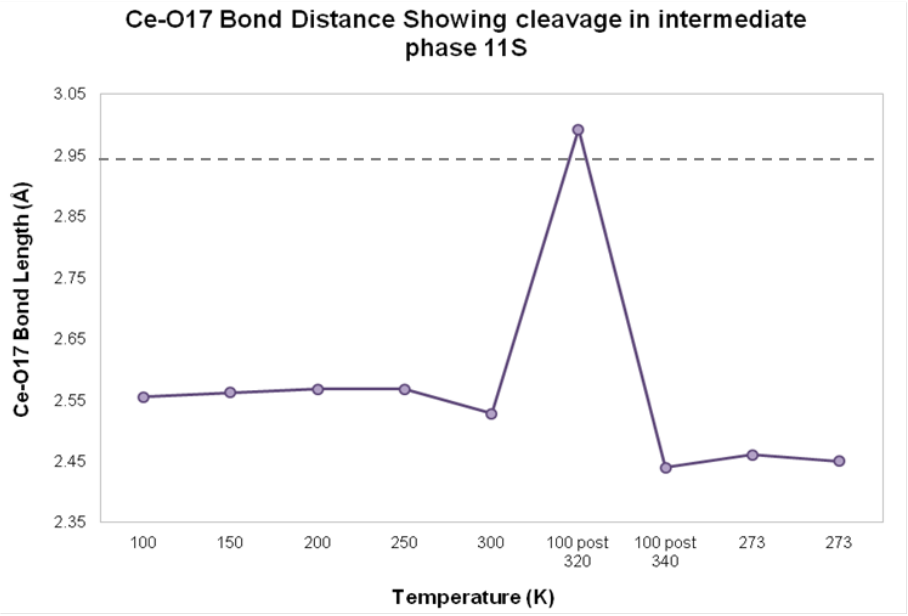

Figure 20: *Ce-O17 bond distance over the single crystal variable temperature experiment. O17 becomes detached from Ce at 320 K, at which point phase **11S** is present. Ce-O bond distance limit based on the van der Waals radii of each element of 2.95 Å shown as grey dashed line.*

Study of the Ce-O17 bond distance throughout this variable temperature experiment shows that the bond breaks between **11** and **11S** (*Figure 20*). The Ce-O bonding distance limit is 2.95 Å (based on the Van der Waals radii of the elements): In **11S**, the Ce-O17 distance is 2.997 Å which is outside of the Ce-O bonding region, showing that within **11** there is a free carboxylic acid within the channels. Removal of H_2O and one monodentate ligand, and formation of a new Ce-O bond leaves Ce with a coordination number of 7.

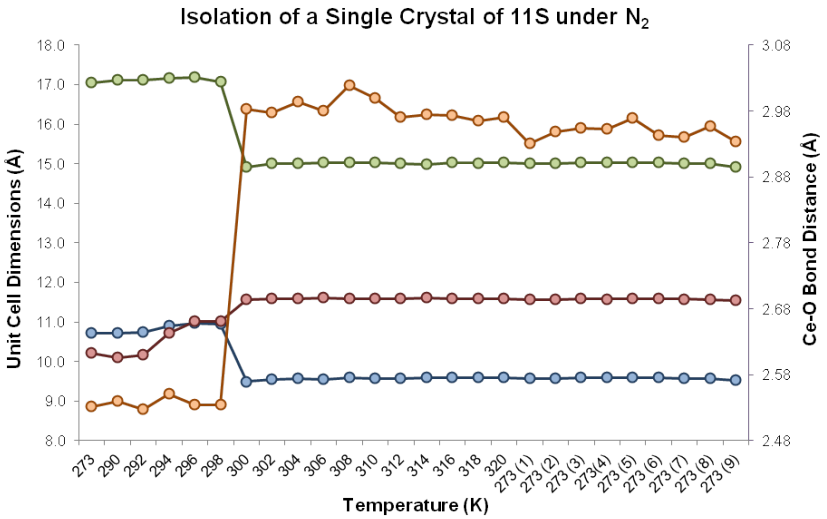

Figure 21: *Graph to show isolation of phase **11S** under N_2. Unit cell dimensions demonstrate change in structure from **11 - 11S**, at which point O17 becomes detached from Ce and remains free through 9 consecutive data collections at 273 K under the N_2 stream. (Primary axis (left); a-axis (blue), b-axis (red), c-axis (green); secondary axis (right): Ce-O17 bond distance (orange).*

11S can be isolated at room temperature under N_2, shown in a separate experiment in which a single crystal of **11** was heated until the expected unit cell transition had occurred and then cooled to 273 K and held at that temperature for 9 consecutive 3 hour data collections (*Figure 21*). Study of the Ce-O17 bond length during this experiment shows that the bond cleaves and remains unbound from the metal. Removal of the crystal from the cryostream at this stage in a separate experiment and subsequent standing in air for 6 days shows that **11S** is also stable in air.

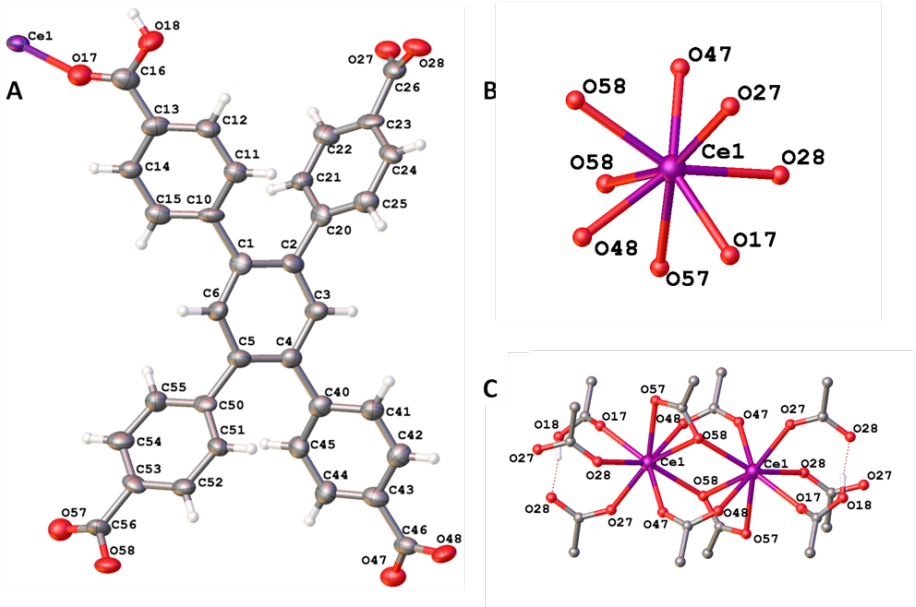

Figure 22: *Single Crystal Structure of **11D**. A: Asymmetric unit; B: Ce coordination; C: Ce dimer with carboxylate and solvent coordination shown. Ce (purple), O (red) C (grey), H (white).*

11S was then further heated until the next unit cell shift which occurs at 340 K. This transition corresponds to the full desolvation of the materials in which the coordinated EtOH is removed, yielding the desolvated structure, **11D**, in which Ce has a coordination number of 8 (*Figure 24*). As coordinated EtOH leaves the framework, the unbound protonated carboxylate of ring 1 re-joins Ce at O17, retaining a coordination number of 7, however O58 forms a μ_2-O bond to both Ce within the Ce_2 dimer, bringing the coordination number up to 8 (*Figure 22C*). The 3D structure only alters slightly upon full desolvation from **11S** which can be seen in the similar unit cell parameters (*Table 1*); the main difference can be seen in the unit cell angles, whereas unit cell parameters a, b and c remain very similar.

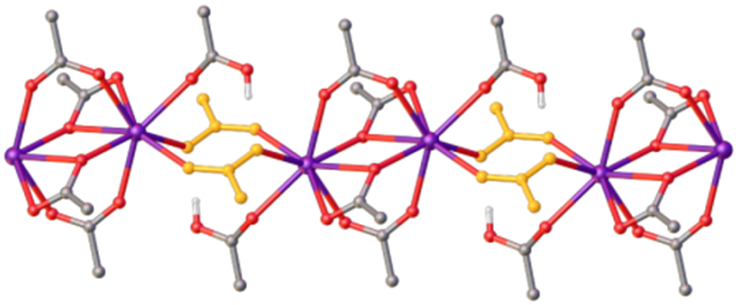

Figure 23: *Coordination environment of Ce in **11D**. Monodentate non-protonated carboxylate on ring 2 that formed a bridge in the first stage of the desolvation process (**11-11S**) between the Ce_2 dimers shown in orange.*

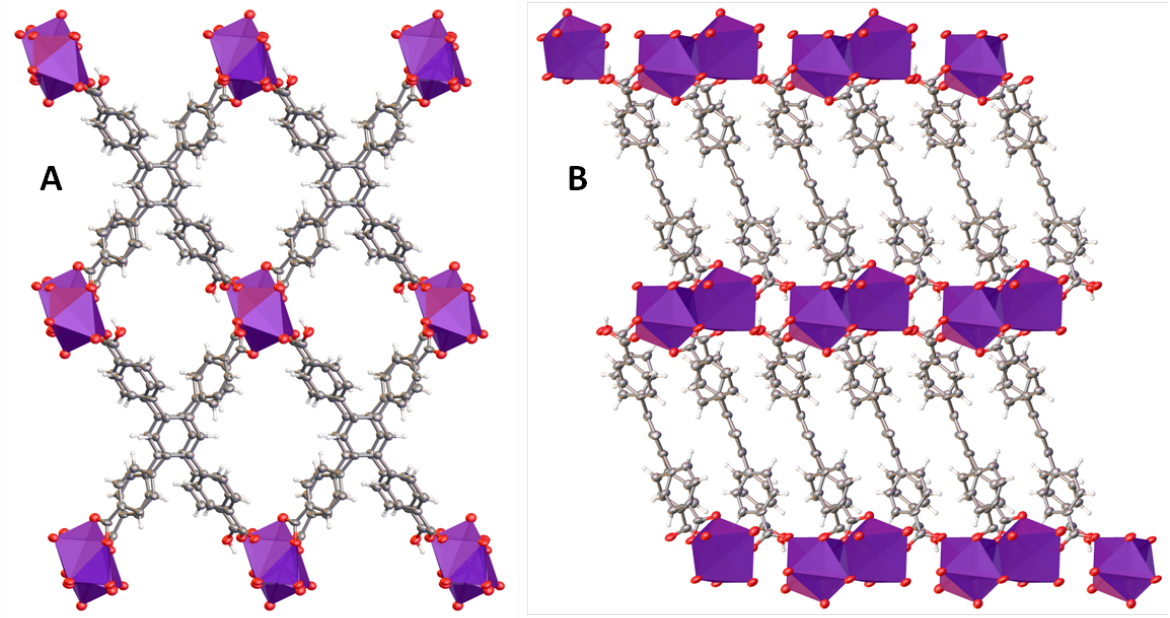

Figure 24: *View down A: 100 and B: 010 desolvated **11D**. Ce (purple), oxygen (red), carbon (grey), hydrogen (white). Channel 1 surface shown in magenta and channel 2 surface shown in blue.*

Phase **11D** is a 3D framework with 1D porosity down the a-axis. All channel and coordinated solvent H_2O and EtOH has been completely removed from the framework leaving the fully desolvated, open **11D**. The framework can be penetrated by a spherical probe radius of 2.1 Å, 0.6 Å and 0.3 Å down the *a*, *b* and *c*-axes respectively, with the largest spherical void being 4.6 Å in diameter with a packing index of 56.17 %, meaning the structure occupies 56.17 % of the unit cell volume, the rest being void space. **11D** has two distinct channels present. The larger channel 1 lies between the 2-/4- and 5-/1- positions of the central aromatic ring of the HTCPB ligand. The carboxyphenyl groups line the channels, forming a rectangular shape void. The inversion centre is at the centre of the channel, meaning both channels are symmetrical. Channel 2 is the smaller of the two channels and is square in shape. It lies between the 1-/2- and 4-/5- positions of the central aromatic ring of the HTCPB ligand, with the pendent carboxyphenyl groups leading to Ce lining the channels. The inversion centre again is in the middle of the channel and within channel 2, the protonated O17-C16-O18(-H) carboxylate unit is present.

The total solvent accessible volume of **11D** is 405 $Å^3$, corresponding to 24.9 % of the total volume of the unit cell calculated using Olex2. This can be broken down into the two channels: Channel 2 is responsible for 11.4 % of this void space with a volume of 186.2 $Å^3$ per unit cell. Channel 1 accounts for the remaining 13.5 % of the void space, with a volume of 218.8 $Å^3$.

Whereas **11** and **11S** are stable in air and N_2, **11D** is only stable when kept under N_2. Exposure to air causes a fourth and final phase transition to a rearranged phase, **11R**.

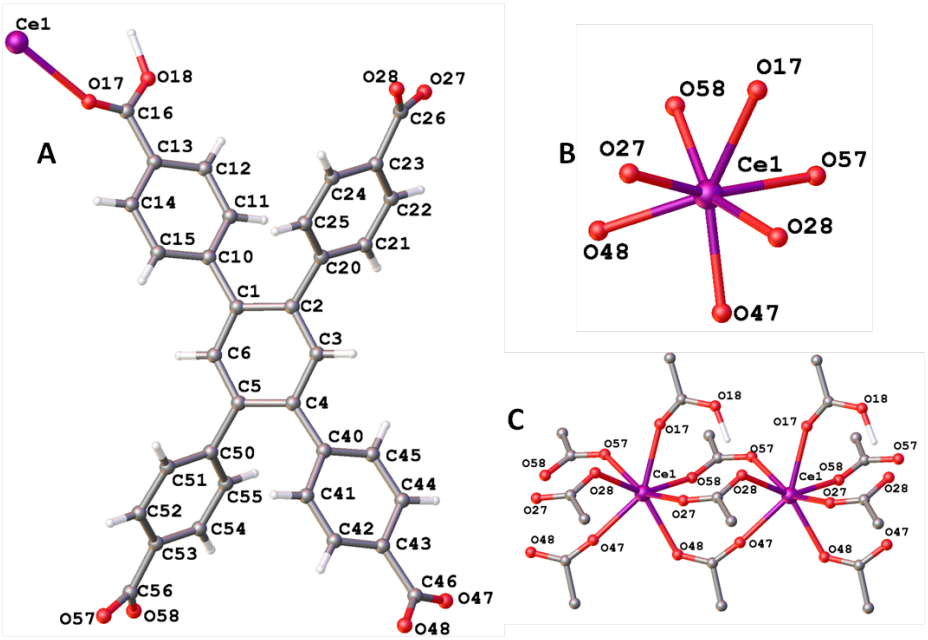

Figure 25: *Single Crystal Structure of **11R**. A: Asymmetric unit; B: Ce coordination; C: Ce dimer with carboxylate and solvent coordination shown. Ce (purple), O (red) C (grey), H (white). No H_2O can be seen coordinated to Ce in this structure as it was only exposed to the air for 10 minutes.*

When crystals of **11D** were removed from the cryostream and allowed to stand in air for as little as 10 minutes, a data collection at 100 K showed that the material had transformed into a new 'rearranged/rehydrated' structure (**11R**) with the uptake of atmospheric H_2O, identified firstly by a shift in unit cell parameter (*Table 1*) followed by structure determination. Coordination of H_2O to Ce causes an increase in coordination number from 7 to 8, and causes the structure to shift to accommodate this (*Figure 27*). After the short time of only 10 minutes in air, H_2O cannot be seen coordinated to the Ce centres of within the channels. The change in structure is the only indication that material **11D** has been exposed to moisture.

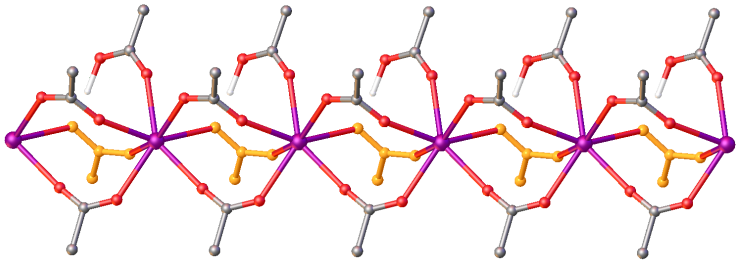

Figure 26: *Coordination environment of Ce in **11R**. Monodentate non-protonated carboxylate on ring 2 which formed a bridge between the Ce_2 dimers present in the first step of desolvation shown in orange.*

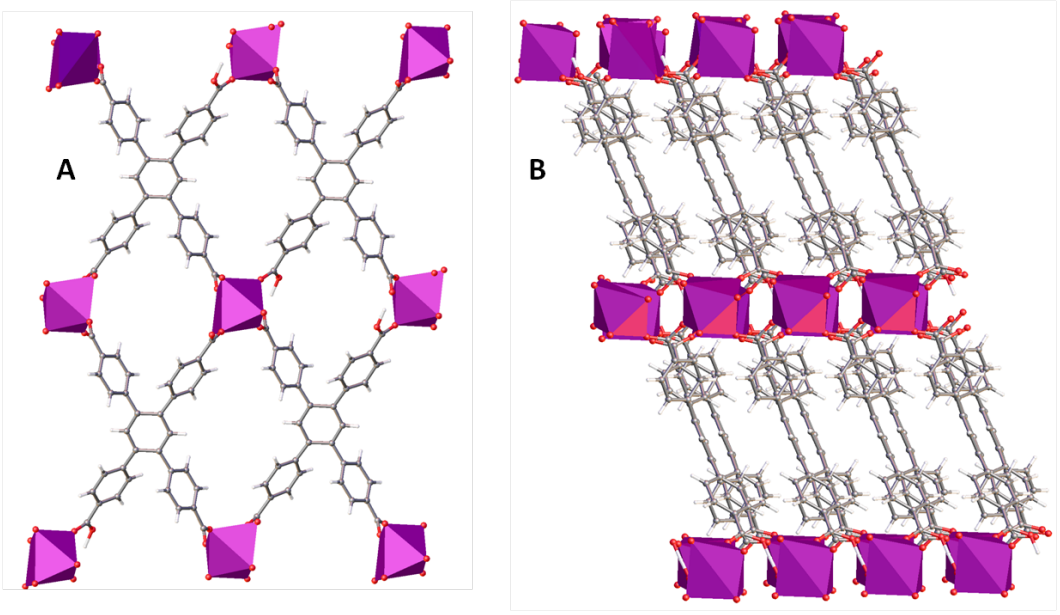

Figure 27: *View down A: 100 and B: 011 rearranged **11R** after exposure of **11D** to air for 5 minutes. Ce (purple), oxygen (red), carbon (grey), hydrogen (white).*

Phase **11R** remains a 3D framework with channels down the a-axis. With the coordination of H_2O, the Ce coordination number increases from 7 to 8. This causes the ligand to shift in order to

accommodate the increase in coordination and the structure overall shows enhanced π-π stacking, and a more uniform coordination between lanthanide ions (*Figure 27*).

It is possible that difference between **11D** and **11R** involves the movenent of a proton between the carboxylate group on rings 1 and 2 in **11D**. As the numbering scheme for this structure used the protonated ring carboxylate as ring 1, this movement would in turn, change the ring numbering scheme of **11R**: If ring 2 becomes protonated instead of ring 1, this means ring 2 becomes ring 1, ring 1 becomes ring 2, ring 4 becomes ring 5 and ring 5 becomes ring 4. Therefore the observed carboxylate coordination and bridging between Ce centres changes as shown in Figure 28. However, Ce in both **11D** and **11R** still has monodentate coordination from its 'ring 1' and (Ce)-O-C-O-(Ce) carboxylate bridging from rings 2 and 4, but whereas in **11D** ring 5 forms a μ_2-O bidentate bridge between Ce centres (*Figure 28C*), in **11R**, the shift in stucture means the distance between two Ce centres has become longer, so the carboxylate on ring 5 forms a third (Ce)-O-C-O-(Ce) bridge (*Figure 28F*).

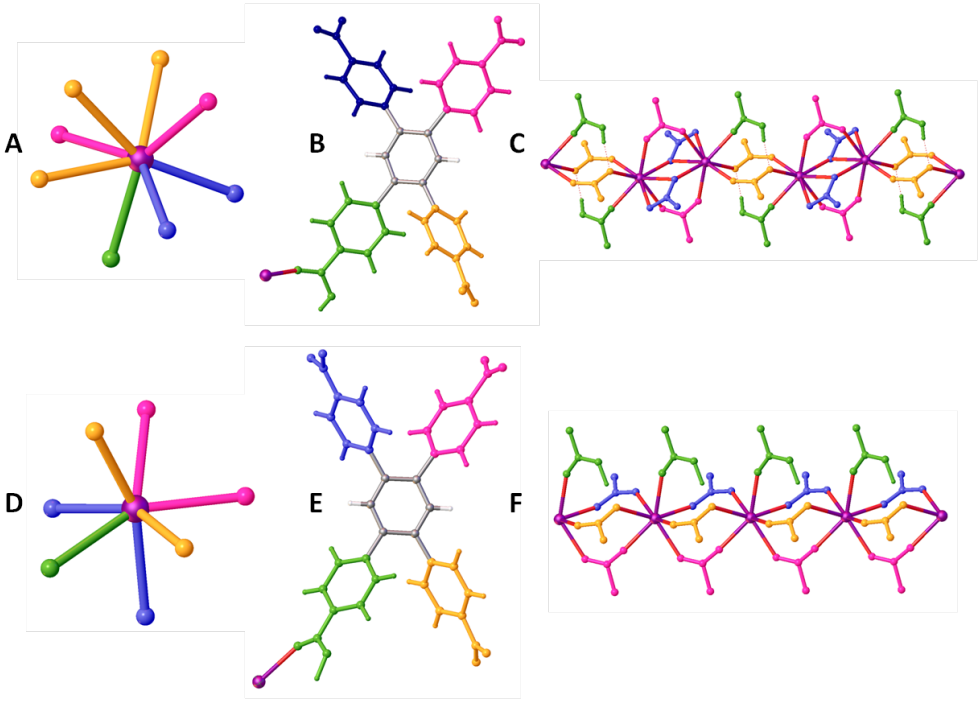

Figure 28: *Difference in structure of **11D** compared to **11R**. Coordination environment of Ce with O coloured as the ring to which it is bonded for A: **11D** and D: **11R**; Ring numbering for B: **11D** and E: **11R** – ring 1 (green), ring 2(orange), ring 3 (magenta), ring 4 (blue); Ce-carboxylate bridges and in chains with carboxylate colouring as in B and E for C: **11D** and F: **11R**.*

The overall 3D structure changes to enhance π-π stacking between the aromatic rings of the HTCPB ligand, which changes the unit cell parameters.

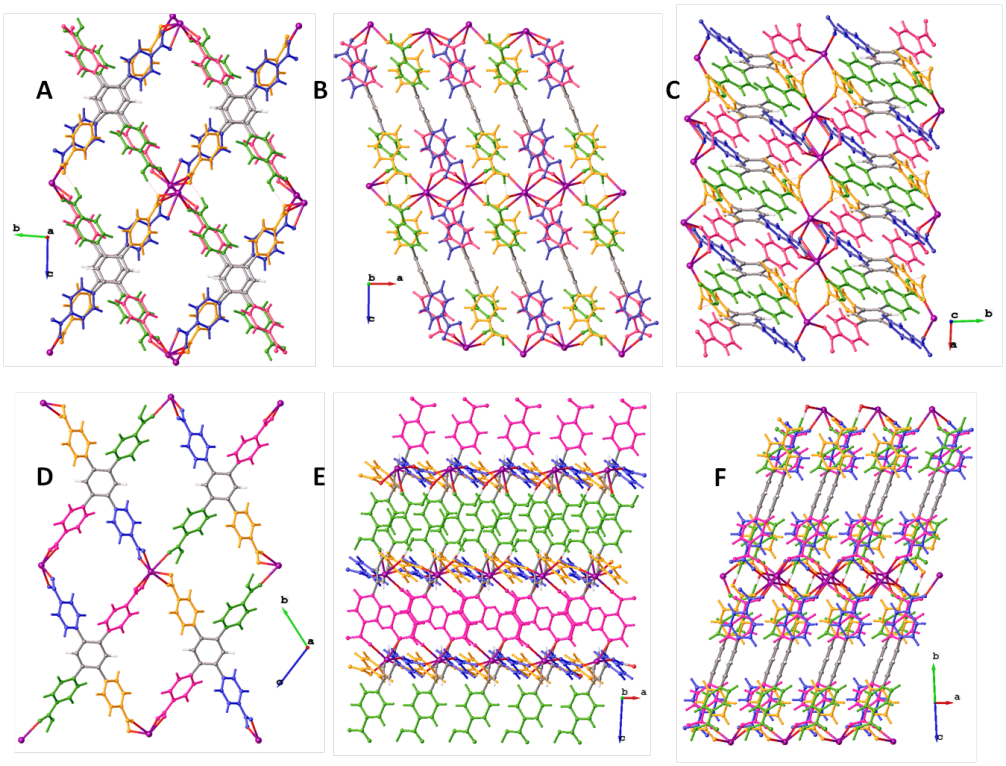

Figure 29: *Difference in structure between **11D** and **11R**. A: View down 100 of **11D**; B: View down 010 of **11D**; C: view down 001 of **11D**; D: View down 100 of **11R**; E: View down 010 of **11R**; F: View down 011 of **11R**.*

4.3.3.2 Variable Temperature PXRD Analysis of Bulk Ce(HTCPB) (11)

Analysis of the bulk material was needed to confirm that the structural transisions seen in the single crystal variable temperature study were true of the whole sample.

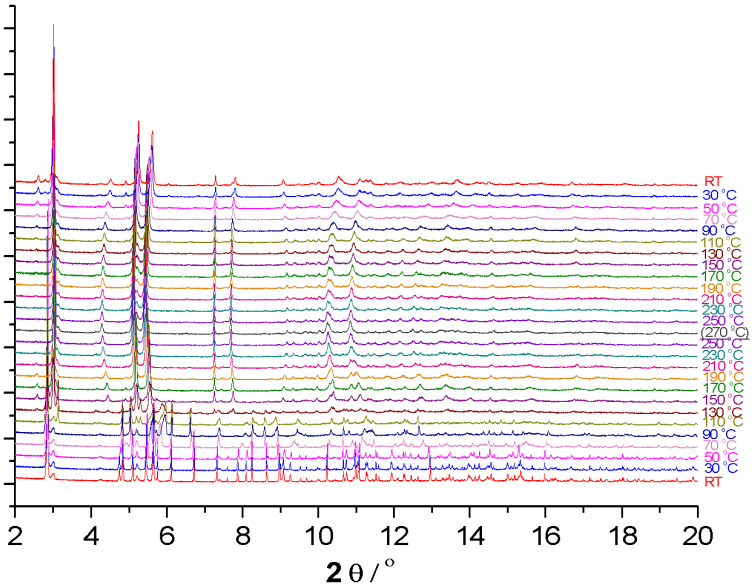

Figure 30: *Variable temperature PXRD experiment showing transition of **11** to **11R** via **11S**. (**11D** not seen due to all 'removed' solvent remaining within the sealed capillary, therefore changing **11D** immediately into **11R**).*

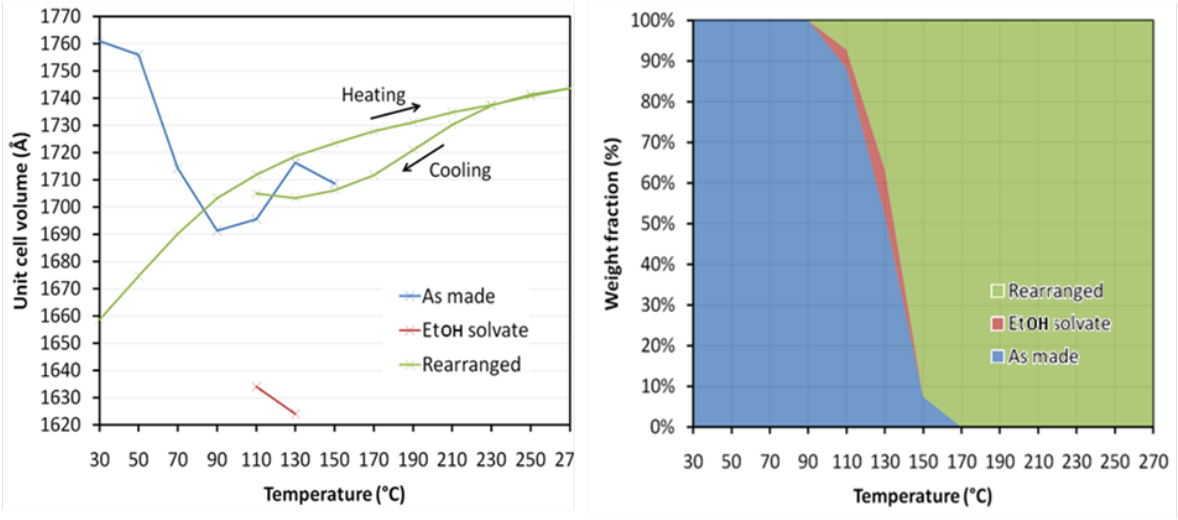

Figure 31: *Graphical Representation of the phases present during the variable temperature PXRD experiment on **11**. As made **11** (blue) EtOH solvate **11S** (red) and rearranged **11R** (green)*[30].

A variable temperature PXRD study was carried out on a sealed capillary of **11** by heating at 20 °C temperature intervals between room temperature and 270 °C and then back down to room temperature (*Figure 30*). Rietveld analysis[30] of the PXRD profile at each temperature shows that bulk **11** is present at room temperature and is so until the desolvation process starts to occur at 70 °C. It then proceeds to **11R** via **11S.** However the desolvated phase, **11D**, is not seen in this experiment *(Figure 31)*. This is due to the fact that the experiment is carried out in a sealed capillary meaning that the coordinated and guest solvent which is removed from the framework is still present in the area surrounding the material. As **11** is heated to the temperature at which **11D** would be present if in an inert atmosphere, the H_2O present within the sealed environment will immediately coordinate to Ce, hence the structure observed moves straight from **11S** to **11R**. This phase is stable up to 270 °C and subsequent cooling shows no change, so the material exists as **11R** back down to room temperature, showing that the structural change is irreversible as was seen in the single crystal experiments.

4.3.4 Isolation of Bulk Phases 11, 11S, 11D and 11R

Of the four phases seen in the single crystal VT experiment (**11**, **11S**, **11D** and **11R**), an investigation was carried out to determine whether the same phases could be isolated in the bulk sample. As previously mentioned, a single crystal of **11** is stable at room temperature in air once removed from the mothor liquor for 7 days. The same can be said for the bulk crystalline sample of **11** as shown by PXRD.

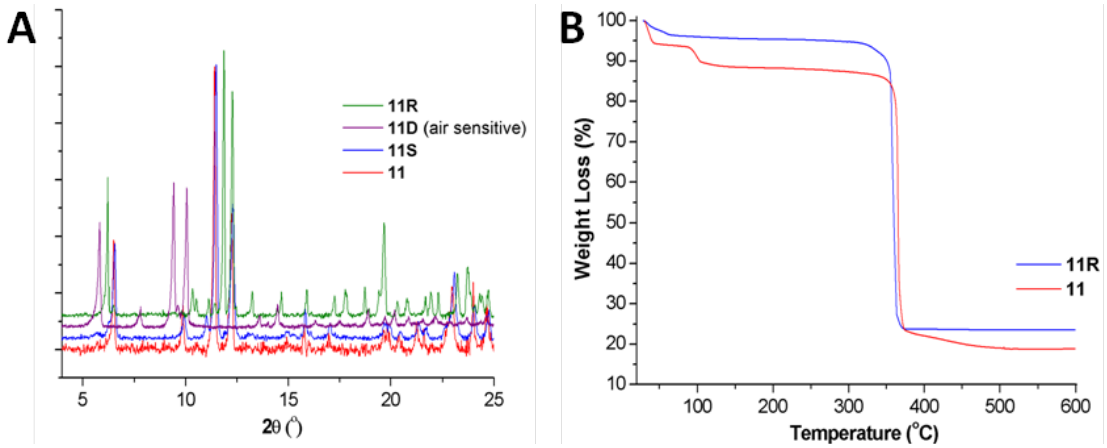

Figure 32: *A: PXRD profiles of isolated phases **11** (red), **11S** (blue) and **11R** (green, run in reflection geometry using Cu Kα radiation in air at room temperature; B: TGA profiles of **11** and **11R**.*

The single crystal of **11S** was also found to be stable in air following removal of from the cryostream and leaving in air for 7 days. In order to isolate bulk **11S**, an experiment was set up to mimic the cryostream, holding the sample under a flow of nitrogen at a set temperature so as not to fully desolvate the material: A sample of **11** was placed in an open vial in a Dreschel bottle and was then heated to 65 °C under a flow of N_2 for 12 hours. After this time the vial was removed, exposed to the air, and inspected under a microscope, which showed that the material was still crystalline. PXRD analysis showed that **11** had been converted to **11S** (*Figure 32A*). Phase **11D** was found not to be stable in air, as following removal of the single crystal from the cryostream, conversion to phase **11R** was seen. The same thing occurs in the bulk phase. Desolvation of **11** was carried out by heating to 100 °C at 10^{-2} mbar for 12 hours. Removal of the sample following desolvation and subsequent exposure to air showed the material was still crystalline, however PXRD analysis showed complete conversion to phase **11R** had occured (*Figure 32A*). However bulk **11D** can be isolated under N_2, by activating **11** at 100 °C at 10^{-5} mbar for 12 hours and then being kept under N_2. This is confirmed by PXRD and CH analysis (*Table 2*).

Table 2: CH microanalysis and TGA data for **11**, **11D** and **11R**:

Formula	Theory (%)	Found (%)	Solvent content from CHN (%)	Solvent content from TGA (%)
$Ce(HTCPB)(EtOH)(H_2O).(H_2O)_{2.75}(EtOH)_{0.28}$ **(11)**	**C:** 54.76 **H:** 3.37	**C:** 54.76 **H:** 3.48	9.80	11.00
Ce(HTCPB) **(11D)**	**C:** 58.70 **H:** 2.75	**C:** 58.20 **H:** 2.66	-	-
$Ce(HTCPB).(H_2O)_{1.8}$ **(11R)**	**C:** 56.17 **H:** 2.99	**C:** 56.15 **H:** 2.86	4.46	4.79

TGA and CH microanalysis of **11R** shows that the H_2O taken up gives a formula of $Ce(HTCPB)(H_2O)_{1.8}$, which gives the material a solvent content of 4.79 % shown from TGA (*Figure 32B*). This value indicates that H_2O is filling around half of the total accessible volume of the structure. This is expected as of the two channels present in **11D**, the larger channel 1 is hydrophopic whereas the smaller channel 2 is more hydrophilic in nature due to the presence of the protonated carboxylate OH group. In the as-made compound **11**, H_2O is only found in channel 2 (EtOH found in channel 1) and hydrogen bonds to the carboxylate OH. The same carboxylate OH is present in **11D** and **11R**, so it would be expected that H_2O would only enter this channel.

4.3.5 Porosity

The porosity of **11** towards N_2, CO_2, CH_4 and H_2O was investigated by collecting full isotherms following activation using conditions of 100°C under 10^{-5} mbar overnight to form **11D**. In all cases an initial weight loss of 10 % was observed with the loss of coordinated and guest EtOH and H_2O, which is comparable with the solvent loss observed in the TGA data.

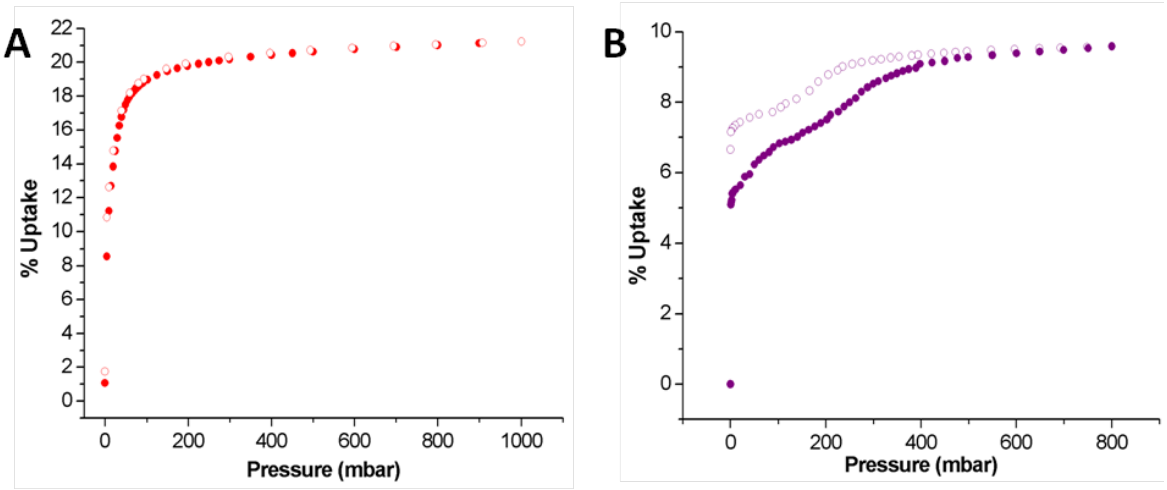

Figure 33: *A: CO_2 isotherm of **11D** collected at 195 K; B: N_2 isotherm of **11D** collected at 77 K. Both samples were activated by heating to 100 °C at 10^{-5} mbar overnight.*

A reversible type I isotherm shows that **11D** is permanently porous to CO_2 at 195 K and 1 bar (*Figure 33A*). Type I isotherms are characteristic of microporous materials[31]. The BET model was applied over the initial pressure ranges of $p/p_0 = 0.02\text{-}0.2$ for **11**, and gave a calculated BET surface area of 378.95 m^2/g. The Dubinin–Radushkevich[32] (DR) pore volumes of 0.198 cm^3/g was calculated from the CO_2 adsorption branch. This is in good agreement with the pore volume of 0.182 cm^3/g calculated from the single crystal structure of **11D**.

A step isotherm shows that **11** is permanently porous to N_2 at 77 K and 1 bar *(Figure 33B)*. The isotherm shows a step in adsorption between 50 and 200 mbar which is also apparent in the desorption curve over the same range, however some hysteresis is seen in the desorption. These factors suggest there may be a phase change with adsorption of N_2, similar to that observed as a result of the pressure induce phase transition of ZIF-8[33]. Salles *et al.* also observed multi-step breathing with Co(BDP) (BDP) 1,4-benzenedipyrazolate), resulting from pressure induced structural changes with N_2 uptake[34]. This step in the N_2 isotherm of **11** could potentially be a shift from **11D** to **11R** with increasing pressure and guest concentration, however this has not been confirmed experimentally.

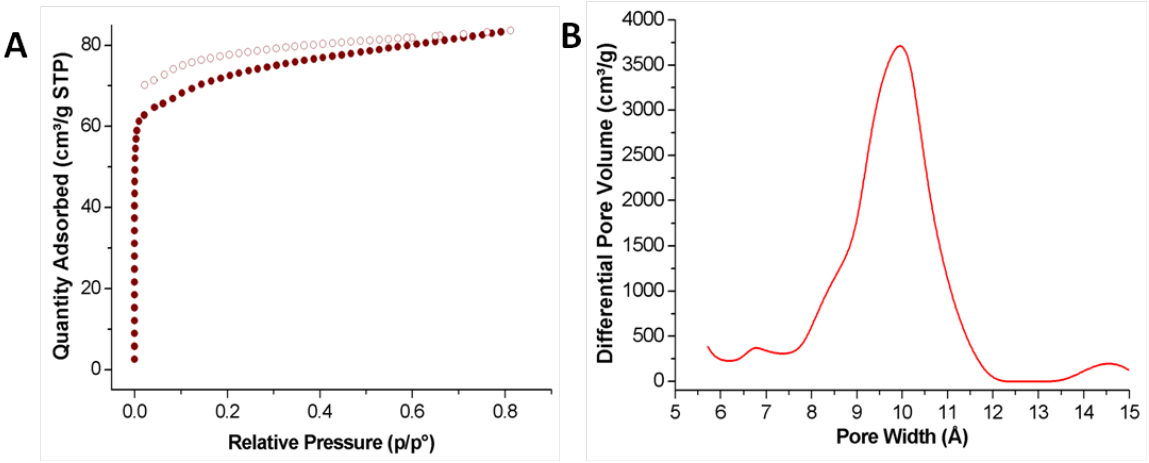

Figure 34: *A: Ar isotherm collected at 77K for determination of the PSD. B: PSD of* ***11D****.*

The pore size distribution (PSD) was determined by means of an Ar isotherm collected at 77K (*Figure 34*). The type I Ar isotherm shows a total uptake of 80 cm^3/g with a slight hysteresis in desorption. The PSD curve shows a maximum pore size of 10 Å. Pore dimensions measured from the single crystal structure of **11D** in which channels 1 and 2 have approximate dimensions of 8.504 x 6.838 Å and 8.113 x 6.575 Å respectively, when measuring across the channel perpendicular to the channel direction. These values are atom centre-atom-centre and not normalised, however if we deduct the van der Waals radii of each atom involved in the atom-atom distance, this gives channel 1 and 2 pore dimensions of 5.104 x 4.658 Å and 4.913 x 4.395 Å respectively (*Figure 35*), which implies that the channels expand upon gas loading during the isotherm.

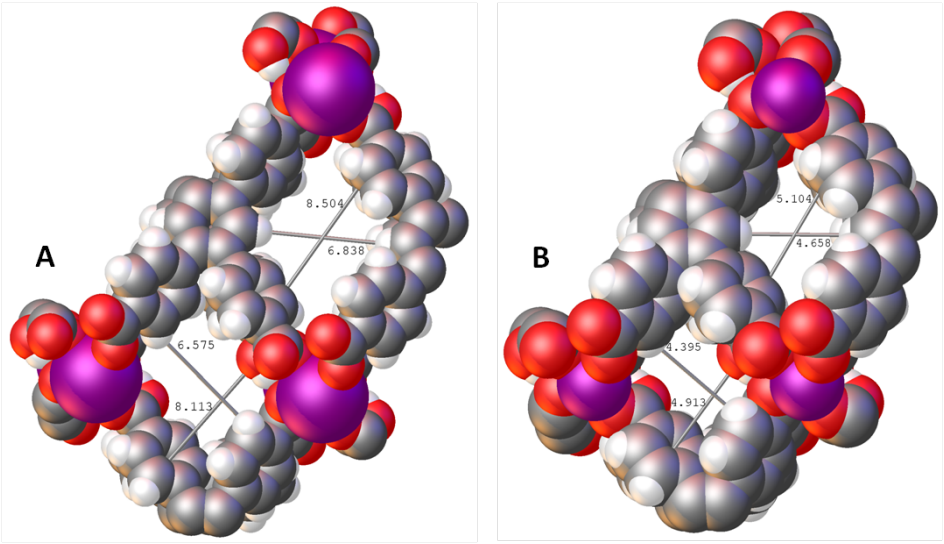

Figure 35: *A: Spacefill view of channel 1 and 2 along 100 in* ***11D****. Pore dimensions measured from atom centre-atom centre, not normalized or corrected to include van der Waals; B: Spacefill including van der Waals view down 100 of* ***11D****. Van der Waals radii deducted from measured distance to give pore dimensions corrected for van der Waals.*

The discrepancy seen in the maximum pore size of 10 Å and the measured pore dimensions from the single crystal structure can be attributed to the dynamic nature of the framework. Pore measurements were calculated from rigid **11D**, however we know the framework is very flexible in nature, given the ability to structurally change from **11-11S-11D-11R.**

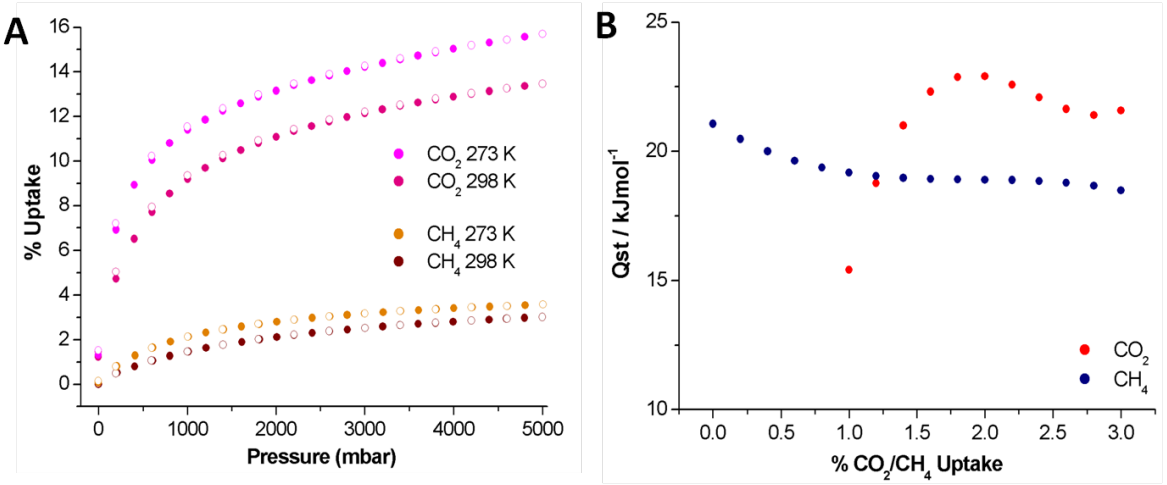

Figure 36: *Isosteric Heat (Q_{st}) Determination of* ***11D****: A: CO_2 isotherms collected at 273 K and 298 K; B: CO_2 Qst; C: CH_4 isotherms of collected at 273 K and 298 K; D: CH_4 Qst.*

CO_2 and CH_4 isotherms were also collected for **11D** at 273 K and 298 K. Isosteric heats of adsorption, Q_{st}, for CO_2 and CH_4 were derived from a virial-type expression fitted to the adsorption branches of the isotherms measured at 273 K and 298 K. The strength of interaction between **11D**

and the CO_2 increases from 18 $kJmol^{-1}$ at zero coverage to 22 $kJmol^{-1}$ at high loading. The interaction between **11D** and CH_4 decreases from 21.5 $kJmol^{-1}$ at zero coverage to 18 $kJmol^{-1}$ at high loading.

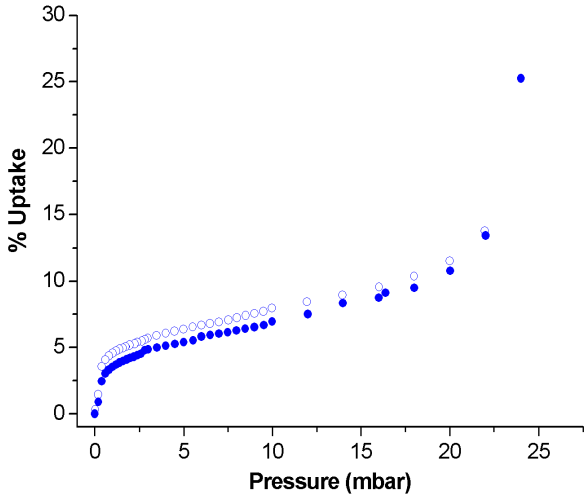

Figure 37: *H_2O isotherm of **11D** collected at 295 K following activation **11** at 100 °C at 10^{-5} mbar overnight.*

A H_2O isotherm was also carried out on **11D** at 295 K. This produced a type I isotherm which showed that is permanently porous to H_2O at 295 K and 25 mbar (*Figure 37*). The % weight uptake of 26 % implies that 18.2 H_2O molecules are being taken up into **11D**. This is in good agreement with the prediction based on the total solvent accessible volume of **11D** (405 $Å^3$), which can theoretically take up 20.2 H_2O molecules.

The framework is structurally stable following all the isotherm measurements, seen from PXRD analysis. The material is still crystalline after gas sorption, and we see 100 % phase **11R** present in the PXRD profile as a result of the samples being activated for isotherm measurement then exposed to air in sample removal from the instrument.

4.3.6 Uptake Experiment of Xe into 11R

To further demonstrate the flexibility of the framework, a gas cell experiment was carried out at the Advanced Light Source (ALS), Berkeley Labs. A single crystal of **11** was glue-mounted onto a mitegen tip and placed under an N_2 flow at 100K. It was converted to **11R** by heating slowly until all guest and coordinated solvent had been removed, then exposed to a flow of air. Full data collections were collected for structure determination. Data collections 1-7 show the conversion from **11-11S** which was determined by both the unit cell dimensions and the single crystal structure (*Figure 38*).

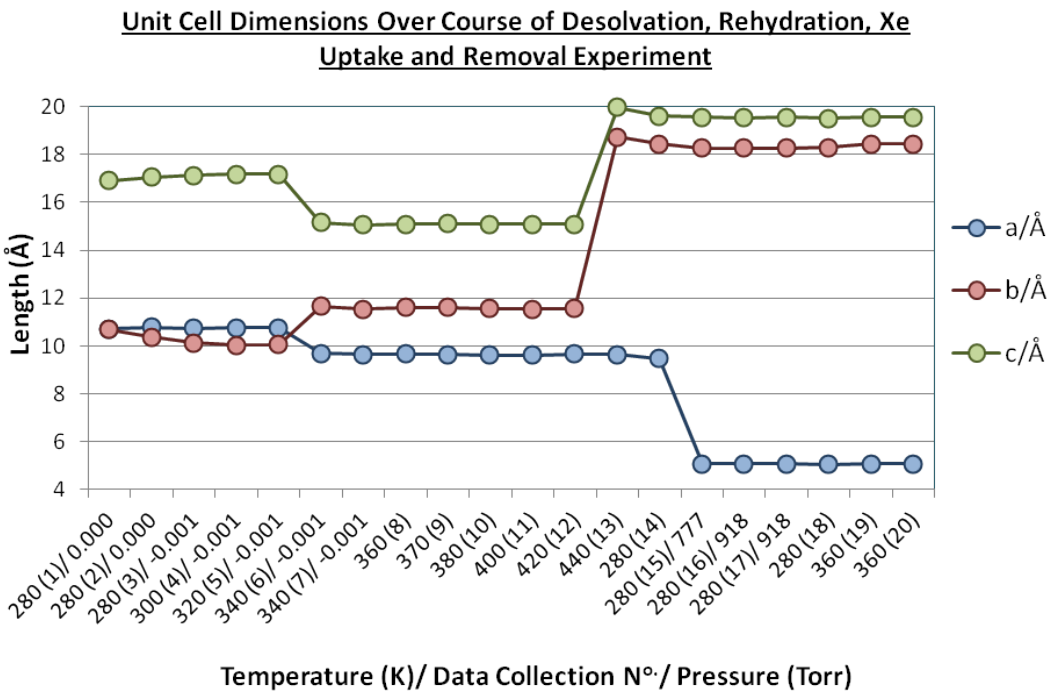

Figure 38: *a, b, c Unit cell dimensions recorded at each step in the desolvation and Xe uptake experiment on **11R**. Xe added to gas cell at data collection 15, which caused a structural change to 11R, and Xe uptake. Vacuum and heating of the crystal between data collections 15-20 caused all the Xe to then leave the framework.*

As made **11**, with unit cell dimensions of around a=10.70, b=10.68, c=16.91, α=83.25, β=76.67 and γ=68.67 is present at the start of the experiment and through heating up to 320 K under vacuum (data collections 1-5). After this point, at 340 K (data collection 6), a shift in unit cell parameters to a=9.69 Å, b=11.67 Å, c=15.15 Å, α=87.00 °, β=87.59 ° and γ=81.11 ° was observed, confirming a change from **11** to **11S**. This phase **11S** was present through heating from 340 K to 420 K (data collections 6-12), after which time a change to a=9.64 Å, b=18.73 Å, c=19.96 Å, α=106.54 °, β=91.39 ° and γ=93.54 ° was observed with the conversion to **11R**. The crystal was exposed to air and Xe, converting the structure to **11R** loaded with Xe gas with unit cell dimensions of a=5.08 Å, b=18.27 Å, c=19.56 Å, α=111.83 °, β=91.06 ° and γ=94.09 °. The unit cell present remained as **11R** for the rest of the experiment (data collections 15-20) with the uptake and subsequent removal of Xe gas and H_2O.

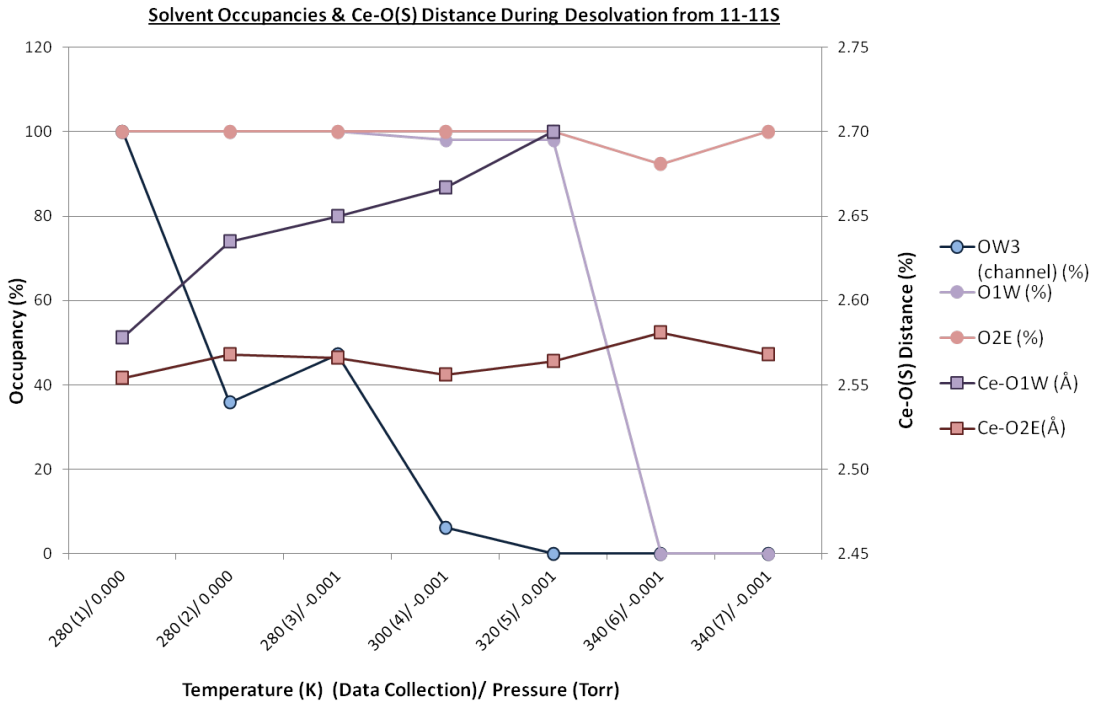

Figure 39: *Ce-OX(S) bond distances and corresponding Ce-OX(S) occupancies and guest OW3 occupancy during initial change from* ***11-11S****.*

The guest (OW3) and coordinated (O1W) H_2O occupancies and their bond distances to Ce1 were recorded during the initial guest removal (data collections 1-7): An extension in the Ce1-O1W bond length was observed between 280 K (1) and 320 K (5) after which time the coordinated H_2O left the framework taking the occupancy from 100 % to 0 %. The guest O3W H_2O make a gradual exit from the framework between 280 K (1) and 320 K (5) leaving only EtOH (O2E) coordinated to Ce1 in **11S** *(Figure 39*).

Following this, the crystal was continually heated under vacuum until the unit cell of **11R** was determined, at which point the crystal was cooled to 280 K (*Figure 38*). The crystal was then put under a positive pressure of Xe and air in the gas cell at data collection 15, converting the framework to **11R** and allowing Xe to enter the channels.

Single crystal structure analysis of data collection 15 showed uptake of 3 Xe molecules per formula unit of **11R** into channel 1 (Xe1), channel 2 (Xe2) and channel 3 (Xe3) (*Figure 40*); with occupancies of 72 %, 54 % and 55 % respectively, with H_2O coordinated to Ce in channel 4 with an occupancy of 100 % (*Figure 41*). Channel assignments shown in Figure 40. The crystal was left under a positive pressure of Xe for 2 further data collections, during which time the occupancies of Xe1, 2 and 3 increased slightly to 76 %, 58 % and 62 % respectively, producing $Ce(HTCPB)(H_2O)\cdot Xe_{1.96}$ (**11RXe**).

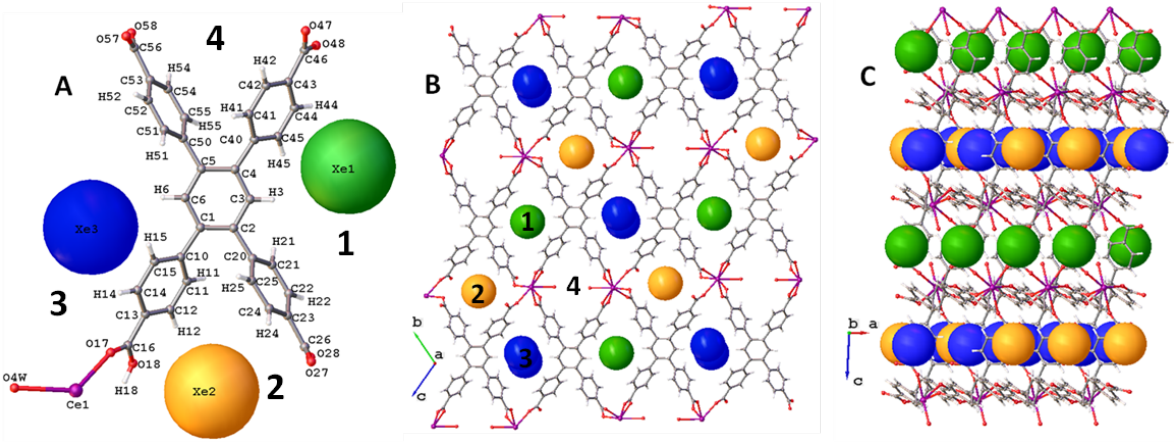

Figure 40: *Single crystal structure of **11RXe**. A: Asymmetric unit with atom and channel 1-4 numbering; B: View down 100;l C: View down 010. Ce (purple), C (grey), O (red), H (white), Xe1 (green), Xe2 (orange) and Xe3 (blue).*

A vacuum (<0.01 torr) was then applied to the Xe loaded single crystal of **11R** in the gas cell which caused a initial decrease in occupancy of Xe1, 2 and 3 and coordinated H_2O to 63 %, 34 %, 56 % and 82 % respectively and subsequent heating to 360 K caused a sharp decrease in occupancies to 7.4 % for Xe1 whilst all other guests had left the framework at data collection 19. By data collection 20, at 360 K and 0 torr, all Xe and H_2O guests had been completely removed from the framework, leaving Ce(HTCPB) (*Figure 41*).

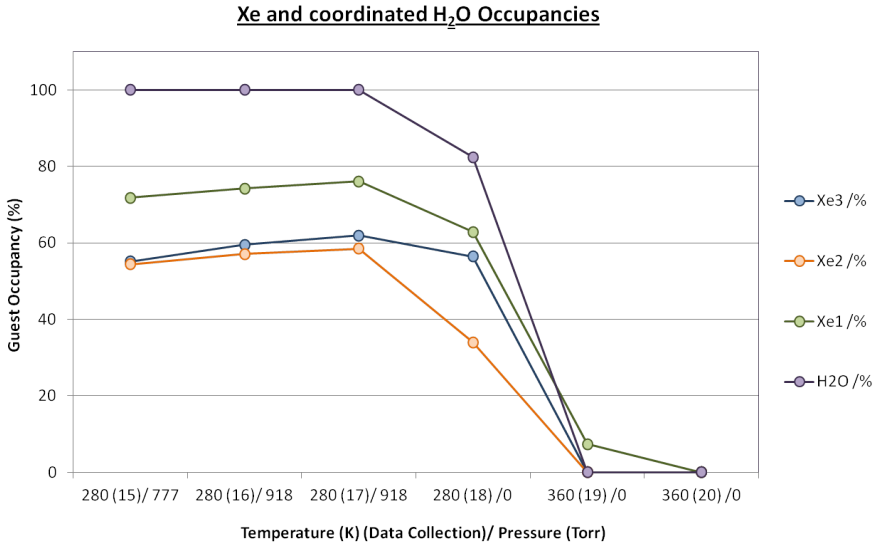

Figure 41: *Guest Xe and coordinated H_2O occupancies following exposure of a single crystal of **11R** to Xe and subsequent heating to remove both guests.*

This experiment clearly shows the stability of single crystals of Ce(HTCPB) across all phases. Over the course of this experiment, the crystal was exposed to vacuum, heating and a positive pressure of Xe gas, and retained its diffraction resolution throughout.

4.4 Conclusions

Combination of H_4TCPB and Ce(III) results in the formation of a phase pure neutral 3D framework with the formula Ce(HTCPB)(EtOH)(H_2O).(EtOH)$_x$.(H_2O)$_y$ (**11**) with potential 2D porosity with removal of solvent from the single crystal structure. **11** is porous to CO_2, N_2, CH_4 following activation at 100 °C and 10 $^{-5}$ mbar overnight. Single crystals of **11** are stable in air and on standing in H_2O for 7 days, and a reversible H_2O isotherm shows that the material is porous to H_2O.

A single crystal variable temperature experiment was used to investigate the desolvation process of **11**. The desolvated structure **11D** was accessed *via* an air stable intermediate **11S** in which coordinated and channel H_2O have left the framework but coordinated and channel EtOH remain, resulting in the formation of a Ce-carboxylate bridged chain running down the a-axis. Further heating of **11S** in which coordinated and channel EtOH leave the framework leads to desolvated **11D**. Phase **11D** is converts to **11R** with exposure to the air in as little as 5 minutes with the reversible coordination to Ce. After 24 hours in air, H_2O can be refined in the single crystal structure at the Ce centre within channel 2, implying that H_2O coordination is responsible for the change in Ce geometry and overall 3D structure of **11R** from **11D**, however the small amount of H_2O present after only 5 minutes cannot be resolved.

A variable temperature PXRD study shows the same structural transitions occurring in the bulk crystalline material, however **11D** is never seen, as the experiment was carried out in a sealed capillary so all solvent lost was trapped meaning the material went straight from **11S** to **11R**.

Phases **11**, **11S** and **11R** are stable on standing in air whereas **11D** can only be isolated under N_2, and can all be isolated in both the single crystal and bulk crystalline phases. The transformation from **11D** to **11R** is fully reversible, with exposure of **11D** to air giving rise to **11R** and reactivation (at 100°C and 10^{-5} mbar) taking **11R** back to **11D**.

The Xe uptake study on a single crystal of **11** demonstrates the structural stability and flexibility of the framework. The SCSC transformations from **11-11S-11R-11Xe-11R** could all be observed in the single crystal phase, after which time the crystal was still diffracting with good intensity and resolution.

This investigation highlights the structural stability and flexibility of **11**. The flexible coordination geometry of the lanthanide Ce(III) centre has allowed variable coordination geometries to be accessed with the breaking and forming of bonds, whilst retaining diffraction resolution in the single crystal phase. If another metal with restricted coordination geometry such as Zn had been used in this study, the same detailed insight into the desolvation process using SCXRD may not have been possible.

4.5 References

[1] X. J. Zhao, T. Ben, M. Xue, G. S. Zhu, Q. R. Fang, S. L. Qiu, *J. Mol. Struct.* **2009**, *931*, 25-30.

[2] J. Zhao, L. S. Long, R. B. Huang, L. S. Zheng, *Dalton Trans.* **2008**, 4714-4716.

[3] R. J. Hill, D. L. Long, P. Hubberstey, M. Schroder, N. R. Champness, *J. Solid State Chem.* **2005**, *178*, 2414-2419.

[4] D. B. Dang, Y. Bai, C. He, J. Wang, C. Y. Duan, J. Y. Niu, *Inorg. Chem.* **2010**, *49*, 1280-1282.

[5] L. Q. Ma, C. Abney, W. B. Lin, *Chem. Soc. Rev.* **2009**, *38*, 1248-1256.

[6] B. L. Chen, Y. Yang, F. Zapata, G. N. Lin, G. D. Qian, E. B. Lobkovsky, *Adv. Mater.* **2007**, *19*, 1693.

[7] S. Q. Ma, D. Q. Yuan, X. S. Wang, H. C. Zhou, *Inorg. Chem.* **2009**, *48*, 2072-2077.

[8] Y. He, S. Xiang, Z. Zhang, S. Xiong, F. R. Fronczek, R. Krishna, M. O'Keeffee, B. Chen, *Chem. Commun. (Cambridge)* **2012**, *Advance Article*.

[9] H. Y. He, D. Q. Yuan, H. Q. Ma, D. F. Sun, G. Q. Zhang, H. C. Zhou, *Inorg. Chem.* **2010**, *49*, 7605-7607.

[10] K. A. White, D. A. Chengelis, K. A. Gogick, J. Stehman, N. L. Rosi, S. Petoud, *J. Am. Chem. Soc.* **2009**, *131*, 18069.

[11] H. Zhou, G. W. Diao, S. Y. Qian, X. Z. Yang, A. H. Yuan, Y. Song, Y. Z. Li, *Dalton Trans.* **2012**, *41*, 10690-10697.

[12] T. Devic, V. Wagner, N. Guillou, A. Vimont, M. Haouas, M. Pascolini, C. Serre, J. Marrot, M. Daturi, F. Taulelle, G. Ferey, *Micropor. Mesopor. Mat.* **2011**, *140*, 25-33.

[13] T. Devic, C. Serre, N. Audebrand, J. Marrot, G. Ferey, *J. Am. Chem. Soc.* **2005**, *127*, 12788-12789.

[14] R. A. Zehnder, R. A. Renn, E. Pippin, M. Zeller, K. A. Wheeler, J. A. Carr, N. Fontaine, N. C. McMullen, *J. Mol. Struct.* **2011**, *985*, 109-119.

[15] D. Saha, S. G. Deng, *J. Phys. Chem. Lett.* **2010**, *1*, 73-78.

[16] A. G. Wong-Foy, A. J. Matzger, O. M. Yaghi, *J. Am. Chem. Soc.* **2006**, *128*, 3494-3495.

[17] T. Loiseau, C. Serre, C. Huguenard, G. Fink, F. Taulelle, M. Henry, T. Bataille, G. Ferey, *Chem.-Eur. J.* **2004**, *10*, 1373-1382.

[18] O. V. Zenkina, E. C. Keske, R. Y. Wang, C. M. Crudden, *Angew. Chem. Int. Ed.* **2011**, *50*, 8100-8104.

[19] Y. Inokuma, M. Kawano, M. Fujita, *Nat. Chem.* **2011**, *3*, 349-358.

[20] J. Liu, X. P. Zhang, T. Wu, B. B. Ma, T. W. Wang, C. H. Li, Y. Z. Li, X. Z. You, *Inorg. Chem.* **2012**, *51*, 8649-8651.

[21] Y. C. He, J. Yang, G. C. Yang, W. Q. Kan, J. F. Ma, *Chem. Commun.* **2012**, *48*, 7859-7861.

[22] O. K. Farha, K. L. Mulfort, J. T. Hupp, *Inorg. Chem.* **2008**, *47*, 10223-10225.

[23] C. Y. Lee, Y. S. Bae, N. C. Jeong, O. K. Farha, A. A. Sarjeant, C. L. Stern, P. Nickias, R. Q. Snurr, J. T. Hupp, S. T. Nguyen, *J. Am. Chem. Soc.* **2011**, *133*, 5228-5231.

[24] Y. S. Bae, O. K. Farha, J. T. Hupp, R. Q. Snurr, *J. Mater. Chem.* **2009**, *19*, 2131-2134.

[25] O. K. Farha, C. D. Malliakas, M. G. Kanatzidis, J. T. Hupp, *J. Am. Chem. Soc.* **2010**, *132*, 950.

[26] T. Gadzikwa, O. K. Farha, C. D. Malliakas, M. G. Kanatzidis, J. T. Hupp, S. T. Nguyen, *J. Am. Chem. Soc.* **2009**, *131*, 13613.

[27] K. L. Mulfort, O. K. Farha, C. L. Stern, A. A. Sarjeant, J. T. Hupp, *J. Am. Chem. Soc.* **2009**, *131*, 3866.

[28] O. V. Dolomanov, L. J. Bourhis, R. J. Gildea, J. A. K. Howard, H. Puschmann, *J. Appl. Crystallogr.* **2009**, *42*, 339-341.

[29] L. J. Bourhis, O. V. Dolomanov, R. J. Gildea, J. A. K. Howard, H. Puschmann, *olex2.solve* **2011**.

[30] *Analysis carried out by Dr. Phil Chater at the University of Liverpool.*

[31] Jean Rouquerol, Françoise Rouquerol, K. S. W. Sing, *Adsorption by Powders and Porous Solids: Principles*, Academic Press, London, **1999**.

[32] Y. K. Tovbin, *Russ. Chem. Bull.* **1998**, *47*, 637-643.

[33] D. Fairen-Jimenez, S. A. Moggach, M. T. Wharmby, P. A. Wright, S. Parsons, T. Duren, *J. Am. Chem. Soc.* **2011**, *133*, 8900-8902.

[34] F. Salles, G. Maurin, C. Serre, P. L. Llewellyn, C. Knofel, H. J. Choi, Y. Filinchuk, L. Oliviero, A. Vimont, J. R. Long, G. Ferey, *J. Am. Chem. Soc.* **2010**, *132*, 13782-13788.

4.6 Additional Information

Table 3: CIF tables for compounds **11**, **11S**, **11D** and **11R**:

Identification code	fs_100KT	snt100K_4V_final	snt100K-3	snt273k-2
Sample Code	**11**	**11S**	**11D**	**11R**
Empirical formula	$C_{37.5}H_{34.75}CeO_{12.5}$	$C_{36.88}H_{27.65}CeO_{9.44}$	$C_{34}H_{19}CeO_8$	$C_{34}H_{19}CeO_8$
Formula weight	825.52	762	695.61	695.61
Temperature/K	100	373.15	100	273.15
Crystal system	Triclinic	Triclinic	Triclinic	triclinic
Space group	P-1	P-1	P-1	P-1
a/Å	10.57830(10)	9.5629(7)	9.2989(11)	5.0714(9)
b/Å	10.42710(10)	11.5520(8)	11.4163(13)	18.452(3)
c/Å	16.9210(11)	15.0214(10)	15.2492(17)	19.543(4)
α/°	83.158(6)	87.067(2)	93.756(5)	109.850(9)
β/°	76.314(5)	86.910(2)	90.263(6)	90.950(10)
γ/°	70.023(5)	81.372(3)	93.814(6)	94.481(9)
Volume/Å^3	1702.80(11)	1636.7(2)	1611.7(3)	1713.1(5)
Z	2	2	2	2
ρcalcmg/mm^3	1.61	1.546	1.433	1.349
m/mm^{-1}	1.405	1.448	1.46	1.373
F(000)	836	765	690	690
Crystal size/mm^3	0.055 × 0.055 × 0.044	0.167 × 0.095 × 0.05	0.055 × 0.055 × 0.045	0.055 × 0.055 × 0.044
2Θ range for data collection	6.14 to 61.02°	3.56 to 61.02°	3.58 to 9.42°	2.22 to 42.4°
Index ranges	$-15 \le h \le 12$, $-14 \le k \le 14$, $-23 \le l \le 24$	$-12 \le h \le 13$, $-15 \le k \le 16$, $-21 \le l \le 18$	$-10 \le h \le 10$, $-13 \le k \le 13$, $-17 \le l \le 17$	$-5 \le h \le 4$, $-18 \le k \le 18$, $-19 \le l \le 19$
Reflections collected	34351	29704	18718	13522
Independent reflections	10336[R(int) = 0.0768]	9930[R(int) = 0.0594]	5476[R(int) = 0.1273]	3654[R(int) = 0.1448]
Data/restraints/ parameters	10336/60/514	9930/20/447	5476/0/389	3654/0/392
Goodness-of-fit on F2	1.04	1.053	0.935	1.041
Final R indexes [I>=2σ (I)]	R_1 = 0.0511, wR_2 = 0.0975	R_1 = 0.0617, wR_2 = 0.1645	R_1 = 0.0832, wR_2 = 0.1872	R_1 = 0.0898, wR_2 = 0.2066
Final R indexes [all data]	R_1 = 0.0726, wR_2 = 0.1056	R_1 = 0.0826, wR_2 = 0.1782	R_1 = 0.1224, wR_2 = 0.2072	R_1 = 0.1319, wR_2 = 0.2349
Largest diff. peak/hole / e Å^{-3}	1.07/-0.99	3.795/-3.813	6.167/-1.316	4.05/-1.2

Chapter 5

Ce(HTCPB) for Xylene Separation and Analysis of Uptake of Aromatic Guests

5.1 Introduction

Xylenes are aromatic hydrocarbons that exist commercially as a random mixture of C_8 isomers: *Para*-xylene (pX), *meta*-xylene (mX), *ortho*-xylene (oX) and ethylbenzene (EB). Xylenes represent around 0.5 – 1 % of crude oil and are extracted alongside toluene and benzene by catalytic reforming in the petroleum refining process. They can also be produced through disproportionation of toluene, methylation of benzene or toluene[1-2] and coal carbonisation in coke manufacture. Xylenes play an important role in many industrial chemical syntheses and therefore need to be isolated as single isomers in the purest possible form.

Table 1: *Structure, boiling point and melting point of all C_8 isomers:*

Xylene	Structure	Boiling Point (°C)	Melting Point (°C)
pX	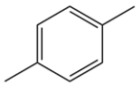	137-138	13.3
mX	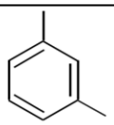	138-139	-47.9
oX	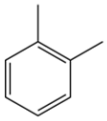	143-145	-25.2
EB	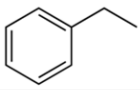	136	-95.0

Fractional distillation is not an appropriate method to separate aromatic hydrocarbons into individual fractions from crude oil. The non-aromatic molecules azeotrope with aromatics, which hinders effective separation and the difference in the boiling points of the C_8 isomers is negligible in terms of fractional distillation and therefore successful separation is not possible. For this reason, aromatic hydrocarbons are first separated from the non-aromatic hydrocarbons by stripping into a low boiling solvent. At this stage, benzene and toluene can be separated by simple distillation at 99.9 % and 98.5 % purity respectively. Xylenes are separated into a fraction containing all four C_8 isomers by this method with an overall purity of 95 %[3].

Due to their similar boiling points, separation by distillation of these compounds would require a column with 800 theoretical plates, which is uneconomical and unrealistic on an industrial scale. Xylenes (pX, mX, oX and EB) are therefore separated by fractional crystallisation which relies on the melting point of the individual compounds rather than the boiling point (*Table 1*). This involves firstly removing the high boiling oX leaving a mixture of pX, mX and EB, from which the lower boiling EB can be removed by distillation. This leaves pX and mX. PX can be isolated with around 99 % purity through cycling of melting/crystallisation, whereas mX can only be isolated at 85 % purity as it forms a eutectic mixture with pX[3]. Currently, separation is achieved by fractional crystallisation or adsorption using the faujasite zeolite in which the simulated moving bed technology is used[4].

At this stage, mX can be converted into pX and oX by cracking, as it is the least in demand of all the C_8 isomers. Zeolite Socony Mobil - 5 (HZSM-5) is a commercial zeolite used for the isomerisation and alkylation of hydrocarbons and has n Si/Al ratio of 64, a pore size of 5.6 Å and a BET surface area of 380 m^3g^{-1}. Its acidic channel chemistry means it is used in acid-catalysed reactions. It has 2D channels running down the a- and c-axes, with apertures of 5.4Å × 5.6Å and 5.1Å × 5.5Å, respectively[5]. HZSM-5 is capable of isomerisation of mX to pX as it is highly size selective to pX which has a high diffusion rate through the channels, meaning isomerisation can occur at a fast rate with high yield. The ability of this zeolite to conduct xylene isomerisation was discovered in 1975 using Mobil's Vapour Phase Isomerisation (MVPI) and have since been optimised to reduce xylene loss and the ability to work within a larger temperature window[6].

As mentioned, xylenes are extremely valuable as single isomers in industry. OX is oxidised to phthalic anhydride[7-8] which is used as plasticiser in the Polyvinyl Chloride (PVC) manufacture[9] and mX can be used to produce isophthalic acid and for conversion to pX using zeolites. But the most sought-after isomer is pX, the oxidation of which forms terephthalic acid which is the precursor of polyethylene terephthalate (PET)[10], more commonly known as polyester, which is used to make plastics and textiles. Almost all of the terephthalic acid produced is used in PET synthesis with only a small percentage being used for other causes. The polyester market has hugely increased in recent years with an expected increase to 39.3 million tonnes per year by 2015[11]. This increases demand for the pX precursor with which comes a need for more efficient and timely production of pure pX from efficient separation crude oil and by xylene isomerisation (the total worldwide capacity for xylene isomerisation is 2.5 million tonnes, mX to pX and oX per year[12]).

From the aromatic hydrocarbon fraction, benzene is the most used compound, however pX comes in second (*Table 2*) with an extremely large quantity used over the other xylene isomers, the reason for which synthesis of pX, conversion of oX/mX to pX and efficient separation is so important.

Table 2: *World demand for aromatics between 2005-2008*[13]*:*

Aromatic Hydrocarbon	10^6 Tonnes/year
Benzene	40
pX	26
oX	5
mX	0.4

Tecnon OrbiChem has stated that world demand for pX is expected to rise 7 % each year between the years 2008 -2013. This escalation has been instigated by the increasing demand for PET and TPA in Asian countries (mainly China) and other countries in the Middle East (*Figure 1*)[14].

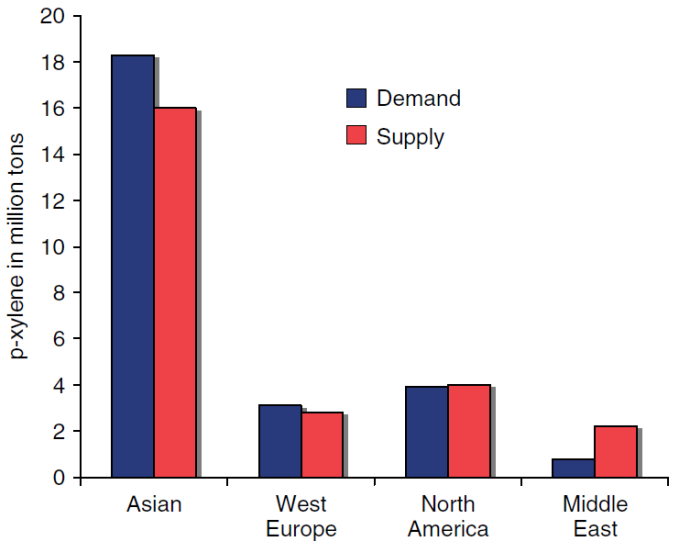

Figure 1: *World supply and demand for xylenes (especially pX). Figure taken from reference*[14].

Research is being conducted into selectively separating C_8 isomers via chromatographic separation which would allow for a more economical way to isolate the pure compounds. Separation of pX from mX is the key step, as it currently requires the most time and energy, with the pX component being that in most demand. This is done by first investigating the batch separation of isomers.

$$\propto_{\mathrm{XiXj}} = \frac{[Xi]/[Xj]}{[Xi_o]/[Xj_o]}$$

Equation 1: *Selectivity (α_{XiXj}) where Xi and Xj are the final concentration of components and Xi_o and Xj_o are the initial concentrations of components Xi and Xj* [15].

Current processes use (K, Ba)- Exchanged zeolite Y with a Dubinin-Raduschevitz (DR) pore volume of 0.241 cm^3g^{-1}[15] which has been shown to separate xylene isomers, including pX from mX with a selectivity of $\alpha_{pXmX} = 4.0$[16]. The selectivity (α_{pXmX}) is the ratio of pX sorbed to mX sorbed and is calculated using equation 1, thus meaning that the zeolite will take up 4 times more pX than mX from a mixture. The selectivity of the material is due to xylene packing within the pores of the zeolite, which are more effective in the case of pX which fits well into the pores and lines up to form intermolecular interactions with other pX molecules, whereas the larger size of mX means it cannot stack in the same way. Selectivities of $\alpha_{pXmX} = 4.5$ have also been observed for Zeolite K-exchanged zeolite Y[17]

Table 3: *MOFs that have recently been used for liquid batch separation of pX from mX with their respective selectivitys (MIL = Materials from Institut Lavoisier; UiO = University of Oslo):*

	Selectivity ($\alpha X_i X_j$)		
MOF	α_{pXmX}	α_{pXoX}	α_{pXEB}
MIL-125(Ti)-NH_2 [18]	4.4	-	-
CAU-1(Al)-NH_2 [18]	2.8	-	-
MIL-125(Ti) [18]	3.5	2.2	-
MIL-47(high pressure) [19]	2.1	-	-
MIL-47 [20]	2.9	0.7	9.7
MIL-53(Al)ht [20]	0.8	0.3	3.1
HKUST-1 [20]	0.9	1.4	1.2
MOF-1 [21]	-	0.5	-
UiO-66 [22]	-	0.4	-
Zeolite KBaY [16]	4.0	-	2.1
Zeolite KY [17]	4.5	-	-
ZSM-5 membrane [23]	4.3	4.4	-

Recent research has shown that MOFs can produce comparable if not superior performance in pX/mX separation, with selectivities shown in table 3. If the channels are large enough to accommodate xylenes and possess the appropriate environment for xylene inclusion, they can theoretically uptake one isomer in preference to the others which can later be extracted in a more pure form[20].

There are many examples of xylene separation using gas chromatography (GC), including the use of MIL-47[24] and MIL-101. The MOF is used to coat a capillary column and the C_8 isomers are vaporised and passed through with a carrier gas, resulting in the complete separation of pX, mX,

oX and EB. Gas phase separation of the C_8 isomers has also been demonstrated using MIL-47, which exhibits pore-filling selectivity and can resolve all isomers using gas chromatography (GC)[20]. MIL-53 can separate oX from all other isomers by packing a column with crystallites of the MOF and is shown to be selective through specific interactions forming with the pore walls[25]. It has more recently been reported that baseline resolution of pX, mX, oX and EB in the vapour phase can be accomplished in less than 2 minutes by coating a GC column with the MIL-101. The outstanding selectivity of MIL-101 coated capillary column was attributed to both suitable polarity of the framework and host-guest interactions[19].

However, separation of C_8 isomers by liquid chromatography is the ideal solution for production of pure pX, eliminating the need to operate at high temperatures. DeVos *et al.* have shown the batch and liquid separation of all xylene and EB isomers using MIL-53[25], a framework that in the batch experiments has a preference for oX but in the liquid and gas phase interacts with each isomer to a different extent, making separation by chromatography possible. They have also shown the separation of pX and mX from EB using MIL-47 via batch separation and liquid chromatography using hexane as a desorbent[20]. UiO-66 (which has average channel diameters 1.1 and 0.8 nm) has been shown to have reverse shape selectivity in the liquid phase towards pX, mX and oX xylene isomers with the strongest preference towards oX[22, 26]. This is explained by retention of structural isomers within the pores due to restricted progress through the smaller tetrahedral cavities of the framework, similar to the effects seen for MIL-47. PX can pass through easily whereas the oX and mX isomers have limited rotational degrees of freedom in the smaller channel space, and are therefore retained within the framework for longer. Hence separation of isomers is possible. Other reported xylene separation methods being investigated include distillative freezing[27] and pervaporation separation using MFI-type zeolite membranes[28-29].

In this chapter the separation of xylene isomers and EB is examined by means of a series of batch experiments using Ce(HTCPB) (**11**), the synthesis, structure and properties of which were discussed in chapter 4. GCMC calculations carried out on the desolvated phase **11D** predict the framework should preferentially take up pX over mX, with no mX entering the rigid structure. The 1D channels present are an ideal size and shape for the separation of pX from a mixture of pX and mX. Experimental data backs up this prediction, although flexibility of the framework means mX does enter but the material still produces pX/mX batch selectivities comparable to reported MOF materials. Single crystal structure anaysis of the xylene loaded phases allows an understanding of this selectivity on a molecular level, looking at the change in sturcture observed on guest uptake and analysing the intermolecular interactions present between the channel walls and the guest xylene molecules.

5.2 Experimental

5.2.1 MOF Synthesis

For the xylene separation experiments, as described in chapter 4, $Ce(NO_3)_3.6H_2O$ (90 mg) and H_4TCPB (30 mg) were added to a 40 mL borosilicate glass vial. EtOH (9 mL) and H_2O (9 mL) were then added and the vial was sealed and the mixture was sonicated for 15 minutes. Multiple reactions were carried out in parallel for combination following synthesis for use in the selectivity experiments. The vials were then placed in an oven and heated at a rate of 2 °C/ minute up to 120 °C at which temperature they remained for 48 hours. The solutions were then cooled to RT at 0.2 °C/ minute. The products were isolated as crystalline material with the formula $Ce(HTCPB)(EtOH)(H_2O)\cdot x EtOH\cdot y H_2O$. For the single crystal experiments, the same synthesis was used at 1/3 quantities in a 12 mL borosilicate glass vial.

5.2.2 Xylene Separation

An initial set of experiments were carried out on all isomers individually (pX, mX, oX and EB) to ascertain whether the framework would take up each isomer. Four batches of 50 mg of **11** were activated at 100 °C under vacuum (10^{-2} mbar) overnight after which time 1 ml of pX, mX, oX, or EB were added separately under N_2 and left for 24 hours. The framework was then filtered, washed with dichloromethane (DCM) to remove any surface xylenes and allowed to air dry before analysis.

5.2.3 Single Crystal Data Collection and Analysis

In this chapter, data for the single crystal structure solution of **11P**, **11M**, **11PM**, **11O**, **11EB**, **11T**, **11B**, **11RP**, **11RP** and **11R'P** were collected from the Rigaku Rotating Anode Diffractometer at the University of Liverpool. The structures were solved and refined using Olex2[30-31]. All structure solution and refinement was carried out with the assistance of Dr John Warren.

5.2.4 Calculations

In order to determine whether the pX, mX, oX and EB xylene isomers were able to fit and successfully dock within 11D, simulations were performed using a 2 × 2 × 2 supercell of the structure 11D, with the framework held fixed. All calculations were carried out by Dr Kim Jelfs at the University of Liverpool.

5.2.4 Powder X-Ray Diffraction and Analysis

Powder X-ray diffraction (PXRD) data of pX/mX loaded frameworks was collected in transmission geometry on a Bruker D8 Advance with Cu Kα radiation in a sealed 0.5 mm borosilicate capillary at room temperature. LeBail analysis of xylene loaded frameworks was carried out by Dr Phil Chater at the University of Liverpool.

5.3 Results and Discussion

As discussed in chapter 4, the total solvent accesible volume of **11D** is 405 Å^3, corresponding to 24.9 % of the total volume of the unit cell, calcaulated using Olex2[30]. This can be broken down into the two channels: Channel 1 accounts for 13.5 % of the void space, with a volume of 218.8 Å^3 and the smaller channel 2 is responsible for the remaining 11.4 % of this void space with a volume of 186.2 Å^3 per unit cell.

5.3.1 Calculations

Configurational Bias Grand Canonical Monte Carlo (CB-GCMC) calcualtions predict that if the structure of **11D** is rigid, it should favour pX and EB over mX and oX[32]. GCMC simulations have previously been used to understand xylene sorption in zeolites[33-34] and MOFs including MIL-47[35]. More recently these simulations have been used to attempt to predict likely xylene selectivity in MOFs for both sensor[36] and separation applications[37].

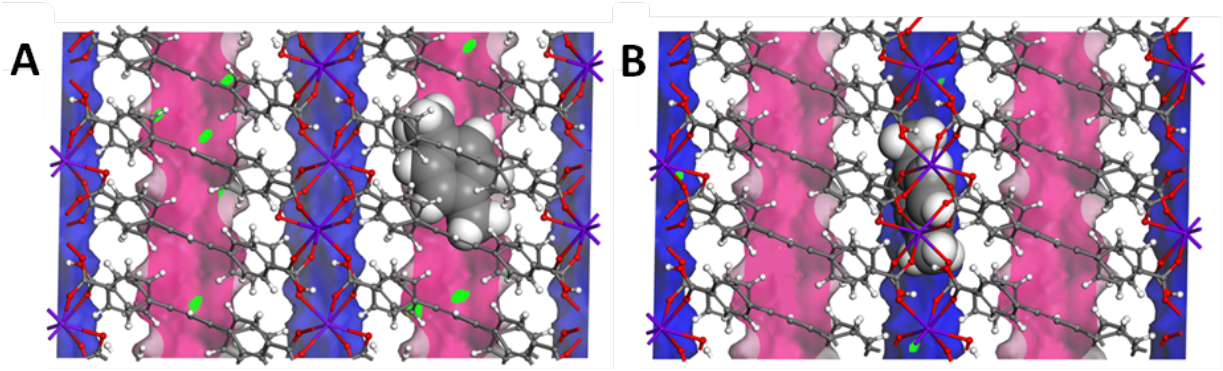

Figure 2: *An energetically favourable docking site from the simulations is shown for the pX in both A: Channel 1 (pink) and B: Channel 2 (blue) of* ***11D****[32]. Figure taken from reference[38].*

Given that the single crystal structure of **11D** had been determined, docking calculations were run and pX, mX, oX and EB were sorbed into the crystal structure of **11D** using Materials Studio Adsorption Locator to establish whether they would fit into the channels of the desolvated structure. These predicted that pX and EB would fit into both channels of **11D** but the oX and mX isomers would not fit into either. As pX/mX separation is the most challenging separation, these results imply that **11D** is the ideal candidate for pX/mX separation (*Figure 2*). Maximum uptake CB-GCMC calculations were used to predict the selectivity of **11D** which predicted 100 % selectivity for the rigid **11D** framework; only pX entered the channels[32].

5.3.2 Uptake of Individual Xylene Isomers and EB

TGA and CH analysis show loadings of 0.65, 0.42, 0.95 and 0.66 molecules per formula unit for pX, mX, oX and EB respectively, making the assumption that two xylenes to be taken up per unit cell; one in each channel (one per formula unit) (*Table 4, Figure 3*). From these experiments, it appears order of preference to enter **11D** falls in the order oX>pX=EB>mX.

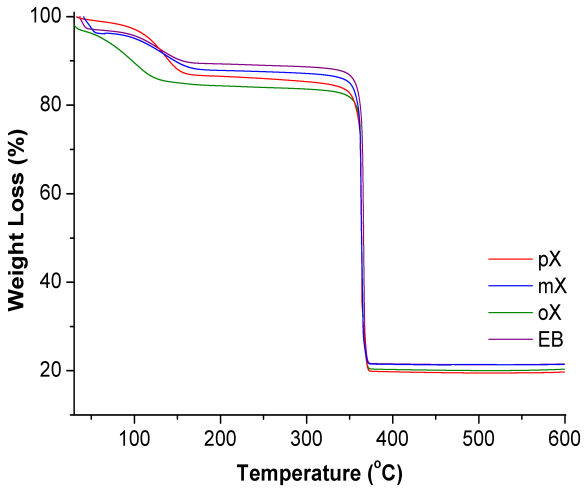

Figure 3: *TGA profiles of **11D** at the loaded with individual C_8 isomers after 24 hours.*

Table 4: *CH and TGA data for xylene loaded **11D.***

Xylene	Formula	Theory (%)	Found (%)	Solvent content from CH (%)	Solvent content from TGA (%)
pX	Ce(HTCPB).0.65pX.0.02DCM.2.1 H_2O	**C:** 57.58 **H:** 3.73	**C:** 57.59 **H:** 3.80	13.50	13.00
mX	Ce(HTCPB).0.42mX.0.37DCM.1.47 H_2O	**C:** 56.78 **H:** 3.39	**C:** 56.76 **H:** 3.36	12.84	12.05
oX	Ce(HTCPB).0.95oX.0.34DCM.0.03 H_2O	**C:** 60.99 **H:** 3.57	**C:** 60.99 **H:** 3.50	15.77	16.00
EB	Ce(HTCPB).0.66EB.0.09DCM.0.15H_2O	**C:** 60.93 **H:** 3.39	**C:** 60.95 **H:** 3.36	10.36	10.99

The calculations described in section 5.2.1 predicted that whereas pX and EB would be able to enter the framework of **11D**, oX and mX would not. The experimental data shows that all isomers can enter the framework, which is expected due to framework flexibility. The variable temperature single crystal experiment in chapter 4 shows that **11** can undergo structural changes during the desolvation process and rehydration following exposure to air, so it is not unexpected that flexibility will allow all the isomer to fit into the channels.

5.3.3 Single Crystal Structure Determination of Xylene and EB Loaded 11D

5.3.3.1 Data Collection and Processing

A series of single crystal diffraction experiments were carried out to determine the structure of the xylene and EB loaded materials for comparison with the GCMC calculations and to gain understanding at the molecular level as to how the isomers interact with the host framework.

For xylene loaded **11D**, single crystals were activated at 100 °C in a Schlenk tube under a vacuum of 10^{-2} mbar overnight. Following activation the samples were back filled with N_2 and allowed to cool to room temperature after which time, 1 ml of pX (**11P**), mX (**11M**), a 1:1 mixture of pX and mX (**11PM**), oX (**11O**) and ethylbenzene (**11EB**) were added to five separate samples respectively. The Schlenk tubes were sealed under N_2 and left for 24 hours before a single crystal was transferred under N_2 directly into fombilin oil, mounted onto a mitegen tip and put directly into a N_2 flow. Single crystal data was collected. Following structure solution and refinement, the same framework atom numbering scheme was used as for **11D** (*Chapter 4*).

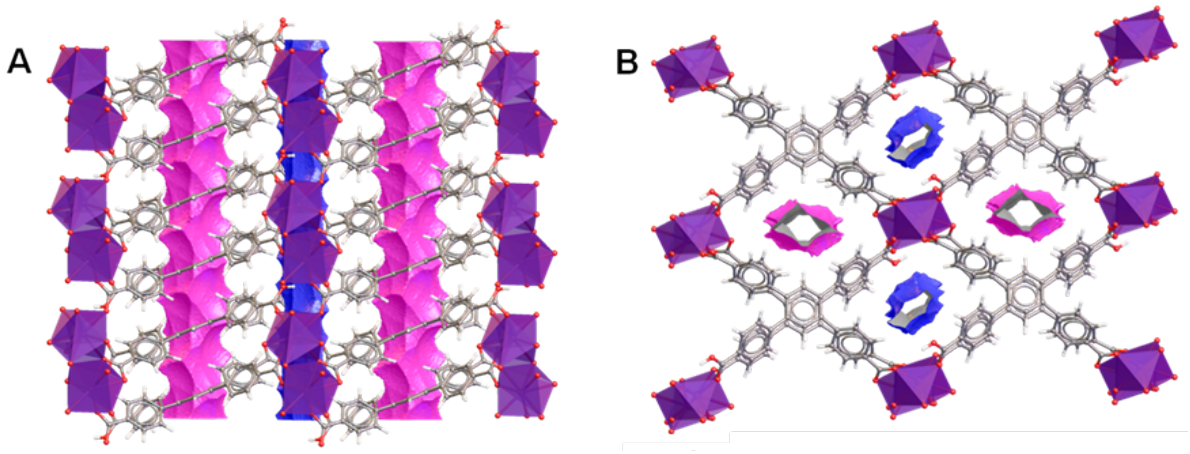

Figure 4: *A and B: Single crystal structure of **11D** along the b-axis (A) and a-axis (B) showing void 1 (pink) and void 2 (purple). Figure adapted from reference*[38].

As described in chapter 4, **11D** has two distinct channels; the larger channel 1 and the smaller channel 2 (*Figure 4*). For **11P**, **11M**, **11PM**, **11O** and **11EB**, the same channels are present albeit with different morphologies which will be discussed later, but the same channel numbering will be used.

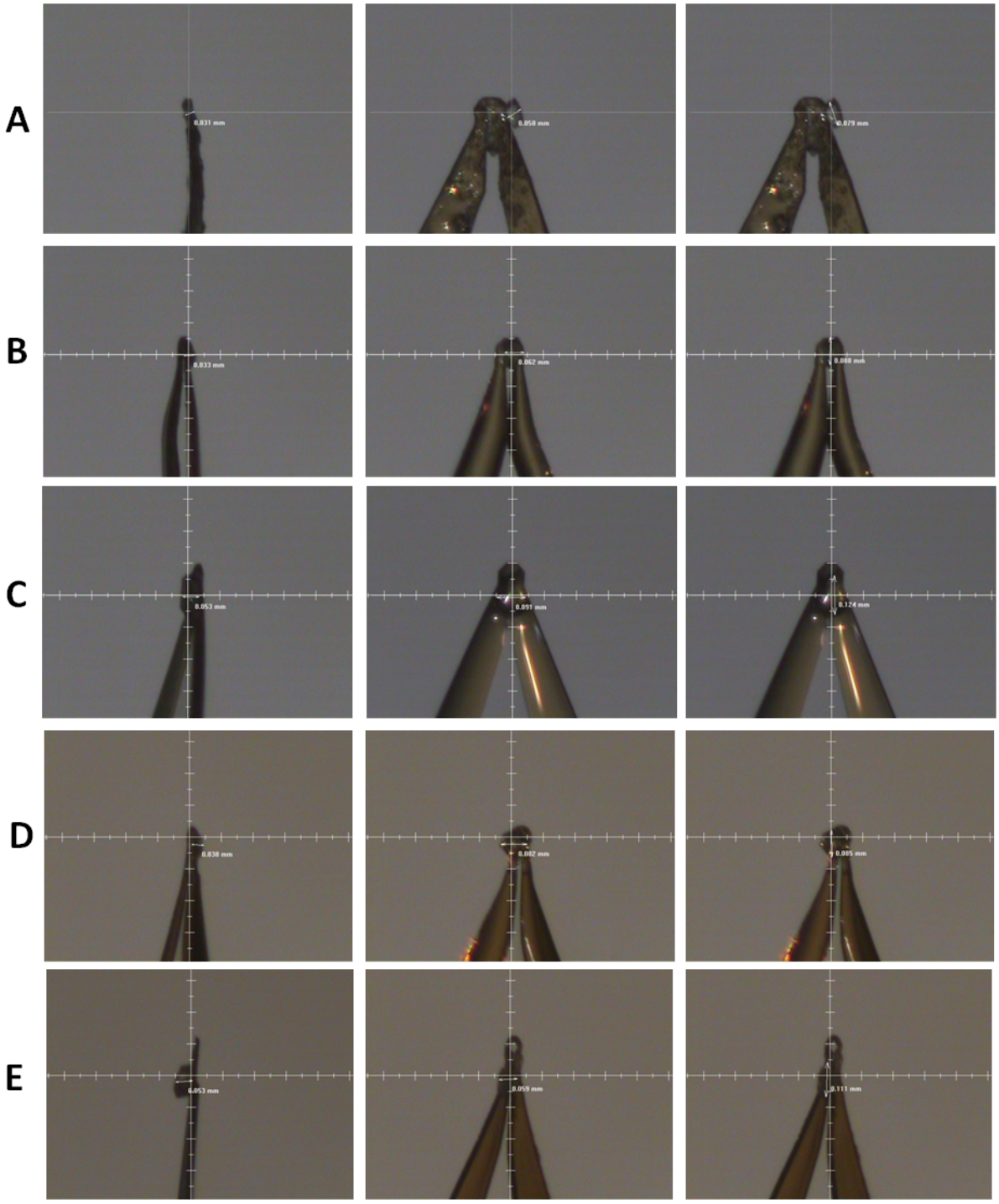

Figure 5: *Pictures of the crystal taken on the diffractometer displaying the crystal measurements: A:* ***11P****; B:* ***11M****; C:* ***11PM****; D:* ***11O****; E:* ***11EB****.*

Table 5: *Unit cell dimensions of* ***11D*** *with xylenes included.*

	Unit Cell Dimensions			
	a /Å	**b /Å**	**c /Å**	**V / Å^3**
11D	9.2989(11) 93.756(5)	11.4163(13) 90.263(6)	15.2492(17) 93.814(6)	1611.70(30)
11P	9.5603(4) 88.455(10)	12.1386(5) 74.417(10)	15.9458(10) 70.233(10)	1673.27(12)
11PM	9.5976(3) 88.6100(10)	12.1928(4) 75.1240(10)	15.9099(5) 70.0890(10)	1687.75(9)
11M	9.7441(6) 88.979(2)	12.3318(7) 77.299(2)	15.7737(9) 69.498(2)	1729.02(18)
11O	10.2595(17) 91.235(10)	12.3951(19) 93.970(1)	15.7870(3) 110.520(9)	1873.50(6)
11EB	9.5873(2) 88.936(6)	12.4039(3) 75.581(5)	15.7803(11) 70.035(5)	1703.70(15)

The data shows an overall expansion in the unit cell dimensions and volume with uptake of guests (*Table 5*). The expansion from the empty desolvated framework **11D** is proportional to the size of the guest taken up: The greatest unit cell volume expansion is seen with uptake of oX and mX which have the largest kinetic diameters of all the isomers at 6.5 Å and 6.4 Å respectively (*Figure 6*), causing an increase from 1632.08 Å^3 to 1873.50 Å^3 and 1729 Å^3 respectively. pX causes the smallest change to 1673.27 Å^3, as it is the smallest of all the isomers with a kinetic diameter of 5.8 Å and EB produces a slightly larger increase to 1687.75 Å^3 due to its slightly larger kinetic diameter of 6.0 Å^3

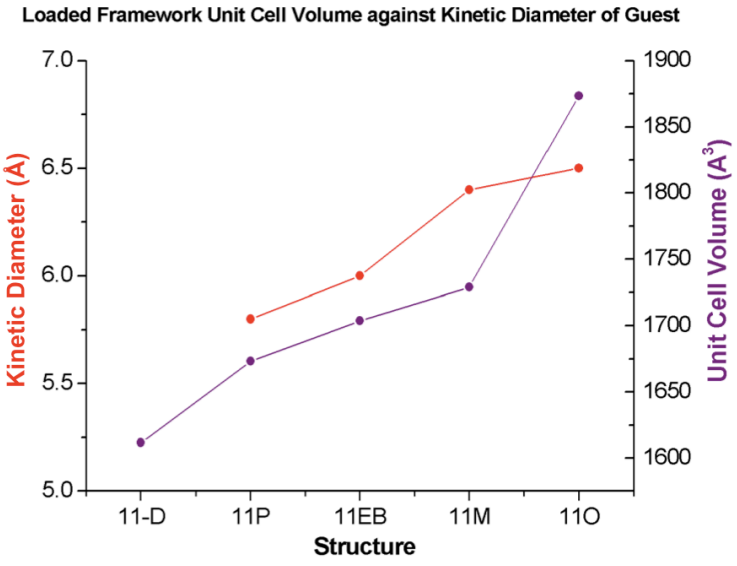

Figure 6: *Graph to show increasing unit cell volume of C_8 loaded framework from* ***11D****, with increase in kinetic diameter of the C_8 guest used.*

Looking in more detail at how the C_8 isomers induce structural change of their host frameworks, void analysis of the channel space and the separate channels 1 and 2 were calculated using Olex2[30] (*Table 6*).

Table 6: *Void space analysis of xylene loaded single crystal structures of **11D**:*

Ln(HTCPB)	Total Accessible Volume (Å^3) [a]			kinetic diameter σ (Å) of guest [b]
	Overall	Void 1	Void 2	
11D	389.7	207.1	182.5	-
11P	448.9	242.5	206.4	5.8
11M	501.8	283.6	218.2	6.0
11PM	503.8	280.7	223.1	5.8/6.0
11O	628.0	363.5	264.5	6.5
11EB	485.8	270.8	215.0	6.4

[a]Calculated using Olex2[30] [b]Taken from reference [18].

The outcome of single crystal diffraction experiments on crystals loaded from the equimolar pX/mX solution (**11PM**) produces a structure more similar to **11P** than **11M,** with only pX locatable in the pores. The pX molecule found in channel 2 is in similar a position to pX in pure **11P**, but there is translational disorder of pX in channel 1 (similar to that seen for mX in channel 1 of **11M**). PXRD does not distinguish between **11P** and **11M** but shows a guest loaded phase **11PM** which evolves to smaller lattice parameters as the experiment proceeds suggesting some ordering of the guests within the pores (*see later: Figure 13,14*).

5.3.3.2 pX loaded 11D: 11P

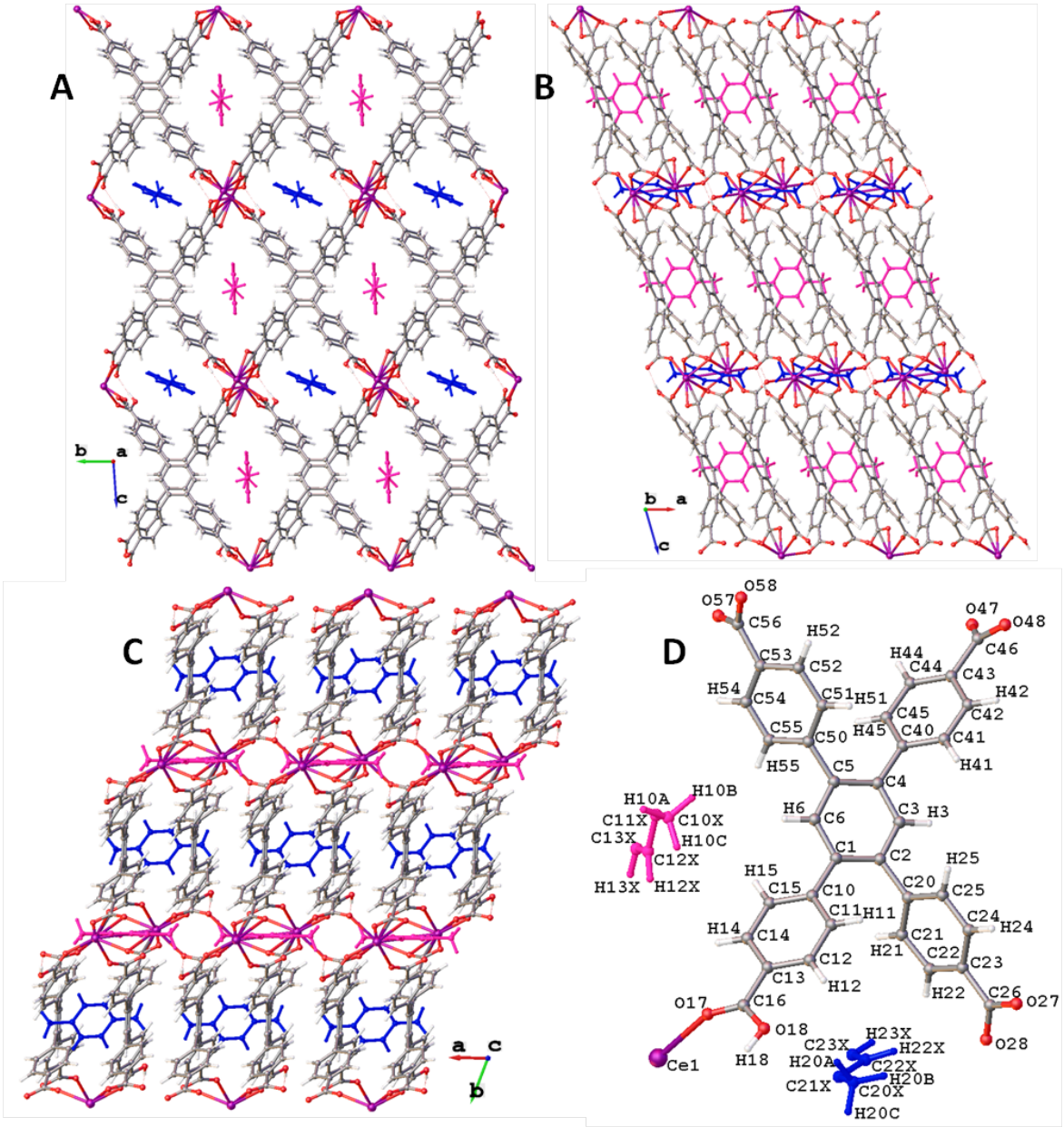

Figure 7: *Single crystal structure of* ***11P****. A: View down 100; B: View down 010; C: View down 001; D: Asymmetric unit with pX1 in channel 1 (pink) and pX2 in channel 2 (blue with atom numbering scheme).*

The single crystal of **11P** used had dimensions of 0.079 × 0.05 × 0.031 mm (*Figure 5A*). **11P** has the same overall structure as **11D** but with slightly different unit cell dimensions resulting in a larger unit cell volume (*Figure 7A-C*). The asymmetric unit contains two half pX molecules both of which refine to 100 % occupancy, one found in each of the two channels: pX1 in channel 1 and pX2 in channel 2 (*Figure 7D*). This means that per unit cell there are two whole pX molecules, one per Ce(HTCPB) formula unit. This gives **11P** the formula Ce(HTCPB)·pX.

5.3.3.3 mX loaded 11D: 11M

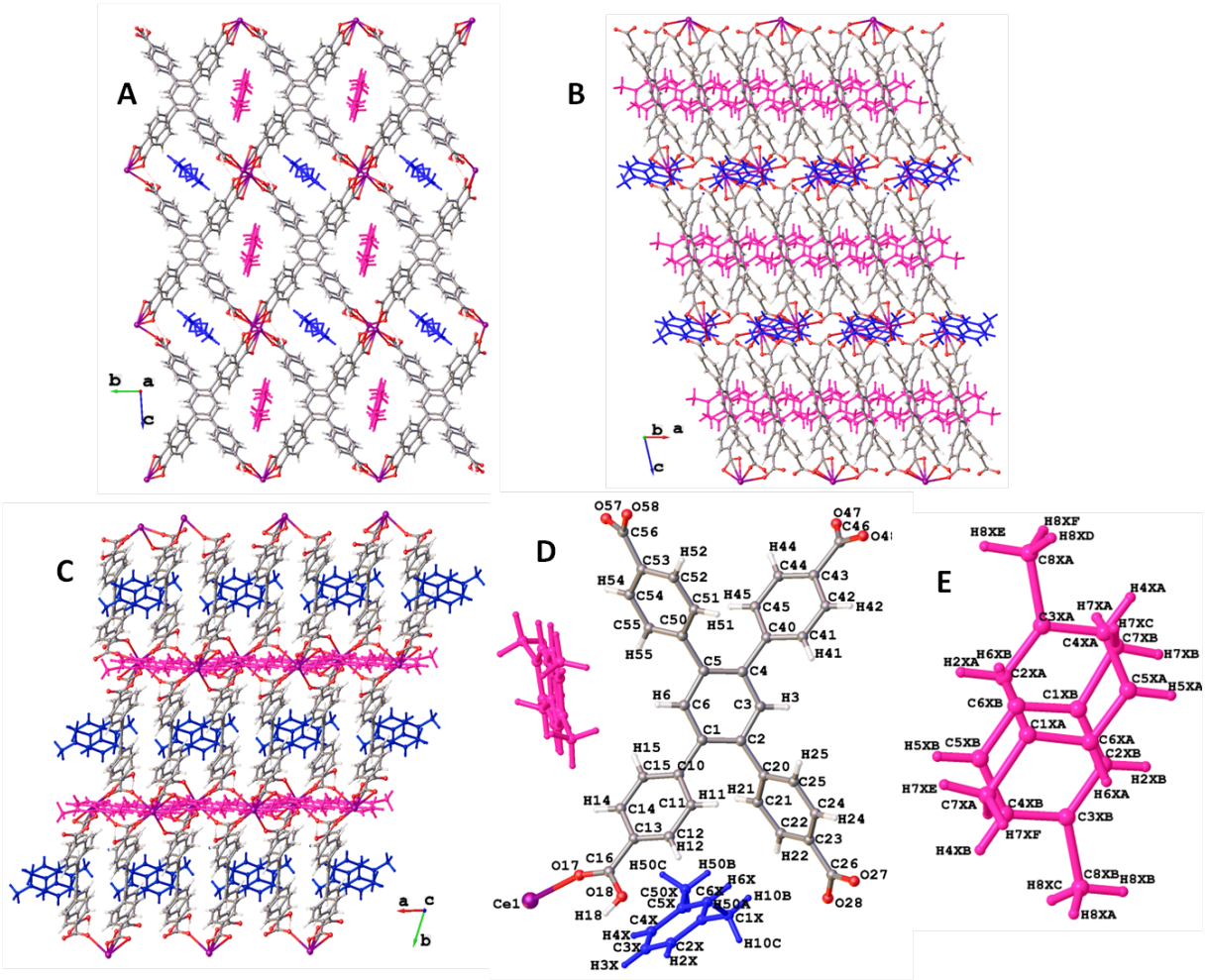

Figure 8: *Single crystal structure of* ***11M****. A: View down 100; B: View down 010; C: View down 001; D: Asymmetric unit with mX1 in channel 1 (pink) and mX2 in channel 2 (blue with atom numbering scheme; E: Numbering scheme for disordered mX1.*

The single crystal of **11M** used had dimensions of 0.088 × 0.062 × 0.033 mm (*Figure 5B*). **11M** contains two disordered sites of mX; one per channel. In channel 1, two partial overlapping mX molecules grow to produce two distinct overlapping mX molecules when symmetry is applied. These two molecules are fully disordered when translational symmetry is also applied. In the model, the partial mX molecules were grown individually to produce the full mX molecules thus producing 1 mX molecule in the grown structure for channel 1. In channel 2, a disordered partial single mX unit could be resolved which on the application of symmetry grew into two overlapping mX molecules, producing two overlapping mX molecules at an 0.5 occupancy giving 1 mX molecule in total in the grown structure for channel 2 (*Figure 8*). This gives one whole mX

molecule per formula unit of Ce(HTCPB), two per unit cell. This gives **11M** the formula Ce(HTCPB)·mX.

5.3.3.4 pX/mX loaded 11D: 11PM

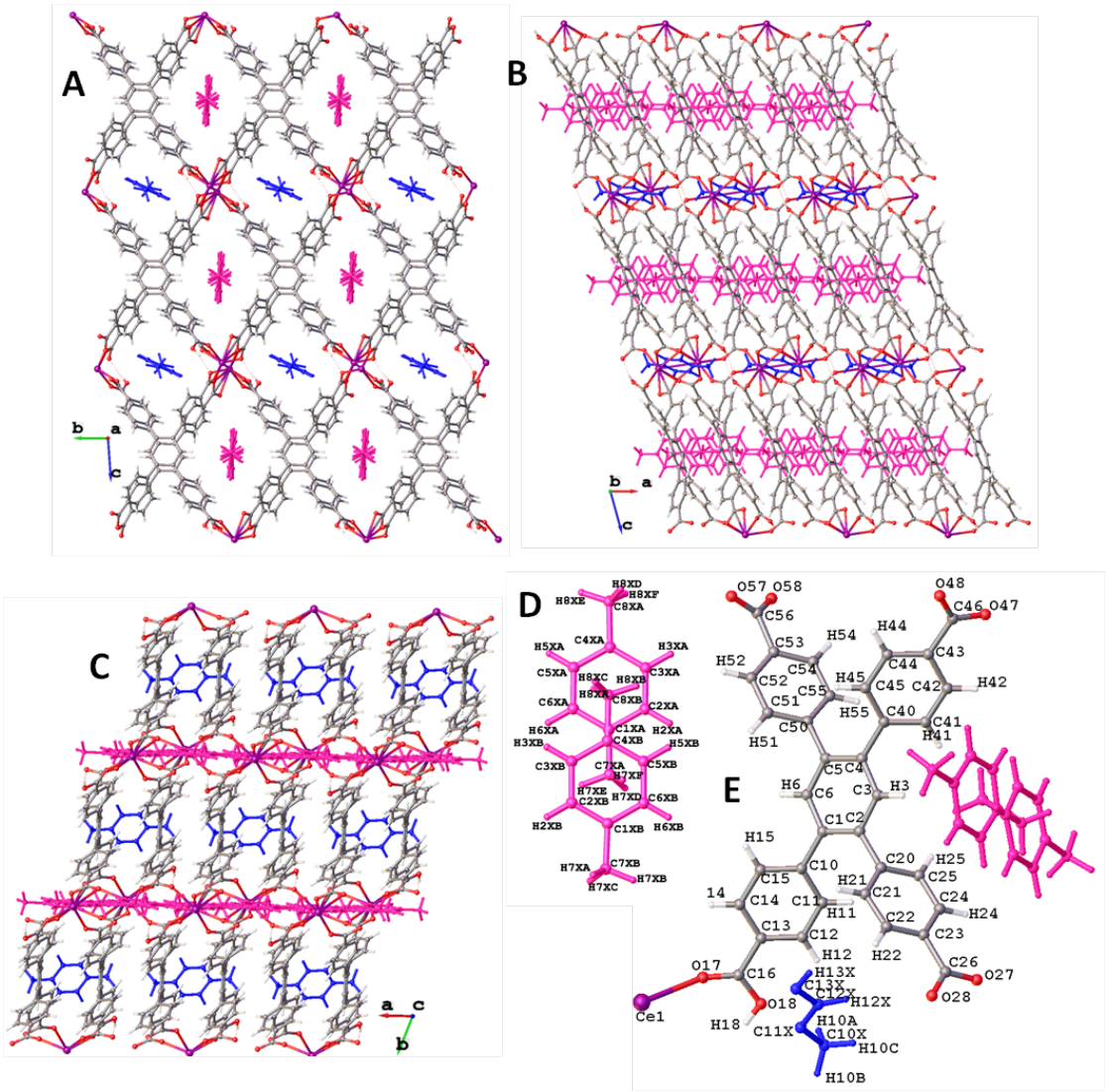

Figure 9: *Single crystal structure of **11PM**. A: View down 100; B: View down 010; C: View down 001; D: Numbering scheme for disordered pX1; E: Asymmetric unit with pX1 in channel 1 (pink) and pX2 in channel 2 (blue with atom numbering scheme).*

The single crystal of **11PM** used had dimensions of 0.053 × 0.091 × 0.124 mm (*Figure 5C*). **11PM** contains two disordered sites for pX in channel 1. On the application of symmetry the two partial overlapping pX molecules grow over the symmetry operator producing two distinct overlapping pX molecules, which are found to be fully disordered when translational symmetry is also applied. The occupancy of each pX was set to 0.5; pX1a and pX1b thus producing 1 pX

molecule in the grown structure for channel 1. In channel 2 a 1/2 pX unit could be resolved which on the application of symmetry grew into a full pX molecule (pX2) which when refined against a free variable gave an overall occupancy of 92.6% thus producing 92.6% of a full pX molecule per unit cell for channel 2 (*Figure 9*). Attempts to model disordered mX in channel 1 or channel 2 were unsatisfactory. This gives **11PM** the formula Ce(HTCPB)·$pX_{0.926}$.

5.3.3.5 oX loaded 11D: 11O

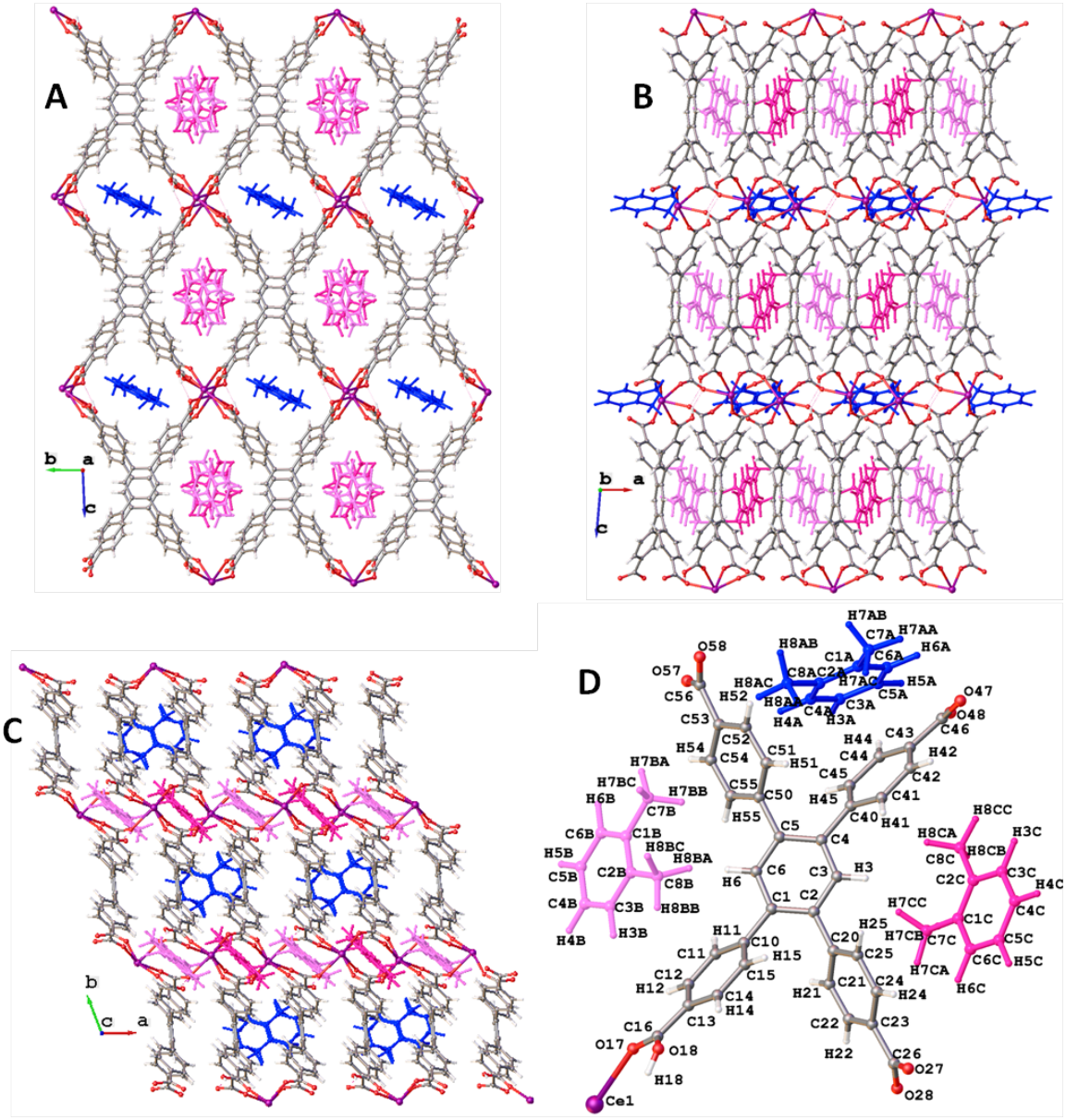

Figure 10: *Single crystal structure of **11O**. A: View down 100; B: View down 010; C: View down 001; D: Asymmetric unit with oX1 (dark pink) and oX2 (pale pink) in channel 1 and oX2 (dark blue) in channel 2, with grown oX molecules shown.*

The single crystal of **11O** used had dimensions of 0.085 × 0.082 × 0.038 mm (*Figure 5D*). **11O** contains three disordered sites of oX; two in channel 1 and one in channel 2. In channel 1, two half occupancy symmetry equivalent oX molecules (oX1 in dark pink and and oX2 in pale pink) are present either side of an inversion centre, each refining in total to 50 % occupancy (*Figure 10*). Each oX1 and oX2 is disordered over 2 positions. In channel 2, one oX3 molecule is disordered over 2 positions. This gives 1.5 oX molecule per formula unit of Ce(HTCPB), 3 per unit cell. This gives **11O** the formula Ce(HTCPB).$oX_{1.5}$.

5.3.3.6 EB loaded 11D: 11EB

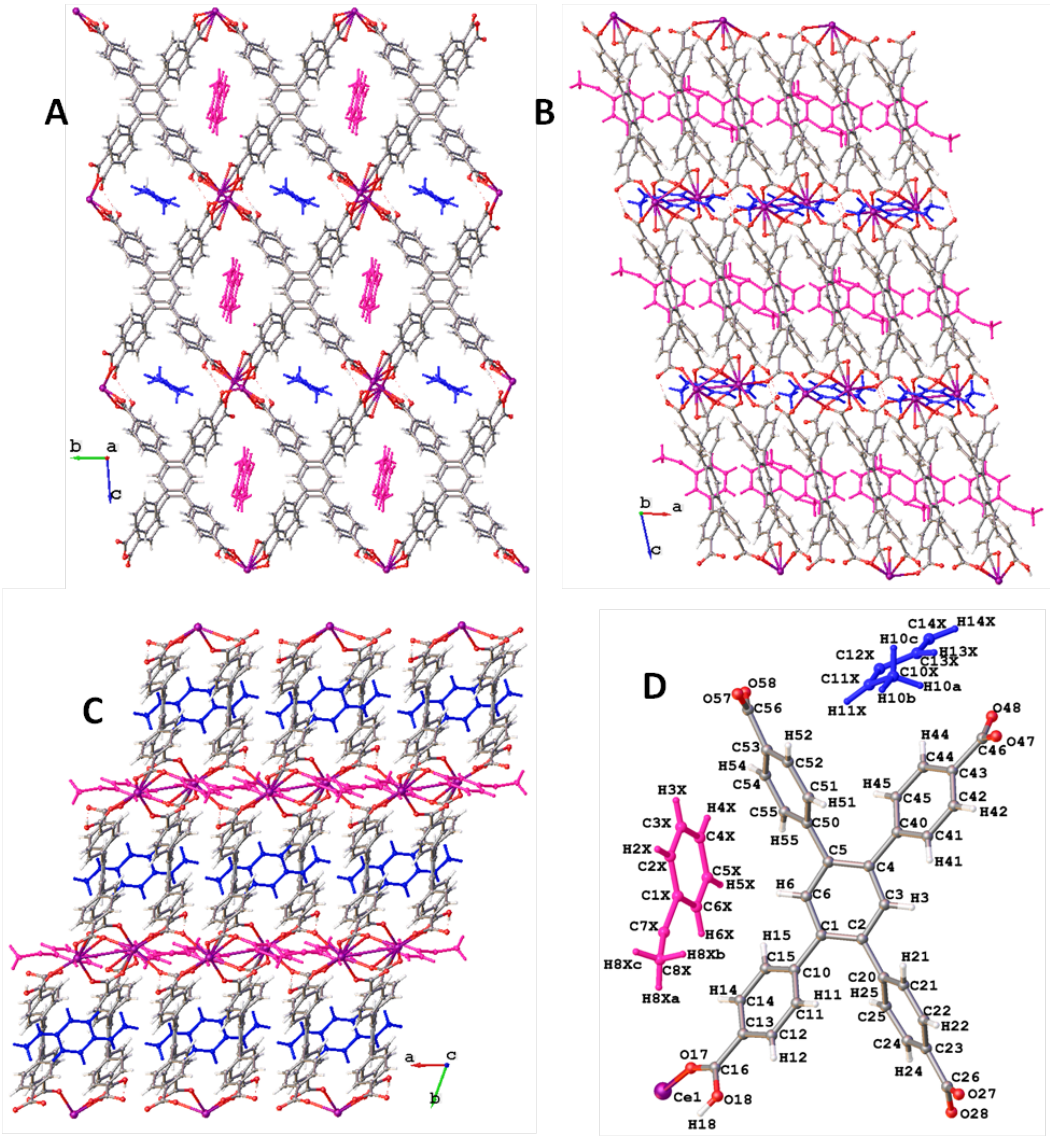

Figure 11: *Single crystal structure of* ***11EB****. A: View down 100; B: View down 010; C: View down 001; D: Asymmetric unit with EB1 in channel 1 (pink) and EB2 in channel 2 (blue).*

The single crystal of **11EB** used had dimensions of 0.111 x 0.059 x 0.053 mm (*Figure 5E*). **11EB** contains one disordered EB in channel 1 (EB1) and one EB in channel 2 (EB2). EB1 is disordered over 2 positions across the inversion centre, each part refining to 50 % occupancy thus producing 1 EB molecule in channel 1. EB2 has an idealised location for the central aromatic ring, with the pendent ethyl group disordered over two positions, from C10X and H13X, each part of the ethyl disorder refining to 50%, producing 1 EB molecule in channel 2 (*Figure 11*). This leaves one whole EB molecule per formula unit of Ce(HTCPB), two per unit cell. This gives **11EB** the formula Ce(HTCPB).EB.

5.3.4 Selectivity and Framework Loading with Equimolar Mixtures of Xylene and EB Isomers

In order to test the selectivity of **11D** towards the four C_8 isomers, a protocol was set up for screening xylene separation. 50 mg of **11** from the scaled up synthesis method B (*Chapter 4, section 4.2*) was activated at 100 °C under vacuum overnight in a Schlenk tube to give **11D**. 1 mL of equimolar solutions of mixed xylenes and EB (XiXj, where Xi and Xj are two equimolar xylene components Xi and Xj) were then added to **11D** under N_2 and left for 24 hours after which time they were filtered and washed with DCM to remove any surface xylenes. All loaded frameworks were characterised for xylene uptake by TGA and CH microanalysis (*Figure 12, Table 8*). The loaded frameworks were then broken down with 1M $NaOH_{(aq)}$ solution and filtered, leaving an aqueous solution of the ligand (Na_4TCPB) and the xylenes. The xylenes were then extracted by washing three times with DCM, dried with $MgSO_4$ and filtered ready for GC analysis. The selectivity (α_{ij}) was calculated for each product solution using equation 1. All resultant xylene solutions were run against a standard equimolar solution of Xi and Xj, under investigation (*Table 7*).

Table 7: Selectivity (α_{XiXj}) of **11D** towards mixtures of pX, mX, oX and EB:

		Xj			
		oX	**mX**	**pX**	**EB**
Xi	**oX**	-	1.22	0.18	0.64
	mX	0.82	-	0.22	0.42
	pX	5.65	4.55	-	2.38
	EB	1.56	2.38	0.42	-

Selectivities (α_{XiXj}) calculated using equation 1.

These batch measurements show size selectivity in the order pXoX > pXmX > EBmX = pXEB > oXmX > mXoX > mXEB = EBpX > mXpX > oXpX. pX has the smallest kinetic diameter of 5.8 Å, followed by EB at 6.0 Å and the largest isomers, oX at 6.5 Å and mX at 6.4 Å. This is consistent with the idea that pX will enter the channels and pass through more easily than the larger EB, both of which will enter and leave more quickly than the largest mX and oX isomers. Hence the highest selectivity observed is between the largest and smallers isomers with $\alpha_{pXoX} = 5.65$ and the second highest selectivity being the key pX/mX separation under investigation with $\alpha_{pXmX} = 4.55$. This value can be compared to the best performing zeolite in pX/mX xylene separation, KBaY, which shows $\alpha_{pXmX} = 4.0$. The pX/EB selectivity is also higher for Ce(HTCPB) than KBaY with of $\alpha_{pXEB} = 2.38$ and 2.1 respectively.

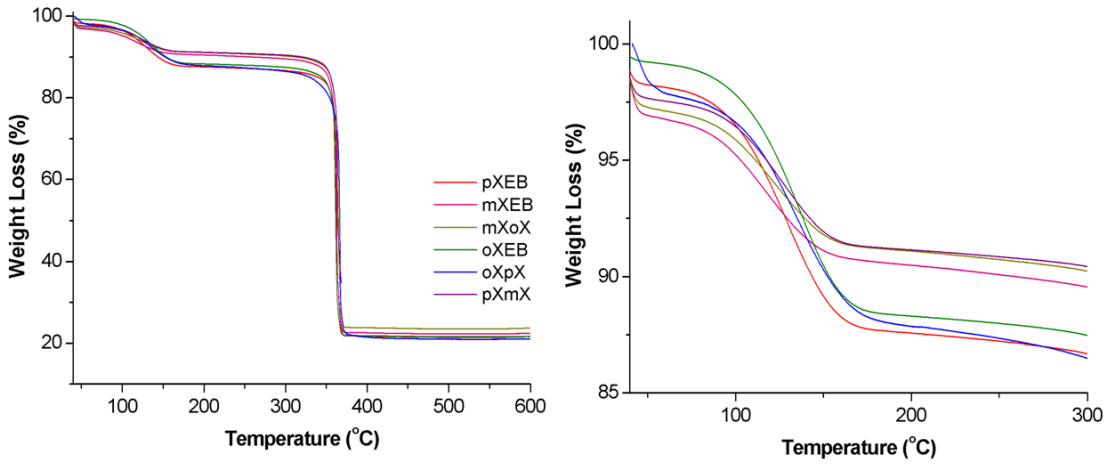

Figure 12: *TGA profiles for mixed xylene uptake and separation experiments.*

Table 8: *CH microanalysis for xylene loaded samples of* ***11D.***

Xylene Mixture/ Formula, ij	Theory (%)	Found (%)	Solvent content from CH (%)	Solvent content from TGA (%)
pXEB Ce(HTCPB)·0.75pXEB·0.22DCM·0.16H_2O	**C** 60.63 **H** 3.45	**C** 60.62 **H** 3.32	12.70	12.75
pXmX Ce(HTCPB)·0.74pXmX·0.16DCM·0.11H_2O	**C** 60.95 **H** 3.45	**C** 60.95 **H** 3.36	11.92	12.25
pXoX Ce(HTCPB)·0.75pXoX·0.13DCM·0.10H_2O	**C** 61.16 **H** 3.45	**C** 61.13 **H** 3.39	11.73	12.04
mXEB Ce(HTCPB)·0.55mXEB·0.15DCM·0.23H_2O	**C** 60.06 **H** 3.30	**C** 60.06 **H** 3.31	9.76	9.18
mXoX Ce(HTCPB)·0.55mXoX·0.11DCM·0.62H_2O	**C** 59.72 **H** 3.38	**C** 59.71 **H** 3.36	10.19	9.85
oXEB Ce(HTCPB)·0.38oXEB·0.33DCM·0.44H_2O	**C** 58.15 **H** 3.18	**C** 58.14 **H** 3.15	9.88	9.16

TGA and CH analysis of each individual XiXj experiment showed that the loading in each case was also affected by the xylene size. When pX was one of the two components, the loadings observed were the highest, at 0.75, 0.74 and 0.75 xylenes per Ce(HTCPB) formula unit for pX/EB, pX/mX and pX/oX experiments respectively. When the larger xylenes were tested against each other, the overall loadings decreased to 0.55, 0.55 and 0.38 xylenes per formula unit for mX/EB, mX/oX and oX/EB respectively, possibly due to restricted diffusion through the 1D channels of the structure.

5.3.5 Time Dependance of pX/mX Selectivity

With the main aim of research in this area being on the separation of pX and mX, the time dependence on the selectivity of **11D** towards these two isomers was investigated. The times chosen for this series of experiments were 1 minute, 10 minutes, 24 hours and 7 days (*Table 9*). The procedure used was the same as for the previous batch experiments.

Table 9: *Selectivity of a crystalline sample of **11D** towards an equimolar mixture of pX and mX after the period of time shown. Selectivity calculated using equation 1:*

Time	Selectivity, α_{pXmX} [a]
1 minute	3.28
10 minutes	3.72
24 hours	4.55
7 days	4.91

The results show that **11D** is immediately highly selective to pX, with α_{pXmX} of 3.28 after only one minute. This value increases with longer times up to a high of $\alpha_{pXmX} = 4.91$ after 7 days. This is in closer agreement with the predicted selectivity of 5:1, indicating that longer time periods are required for system to reach equilibrium.

Table 10: *CH microanalysis for xylene loaded samples of* ***11D.***

Time/ Formula	Theory (%)	Found (%)	Solvent content from CH (%)	Solvent content from TGA (%)
1 minute Ce(HTCPB).0.39(xylene).0.2(H_2O)0.08(DCM)	C: 56.33 H: 3.10	C: 56.33 H: 3.07	9.0	7.5
10 minutes Ce(HTCPB).0.46(xylene).1.25(H_2O)0.41(DCM)	C: 57.06 H: 3.38	C: 57.06 H: 3.35	10.5	10.1
24 hours Ce(HTCPB).0.65(xylene).0.68(H_2O)0.05(DCM)	C: 60.36 H: 3.43	C: 60.35 H: 3.48	13.9	13.5
7 days Ce(HTCPB).0.70(xylene).0.61(H_2O)0.07(DCM)	C: 60.55 H: 3.50	C: 60.51 H: 3.48	13.6	13.5

TGA and CH microanalysis show that the extent of loading increases over time, with a loading of 0.39 xylenes per formula unit after 1 minute up to 0.70 after 7 days, alongside an increase in selectivity (*Table 10*). The material never reaches a 'fully loaded' state during the time course of this experiment, which would leave 1 xylene molecule per formula unit.

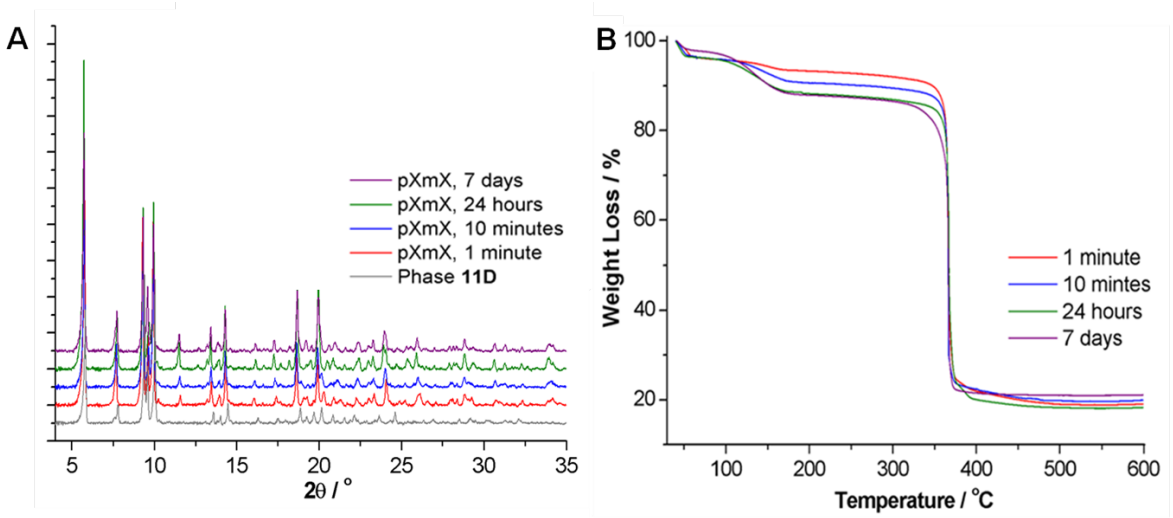

Figure 13: *A: Powder X-ray diffraction profiles of loaded material following xylene uptake experiments on* ***11D*** *after 1 minute, 10 minutes, 24 hours and 7 days; B: TGA profiles of loaded material following xylene uptake experiments on* ***11D*** *at the same times.*

PXRD analysis of the loaded material over these time periods show a shift in structure compared to the original desolvated phase[39]. Phase **11D** is still present at around 30 % after 1 minute alongside a 'loaded' phase, **11PM**, which has a larger unit cell volume than **11D**. After 10 minutes, the amount of **11D** has reduced to 20 % and has completely disappeared by 24 hours. The unit cell volume of **11D** increases slightly between 1 and 10 minutes due to loading of the material before conversion to **11PM**. Phase **11PM** is present at all times throughout the experiment, however the unit cell volume is decreasing with time. This may be due to ordering of the xylene molecules

within the channels; initially at 1 minute there is a large amount of disorder so the structure has a larger unit cell volume, but as the xylenes become more ordered and form interactions with the channel walls, the unit cell volume decreases (*Figure 14*).

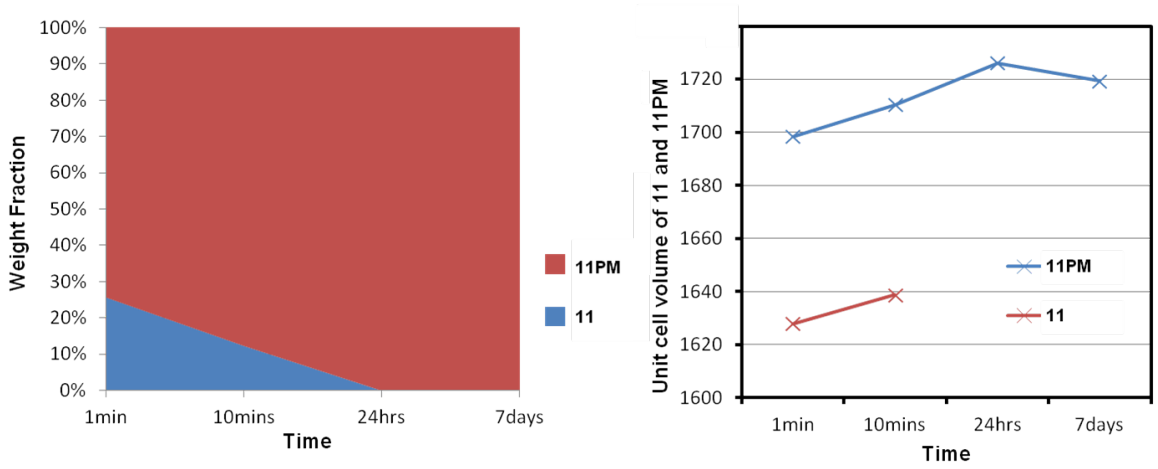

Figure 14: *Analysis of the relative amounts of **11D** (red) and xylene loaded **11PM** (blue) over the time course of the pXmX selectivity experiments[39]. Figure adapted from reference[38].*

The maximum overall xylene uptake calculated using TGA and CH analysis is 0.70 per Ce(HTCPB) formula unit after 7 days. Using the structure of **11D** and making the assumption that 1) the framework is rigid and 2) that 100 % loading would result in 1 xylene per formula unit, the volume of absorbed xylene expected per mass of framework can be calculated. This gives us a theoretical 100 % adsorption capacity of 177 ml/kg = 152.624 g/kg = 1.438 mol/kg. All faujazite zeolites have a xylene adsorption capacities in the range of 1 to 1.75 mol/kg[16]. This means that **11D** has the potential to adsorb comparable amounts of xylene with zeolites, but shows higher pX/mX selectivities.

We know that **11D** in fact is not rigid, however even with small changes in the total accessible volume of '**11D**' with xylene guest uptake, the overall adsorbed quantity will still lie within the region of zeolite uptakes.

11D has a D-R pore volume of 0.208 cm^3/g and zeolite KBaY has a D-R pore volume of 0.241cm^3/g[15]. This further demonstrates the similarity in pore size of Ce(HTCPB) in comparison with the current commercial zeolite KBaY used for pX/mX separations. Ce(HTCPB) produces selectivities as high as 4.91, improving the value of 4 generated by KBaY.

5.3.6 Weighted Xylene Ratio vs Xylene Uptake Composition

The pX/mX selectivity of **11D** was determined using initial solutions with varying pX/mX ratios in order to investigate it's selectivity. The initial pX/mX ratios used are shown in table 10 and these experiments were carried out after 24 hours using 50 mg of **11D**.

The batch experiments were carried out in the same way as described in section 5.2.5, and a final ratio of pX/mX was recorded for the xylene composition extracted from the framework. The pX/mX selectivity, α_{pXmX}, was calculated from this using equation 1.

There is enhanced pX/mX selectivity for pX as more pX is loaded into **11D**. GCMC docking calculation based on competitive 2-component simulations predicts a selectivity of 5.00-5.33 for **11P** and 4.33 for **11M** (compared to 45-50 for rigid vacant host **11D**)[32]. This experimental batch selectivity data agrees with the GCMC calculations which predict that **11P** is more selective than **11M**, so as more pX is introduced to the framework, it becomes more selective to pX (*Figure 15*).

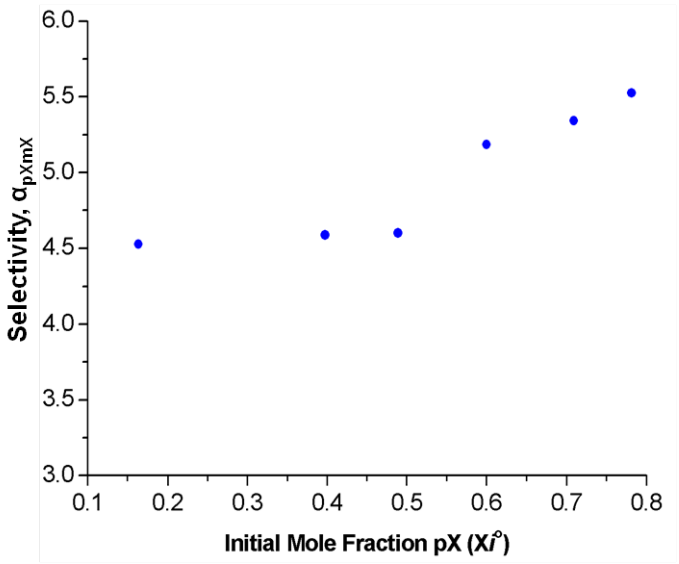

Figure 15: *Selectivity, αpXmX, of **11D** with increasing pX uptake, calculated using equation 1. The pX/mX ratio in the supernatant does not change during these experiments, confirmed by direct GC analysis.*

A similar effect has been observed with increasing the partial pressure of one gas in a binary mixture during separation using MOF-5 membranes: Increasing the partial pressure of CO_2 in a CO_2/N_2 mixture results in a higher CO_2 selectivity[40]. Also, CO_2 cooperative interactions between CO_2 molecules and host amino groups on uptake increases the affinity of the Zn-Atz (Amino Triazole) MOF for CO_2[41]. Here, increasing the number of host-guest interactions between pX and **11D** with increasing pX uptake is enhancing the selectivity of the material towards pX.

5.3.7 Single Crystal Structure Analysis to Explain Xylene Selectivity

5.3.7.1 pX/mX Selectivity

As pX/mX is the most required separation, detailed analysis of the pX and mX xylene locations within the channels of **11P** and **11M** respectively and the interactions between the xylene guests and their host framework gives an insight into the high selectivity of the framework towards pX over mX.

Structure analysis of **11P** shows that the core structure is the same as **11D** but with a larger unit cell volume due to the inclusion of pX into the framework; **11D** has a unit cell volume of 1632.08 $Å^3$, which increases to 1673.27 $Å^3$ in **11P**. Analysis of the void space in **11P** with xylenes removed give a total accessible volume of 448.9 $Å^3$, corresponding to 26.8 % of the unit cell volume (compared to 405 $Å^3$ and 24.9 % respectively in **11D**).

As mentioned in chapter 4, there are two voids within the structure of **11D**; channel 1 being the larger and channel 2 the smaller. Analysis of channels 1 and 2 individually in **11P** with pX removed show increases in the size of both from **11D** to **11P**, with channel 1 being 242.5 $Å^3$ and void 2 now being 206.4, compared to 186.2 $Å^3$ and 218.8 $Å^3$ respectively in **11D**. This shows an overall expansion in the void space from **11D** to **11P,** consequential of pX inclusion into the framework. Within the structure of **11P**, two crystallographically unique pX molecules are present within the two independent channels which both refine to 100 % occupancy (pX1 and pX2 respectively). Both xylenes line up down the channels along the a-axis (*Figure 7A*).

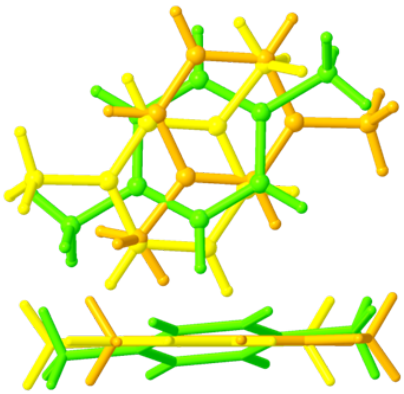

Figure 16: *Orientation of pX in **11P** (green) and two parts of disorder of mX in **11M** (yellow/orange) in channel 2. Figure adapted from reference*[38].

The single crystal structure of **11M** again has the same structure as **11D**, but it has an even larger unit cell volume than both **11D** and **11P** of 1729.02 $Å^3$. Analysis of the void space in **11M** with

xylenes removed give a total accessible volume of 501.8 Å^3, corresponding to 29.0 % of the unit cell volume (compared to 405 Å^3 and 24.9 % respectively in **11D** and 448.9 and 24.9 % respectively in **11P**) (*Table 6*). Analysis of channel 1 and 2 individually shows an increase in the size of both from **11D** and **11P**, with solvent accessible volumes of 283.6 Å^3 and 218.2 Å^3 respectively, compared to 218.8 Å^3 and 186.2 Å^3 respectively in **11D** and 242.5 Å^3 and 206.4 Å^3 and respectively in **11P**. The framework has had to distort to a greater extent in the case of **11M** due to the inclusion of the larger mX and its disordered presence within both channels. In the channel 2, the mX2 molecule is disordered about the central aromatic ring, and occupies a total volume of 125 Å^3 at isolated 'pinch points' along the 1D channel, with the aromatic rings from both parts of the disorder offset from the idealised location of the pX central aromatic ring seen in **11P** mX2) (*Figure 16*). In the channel 1, mX is disordered over two positions across an inversion centre occupying 135 Å^3, and the whole molecule is disordered throughout the length of the channel (2 part disorder (mX1a and mX1b). However, the relative occupancies of both mX molecules are 100 % and 50 % in the channels 1 and 2 respectively, giving an average amount of 75% mX per formula unit (compared to 100 % occupancy of pX in **11P**).

The GCMC calculations predicted that no mX would fit into **11D**, however the large expansion in unit cell volume between **11** and **11M** accounts for this uptake. Calculations re-run on **11M** with all xylene molecules removed show an uptake of mX into the larger channel 1 but no uptake into the smaller channel 2, meaning theoretically based on this structure we could expect a maximum loading of 50 % mX.

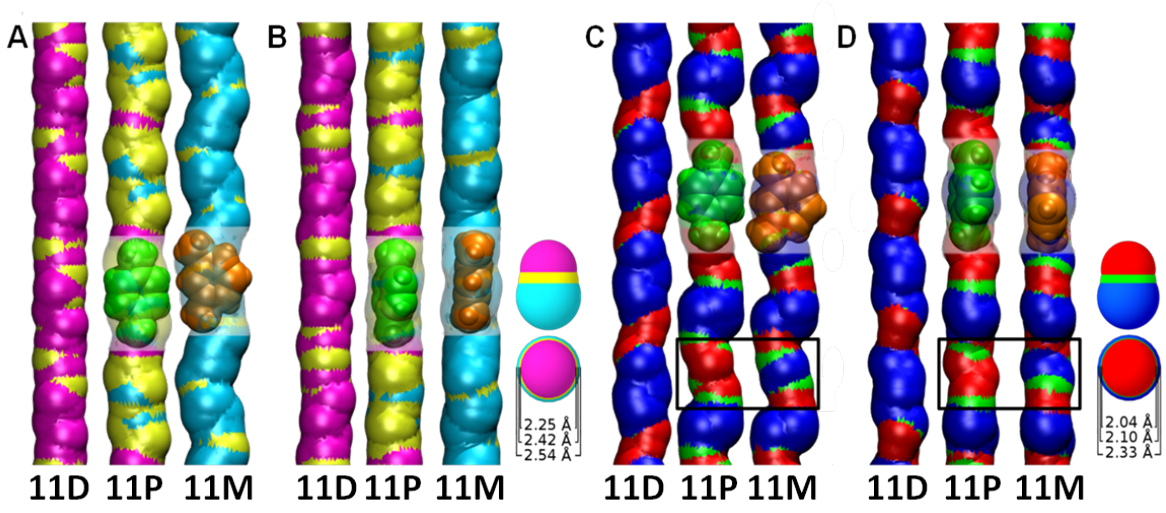

Figure 17: *Channel analysis using HOLE2[42-43]. In each part A-D, phase **11D**, **11P** with location of pX shown and **11M** with mX shown respectively. A: void 1 top view; B: void 1 side view; C: void 2 top view; D: void 2 side view. Only one part of mX disorder is shown in each channel for clarity. Figure adapted from reference[38].*

Analysis of the xylene locations within the channels allows an initial insight into the selectivity of the material. In channel 1 of **11P**, the pX1 molecules lie at fixed pinch points along the channel (*Figure 17A*). The central aromatic ring lies at the largest part of the channel (green), with the methyl groups pointing towards the smaller regions (magenta). There is less definition in channel 1 of **11M**, hence mX1 is disordered throughout the channel, causing the channel to almost take on the shape of an mX molecule, with a zig-zag continuum (*Figure 17A*). There is a tilt in the plane of the central aromatic ring of pX1 in **3P** channel 1 and mX1 in **3M** channel 1 (*Figure 17B*). The mX molecule needs to shift from the largest point in the channel in order to allow the methyls to fit. This has an effect on the intermolecular interactions formed between the guest mX and framework **11M**, which are discussed later.

There is not a great expansion in channel 2 upon guest uptake; the change affects the morphology of the channel. As seen in channel 1, pX2 lies at pinch points in channel 2 of **11P**, with the central aromatic ring found at the largest diameter section if the channel (blue), with smaller diameter regions found surrounding this (red), housing the methyl group of pX2 (*Figure 17C*). In **11M**, mX2 is found at the same large region of the channel, but is disordered over two positions, with both parts of the disorder offset from the pX central aromatic ring location, a shift which is necessary to fit the mX-methyl groups into the channel (*Figure 16*). Again there is a tilt between the plane of pX in **11P** and mX in **11M** in channel 2 (*Figure 17D*). There is also an additional large diameter region (blue) created in channel 2 of **11M**, created as a result of the interaction of mX with the framework (*Figure 18*).

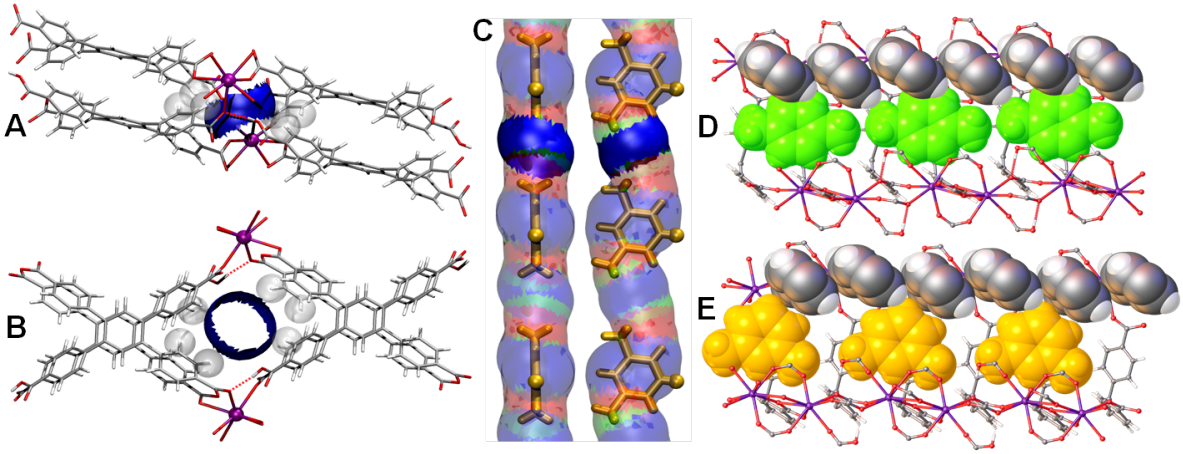

Figure 18: A: *Extra blue region in* ***11M*** *channel 2; B: 100 direction of channel 2. H12, H51 and H52 are highlighted; C: Pore surface of channel 2 in* ***11M*** *showing (pX2a only shown); D: Channel 2 of* ***11P*** *with pX2 guest (green) and the channel cut away. Rings 2 and 5 are shown in spacefill; E: Channel 2 of* ***11M*** *with mX2a guest (orange) and channel cut away. Rings 2 and 5 are shown in spacefill*[43]*.Figure taken from reference* [38].

Channel 2 of **11M** has a large diameter region (blue) in an area at which no guest mX is found. This is in contrast to **11P**, in which the specific locations along the channel at which pX enter and sit are optimised following inclusion of pX into **11D** to form **11P**. This extra blue region is surrounded by the H atoms on rings 2 and 5 (*Figure 18A,B*). When mX enters the framework and sits at the largest point in the channel, the H at position 5 of the mX molecule interdigitates between rings 2 and 5 of the HTCPB ligand (*Figure 18C*), causing them to twist from the positions observed in **11P** with a O58-C56-C53-C52 torsion angle of 4.16° for ring 5 and a smaller O28-C26-C23-C22 torsion angle of 0.77° for ring 2, which in turn creates the extra blue region (*Figure 18D,E*). The torsions created result from the close contact of the hydrogen at the 5 position of the mX guest aromatic ring with rings 2 and 5 of the framework HTCPB ligand. This emphasises that despite the fact flexibility will allow mX to enter the framework, its position within the channel is compromised and creases unnecessary pore space away from the site at which mX sits.

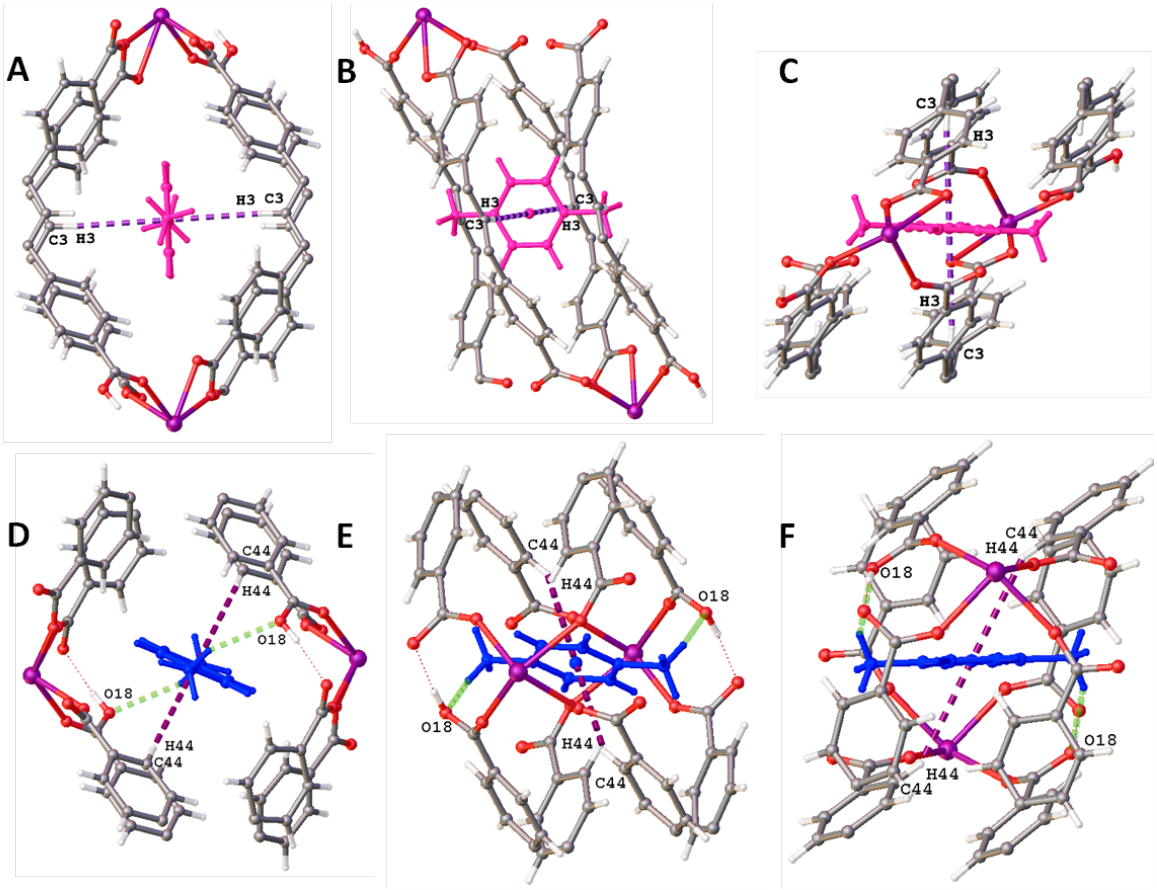

Figure 19: *Interactions between guest pX1 (pink) in channel 1 and pX2 (blue) in channel 2 and host framework* ***11P****. A,D: View down 100; B,E: View down 010; C: View down 001; F: View along plane of guest pX2. C-H···π interactions shown in purple, C-H···O interactions shown in green.*

In channel 1, the pX molecule sits in the ideal location allowing the formation of two symmetry equivalent C3-H3···π interactions between hydrogen on the central ring of the HTCPB ligand with the π-system of pX with a distance of 5.658 Å at an almost perfect angle of 92.097 ° (*Figure 19A-C, Table 11*). Aromatic C-H···π interaction lengths are quoted using protein structure cut-offs, in which the distance between the centroid of the donor and acceptor aromatic rings are measured and this is the case throughout this thesis[44]. This reports that all interactions to be considered C-H···π are between 4.5-7 Å.

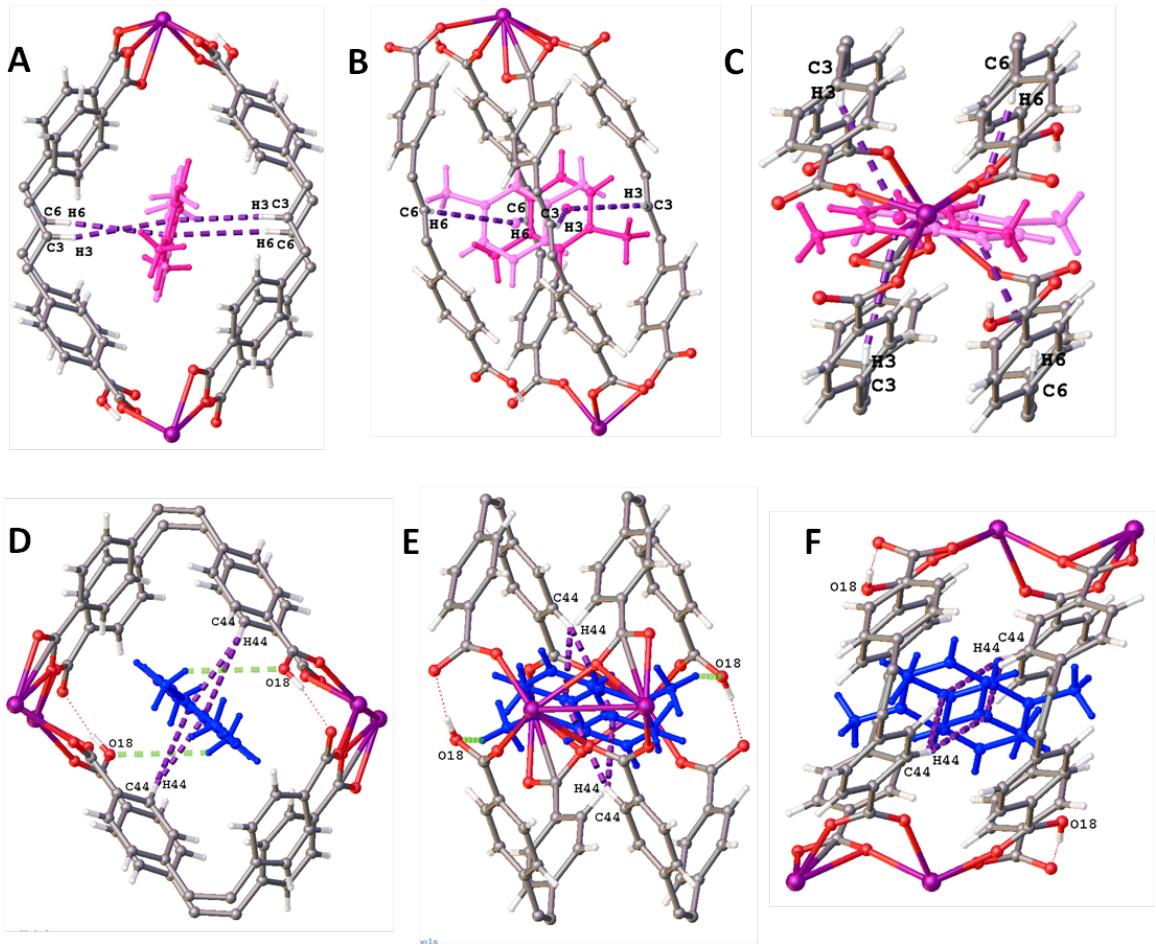

Figure 20: *Interactions between guest mX1a (pink) and mX1b (pale pink) in channel 1 and mX2 (blue) in channel 2 and host framework* ***11M****. A,D: View down 100; B,E: View down 010; C: View down 001; F: View along plane of guest pX2. C-H···π interactions shown in purple, C-H···O interaction*

In order for mX to fit into channel 1 in **11M**, it has to twist from the pX ring plane by 16 ° and disorder with the central aromatic ring offset from the pX central aromatic ring location. This poorer fit for mX means that the C-H···π interactions are strained and weaker than the corresponding interactions found between **11P** and pX for both of the partial mX molecules, called mX1a and mX1b in **11M**. Both mX1b and mX1b sit away from the inversion centre meaning their

C-H···π interactions are not symmetrical: mX1a has C3-H3···π interactions of 5.811 Å at 93.75 ° and 6.026 Å at 93.75 °; mXb has C6-H6···π interactions of 6.184 Å at 89.067 ° and 5.961 Å at 89.067 ° (*Figure 20A-C, Table 11*).

Table 11: *Interactions present between guest pX, mX, oX and EB and host frameworks* ***11P****,* ***11M,*** ***11O*** *and* ***11EB*** *for comparison. Where 2 interactions per X, this indicates 2 symmetrical contacts:*

Interaction	Donor Atom/ Interaction	C-H···π centroid-centroid		C-H···O18		Nº interactions per X
		Length (Å)	Plane-Plane Angle (°)	Length (Å)	Angle (°)	
11P –pX1	H3···π	5.658	92.097	-	-	2
11P – pX2	H44···π	5.561	146.230	-	-	2
11P – pX2	O18···H20C-C20X	-	-	2.583	146.296	2
11M – mX1a	H3···π	5.811	93.750	-	-	1
11M – mX1a	H3···π	6.026		-	-	1
11M – mX1b	H6···π	6.184	89.067	-	-	1
11M – mX1b	H6···π	5.961		-	-	1
11M – mX2	H44···π	5.938	142.140	-	-	1
11M - mX2	H44···π	4.931		-	-	1
11M - mX2	O18···H10A-C10X	-	-	3.351	128.200	1
11PM – pX1a	H3···π	5.694	9.993	-	-	1
11PM – pX1a	H3···π	5.665		-	-	1
11PM – pX1b	H6···π	5.903	89.004	-	-	2
11PM – pX2	H44···π	5.503	145.390	-	-	2
11PM –pX2	O18···HXA-C10X	-	-	2.015	143.200	2
11O – oX1	H3···π	5.336	136.978	-	-	1
11O – oX1	H3···π	6.325		-	-	1
11O – oX2	H6···π	5.363	140.902	-	-	1
11O – oX2	H6···π	6.406		-	-	1
11O – oX3	H44···π	5.828	136.692	-	-	1
11O – oX3	H44···π	4.787		-	-	1
11EB – EB1	H6···π	6.138	76.885	-	-	2
11B – EB2	H44···π	5.497	138.900	-	-	2

In channel 2, the intermolecular interactions are also a lot more favourable for pX in **11P.** The pX molecule sits at the centre of the channel on the inversion centre and is held in place by both C44-H44···π interactions of 5.561 Å at 96.77 ° and C20-H20C···O18 hydrogen bonds of 3.442 Å at 146.3 °[45]. These create a perfect pocket for the pX molecule (*Figure 19D-F, Table 11*). In the case of mX in **11M**, the mX molecule is disordered over two positions which again sit offset from the pX ring position in **11P**. As a result of this, asymmetric C-H···π seen for pX in channel 2 of **11P** can be picked up: both C44-H44···π interaction at 4.931 Å and 5.938 Å at 142.14 ° and a C10X-H10A···O18 interaction of 3.450 Å at an angle of 143.2 ° (*Figure 20D-F, Table 11*).

For **11P**, in channel 2, the interactions between pX and the framework form a perfect pocket in which the molecule can sit. In channel 1, such interactions are less pronounced due to the channel being larger, however deviation of the structure from **11D** allows for pX molecules in both channels to fit in exactly. The position and orientation of the pX molecule in channel 2 agrees with the lowest energy docking sites in the GCMC calculations.

Due to the larger and less streamlined size and shape of the mX molecule, it has to distort the framework more to enter the channel and once inside, it tries to optimise interactions with the framework but as it is unable to sit at the centre of either channel 1 or 2, the interactions formed are weaker and more strained than the corresponding interactions formed with pX, which account for the disorder seen in the single crystal structure of **11M** and also explains the high selectivity of the material for pX.

As previously mentioned, the GCMC calculations carried out on the rigid structures of **11P** and **11M** predict a pX/mX selectivity of 5.00-5.33:1 for **11P** and 4.33 for **11M**[32]. This suggests that the framework has a thermodynamic preference to sorb pX as result of three factors: the first being that the framework has to distort itself to a lesser extent for the uptake of pX to form **11P** than it does for mX to form **11M**. The second is that there are clearly more energetically favourable sorption sites for pX in the structure and the third and final factor are the interactions between pX and the host that perfectly suit to the shape of the pX molecule, whereas those formed for mX are either strained or non-existent. The **11M** structure also prefers pX in the competitive GCMC calculations. As pX is therefore preferred in all **11D**, **11P** and **11M** structures, this confirms and highlights the overall selectivity of the material for pX.

The single crystal structure of **11PM** was determined following exposure of **11D** to an equimolar mixture of pX and mX. **11PM** has unit cell dimensions more similar to that of **11P** than **11M** (*Table 5*) with a unit cell volume of 1687.75 $Å^3$, closer to that of **11P** (1673.27 $Å^3$) than **11M** (1729.02 $Å^3$). Within the single crystal structure, only pX can be resolved and no mX can be seen. However, the overall total accessible volume of **11PM** is extremely close to that of **11M** at 503.8 $Å^3$ and 501.8 $Å^3$ respectively, larger than that of **11P** which is 448.9 $Å^3$. Both channels are affected by the presence of mX: mX opens up the channels more than pX due to its larger size, however structure analysis of **11P** and **11M** shows that pX forms much stronger interactions with the framework so despite mX having an effect on the overall morphology of the channels, pX is still the preferred guest, hence only pX can be found in the both channel 1 and 2. As a result of the larger unit cell volume and channel void volumes in **11PM** (*Table 6*), pX is disordered along channel 1 unlike in **11P** in which pX is found at isolated positions forming intermolecular interactions with the framework. However in channel 2, pX is found at the same location as in **11P**, with the same set of C-H···O and C-H···π interactions holding it in a pocket. PXRD analysis of the

pXmX loaded frameworks in the time dependence experiments index more closely to the structure of **11PM** than either **11P** or **11M**, showing that in the experiments the active phase is **11PM**. **11P** and **11M** individually are used to clearly demonstrate the interactions formed between either xylene and the framework, but **11PM** shows that in a mixture of both isomers the presence of mX affects the framework and causes it to distort and expand more than if it was in pure pX, but the same interactions between pX and the host framework remain, ensuring the high selectivity of the framework.

5.3.7.2 Other Xylene Selectivity

Following on from the docking calculations which showed that only pX and EB could fit into the rigid structure of **11D**, whereas oX and mX would not, maximum uptake calculations were run to forecast the selectivity of **11D** to pX/EB, pX/oX and EB/mX. The results predicted a pX/EB selectivity of 8, with infinite pX and EB selectivities for pX/oX and EB/mX mixtures respectively. As shown in table 7, the actual pX/EB, pX/oX and EB mX selectivities are 2.38, 5.65 and 2.38 respectively. The lower pX/EB selectivity observed can be attributed to the flexibility of the framework, allowing both similar sized isomers to diffuse into the channels and form similar interactions with the host framework. The lower experimental pX/oX and EB/mX selectivities again can be explained by framework flexibility, as both oX and mX can be taken up by **11D**, whereas the initial docking calculations did not expect this, hence infinite selectivities were predicted by the maximum uptake calculations[32].

Structure analysis of **11O** and **11EB** shows that the core structure, as seen with **11P** and **11M**, is the same as **11D** but with a larger unit cell volume; **11D** has a unit cell volume of 1632.08 $Å^3$, which increases to 1873.50 $Å^3$ in **11O** with the larger oX guest and 1703.70 $Å^3$ in **11EB**.

As discussed in section 5.8.2.1, a combination of xylene guest size and fit, together with intermolecular interactions which form between the guest and host framework, give rise to the xylene selectivity of **11D**: The more streamline pX fits into the channels more easily, allowing the framework to relax around the guest and form C-H···π and C-H···O and interactions which anchor the guest at isolated locations along the channel, whereas mX is unable to fit in in the same way which causes a greater expansion in the channel dimensions, reducing the effectiveness of any potential interactions which in turn causes mX to become disordered throughout the channel. This difference explains the high pX/mX selectivity of **11D**.

In the case of **11EB**, the guest EB is similar in size to pX (kinetic diameters of 6.0 Å and 5.8 Å respectively *(Figure 6*), however the extra carbon in the pendent chain provoke changes in guest

uptake and the position at which the guest is found in the channels; the position at which the guest fits best and can pick up the most favourable interactions.

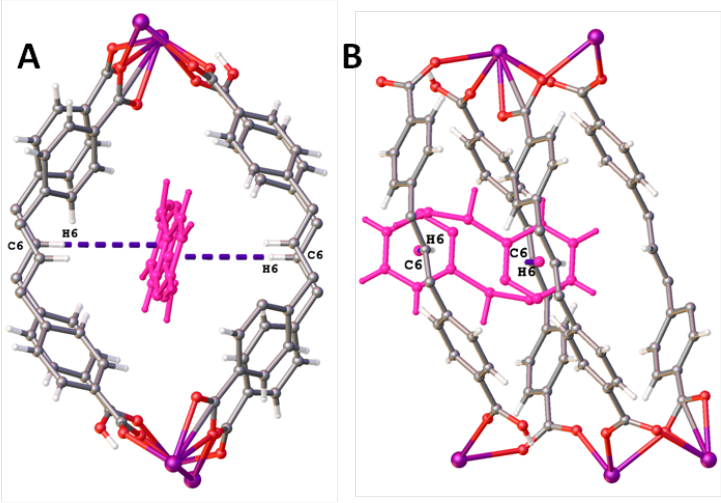

Figure 21: *C-H···π interactions between guest EB1 (dark pink) and host framework* ***11EB*** *in channel 1. A: View down 100; B: View down 010.*

In channel 1, C6-H6···π interactions of 6.138 Å (centroid-centroid[44]) between the central aromatic ring of the HTCPB ligand and the π-system of the EB guest anchor the guest at these specific locations in the channel (*Figure 21, Table 11*). However, unlike pX in channel 1 of **11P** in which two symmetrical interaction are formed with the framework on either side of the pX aromatic ring, only one interaction is formed with each part of the EB disorder.

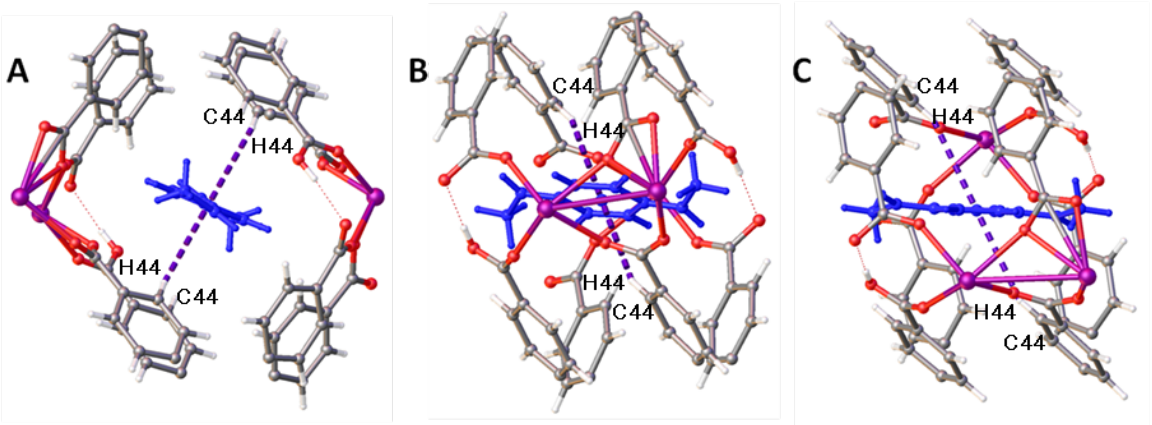

Figure 22: *C-H···π interactions between guest EB2 and host framework* ***11EB*** *in channel 2. A: View down 100; B: View down 010; C: view along plane of guest EB.*

In channel 2, the central aromatic ring of EB lies at a similar position to where pX lies in channel 2 of **11P**, with the pendent ethyl groups disordered over the 1- and 3- positions of the ring, almost mimicking an extended pX molecule. C44-H44···π interactions of 5.497 Å (centroid-centroid[44]) are present between ring 4 of the HTCPB ligand and the π-system of the EB guest

(*Figure 22, Table 11*). The C-H···O interactions observed in **11P** cannot be picked up with EB due to the orientation of the ethyl groups.

In the case of **11O**, the guest oX is the largest of all the xylene isomers with a kinetic diameter of 6.5 Å *(Figure 6*), so as may be expected, uptake of oX induces the biggest change in unit cell dimensions. The overall structure is the same as **11D**, but with a much larger void space and unit cell volume (*Table 5,6*).

In channel 1 of **11O**, there are two oX molecules, both disordered in the same way over two sites. Either part of the disorder is present with 50 % occupancy, meaning in channel 1 there are two whole oX guests. This is the only xylene loaded structure in which there are more than two guest molecules per unit cell; in **11O** there are 3 guests, two in channel 1 and one in channel 2. Either part of the disorder picks up one of two asymmetrical interactions. The centre of the disorder lies off the inversion centre, meaning the central aromatic ring of both disordered oX1 and oX2 each pick up two interactions, but as the central aromatic ring of the oX guest is offset from the centre of symmetry, these two interactions are not the same length, similar to that seen with mX in **11M**.

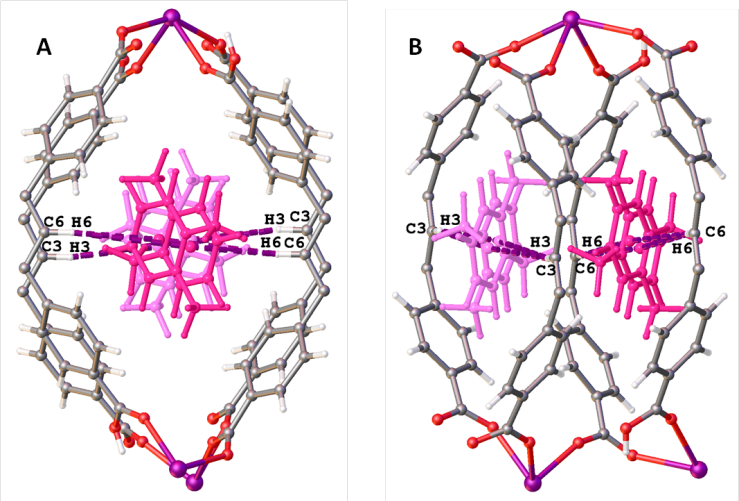

Figure 23: *C-H···π interactions between guest oX1 (dark pink) and oX2 (pale pink) and host framework* ***11O*** *in channel 1. A: View down 100; B: View down 010.*

A similar effect is observed for mX in **11M**; the guest has to shift off the ideal location in order to fit into channels meaning that intermolecular interactions cannot be optimised in the same way. For oX1, C6-H6···π interactions of 5.336 Å and 6.325 Å (centroid-centroid[44]) are present either side of the oX central aromatic ring from the central aromatic ring of the HTCPB ligand (*Figure 23, Table 11*). For oX2, C3-H3···π of 5.363 Å and 6.406 Å (centroid-centroid[44]) are present either side of the oX central aromatic ring from the central aromatic ring of the HTCPB ligand (*Figure 23, Table 11*).

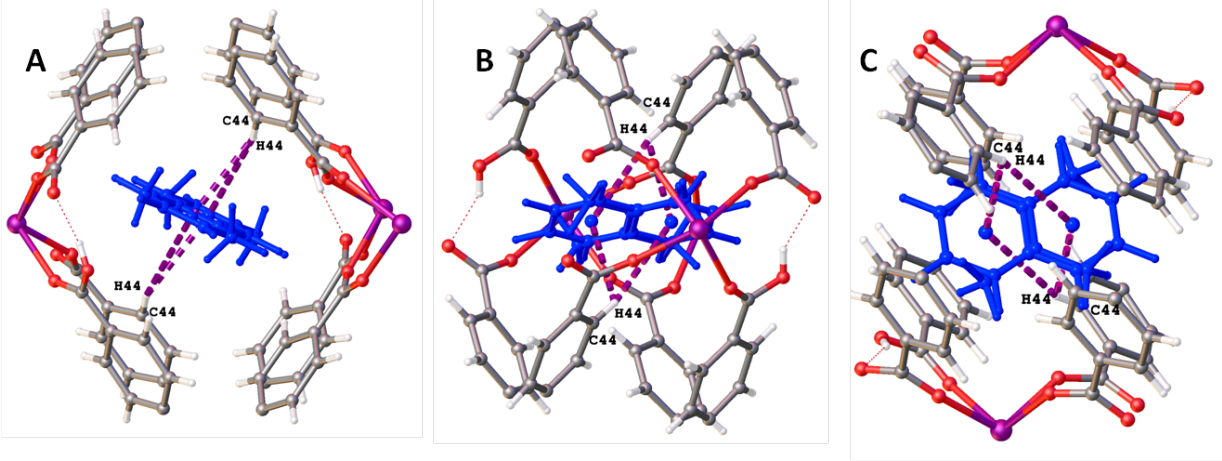

Figure 24: *C-H···π interactions between guest oX3 and host framework* ***11O*** *in channel 2. A: View down 100; B: View down 010; C: view along plane of guest oX.*

In channel 2, oX 3 is disordered over two positions. Both parts of the disorder pick up the same interactions with the host framework, but only one per part of the disorder. Two asymmetric C44-H44···π interactions of 5.828 and 4.787 Å (centroid-centroid[44]) are present between ring 4 of the HTCPB ligand and the π-system of each part of the disorder of the the oX guest (*Figure 24, Table 11*). Again, as for **11M** and **11EB**, the C-H···O interactions observed in **11P** cannot be picked up with oX.

If all xylene loaded framework are compared to each other, the selectivity observed can be explained (*Table 7*). The data shows that the selectivity towards pX, mX, oX and EB falls in the order pXoX > pXmX > EBmX = pXEB > oXmX > mXoX > mXEB = EBpX > mXpX > oXpX (*Table 7*). pX has the smallest kinetic diameter of 5.8 Å and can enter the channels of **11D** more easily than all the other isomers. The single structure of **11P** shows symmetrical C-H ···π interactions between the host framework and guest for both pX 1 in channel 1 and pX2 in channel 2, with an additional C-H···O interaction between HTCPB ligand carboxylate of ring 1 (COOH) and the methyl group of pX in channel 2. This is followed by EB with the second smallest kinetic diameter of 6.0 Å. Symmetrical C-H ···π interactions form between both disordered parts for EB1 in channel 1 of **11EB** and for EB2 in channel 1, however only one interaction can form for each part of the disordered EB in each channel. The second largest isomer is mX with kinetic diameter of 6.4 Å. mX is disordered in both channels due to the weaker interactions that form between host **11M** and guest mX. Asymmetric C-H ···π interactions form between each part of the disordered mX1 in channel 1 and mX2 in channel 2, due to the poor fit of the guest within the channels. Finally the largest guest isomer is oX with kinetic diameter of 6.5 Å. The structure must expand to such a large extent when taking up this isomer that it enters at a tilt, allowing two oX molecules

(oX1 and oX2) into channel 1 of **11O**, each of which forms asymmetric C-H ···π interactions with the channel walls. In channel 2 of **11O**, oX3 is also disordered and each part forms only one C-H···π interaction with the channels walls.

From this data, it can expected that the largest selectivity difference will be between the largest and smallers isomers, pX and oX, which is confirmed experimentally with an observed α_{pXoX} of 5.65. The second highest selectivity would be expected between the second largest and smallest isomers, pX and mX, which again is confirmed experimentally with an observed α_{pXmX} of 4.55. This trend follows with the smallest selectivity being between the two smallest isomers, pX and EB with an α_{pXEB} of 2.38.

Single crystal structure analysis of pX, mX, oX and EB loaded **11D** has allowed the high xylene selectivities observed experimentally to be explained through investigation of the channel space and intermolecular interactions present that form between guest xylene and host framework with guest uptake.

5.4 Benzene and Toluene loaded 11D

The single crystal structure of **11P** highlights a symmetrical set of C-H···π interactions either side of the pX molecule between the pX aromatic ring and the central aromatic ring of the HTCPB ligand-H in both channel 1 and channel 2 and C-H···O interactions between pX C-H and O17 of the protonated carboxylate 1 at either side of the molecule. These interactions form a perfect pocket around the pX molecule that result in the framework being highly selective to pX over mX.

In order to determine whether the framework would pick up these interactions with other similar aromatic guests, the desolvated framework **11D** was loaded with toluene (pX minus one methyl group) and benzene (pX minus both methyl groups).

5.4.1 Data Collection and Analysis

Two samples of single crystals of **11** were added to a Schlenk tube and were activated by heating at 100 °C at 10^{-2} mbar overnight to form **11D**. The Schlenk was then back-filled with N_2 and 1 ml of anhydrous toluene (Tol) and anhydrous benzene (Benz) was added. The Schlenk tubes were then sealed under N_2 and left for 24 hours after which time a single crystal was selected from each for data collection to determine the single crystal structure of toluene loaded **11D**: **11T** (*Figure 26*, *Table 12*) and benzene loaded **11D**: **11B** (*Figure 27, Table 12*).

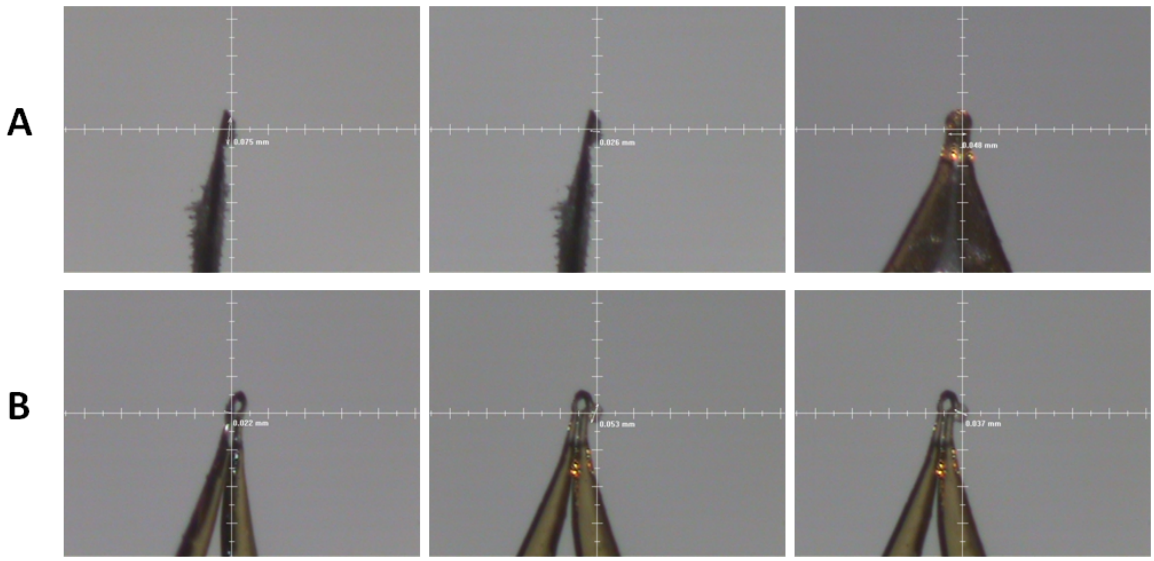

Figure 25: *Pictures of the crystals taken on the diffractometer displaying the crystal measurements: A:* ***11T****; B:* ***11B****.*

Table 12: *Unit cell dimensions for* ***11T*** *and* ***11B****:*

	Unit Cell Dimensions			
	a /Å	**b /Å**	**c /Å**	**V / Å^3**
11T	10.1080(2) 89.544(10)	12.3030(3) 80.514(6)	15.8855(4) 68.951(7)	1815.60(7)
11B	10.1368(16) 89.408(5)	12.0191(19) 79.391(5)	16.0650(2) 68.528(5)	1786.81(5)

5.4.1.1 Toluene Loaded 11D: 11T

The single crystal of **11T** used had dimensions of 0.075 × 0.048 × 0.026 (*Figure 25A*). The asymmetric unit of **11T** contains one Ce, one HTCPB ligand and 2.875 toluene (Tol) molecules (*Figure 26D*). In channel 1 there are two crystallographically unique Tol molecules; Tol1 (dark pink) and Tol2 (pale pink). Both refine to 50 % occupancy and when translational symmetry is applied, two distinct overlapping Tol molecules are found at each site. This produces two half Tol1 and two half Tol2 leaving 1 Tol molecule at each site meaning there are two whole Tol molecules per unit cell in channel 1.

In channel 2, when FVAR is applied to the refinement, 0.875 Tol3 molecules are present at 50 % occupancy. Upon application of translational symmetry, two '0.875' Tol3 molecules are present in the grown structure, both at 50 % occupancy, meaning 0.875 Tol molecules are present in channel 2 per unit cell. Thus overall 2.875 Tol are present within the unit cell of **11T**.

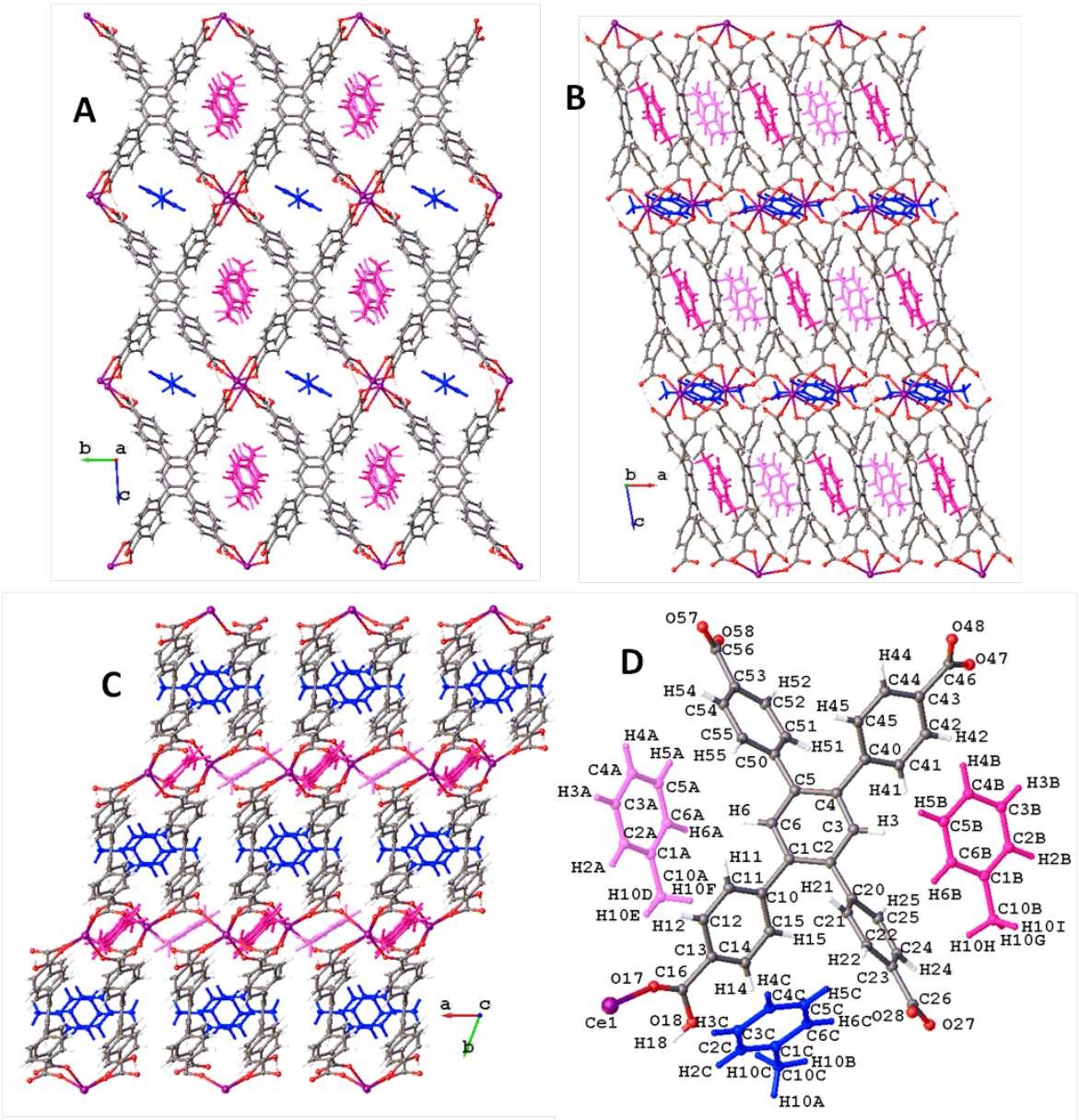

Figure 26: *Single crystal structure of **11T**. A: View down 100; B: View down 010; C: View down 001; D: Asymmetric unit with Tol1 (dark pink) and Tol2 (pale pink) in channel 1 and Tol3 in channel 2 (blue).*

5.4.1.2 Benzene Loaded 11D: 11B

The single crystal of **11B** used had dimensions of 0.053 × 0.037 × 0.022 *(Figure 25B)*. The asymmetric unit of **11B** contains one Ce, one HTCPB ligand and 2.5 benzene molecules: 0.5 Benz1 and 0.5 benz2 are found in channel 1 per asymmetric unit and in channel 2 there are 1.5 benzene molecules: 1 benz3 and 0.5 benz4 (*Figure 27D*). However there is also H_2O coordinated to Ce in channel 2 some of the time. When H_2O at 26 % occupancy is present at Ce1, only benz4 is present in channel 2 also at 26 % occupancy. When H_2O is not coordinated, benz4 is not longer seen and

benz 3 is present at 37 % occupancy. This means that in channel 1 there is 1 benzene molecule per formula unit and in channel 2 there are 0.26 H_20 and 0.5 benzene molecules per formula unit, giving 3 benzenes per unit cell, compared to the 2.975 guest Tol molecules per unit cell in **11T** and 2 guest pX or mX molecules in **11P** and **11M** respectively.

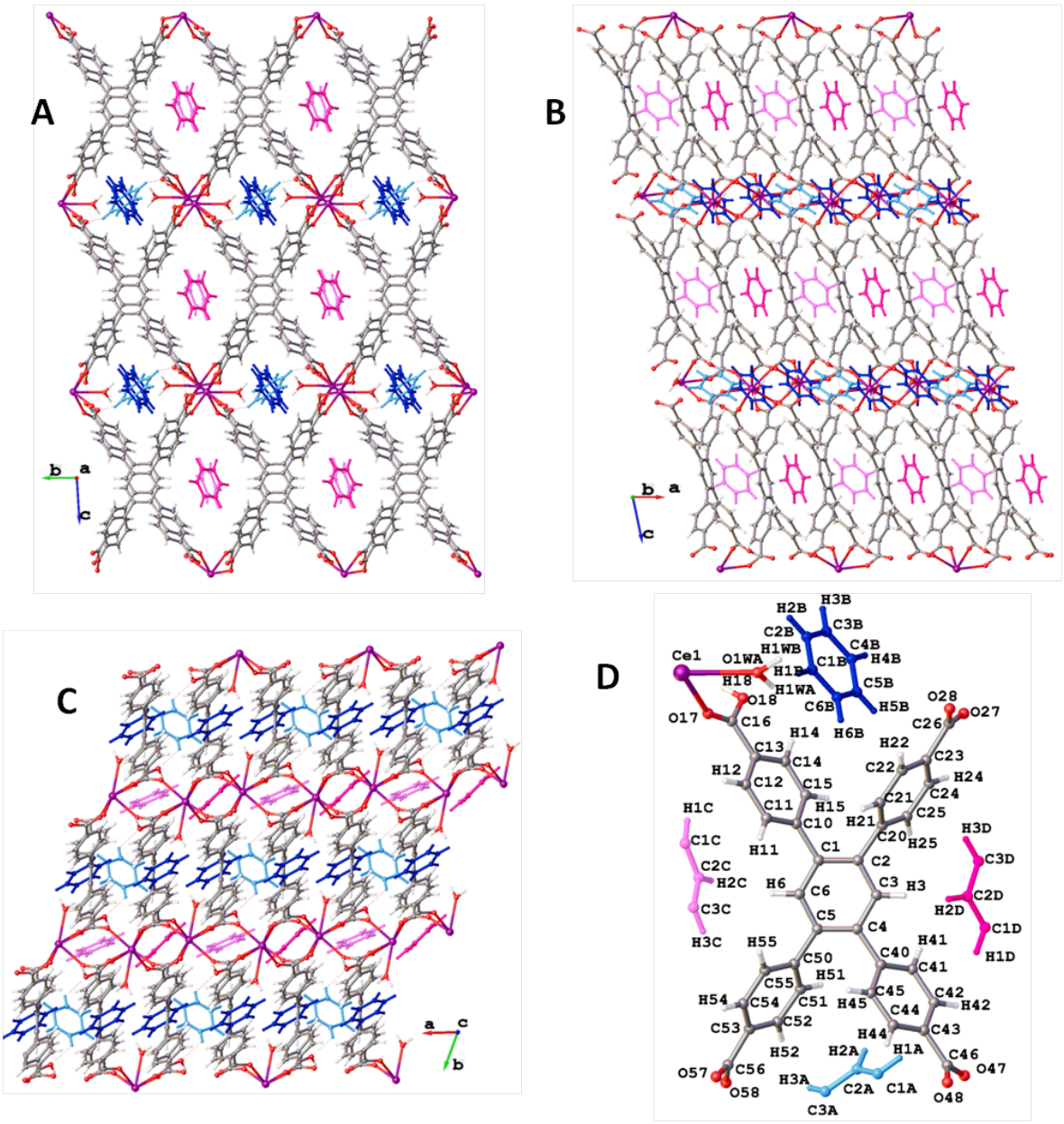

Figure 27: *Single crystal structure of* ***11B****. A: View down 100; B: View down 010; C: View down 001; D: Asymmetric unit with Benz1 (dark pink) and Benz2 (pale pink) in channel 1 and Benz3 (dark blue) and Benz4 (pale blue) in channel 2.*

5.4.2 Single Crystal Structure Description

In the single crystal structure of **11P**, two intermolecular interactions between each pX and the framework HTCPB ligand hold pX at isolated positions throughout the channel and four interactions hold pX within a perfect pocket in channel 2. In channel 1 these are two symmetric C—H···π interactions either side of the pX central aromatic ring and in channel 2 there are two sets of symmetrical interactions; one set either side of the pX central aromatic ring and the other set between the pX methyls and the framework ligand aromatic rings.

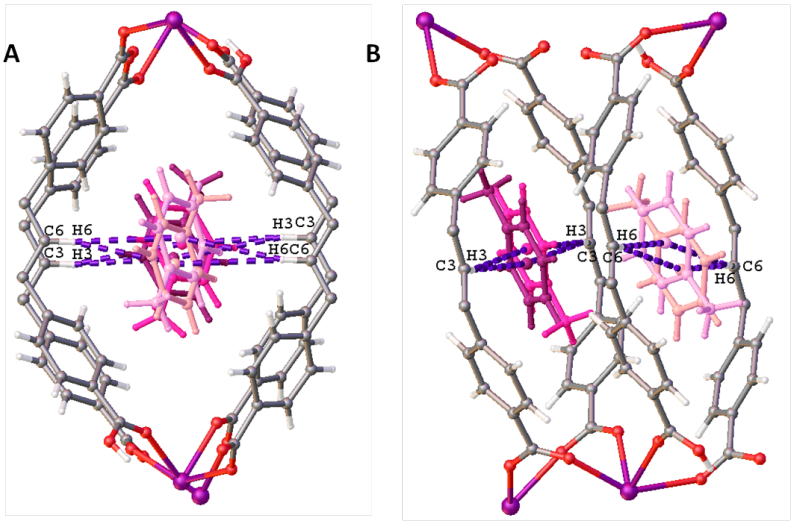

Figure 28: *Toluene location within channel 1 of **11T**. Two parts of Tol1 disorder shown in darker pink (Tol1a) and dark pink (Tol1b) and two parts of Tol2 disorder shown in pale pink (Tol2a) and pale peach (Tol2b). A: View down 100; B: View down 010.*

When pX is substituted with toluene, the structure and position of the guest Tol molecule is very different to than observed for pX in **11P** in channel 1. The removal of one methyl from pX in Tol1 and Tol2 means that the molecule has reduced in length and can therefore fit into the channel in a different way; pX must stay streamline in order to pass through the channel but the shortened Tol can enter at an angle. This means that where there was one pX found in channel 1 of **11P**, two Tol (Tol1 and Tol2) are found in channel 1 of **11T**. This removes the possibility of strong C-H···π interactions forming between the Tol aromatic ring and the framework as seen for pX in **11P**, hence each of the two Tol molecules found in channel 1 are disordered over two positions. However, weak C-H···π bonds are present between the central aromatic ring C-H of the HTCPB ligand in the framework and the aromatic ring of the disordered Tol guests (*Table 13*). For Tol1 (dark pink in *Figure 26*), the two parts of the disorder are labelled Tol1a (darker pink) and Tol1b (dark pink) and centroid-centroid C-H···π interactions are measured to the calculated centroid of the toluene aromatic rings[44]. Tol1a forms two symmetrical C3-H3···π interactions of 5.764 Å and

Tol1b also form two symmetrical interactions from the framework to either side of the aromatic ring of 5.858 Å. For Tol2 (shown in pale pink in *Figure 26*), the two parts of the disorder are labelled Tol2a (pale pink) and Tol2b (pale peach). Tol2a and Tol2b each form two symmetrical centroid-centroid aromatic C6-H6··· π interactions with the framework of 5.610 Å and 5.912 Å respectively (*Figure 28, table 13*).

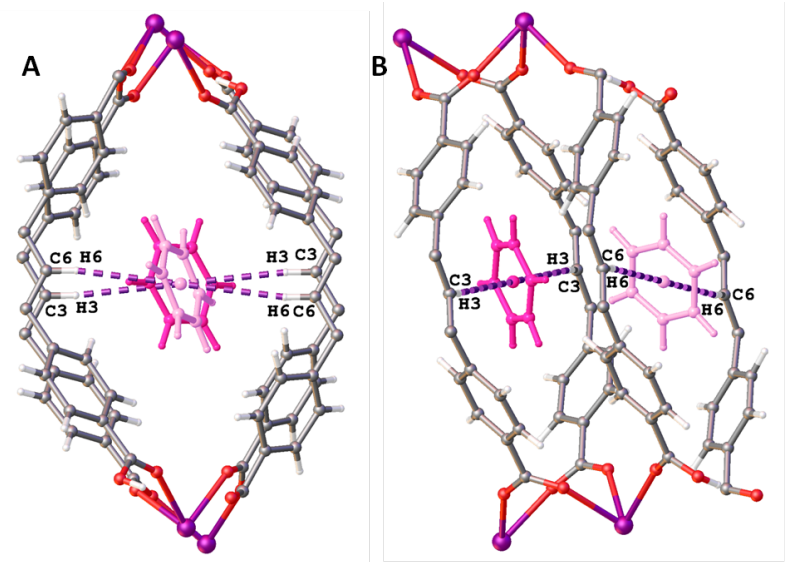

Figure 29: Benzene location within channel 1 of 11B. Benz1 shown in dark pink and Benz2 shown in pale pink. A: View down 100; B: View down 010.

When benzene is loaded into the framework, the position of the benzene rings differs from both the pX loaded (**11P**) and Tol loaded (**11T**) structures. In the larger channel 1, two benzene molecules are present in place of one pX, the same as seen for Tol in **11T**. Two symmetrical weak C-H···π interactions are present between the central aromatic ring C-H of the HTCPB ligand in the framework from H3 and H6 to and the aromatic ring of the Benz1 and 2 molecules respectively (*Table 13*). For Benz1 (dark pink in *Figure 27*), two symmetrical C3-H3··· π interactions from the framework to either side of the aromatic ring of 5.639 Å are present. For Benz2 (shown in pale pink in *Figure 27*), two symmetrical centroid-centroid aromatic C6-H6··· π interactions with the framework of 5.593 Å (*Figure 29, Table 13*) are present. In channel 1 of both **11B** and **11T**, the orientation of the guest in similar to that of oX in **11O**, in which two guests enter the channel 1 per unit cell, rather than one guest per unit cell in **11P**, **11M** and **11EB**.

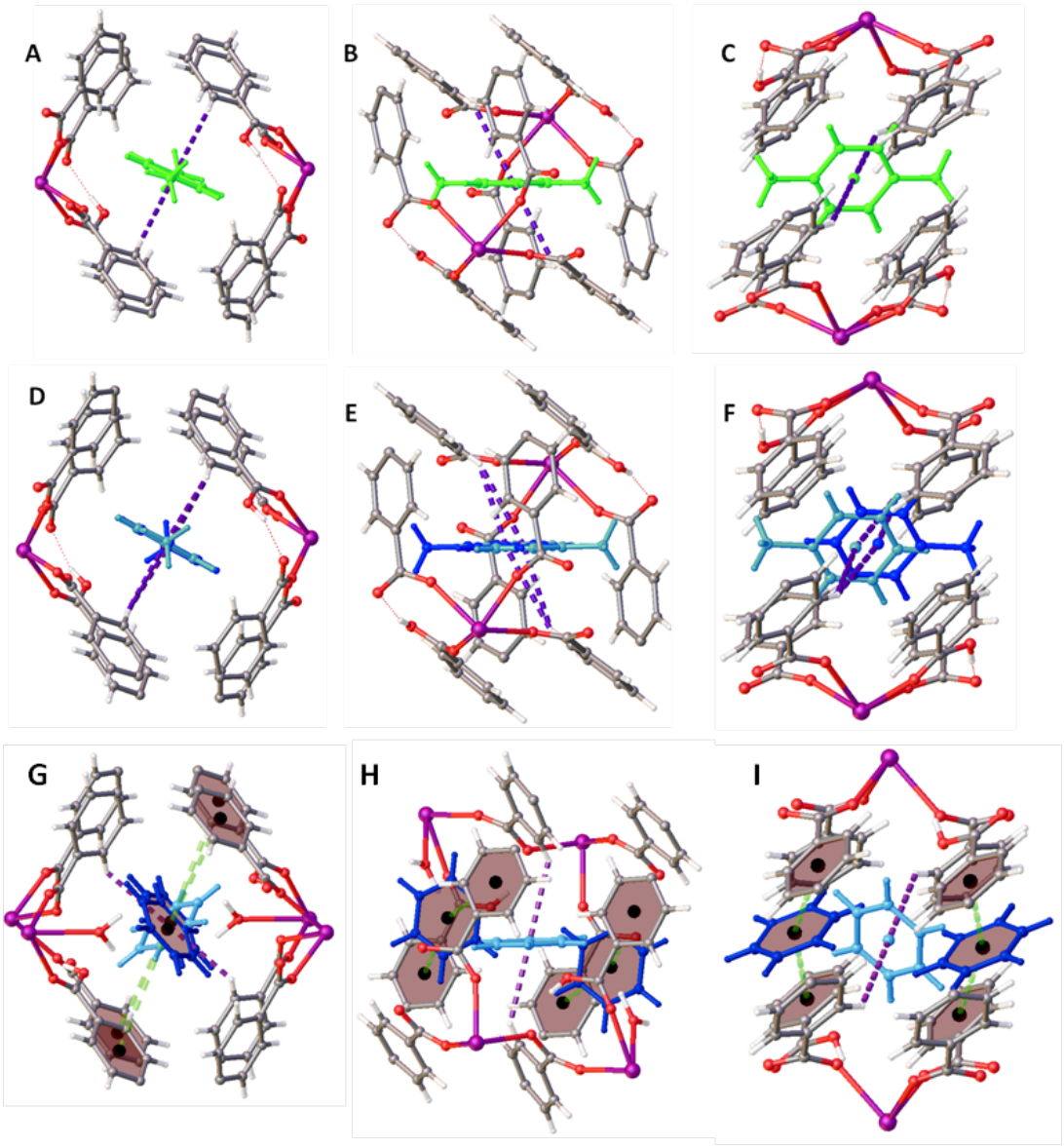

Figure 30: *Position of pX in channel 2 of* ***11P*** *(A-C) compared to symmetry generated Tol3a (dark blue) and Tol3b (pale blue) in channel 2 of* ***11T*** *(D-F) and Benz 3 (dark blue) and benz 4 (pale blue) in channel 2 of 11B (G-I). A,D: View down 100; B,E: View over plane of guest molecule; C,F: View down 001. pX shown in green. C-H···π interactions shown in purple and π···π interactions shown in green.*

In the smaller channel 2 of **11T**, the Tol is disordered over two positions, mimicking a slightly elongated pX molecule (*Figure 30*). The same intermolecular interactions between host framework and guest molecules can be picked up for both pX and symmetry equivalent Tol3a and Tol3b in **11P** and **11T** respectively (*Table 13*).

Table 13: *Interactions present between guest pX, Toluene and Benzene and host framework* ***11P****,* ***11T*** *and* ***11B*** *for comparison:*

Interaction	Donor Atom/ Interaction	C-H···π centroid-centroid		Shift (Å)	C-H···O18		Nº interactions per X
		Length (Å)	Plane-Plane Angle (°)		Length (Å)	Angle (°)	
11P –pX1	H3···π	5.658	92.097	-	-	-	2
11P – pX2	H44···π	5.561	36.770	-	-	-	2
11P – pX2	C20X-H20A···O18	-	-	-	2.583	146.296	2
11T - Tol1	H3···π	5.764	127.536	-	-	-	1
11T - Tol1	H3···π	5.858	157.022	-	-	-	1
11T – Tol2	H6···π	5.610	36.146	-	-	-	1
11T – Tol2	H6···π	5.921	37.007	-	-	-	1
11T – Tol3	H44···π	5.168	37.570	-			1
11T – Tol3	H44···π	5.615	36.910	-			1
11T - Tol3	C10C-H10C···O18	-	-	-	2.510	153.042	1
11B – Benz1	H3···π	5.639	136.056	-	-	-	2
11B – Benz2	H6···π	5.593	110.224	-	-	-	2
11B – Benz3	L(ring 1) ··· B4 π···π	4.894	0.819	3.397	-	-	2
11B – Benz4	H52···π	4.978	116.856	-	-	-	2

Whereas in the larger channel 1, with the loss of the extra docking methyl group the Tol molecules tilt and pack into the channel with two Tol molecules per equivalent 1 pX in **11P**, in channel 2 which is the smaller of the two channels, the Tol enters and sits at a very similar position to pX in **11P**, but the methyl groups at the 1- and 3- positions on the aromatic ring are disordered over two sites, creating the overall appearance of an elongated pX molecule (*Figure 30C,F*). For this reason, the same C44-H44···π interactions between the host framework **11T** and both parts of the toluene disorder, Tol3a and Tol3b can be formed at 5.168 and 5.615 Å respectively, comparable in length with the equivalent C44-H44···π interactions formed between **11P** and pX of 5.561 Å in channel 2.

The same C10C-H10C···O18 between guest Tol3 and **11T** can be formed as seen for the pX C20X-H20A···O18 interaction in **11P**. However, whereas in **11P** two C-H···O interactions form; one at each methyl group, in **11T** only one C-H···O interactions can form per Tol guest; one for each part of the Tol disorder. A combination of these interactions helps anchor the Tol3 in place, however there is a small amount of disorder in the direction of the channel, as the number or methyl hydrogen bonding sites has been halved compared to pX. The width of the channel means that the Tol3 cannot tilt as in channel 1 and can therefore pick up these three interactions per molecule and be held at isolated positions along the channel.

In channel 2 of **11B**, the loss of both methyls (compared to pX and Tol) means that the molecule can fit into the channels at a pronounced tilt, whereas pX in **11P** and Tol in **11T** enter in line with the channel. H_2O is also found coordinated to Ce in channel 2 of **11B**, with an occupancy of 26 %. Benz3 and Benz4 are found in channel 2, however not simultaneously. When H_2O is coordinated, only Benz3 is present also at 26 % occupancy. When neither H_2O or benz3 are present, two symmetry equivalent benz4 molecules are found, each refining to 37 % occupancy. As the benzene guests enter at a tilt, strong C-H···π interactions as seen in **11P** and **11T** in channel 2 cannot form, however two symmetrical weak C52-H52···π interactions at 4.978 Å are seen between the framework and Benz4. Weak π ···π stacking interactions can be seen between Benz3 and ring 1 of the HTCPB ligand at a distance of 4.894 Å, at a shift of 3.397 Å (*Table 14*). No C-H···O interactions are present from the protonated carboxylate of ring 1 and either Benz3 or 4 in channel 2 due to the location of the molecule. This interaction is picked up for pX in **11P** and Tol in **11T** from the pendent methyl groups of the guests, however it cannot be formed for benzene, which does not posess any methyl groups.

In summary, in comparison to the location of pX in **11P**, both **11T** and **11B** loaded structure see a difference in the positions at which the guest molecules are found and the interactions picked up by the guests with the framework. In **11P**, both pX1 in channel 1 and pX2 in channel 2 line up down the channel, picking up symmetrical C-H···π contacts with the central aromatic ring of the pX molecules and in channel 2, an additional C-H···O contact from the protonated carboxylate group on ring 1 of the HTCPB ligand. In **11T**, Tol3 is disordered to mimic a pX molecule in channel 2 and can therefore pick up the same C-H···π and C-H···O as pX. However the loss of a methyl group from the guest molecule means that in channel 1, two Tol molecules enter the channel at a tilt, both disordered, which can only pick up weaker C-H···π interactions. In **11B**, with the loss of both methyl groups compared to pX, the molecule enters both channels at a tilt, with Benz 1 and 2 being found in place of pX 1 in channel 1 and Benz 3 and 4 being found in place of pX2 in channel 2.

These aromatic molecules were loaded into single crystals of **11D** to investigate the reason for the optimal pX docking site and interactions present. The results show that the framework has an almost ideal location in both channels for a pX molecule. Substitution with other similar aromatic guests results in the loss of one or more interactions, causing the guest to form weaker interactions and move within the channels.

5.5 Single Crystal X-Ray Determination of Xylene Loaded 11R

5.5.1 Data Collection and Analysis

Phase **11R** was reached by heating a mitegen tip glue-mounted single crystal of **11** slowly on the diffractometer using the nitrogen stream. The crystal was then removed and exposed to air to induce conversion to **11R** and the crystal was then replaced onto the diffractometer for a data collection to confirm the presence of **11R**. The crystal was then removed and inverted over a vial of pX and left for 24 hours for the xylene vapour to diffuse into the crystal. After this time, data collection on the pX crystal allowed determination of the single crystal structure of **11RP** (*Table 14*).

Table 14: *Unit cell dimensions of pX (**11RP**) and mX (**11RM**) loaded **11R**:*

Ce(HTCPB)	Unit Cell Dimensions			Unit Cell Volume (Å^3)	R_1 (%)
	a (Å) α (°)	b (Å) β (°)	c (Å) γ (°)		
11R	5.0714(9) 109.850(9)	18.4520(3) 90.950(10)	19.5430(4) 94.481(9)	1713.10(5)	8.98
11RP	5.1157(7) 73.971(7)	18.5940(3) 89.081(7)	19.7500(3) 84.768(7)	1798.00(5)	14.86

The single crystal of **11RP** used had dimensions of 0.055 × 0.055 × 0.044 mm (*Figure 31A*). **11RP** has the same overall structure as **11R** but with pX loaded into channel 1 (*Figure 31A-C*). The asymmetric unit contains one half pX molecule in channel 1 which refines to 100 % occupancy (*Figure 31D*). This means that per unit cell there is one whole pX molecule, 1/2 per Ce(HTCPB) formula unit.

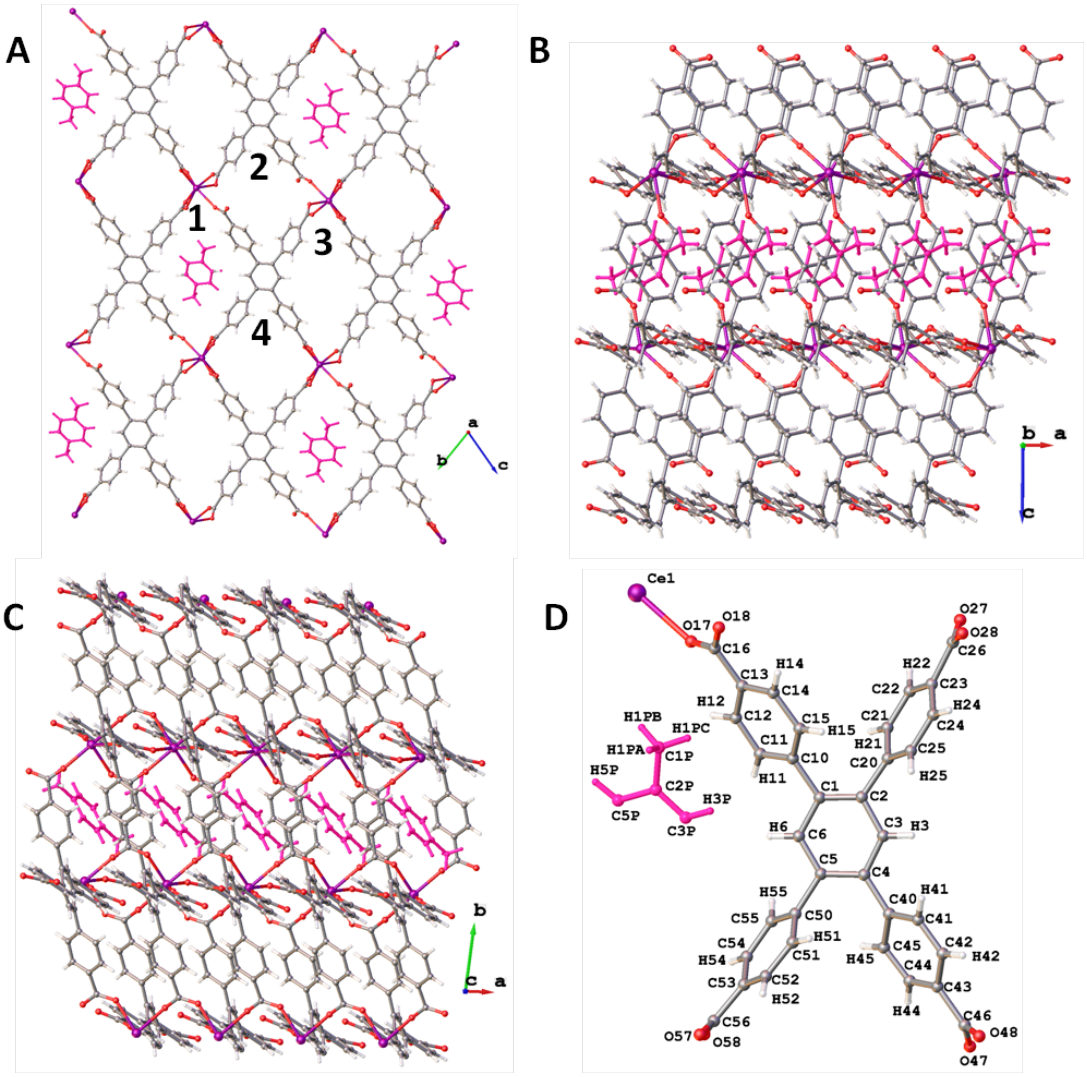

Figure 31: *Single crystal structure of **11RP**. A: View down 100; B: View down 010; C: View down 001; D: Asymmetric unit with P1 (dark pink) in channel 1. Channel numbering scheme shown in A.*

5.5.2 Single Crystal Structure Description

As described in chapter 4, **11R** has 4 unique channels unlike **11D** which has two symmetry equivalent channels. Symmetry equivalent channel 1 in **11D** becomes symmetry inequivalent channels 1 and 3 in **11R** and symmetry equivalent channel 2 in **11D** becomes channels 2 and 4 in **11R** (*Figure 31A*). Vapour loaded **11RP** results in **11R** taking up pX into channel 1 only. There was residual electron density in channels 2-4 that could not be resolved. Platon[46] was used to SQUEEZE the structure and removed 101 electrons per unit cell from a total potential solvent accessible void of 382 A^3 in **11RP**. This corresponds to approximately 10 water molecules (which would have a total volume of 400 A^3).

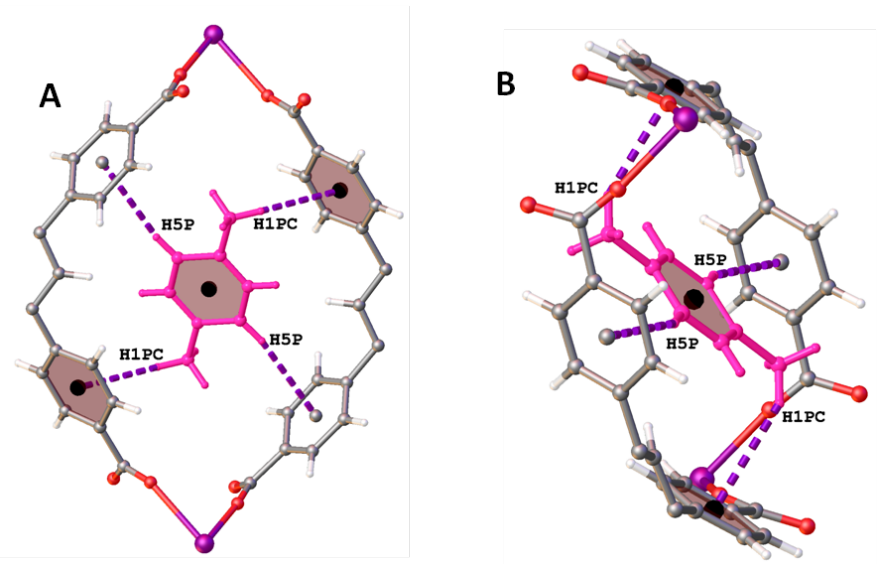

Figure 32: *C-H···π and π···π interactions between guest pX1 (dark pink) and host framework* ***11RP*** *in channel 1. A: View down 100; B: View down 001.*

In channel 1, pX interacts with the framework via two symmetrical C-H···π interactions from the pX aromatic ring to the framework: C5P-H5P···π ring 5 and C1P-H1PC··· π ring 1 at 5.463 Å (measured from ring centroid-ring centroid[44]) and 3.046 Å (measured from H1PC-ring centroid) respectively (*Table 15*). This holds pX at isolated locations along the channel with no disorder observed.

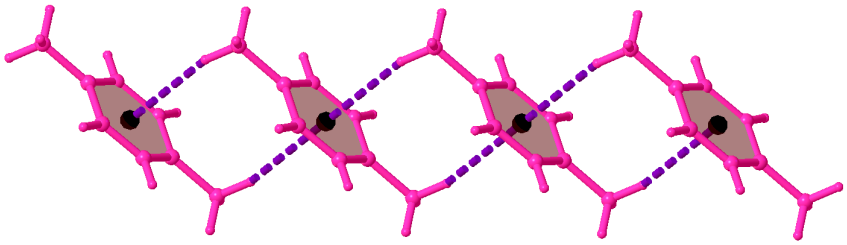

Figure 33: *C-H···π and π···π interactions between pX1 molecules in channel 1 of* ***11RP****.*

There are C-H···π stacking interactions between guest pX molecules within channel 1 from H1PA of the pX methyl group and the aromatic ring of the adjacent pX molecule. As the inversion centre lies at the centre pX1, this means two symmetrical interactions are formed from both pX methyl with adjacent pX ring-systems of 3.015 Å. There are also π···π stacking interactions between the pX π-systems at a distance of 5.116 Å with a shift of 3.385 Å (*Figure 33*, *Table 15*).

Table 15: *Interactions present between guest pX and host framework* ***11RP****:*

Interaction	Donor Atom	C-H···π centroid-centroid/ Atom-centroid			Nº interactions per X
		Length (Å)	Atom-Centroid/ Plane-plane Angle (°)	Shift (Å)	
11RP – pX1	L(ring 1)··· pX1 π···π	5.018	18.999	2.990	2
pX1 - **11RP**	H5P ···L(ring 5)	5.463	112.749	-	2
pX1 - **11RP**	H1PC···L(ring 1)	3.046	148.439	-	2
pX1-pX1 C-H···π	H1PA	3.015	158.029	-	2
pX1-pX1	π···π	5.116	0	3.385	2

5.6 Order of xylene and H_2O Exposure to 11D: Effect on Single Crystal Structure

Phase **11D** and **11R** can be isolated in the single crystal and bulk phases: **11D** is isolated by heating to 100 °C at 10^{-2} mbar overnight and then keeping the material under N_2. In order to isolate **11R**, **11D** is exposed to moisture allowing H_2O to coordinate to Ce, rearranging the 3D structure.

It has been determined that **11D** can take up pX into the structure, producing the single crystal structure **11P** under N_2 and phase **11R** can also take up pX to give **11RP** in air. In both these cases, the phase is isolated before exposure to xylenes and the resulting structure is the same as the parent structure, but with a larger unit cell volume due to the inclusion of guest, but the unit cell dimensions are only affected by a small amount.

An investigation into how the order in which the material is exposed to xylenes affects the single crystal structure was carried out. A single crystal of **11P** was isolated by activating under N_2 is a Schelnk tube, adding pX and leaving for 24 hours. A data collection showed the presence of **11P** after this time. Exposure of the crystal to the air for 24 hours and subsequent data collection showed a unit cell change and a new structure, **11R'P**.

Figure 34: *Single crystal of* ***11R'P*** *mounted on a mitegen tip used for data collection.*

In **11R'P**, each Ce centre is 8 coordinate, but unlike all the other structures involving the Ce(HTCPB) unit (**11**, **11S**, **11D**, **11R**, **11P**, **11M**, **11PM**, **11O**, **11EB**, **11RP**, **11T** and **11B**), **11R'P** has two Ce in each asymmetric unit and crystallises in a triclinic P-1 space group with unit cell dimensions of a=13.5089 Å, b=16.8097 Å, c=18.540 Å, α=110.113 °, β=102.285 °, γ=98.162(7) ° and a unit cell volume of 3755.1(7) $Å^3$.

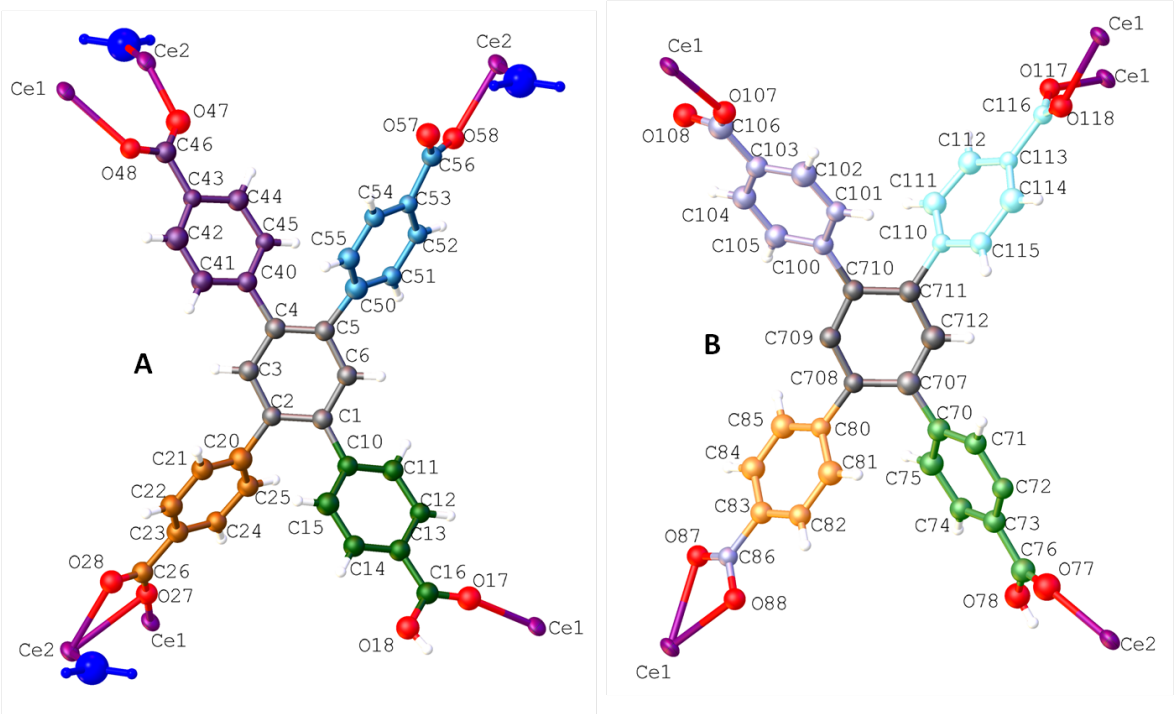

Figure 35: *Numbering scheme for HTCPB ligands **11R'P**. A: Ligand 1. Carboxylate 1 (green), carboxylate 2 (orange), carboxylate 4 (purple) and carboxylate 5 (blue); B: Ligand 2. Carboxylate 7 (light green), carboxylate 8 (light orange), carboxylate 10 (light purple) carboxylate 11 (light blue).*

There are two independant HTCPB ligands and two different Ce(III) atoms in the asymmetric unit of **11R'P** (*Figure 35*). Ce1 is only involved in carboxylate coordination, but H_2O is coordinated to Ce2, making the overall formula of the structure **11R'P** $Ce_2(HTCPB)_2(H_2O)_2.(pX)_3$.

The transition from **11** to **11D** via **11S** involves the formation of a carboxylate bridge between the originally isolated Ce_2 dimers within the 3D structure. In **11R'P**, the bridging carboxylate between every other dimer has broken, allowing a H_2O to coordinate in its place, leaving Ce_4 units, with H_2O and two monodentate carboxylates (COOH and COO) at the terminal ends of each Ce_4.

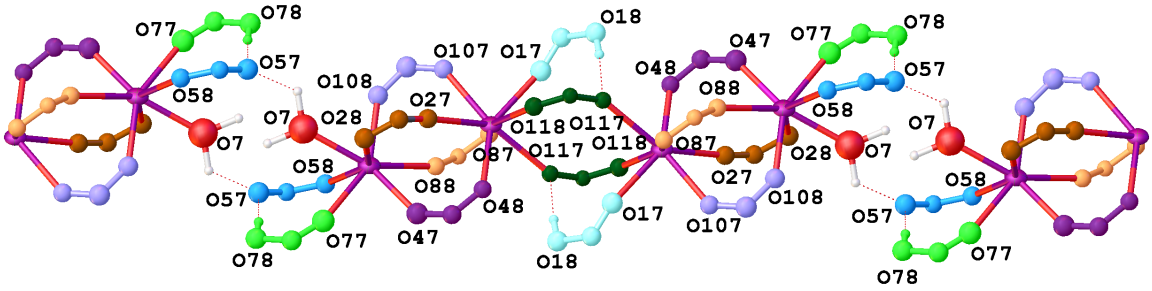

Figure 36: *C-H···O hydrogen bonding between coordinated H_2O and protonated and non-protonated monodentate carboxylates, forming a chain propagating down the 101 direction within* ***11R'P****.Carboxylate colour coding used as in (Figure 35) with hydrogen bonds shown by red dashed lines. Ce (purple), C (grey), O (red), coordinated H_2O (blue), protonated monodentate carboxylate (yellow), non-protonated monodentate carboxylate (green).*

Hydrogen bonding occurs along the Ce-carboxylate chain, connecting to Ce_4 units via intermolecular interactions. Within the Ce1-Ce2 dimers, which are bridged by carboxylates 2 and 4 of ligand 1 and 8 and 10 of ligand 2, the protonated monodentate carboxylate 1 of ligand 1, bound to Ce via O17 forms a O-H···O hydrogen bond with I117 of the bridging carboxylate 1 from ligand 2 of 1.898 Å and an angle of 171.175 °. Between the Ce_4 units, the coordinated water, protonated monodentate carbolylate 7 (Ce2-O77-C76-O78-H78) of ligand 2 and the monodentate carboxylate 5 of ligand 1 (Ce2-O58-C56-O57) form a series of hydrogen bonds that holds the Ce_4 units together (*Figure 36*). Protonated carboxylate 7 forms an O78-H78···O57 interaction of 1.772 Å at an angle of 170.314 °, and O57 also forms a O57···H7A-O7 interaction with the coordainted H_2O. As the Ce_4 units are generated through symmetry, this means two equivalent sets of interactions are formed in each place.

Both ligands are protonated, leaving the framework neutral overall, however the connectivity of each ligand to Ce is different. In the HTCPB ligand, the carboxylates are arranged in the 1, 2, 4 and 5 positions on the central aromatic ring. The central aromatic ring carbons are labelled C1-C6 and C707-C712 for ligands 1 and 2 respectively, so the carboxylates branching are labelled after the carbon atom to which they are attached in each ligand: For ligand 1, these are called carboxylate 1, 2, 4 and 5 respectively with the central aromatic ring being ring 3. For ligand 2 they are called carboxylates 7, 8, 10 and 11 with the central aromatic ring being ring 12.

Ligand 1 (*Figure 35A*) is connected to 5 Ce metal centres. Protonated carboxylate 1 is coordinated to Ce1 via O17 only, and protonated O18 forms O-H···O hydrogen bonds with O117 of ligand 2 of the carboxylate bridge found in the centre of the Ce_4 unit. Carboxylate 2 is bridging bidentate and bound to Ce2 via both O27 and O28 and to Ce1via the μ2-O27 and is the first of the four bridges between Ce1 and Ce2. Carboxylate 4 is bound to Ce1 via O48 and Ce2 via O47, making it the

second of the four bridging groups between Ce1 and Ce2 (*Figure 36*). Carboxylate 5 is also monodentate and coordinated to Ce 2 via O58, while the non-protonated O57 of the same carboxylate is involved in hydrogen bonding with protonated O78 of ligand 2 within the same Ce_4 unit and the coordinated H_2O the the adjecent Ce_4 unit, making carboxylate 5 responsible for the joining of Ce_4 units within the supramolecular structure.

Ligand 2 (*Figure 35B*) is also coordinated to 5 Ce centres. Carboxylate 7 is protonated and bound to Ce2 via O77, leaving O78 free to hydrogen bond with O57 of ligand 1 between the Ce_4 units. Bidentate carboxylate 8 is bound to Ce1 through O87 and O88 and to Ce2 via the μ2-O88 making it the third of the four carboxylate bridges between Ce1 and Ce2. Carboxylate 10 is coordinated to Ce1 via O107 and Ce2 via O108, and is the fourth and final bridging carboxylates found between Ce1 and Ce2. Carboxylate 11 bridges between symmetry equivalent Ce1 atoms via O117 and O118 respectively (*Figure 36*).

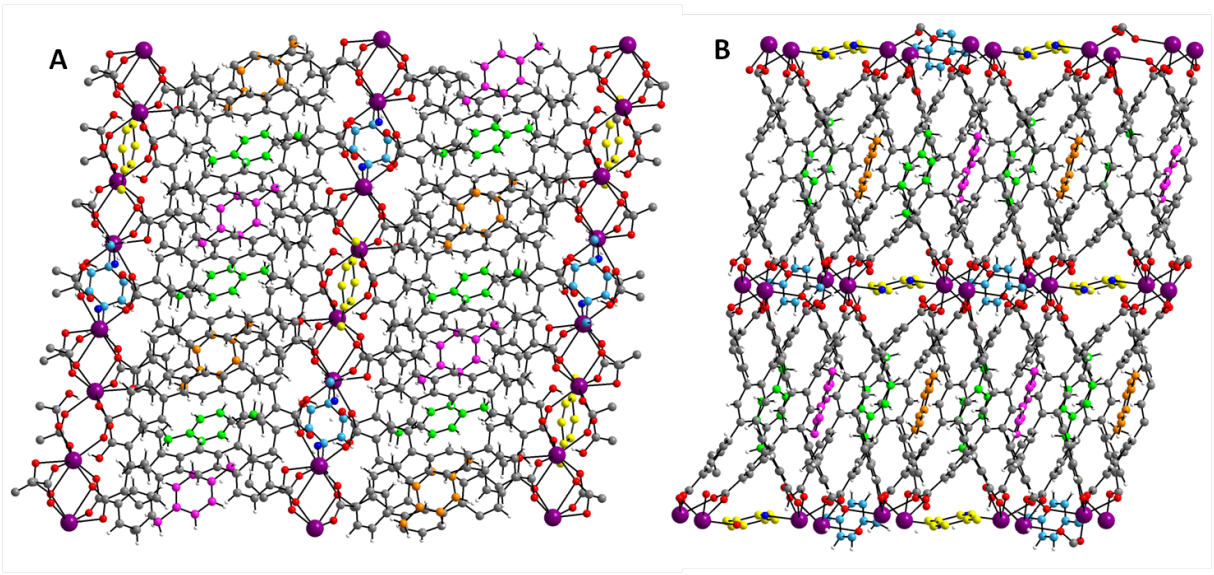

Figure 37: *Single crystal structure of* ***11R'P****. A: View down 100; B: View down 001. Ce (purple), O (red), C (grey), H (white), pX 1-5 (pink, green, blue, yellow, orange respectively).*

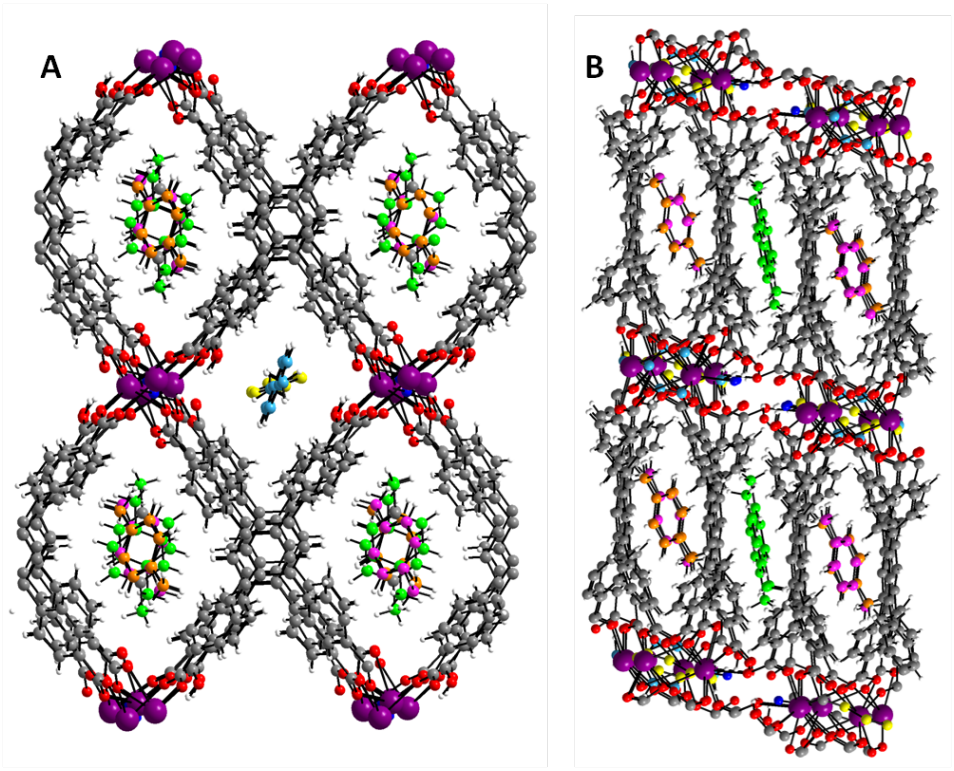

Figure 38: *Views to show 2D porosity of* ***11R'P****. A: View along 101; B: View along hkl = 9.4, 2.0, -15.75. Channel 1 houses pX 1-3 and channel 2 houses pX 4 and 5. Ce (purple), O (red), C (grey), H (white), pX 1-5 (pink, green, blue, yellow, orange).*

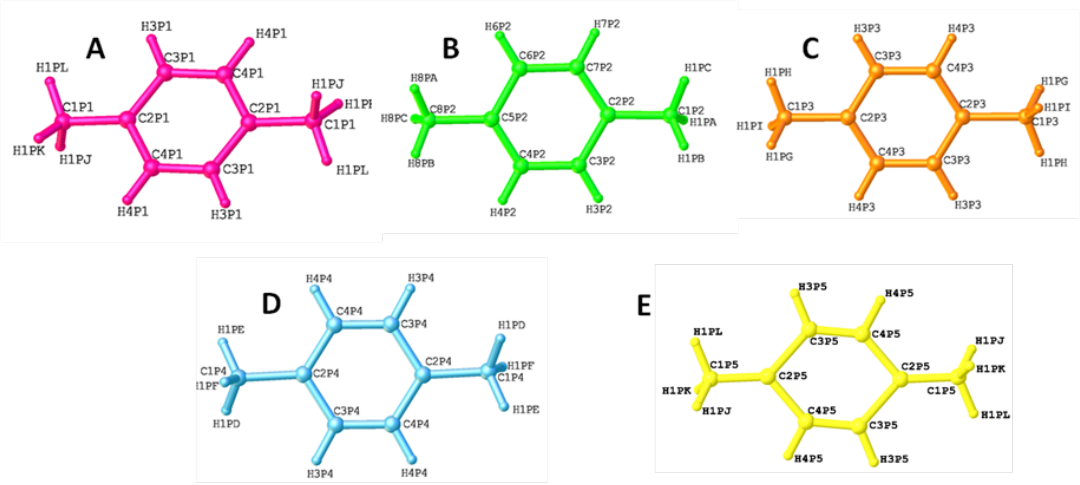

Figure 39: *Numbering and colouring scheme for pX present in* ***11R'P****. A: pX1 (channel 1) B: pX2 (channel 1); C: pX3 (channel 1); D: pX4 (channel 2); E: pX5 (channel 2).*

pX 1-3 are pink, green and orange respectively and found in channel one, in the order 1-2-3-2-1-2-3-2 etc. pX 4 and 5 are yellow and blue respectively and found in channel 2.

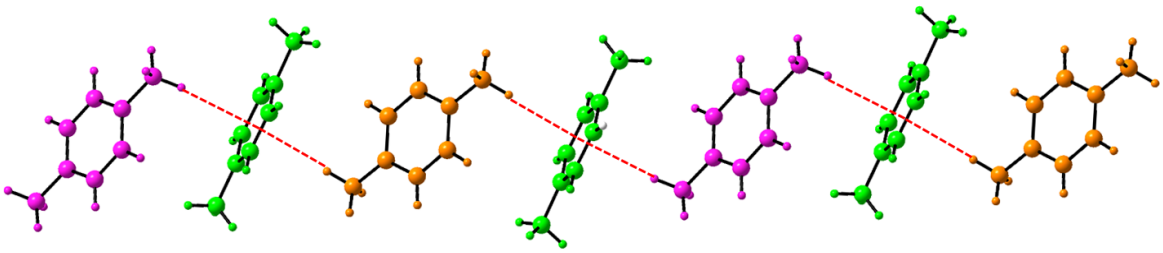

Figure 40: *C-H···π interactions between pX1 (pink), pX2 (green) and pX3 (orange) within channel 1 of* ***11R'P****.*

The methyl groups at each end of pX1 form C1P1-H1PK···π interactions with the central aromatic rings of pX2 molecules on either side of 2.876 Å at an angle of 159.344 °, hence why each pX1 is adjacent to two pX2. The methyl groups at each end of pX3 also form C1P3-H1PG···π interactions with the central aromatic ring of pX2 molecules of 2.798 Å at an angle of 161.581 °, from the opposite side of the ring as the C-H···π interactions formed with pX1. This overall, gives the order 1-2-3-2-1-2-3-2, with C-H···π interactions linking all three pX within channel 1.

The pX2 methyl groups do not form C-H···π interactions pX1 and pX2, but it is held in place by the interactions formed to its central aromatic ring. Conversely, no interaction is formed with the central aromatic ring of pX1 and pX3, which are held in place through interaction of their methyl groups with the π-system of pX2. This network of intermolecular interactions holds the pX at specific dimensions down the larger channel 1, which is apparent from the fact there is no disorder in the locations of these molecules.

This experiment shows that the order of addition of pX and exposure to air is important in isolating a particular final structure. If pX is added to **11D** under N_2, **11P** is formed. If pX is added to **11R** (**11D** followed by exposure to air), **11RP** is formed. But if pX is added to **11D** to form **11P** and is subsequently exposed to air, **11R'P** is formed.

5.7 Benzene Loaded 11R

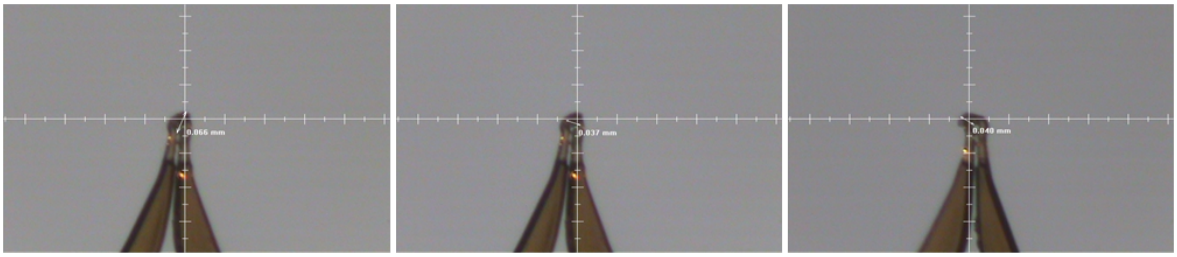

Figure 41: *Single crystal of* ***11RB*** *mounted on a mitegen tip used for data collection.*

A sample of single crystals of **11** was activated at 10^{-2} mbar at 100 °C overnight and then exposed to air. Benzene was then added and the sample was left for 24 hours, after which time a crystal was selected for single crystal structure determination (0.066 x 0.040 x 0.037 mm) (*Figure 41*).

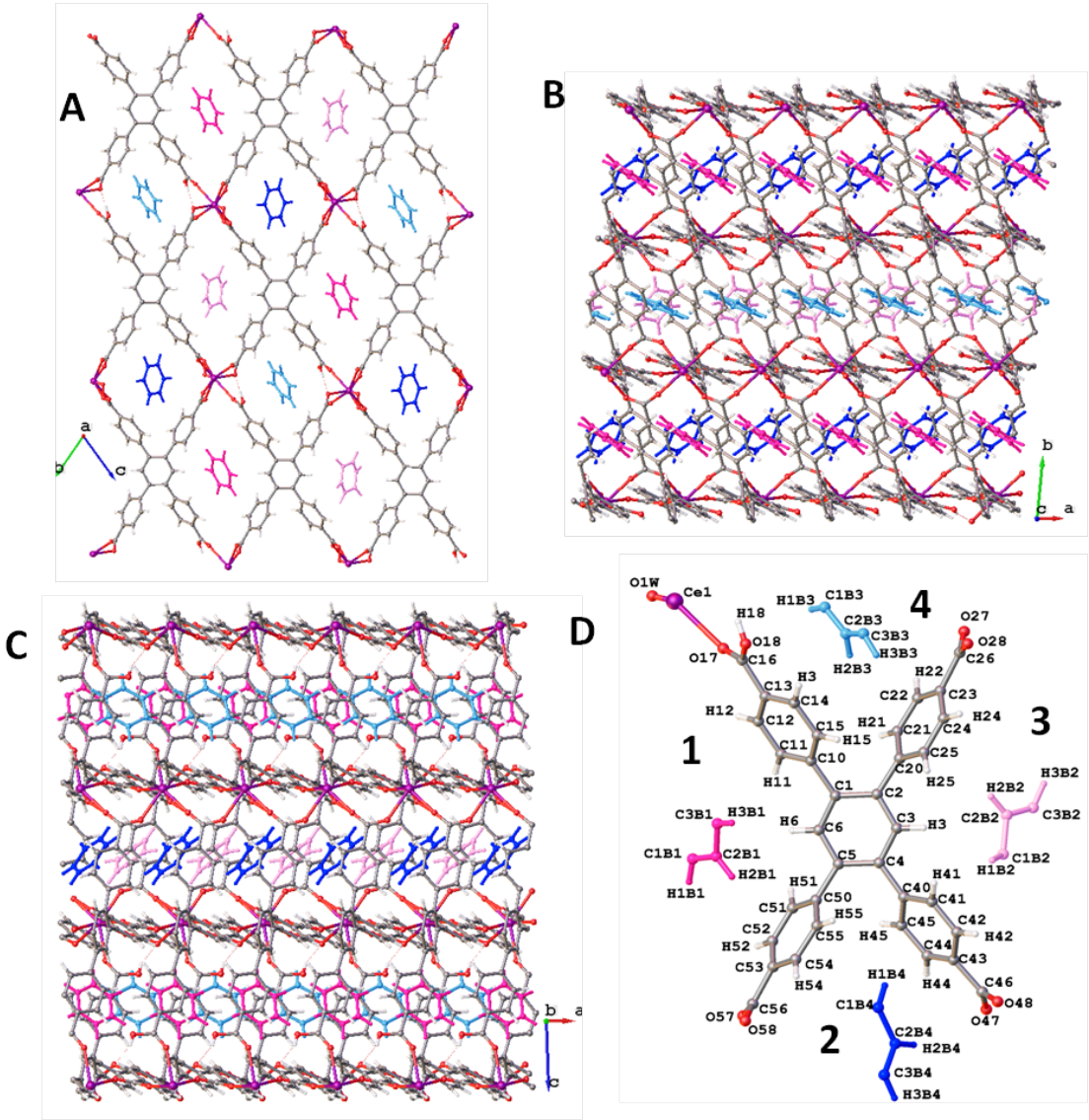

Figure 42: *Single crystal structure of **11RB**. A: View down 100; B: View down 010; C: View down 001; D: Asymmetric unit with Benz1 (dark pink) in channel 1, Benz2 (pale pink) in channel 3, Benz3 (pale blue) in channel 2 and Benz4 (dark blue) in channel 2.Channel numbering shown in D.*

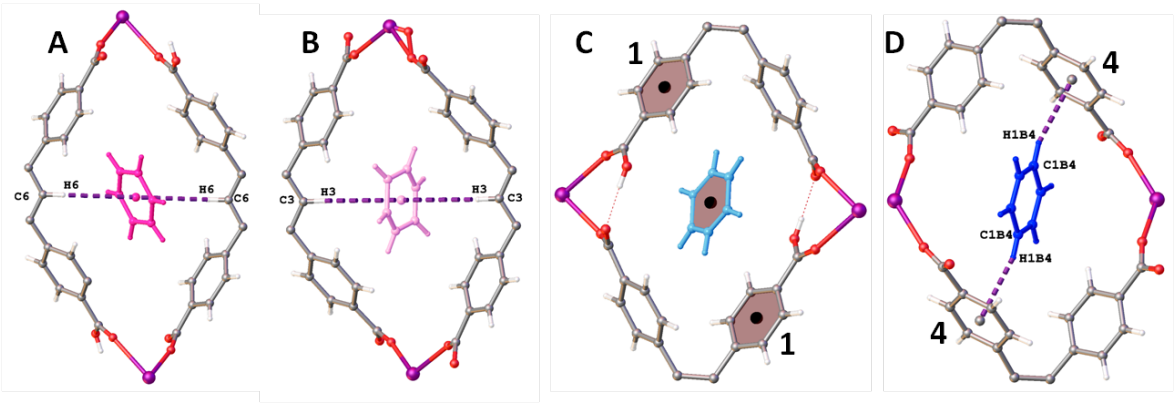

Figure 43: *C-H···π and π···π interactions between guest benzene and host framework in* ***11RB****. A: Benz1(dark pink) in channel 1, B: Benz2 (pale pink) in channel 3, C: Benz 3 (pale blue) in channel 2 and D: Benz4 (dark blue) in channel 4.*

Each benzene forms interactions with the framework, but the nature of these interactions differs with each guest (*Table 16*). Benz 1 in channel 1 of **11RB** forms two symmetrical C6-H6···π interactions between the central aromatic ring of the HTCPB ligand in the framework with the π-system of the benz1 with an aromatic centroid-centroid distance[44] of 5.572 Å (*Figure 43A*). A similar set of symmetrical C3-H3···π interactions form for benz 2 in channel 3 (*Figure 43B*) of 6.305 Å. Benz 3 in channel 2 forms π···π stacking interactions with ring 1 of the HTCPB ligand at a distance of 3.932 Å with a centroid-centroid shift of 3.932 Å and a plane-plane angle of 15.589 ° (*Figure 43C*). Benz 4 in channel 4 forms two symmetrical C1B4-H1B4···π interactions from the benzene hydrogens with the π-system of ring 4 of the HTCPB ligand in the framework of 5.233 Å (*Figure 43D*). These interactions allow the benzene guest molecules to be found at isolated locations along the channel with no disorder observed (*Table 16*).

Table 16: *Interactions present between guest Benzene and host framework* ***11RB****:*

Interaction	Donor Atom	C-H···π centroid-centroid/ π···π plane-centroid			Nº interactions per X
		Length (Å)	Cent-cent/ plane-plane Angle (°)	Shift (Å)	
11RB –Benz1	H6	5.572	45.926	-	2
11RB – Benz2	H3	6.305	60.16	-	2
11RB – Benz3	L(ring 1) ··· B3 π···π	3.932	15.589	3.932	2
Benz4 – **11RB**	H1B4	5.233	102.316	-	2
Benz1-Benz1	π···π	2.884	0	4.337	2
Benz2-Benz2	π···π	2.998	0	4.220	2
Benz3-Benz3	π···π	2.097	0	4.788	2
Benz4-Benz4	π···π	3.248	0	4.094	2

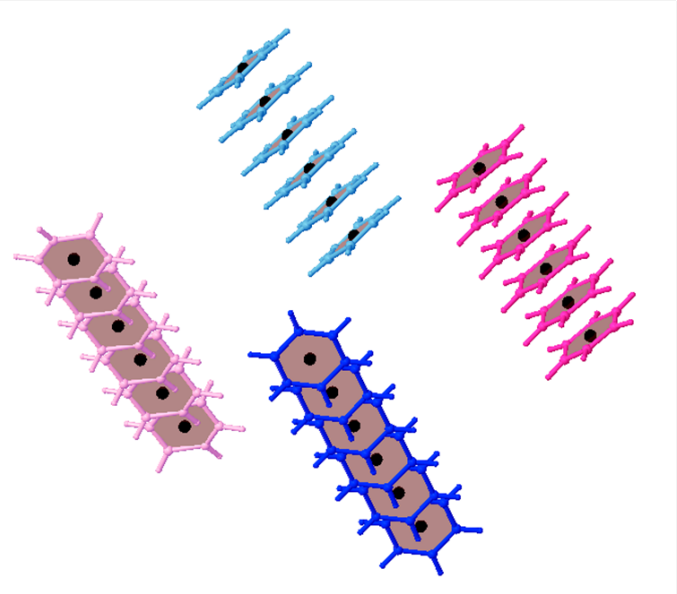

Figure 44: *π···π stacking between guest benzene molecules in* ***11RB****. Benz1 (dark pink) in channel 1, Benz2 (pale pink) in channel 3, Benz 3 (pale blue) in channel 2 and Benz4 (dark blue) in channel 4.*

Each benzene also offset π···π stacks[47] with the adjacent benz molecule within the channel and this is the case for all benz1-4 guests in channels 1, 3, 2 and 4 respectively (*Figure 44*). The π···π stacking interactions between benz1 guests have a length of 2.884 Å with a centroid-centroid shift of 4.337 Å. The corresponding measurements for benz2 are 2.998 Å and 4.220 Å, for benz 3 are 2.097 Å and 4.778 Å and for benz4 are 3.248 Å and 4.094 Å (*Table 16)*. These π···π stacking interactions hold the benz guests at set distances along the channel at the positions at which the framework-guest intermolecular interactions form.

If **11B** is compared to **11RP**, a similar π···π stacking of aromatic guests in channel 1 is observed. However, as **11RP** is vapour loaded, pX only enters channel 1 whereas benz enters all channels 1-4 in **11RB**.

5.8 Conclusions

Analysis of the channels showed that **11D** had the potential to separate xylenes. In the initial GCMC calculations, pX could be loaded into channel 1, whereas mX did not enter either channel. This suggested that **11D** was an ideal candidate for pX/mX separation; the most industrially applicable xylene separation. Docking of other isomers (oX and EB) showed that EB could enter channel 1 and oX could not enter the framework. The material had the potential to separate all xylene isomers from one another.

The size and shape of channels of **11D** respond to guests to maximise loading while retaining high xylene selectivity. Flexibility allows combination of uptake comparable with zeolites and comparable selectivity with other reported zeolite and MOF materials. Zeolites have a xylene adsorption capacity in the range of 1 to 1.75 mol/kg[16] and Ce(HTCPB) (**11D**) has a calculated theoretical adsorption capacity 1.438 mol/kg assuming 100 % uptake with 1 xylene (pX/EB) per formula unit. The experimental capacity was 1.01 mol/kg as we only see a maximum of 70 % loading. Flexibility gives the framework comparable uptake to zeolites, as the theoretical adsorption capacity of the rigid structure **11D** based on the GCMC calculations would be half this for pX and EB which only enter channel 1 and no uptake for mX and oX.

The high pX/mX selectivity of 5:1 produced by **11D** is generated as the channels are flexible enough to take up both pX and mX isomers, but are specific enough to separate them with a strong preference for pX. This preference results from the lower energetic cost of transforming **11D** into **11P** than **11M**, the thermodynamically preferred interactions that form between pX and **11P**, which are not present or are strained between mX and **11M** and the fact the all three structures determined (**11D**, **11P** and **11M**) prefer pX in the GCMC docking calculations.

Investigation into the selectivity of **11D** using weighted xylene ratios shows that with increasing pX uptake, the framework becomes increasingly more selective to pX. This is in agreement with that shown by both the GCMC calculations and single crystal structures of **11P** and **11M**. C-H···π and C-H···O intermolecular interactions between pX and **11P** form, holding pX in isolated locations along the two channels, whereas mX in unable to form such strong and directional interactions, causing a greater swelling in the unit cell and more unfavourable mX sites and interactions. Therefore as more pX enters the framework, the channels become increasingly selectivity to the pX isomer over mX, thus enhancing the selectivity.

An attempt was made to separate the xylene and EB isomers by chromatography, both flash and HPLC, however rate of uptake and solvent makes dynamic frameworks much more complex to utilise in chromatography.

Benzene and toluene guests were loaded into the desolvated phase **11D** in order to determine whether similar intermolecular interactions between the aromatic guests and the framework would form. In the case of toluene, loss of one anchoring methyl group from pX meant that the guest entered the larger channel 1 at a tilt, so although two C-H···π interactions formed, neither were as strong as those observed in the case of pX in channel 1 of **11P** due to a deviation from the ideal interaction geometry as a result of the tilt of the molecule in the channel. However in the smaller channel 2, the toluene enters in line with the channel as seen for pX in channel 2 of **11P**, and two C-H···π and one C-H···O interactions (only one methyl group) form per toluene, which is disordered over two positions, mimicking a pX molecule.

In the case of benzene, both anchoring methyls have been lost, therefore the benzene guests enter both channels at a tilt. This means weaker, more strained C-H···π interactions are formed than seen for both pX and toluene in both channels and no C-H···O interactions are present as there are no methyl groups present on the guest molecule. These results indicate that the channels are an almost ideal size and geometry to house a pX molecule and although similar interactions can form between the framework and other aromatic guests, the size and shape of the pX molecule agrees almost exactly with the pockets present within the channels of **11D**, further explaining the preference of the framework to take up pX over other guests.

The Ce(HTCPB) MOF is an extremely flexible framework that can undergo many structural changes as a result of changing temperature and exposure to different solvents and guest molecules.

In this chapter we showed that **11R** can be used to take up guests despite the presence of H_2O within the structure. H_2O coordinated to Ce immediately upon exposure to air, and the channels begin to fill with water over time. Exposure of **11R** to pX shows that the material is able to take up these aromatic guests into the channels which are not occupied by H_2O, as seen with **11Xe** (chapter 4). PX is able to enter one of the four channels when **11R** is exposed to pX in the vapour phase. The pX guests within channel 1 enter at a tilt due to the larger void space available and π···π stacks with one another and form C-H···π interactions from the pX guest to the **11RP** framework. Benzene was also loaded in the liquid phase into **11R** to compare the interactions formed between guest and framework for comparison with **11RP**. Benzene guests enter all four of the channels at an angle, as seen for pX loaded **11RP**. Each benzene π···π stacks, again as seen with pX, but each benzene interacts with the framework in a different way, depending on their location in the channel and what possible interactions can form at that point: benz1 and 2 form C-H···π interactions from the framework to benzene π-system; benz 3 π···π stacks with the framework ligand benzene rings; benz 4 forms C-H···π interactions from the guest benzene to the framework HTCPB ligand aromatic rings.

It has also been shown that the framework responds to guests depending on the order in which they are introduced. Addition of pX into **11D** showed pX loaded **11D**, **11P**, which has the same parent structure (similar unit cell dimensions to **11D** but with a larger unit cell volume resulting from guest inclusion) but with pX found in all channels. In this chapter it has also been shown that pX can be taken into **11R** to form **11RP**, which again have the same parent structure (**11RP** has unit cell dimensions similar to **11R**), but with pX present within channel 1. 11D is only stable under inert conditions and exposure to air forms **11R**. Once loaded with pX, if **11P** is exposed to air or moisture a new phase **11R'P** is formed, in which H_2O has coordinated to half of the Ce atoms causing a shift in structure, however conversion to **11R** or **11RP** is not achieved. This demonstrated that order of addition of pX and H_2O to **11D** is important, with the selective phase **11D** only being isolated under inert conditions.

Overall, fifteen phases have already been identified for this framework, discussed over chapters 4 and 5 (**11**, **11S**, **11D**, **11R**, **11P**, **11M, 11O**, **11EB**, **11PM**, **11RXe**, **11RP**, **11R'P, 11T**, **11B** and **11RB**) (*Table 16*), all which require varying degrees of flexibility, from the large structural change between **11-11S-11D** in which bonds are broken and made, to overall expansions in the unit cell and torsions of bonds within the structure to allow guests to enter the framework. The most astonishing feature is that all of these transformations can be observed in the single crystal phase and in this chapter we demonstrated that multiple phases can be isolated from the same crystal which although has an increasingly weakened diffracting ability, still diffracts at the end of the whole experiment to the point at which structure solution and refinement is still possible.

Table 17: *Summary of single crystal structure based on Ce(HTCPB) so far, from chapters 4 and 5:*

Framework	Description
11	As made Ce(HTCPB)
11S	Partially desolvated 'EtOH-solvate' intermediate
11D	Desolvated Ce(HTCPB)
11R	Rearranged (HTCPB) following exposure of **11D** to air
11P	pX loaded **11D**
11M	mX loaded **11D**
11O	oX loaded **11D**
11EB	EB loaded **11D**
11PM	**11D** exposed to equimolar mixture of pX/mX
11RXe	**11R** exposed to Xe gas in single crystal gas cell experiment
11RP	**11R** exposed to pX vapour
11R'P	**11D** loaded with pX, then exposed to air
11T	Tol loaded **11D**
11B	Benz loaded **11D**
11RB	Benz loaded **11R**

5.9 References

[1] J. R. L. P. Lattner, TX, US, M. P. H. Hagemeister, TX, US, J. E. R. W. B. Stanat, NY, US), J. D.-Y. H. Ou, TX, US, X. H. Zheng, TX, US, L. H. Han, VA, US, USA, **2011**.

[2] J. D. Y. H. Ou, TX, T. J. L. C. Waddick, TX*, Vol. US 6,459,006 B1*, **2002**.

[3] K. Weissermel, H.-J. Arpe, *Industrial Organic Chemistry, Third Edition*, 3rd ed., VCH Verlagsgesellschaft mbH, Weinheim; VCH Publishers, Inc., New York, NY, USA, Federal Republic of Germany, **1997**.

[4] S. A. Otani, T. Iwamura, M. Kanaoka, K. Matsumura, Y. Noguchi, K. Sando, T. Mori, I. Takeuchi, T. Tsuchiya, T. Yamamoto, *Patent* **1973**, *US3761533*.

[5] L. Zhu, F. S. Xiao, Z. T. Zhang, Y. Y. Sun, Y. Han, S. L. Qiu, *Catal. Today* **2001**, *68*, 209-216.

[6] T. F. Degnan Jr., *From Zeolites to Porous MOF Materials, Vol. 170A*, Elsevier, Beijing, P. R. China, **2007**.

[7] B. K. Sharma, *Fuels and Petroleum Processing*, First Edition., Krishna Prakashan Media (P) Ltd., Meerut, **1998**.

[8] H. Aichinger, W. Ruppel, R. Seubert, K.-H. Boehning, W. Scheidmeir, J. E. Schmidt, M. Schwarzmann, C07D30789 ed., USA, **1993**.

[9] P. A. Carson, M. Lapper, *J. Appl. Chem. Biotechn.* **1976**, *26*, 171-183.

[10] M. Minceva, A. E. Rodrigues, *AlChE J.* **2007**, *53*, 138-149.

[11] *Polyester - A Global Strategic Business Report* **2011**, Global Industry Analysts Inc. .

[12] P. M. M. Blauwhoff, J. W. Gosselink, E. P. Keiffer, S. T. Sie, W. H. J. Stork, *Catalysis and Zeolites: Fundamentals and Applications*, Springer, Germany, **1999**.

[13] Various, *Zeolites in Industrial Separation and Catalysis*, John Wiley & Sons, Great Britain, **2010**.

[14] M. O. Daramola, A. J. Burger, M. Pera-Titus, A. Giroir-Fendler, S. Miachon, J. A. Dalmon, L. Lorenzen, *Asia-Pac. J. Chem. Eng.* **2010**, *5*, 815-837.

[15] H. Tournier, A. Barreau, B. Tavitian, D. Le Roux, C. Sulzer, V. Beaumont, *Micropor. Mesopor. Mater.* **2000**, *39*, 537-547.

[16] M. Guisnet, J.-P. Gilson, *Zeolites for Cleaner Technologies*, Imperial College Press, London, **2002**.

[17] J.-P. Bellat, M.-H. S.-Grange, S. Jullian, *Zeolites* **1995**, *15*, 124-130.

[18] F. Vermoortele, M. Maes, P. Z. Moghadam, M. J. Lennox, F. Ragon, M. Boulhout, S. Biswas, K. G. M. Laurier, I. Beurroies, R. Denoyel, M. Roeffaers, N. Stock, T. Duren, C. Serre, D. E. De Vos, *J. Am. Chem. Soc.* **2011**, *133*, 18526-18529.

[19] Z. Y. Gu, X. P. Yan, *Angew. Chem. Int. Ed.* **2010**, *49*, 1477-1480.

[20] L. Alaerts, C. E. A. Kirschhock, M. Maes, M. A. van der Veen, V. Finsy, A. Depla, J. A. Martens, G. V. Baron, P. A. Jacobs, J. E. M. Denayer, D. E. De Vos, *Angew. Chem. Int. Ed.* **2007**, *46*, 4293-4297.

[21] M. P. M. Nicolau, P. S. Barcia, J. M. Gallegos, J. A. C. Silva, A. E. Rodrigues, B. L. Chen, *J. Phys. Chem. C* **2009**, *113*, 13173-13179.

[22] M. A. Moreira, J. C. Santos, A. F. P. Ferreira, J. M. Loureiro, F. Ragon, P. Horcajada, K. E. Shim, Y. K. Hwang, U. H. Lee, J. S. Chang, C. Serre, A. E. Rodrigues, *Langmuir* **2012**, *28*, 5715-5723.

[23] A. M. Tarditi, G. I. Horowitz, E. A. Lombardo, *J. Membr. Sci.* **2006**, *281*, 692-699.

[24] V. Finsy, H. Verelst, L. Alaerts, D. De Vos, P. A. Jacobs, G. V. Baron, J. F. M. Denayer, *J. Am. Chem. Soc* **2008**, *130*, 7110–7118.

[25] L. Alaerts, M. Maes, L. Giebeler, P. A. Jacobs, J. A. Martens, J. F. M. Denayer, C. E. A. Kirschhock, D. E. De Vos, *J. Am. Chem. Soc.* **2008**, *130*, 14170-14178.

[26] P. S. Barcia, D. Guimaraes, P. A. P. Mendes, J. A. C. Silva, V. Guillerm, H. Chevreau, C. Serre, A. E. Rodrigues, *Micropor. Mesopor. Mat.* **2011**, *139*, 67-73.

[27] L. D. Shiau, *Abstr. Pap. Am. Chem. Soc.* **2006**, *231*.

[28] J. O'Brien-Abraham, Y. S. Lin, *Ind. Eng. Chem. Res.* **2010**, *49*, 809-816.

[29] W. H. Yuan, Y. S. Lin, W. S. Yang, *J. Am. Chem. Soc.* **2004**, *126*, 4776-4777.

[30] O. V. Dolomanov, L. J. Bourhis, R. J. Gildea, J. A. K. Howard, H. Puschmann, *J. Appl. Crystallogr.* **2009**, *42*, 339-341.

[31] L. J. Bourhis, O. V. Dolomanov, R. J. Gildea, J. A. K. Howard, H. Puschmann, *olex2.solve* **2011**.

[32] *Calcualtions carried out by Dr. Kim Jelfs at the University of Liverpool*.

[33] A. B. Véronique Lachet , Bernard Tavitian, Alain H. Fuchs *Langmuir* **1999**, *15*, 8678–8685.

[34] S. Chempath, R. Q. Snurr, J. J. Low, *AlChE J.* **2004**, *50*, 463–469.

[35] J. M. Castillo, T. J. H. Vlugt, S. Calero, *J. Phys. Chem* **2009**, *113*, 20869–20874.

[36] J. A. O. Greathouse, Nathan W.; Criscenti, Louise J.; Guilinger, T. R.; Pohl, Phil; Allendorf, Mark D., *PCCP* **2010**, *12*, 12621-12629.

[37] R. Krishna, J. M. van Baten, *PCCP* **2011**, *13*, 10593–10616.

[38] J. E. Warren, C. G. Perkins, K. E. Jelfs, P. Boldrin, P. A. Chater, M. E. Briggs, K. C. Stylianou, J. B. Claridge, M. J. Rosseinsky, *Submitted* **2013**.

[39] *Analysis carried out by Dr. Phil Chater at the University of Liverpool.*

[40] Z. Zhao, X. Ma, A. Kasik, Z.Li, Y. S. Lin, *Ind. Eng. Chem. Res.* **2013**, *52*, 1102-1108.

[41] R. Vaidhyanathan, S. S. Iremonger, G. K. H. Shimizu, P. G. Boyd, S. Alavi, T. K. Woo, *Angew. Chem. Int. Ed.* **2012**, *51*, 1826-1829.

[42] J. E. Warren, 2.0.1 Ed., **2010**, An automated parametrisation and input file generation for Hole2.

[43] *Data Processing carried out by Dr. John Warren at the University of Liverpool*.

[44] S. K. Burley, G. A. Petsko, *Science* **1985**, *229*, 23-28.

[45] G. R. Desiraju, T. Steiner, *The Weak Hydrogen Bond: In Structural Chemistry and Biology*, Oxford University Press, USA, **2001**.

[46] T. Spek, *Platon* **2011**.

[47] C. A. Hunter, J. K. M. Sanders, *J. Am. Chem. Soc.* **1990**, *112*, 5525-5534.

5.10 Additional Information

Table 18: *Crystal data and structure refinement parameters for xylene loaded structures* ***11P, 11M, 11PM****:*

Sample Code	11P	11M	11PM
Empirical formula	$C_{42}H_{29}CeO_8$	$C_{42}H_{29}CeO_8$	$C_{41.7}H_{28.6}CeO_8$
Formula weight	801.77	801.77	797.84
Temperature/K	100	100	100.0
Crystal system	triclinic	triclinic	triclinic
Space group	P-1	P-1	P-1
a/Å	9.5603(4)	9.7441(6)	9.5976(3)
b/Å	12.1386(5)	12.3318(7)	12.1928(4)
c/Å	15.9458(6)	15.7737(9)	15.9099(5)
α/°	88.4550(10)	88.979(2)	88.6100(10)
β/°	74.4170(10)	77.399(2)	75.1240(10)
γ/°	70.2330(10)	69.498(2)	70.0890(10)
Volume/$Å^3$	1673.27(12)	1729.02(18)	1687.75(9)
Z	2	2	2
ρcalcmg/mm^3	1.591	1.54	1.570
m/mm^{-1}	1.418	1.372	1.405
F(000)	806	806	802
Crystal size/mm^3	0.179 × 0.05 × 0.031	0.088 × 0.061 × 0.033	0.154 × 0.091 × 0.053
2Θ range for data collection	3.58 to 52.88°	4.28 to 47.76°	3.56 to 55.42°
Index ranges	$-11 \le h \le 11$, $-15 \le k \le 15$, $-19 \le l \le 15$	$-11 \le h \le 11$, $-14 \le k \le 14$, $-16 \le l \le 17$	$-12 \le h \le 12$, $-15 \le k \le 15$, $-14 \le l \le 20$
Reflections collected	26198	30736	26717
Independent reflections	6878[R(int) = 0.0681]	5326[R(int) = 0.0657]	7888[R(int) = 0.0784]
Data/restraints/ parameters	6878/0/463	5326/236/570	7888/262/545
Goodness-of-fit on F2	1.034	1.098	1.031
Final R indexes [I>=2σ (I)]	$R_1 = 0.0416$, $wR_2 = 0.0945$	$R_1 = 0.0443$, $wR_2 = 0.1085$	$R_1 = 0.0501$, $wR_2 = 0.1132$
Final R indexes [all data]	$R_1 = 0.0535$, $wR_2 = 0.1001$	$R_1 = 0.0588$, $wR_2 = 0.1185$	$R_1 = 0.0765$, $wR_2 = 0.1256$
Largest diff. peak/hole / e $Å^{-3}$	1.866/-1.966	2.499/-1.014	2.291/-1.781

Table 19: *Crystal data and structure refinement parameters for xylene loaded structures* ***11O*** *and* ***11EB****:*

Sample Code	11O	11EB
Empirical formula	$C_{46}H_{34}CeO_8$	$C_{42}H_{26}CeO_8$
Formula weight	854.85	396.99
Temperature/K	100(2)	100
Crystal system	triclinic	triclinic
Space group	P-1	P-1
a/Å	10.2654(8)	9.5873(2)
b/Å	12.3956(9)	12.4039(3)
c/Å	15.7911(13)	15.7803(11)
α/°	91.213(4)	88.936(6)
β/°	94.045(4)	75.581(5)
γ/°	110.555(3)	70.035(5)
Volume/Å^3	1874.5(3)	1703.69(13)
Z	2	2
ρcalcmg/mm^3	1.515	1.548
m/mm^{-1}	1.271	1.392
F(000)	864.0	796.0
Crystal size/mm^3	0.04 × 0.015 × 0.015	0.111 × 0.059 × 0.053
2Θ range for data collection	3.514 to 43.492°	6.12 to 54.98°
Index ranges	$-10 \leq h \leq 10$, $-12 \leq k \leq 12$, $-16 \leq l \leq 15$	$-12 \leq h \leq 12$, $-15 \leq k \leq 16$, $-20 \leq l \leq 18$
Reflections collected	15895	29453
Independent reflections	4414[R(int) = 0.1329]	7800[R(int) = 0.0858]
Data/restraints/ parameters	4414/198/560	7800/0/484
Goodness-of-fit on F2	1.022	1.052
Final R indexes [I>=2σ (I)]	$R_1 = 0.0612$, $wR_2 = 0.1185$	$R_1 = 0.0496$, $wR_2 = 0.1064$
Final R indexes [all data]	$R_1 = 0.1123$, $wR_2 = 0.1397$	$R_1 = 0.0674$, $wR_2 = 0.1140$
Largest diff. peak/hole / e Å^{-3}	1.55/-1.10	1.44/-1.19

Table 20: *Crystal data and structure refinement parameters for benzene and toluene loaded structures* ***11B, 11T*** *and* ***11RB****:*

Sample Code	11B	11T	11RB
Empirical formula	$C_{40}H_{25.5}CeO_{8.2}$	$C_{44}H_{30.5}CeO_8$	$C_{43.5}H_{28.5}CeO_{8.2}$
Formula weight	778.18	827.54	822.48
Temperature/K	100(2)	100(2)	100
Crystal system	triclinic	triclinic	triclinic
Space group	P-1	P-1	P-1
a/Å	10.1368(16)	10.108(2)	5.2254(3)
b/Å	12.0191(19)	12.303(3)	18.6514(10)
c/Å	16.065(2)	15.885(4)	19.9260(14)
α/°	89.408(5)	89.544(10)	70.096(5)
β/°	79.391(5)	80.514(6)	85.740(6)
γ/°	68.528(5)	68.951(7)	82.791(6)
Volume/Å^3	1786.8(5)	1815.6(7)	1810.53(19)
Z	2	2	2
ρcalcmg/mm^3	1.446	1.514	1.509
m/mm^{-1}	1.326	1.309	1.313
F(000)	779	833	826.0
Crystal size/mm^3	0.053 × 0.037 × 0.022	0.075 × 0.048 × 0.026	0.066 × 0.04 × 0.037
2Θ range for data collection	4.34 to 45.44°	3.56 to 44.52°	6.16 to 49.42°
Index ranges	$-10 \le h \le 11$, $-12 \le k \le 13$, $-17 \le l \le 17$	$-10 \le h \le 10$, $-13 \le k \le 13$, $-16 \le l \le 16$	$-6 \le h \le 6$, $-21 \le k \le 21$, $-23 \le l \le 22$
Reflections collected	24145	22262	26850
Independent reflections	4772[R(int) = 0.1058]	4580[R(int) = 0.1178]	6114[R(int) = 0.1933]
Data/restraints/ parameters	4772/274/523	4580/171/519	6114/0/464
Goodness-of-fit on F2	1.057	1.082	1.012
Final R indexes [I>=2σ (I)]	$R_1 = 0.0882$, $wR_2 = 0.2156$	$R_1 = 0.0767$, $wR_2 = 0.1723$	$R_1 = 0.1018$, $wR_2 = 0.2179$
Final R indexes [all data]	$R_1 = 0.1246$, $wR_2 = 0.2433$	$R_1 = 0.1144$, $wR_2 = 0.1925$	$R_1 = 0.1538$, $wR_2 = 0.2458$
Largest diff. peak/hole / e Å^{-3}	3.56/-2.28	2.77/-1.12	1.75/-1.91

Table 21: *Crystal data and structure refinement parameters for pX and mX loaded* ***11R*** *and* ***11R'P****:*

Sample Code	11RP	11R'P
Empirical formula	$C_{19}H_{11.5}Ce_{0.5}O_4$	$C_{45.8}H_{33.7}CeO_{8.5}$
Formula weight	373.84	860.57
Temperature/K	100	100
Crystal system	triclinic	triclinic
Space group	P-1	P-1
a/Å	5.1157(7)	13.5089(15)
b/Å	18.594(3)	16.8097(19)
c/Å	19.750(3)	18.540(2)
α/°	73.971(7)	110.113(8)
β/°	89.081(7)	102.285(7)
γ/°	84.768(7)	98.162(7)
Volume/Å^3	1798.0(5)	3755.1(7)
Z	4	4
ρcalcmg/mm^3	1.381	1.522
m/mm^{-1}	1.314	1.270
F(000)	746.0	1739.0
Crystal size/mm^3	0.055 × 0.055 × 0.044	0.073 × 0.056 × 0.041
2Θ range for data collection	6.22 to 49.42°	5.98 to 49.42°
Index ranges	$-5 \leq h \leq 6$, $-21 \leq k \leq 21$, $-23 \leq l \leq 22$	$-15 \leq h \leq 15$, $-19 \leq k \leq 19$, $-21 \leq l \leq 21$
Reflections collected	12718	42952
Independent reflections	5006[R(int) = 0.1731]	12434[R(int) = 0.2167]
Data/restraints/ parameters	5006/0/195	12434/0/473
Goodness-of-fit on F2	1.017	1.068
Final R indexes [I>=2σ (I)]	$R_1 = 0.1486$, $wR_2 = 0.3027$	$R_1 = 0.1608$, $wR_2 = 0.3031$
Final R indexes [all data]	$R_1 = 0.2693$, $wR_2 = 0.3668$	$R_1 = 0.2507$, $wR_2 = 0.3581$
Largest diff. peak/hole / e Å^{-3}	2.51/-1.24	2.43/-2.08

Chapter 6

A Series of Isostructural Lanthanide-Based MOFs for Xylene Separation and

A Framework using a Smaller Lanthanide

6.1 Introduction

The Lanthanides (Ln), also known as 'rare earth' elements are located between group 2 and the transition elements in the periodic table. Both Lanthanum (La) and Lutetium (Lu) at either end of the Ln series have one valence electron in the 5d orbital meaning in some cases they are referred to as group 3 elements, however their chemical similarities to the rest of the Ln metals mean they are usually discussed as Ln elements. Upon ionisation of Ln to form Ln(III), the outer $6s^2$ and either 5d/4f electrons are removed, leaving the f-orbitals exposed. Across the lanthanide period from La to Lu, the size of the Ln(III) ion decreases due to the 'lanthanide contraction', a shrinking based on the same principle as 'transition metal contraction' (*Table 1*): as the overall number of protons in the nucleus increases with increasing atomic number, the attraction of the outermost electrons to the nucleus is enhanced and with this increasing attraction comes contraction of the overall atomic diameter.

Table 1: *Atomic Diameter of Ln(III)[1]:*

Lanthanide (Ln) Metal	Electronic Configuration Ln	Electronic Configuration Ln(III) Ion	Atomic Diameter Ln(III) Ion (pm)
La	$[Xe]5d^16s^2$	$[Xe]4f^0$	206.4
Ce	$[Xe]4f^15d^16s^2$	$[Xe]4f^1$	204.0
Pr	$[Xe]4f^36s^2$	$[Xe]4f^2$	198.0
Nd	$[Xe]4f^46s^2$	$[Xe]4f^3$	196.6
Pm	$[Xe]4f^56s^2$	$[Xe]4f^4$	194.0
Sm	$[Xe]4f^66s^2$	$[Xe]4f^5$	191.6
Eu	$[Xe]4f^76s^2$	$[Xe]4f^6$	189.4
Gd	$[Xe]4f^75d^16s^2$	$[Xe]4f^7$	187.6
Tb	$[Xe]4f^96s^2$	$[Xe]4f^8$	184.6
Dy	$[Xe]4f^{10}6s^2$	$[Xe]4f^9$	182.4
Ho	$[Xe]4f^{11}6s^2$	$[Xe]4f^{10}$	180.2
Er	$[Xe]4f^{12}6s^2$	$[Xe]4f^{11}$	178.0
Tm	$[Xe]4f^{13}6s^2$	$[Xe]4f^{12}$	176.0
Yb	$[Xe]4f^{14}6s^2$	$[Xe]4f^{13}$	173.6
Lu	$[Xe]4f^{14}5d^16s^2$	$[Xe]4f^{14}$	172.2

Allowed singlet-singlet state transitions between f-orbitals produces characteristic photoluminescence depending on the Ln(III) ion. The well-shielded f-orbital environment as a result of the closed 5s and 5p shells means that Ln(III) ions have narrow band emission and a long phospholuminescent lifetime. IR/UV radiation in many cases gives emission in the visible or near

IR region; following exposure, Eu(III) emits red, Tb(III) green, Sm(IIII) orange, Tm(III) blue and Yb, Nd, Er, Pr, Dy and Ho(III) in the near IR region. Ce(III) emits in the blue region and is a special case as it has allowed d-f transitions, resulting in an intense broad band emission depending on the ligand environment of the ion[2]. Although the luminescent properties of Ln are well known[3], they are not discussed for the Ln-based compounds in this thesis.

In chapter 4, the synthesis and characterisation of a new porous Ln-MOF with the formula Ce(HTCPB)·*x*EtOH·*y*H_2O (**11**) was discussed. The structural changes upon heating to the fully desolvated structure (**11D)** via an EtOH-solvated intermediate (**11S)** was also investigated. In chapter 5, **11D** was investigated for xylene selectivity, most interestingly its pX/mX selectivity. In this chapter, a series of compounds isostructural with **11** are discussed with the formula Ln(HTCPB)·*x*EtOH·*y*H_2O, where Ln = La (**10**), Ce (**11**), Pr (**12**), Nd (**13**), and Sm (**14**). The desolvated (**10D-14D**) and rearranged (**10R-14R**) structures of these compounds have also been determined and are also isostructural with the corresponding **11D** and **11R** structures respectively as discussed in chapter 4. The series of compounds **10D-14D** are investigated for their pX/mX selectivity for comparison to the **11D** material. Single crystal structure analysis of the pX and mX loaded framework help to explain the selectivity observed, with a peak at α_{pXmX} = 6.36 for Pr(HTCPB). This value is approximately 50 % higher than the current highest reported pX/mX batch separation values for both zeolites (Zeolite KY: α_{pXmX} = 4.5[4] and KBaY: α_{pXmX} = 4.0[5]) and MOFs (MIL-125(Ti)-NH_2: α_{pXmX} = 4.4[6]).

6.2 Experimental

A series of isostructural MOFs were synthesised under similar synthesis conditions as **11**, as discussed in chapter 4. In this chapter the full series of Ln(HTCPB) compounds **10-14** is discussed, where Ln = La (**10**), Ce (**11**), Pr (**12**), Nd (**13**), and Sm (**14**).

6.2.1 MOF Synthesis

In all cases $Ln(NO_3)_3.6H_2O$ (where Ln = La, Ce, Pr, Nd and Sm) (25 mg, 0.036 mmol) and H_4TCPB (10 mg) were added to a 12 mL borosilicate glass vial (For full ligand synthesis see chapter 2). EtOH (3 mL) and H_2O (3 mL) were then added and the vial was sealed and the mixture was sonicated for 15 minutes. The vials were then placed in an oven and heated at a rate of 2 °C/ minute up to 120 °C at which temperature they remained for 48 hours. The solution was then cooled to RT at 0.2 °C/ minute. The products were isolated in the form of block single crystals with the formula $Ln(HTCPB)(EtOH)(H_2O)\cdot x EtOH\cdot y H_2O$, where Ln = La (**10**), Ce (**11**), Pr (**12**), Nd (1**3**) and Sm (**14**). All **10-14** are isostructural with **11** (*Chapter 4*).

6.2.2 Single Crystal Data Collection

In this chapter, data for the single crystal structure solution of **10-14**, **10D-14D**, **10R-14R**, **10P-14P** and **10M-14M** was collected from the Rigaku Rotating Anode Diffractometer at the University of Liverpool. The structures were solved and refined using Olex2[7-8]. All structure solution and refinement was carried out with the assistance of Dr John Warren.

6.2.3 Powder X-ray Diffraction

Powder X-ray diffraction (PXRD) data of **10-14** was collected in transmission geometry on a Bruker D8 Advance with Cu Kα radiation in a sealed 0.5 mm borosilicate capillary at room temperature.

6.2.4 Xylene Separation

Batch pX/mX separation was carried out as described in Chapter 5, section5.2.2: 50 mg of **10-14** were activated at 100 °C under vacuum (10^{-2} mbar) overnight after which time 1 ml of equimolar pX/mX was added under N_2 and left for 24 hours. The framework was then filtered, washed with dichloromethane (DCM) to remove any surface xylenes and allowed to air dry before analysis.

6.3 Results and Discussion

6.3.1 Phase Purity

Compounds **10-14** were isolated in the form of single crystals as shown by OM images (*Figure 1*) and were determined to be isostructural by SCXRD (*Table 3*) and PXRD. The samples were confirmed to be phase pure by indexing of the PXRD (*Figure 2*) to the single crystal unit cell parameters (*Table 3*) using Chekcell[9] and CH microanalysis (*Table 2*).

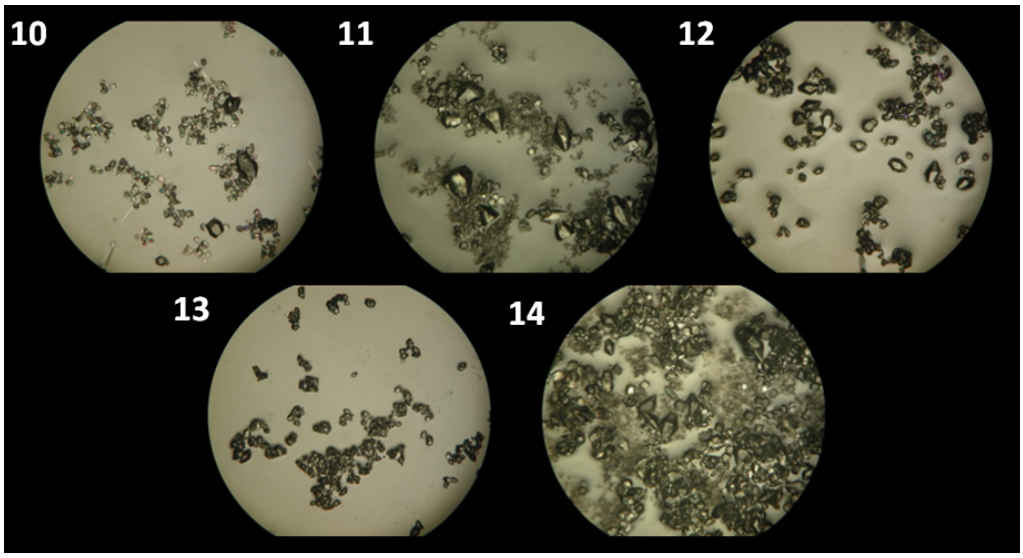

Figure 1: *OM images of single crystals of compounds* ***10-14****.*

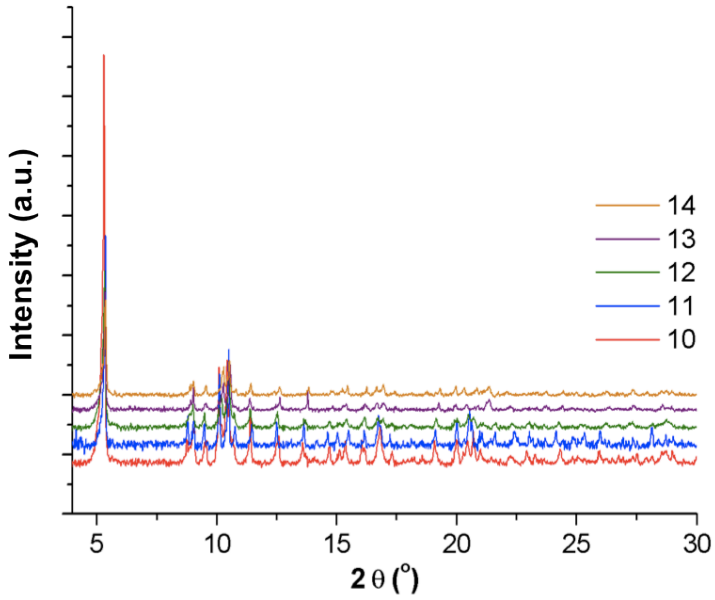

Figure 2: *PXRD profiles of as made compounds* ***10-14****. Data collected in transmission geometry using Cu Kα radiation in a sealed capillary.*

Table 2: *CH microanalysis of as made compounds* ***10-14****:*

Ln(HTCPB)	Formula	Theory (%)	Found (%)
La (10)	$La(HTCPB)(H_2O)_{2.5}(EtOH)_{1.4}$	**C** 55.21 **H** 3.96	**C** 55.23 **H** 3.94
Ce (11)	$Ce(HTCPB)(H_2O)_{2.9}(EtOH)_{0.3}$	**C** 54.76 **H** 3.37	**C** 54.70 **H** 3.25
Pr (12)	$Pr(HTCPB)(H_2O)_{1.5}(EtOH)_{1.3}$	**C** 56.19 **H** 3.71	**C** 56.24 **H** 3.78
Nd (13)	$Nd(HTCPB)(H_2O)_{2.48}(EtOH)_{0.61}$	**C** 54.76 **H** 3.60	**C** 54.77 **H** 3.62
Sm (14)	$Sm(HTCPB)(H_2O)_{3.94}(EtOH)_{0.2}$	**C** 52.56 **H** 3.60	**C** 52.56 **H** 3.59

6.3.2 Single Crystal Structure Determination

In chapter 4, the desolvated and rearranged phases of **11**; **11D** and **11R** respectively, were isolated via a variable temperature single crystal experiment (*Figure 3*). In this chapter, all desolvated phases of **10-14**, **10D-14D,** were obtained through heating to 100 °C in a Schlenk tube at 10^{-2} mbar overnight and storing under N_2 before transfer directly into fomblin oil for single crystal data collection. Samples of **10R-14R** were obtained via the same activation method of **10-14** to give **10D-14D**, then exposure to air in the Schelnk tube.

PX and mX loaded frameworks **10P-14P** and **10M-14M** respectively were isolated via activation at 100 °C and 10^{-2} mbar overnight followed by pX or mX addition under N_2 and transfer of xylene-loaded single crystal directly into fomblin oil after 24 hours for single crystal data collection.

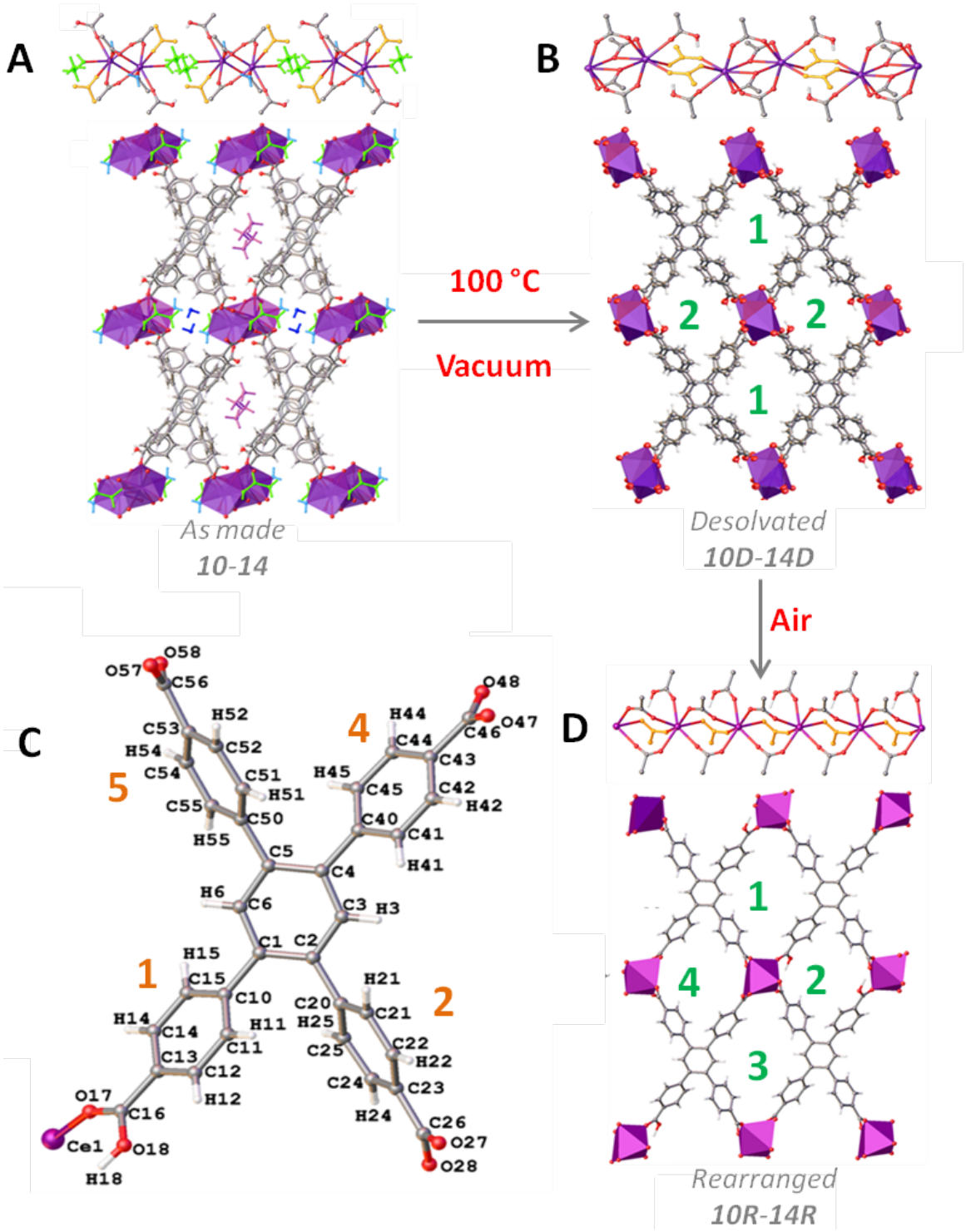

Figure 3: *Single crystal structure transition from A: As made* ***10-14****, to B: Desolvated* ***10D-14D*** *after heating to 100 °C at* 10^{-2} *mbar overnight and subsequent rearrangement to D:* ***10R-14R*** *with exposure of* ***10D-14D*** *to air. Ce(HTCPB) data from chapter 4 shown in the figure as the example. Channel numbering shown in green in B for desolvated frameworks and D for the rearranged frameworks. The HTCPB ligand atom and ring numbering (orange) shown in C.*

6.3.2.1 As-Synthesised Frameworks

All compounds **10-14** were shown to be isostructural in the as-synthesised phase by SCXRD. This was first observed by the similarity in unit cell dimensions (*Table 3*) and confirmed by structure solution, refinement and analysis.

Table 3: *Single crystal structure unit cell dimensions and void analysis of* ***10-14*** *calculated using Olex2 for* ***10-14****:*

Ln(HTCPB)	Unit Cell Dimensions			Unit Cell Volume ($Å^3$)	Probe radii down a, b and c-axis			Largest Spherical Void (Å)
	a (Å) α (°)	b (Å) β (°)	c (Å) γ (°)		a (Å)	b (Å)	c (Å)	
La (10)	10.5983(16) 83.023(4)	10.5437(16) 76.090(5)	17.026(3) 69.992(4)	1733.71	1.5	1.0	0.4	4.4
Ce (11)	10.5783(1) 83.158(6)	10.4271(1) 76.314(5)	16.9210(11) 70.023(5)	1702.80	1.4	0.9	0.5	4.4
Pr (12)	10.5353(11) 83.063(1)	10.5528(14) 76.278(9)	16.930(2) 70.089(6)	1717.55	1.7	1.0	0.5	4.6
Nd (13)	10.5561(1) 83.205(6)	10.5378(1) 76.425(5)	16.8962(11) 69.971(5)	1715.02	1.7	0.7	0.4	4.4
Sm (14)	10.6022(1) 83.482(6)	10.5365(2) 76.562(5)	16.8531(11) 69.635(5)	1715.56	1.7	0.9	0.6	4.6

Compounds **10-14** are isostructural with **11** (*Chapter 4*): Ln_2 dimers are bridged by carboxylates from rings 4 and 5 of the HTCPB ligand (O47, O48, O57, O58) creating two symmetry equivalent (Ln)-O47-C46-O48-(Ln) and two symmetry equivalent (Ln)-O57-O56-O58-(Ln) bridges (Atom and ring numbering shown in Figure 3). The carboxyates from rings 1 and 2 of the HTCPB ligand have monodentate coordination to Ln between the Ln_2 dimers, from O17 of ring 1 and O27 of ring 2, with carboxylate 1 being protonated at O18. EtOH and H_2O molecules are also coordinated to each Ln between the Ln_2 dimers (*Figure 5A*). The structure is propagated into 3D via the HTCPB ligand.

All isostructural as-made frameworks have potential 2D porosity down the 100 and 010 directions (*Figure 5A*) with similar unit cell dimensions, unit cell volumes and largest spherical voids within the 3D structures (*Table 3*).

As discussed for **11** in chapter 4, the HTCPB ligand is mono-protonated in all isostructural compounds **10-14**. Within the as-synthesized single crystal structure, there are two monodentate carboxylate groups coordinated to Ln via only one oxygen (O17 and O28). One of these groups is protonated and the other is not as shown by the asymmetric (Ln-)O17-C16 and C16-O18(-H) bond lengths for the protonated carboxylate groups and more uniform (Ln-)O28-C26 and C26-O27 for the non-protonated carboxylate groups (*Table 4*).

All compounds **10-14** have one EtOH and one H_2O coordinated to Ln(III), with disordered EtOH in channel 1 and H_2O in channel 2, as described for **11** in chapter 4.

Table 4: *Monodentate carboxylate bond distances within compounds **10-14**. Protonated COOH (red) shown by asymmetric O-C=O distances and non-protonated COOH (purple) shown by more symmetrical O-C-O distances:*

Ln(HTCPB)	(Ln-)O17-C16 (Å)	C16-O18(-H) (Å)	(Ln-)O28-C26 (Å)	C26-O27 (Å)
La (10)	1.233	1.303	1.265	1.271
Ce (11)	1.227	1.301	1.248	1.253
Pr (12)	1.226	1.303	1.246	1.274
Nd (13)	1.248	1.283	1.249	1.285
Sm (14)	1.226	1.306	1.243	1.259

6.3.2.2 Desolvated Frameworks

Table 5: *Single crystal structure unit cell dimensions for **10D-14D**:*

Ln(HTCPB)	Unit Cell Dimensions			Unit Cell Volume (Å^3)
	a (Å) α (°)	b (Å) β (°)	c (Å) γ (°)	
La (10D)	9.4426(8) 80.989(6)	11.9218(1) 73.586(5)	15.8565(13) 70.657(5)	1611.69
Ce (11D)	9.2989(11) 93.756(5)	11.4163(13) 90.263(6)	15.2492(17) 93.814(6)	1611.72
Pr (12D)	9.3368(6) 81.122(6)	11.9277(8) 73.804(5)	15.8081(11) 71.018(5)	1594.76
Nd (13D)	9.2977(4) 81.207(6)	11.9415(5) 73.748(5)	15.7797(11) 71.200(5)	1588.46
Sm (14D)	9.2318(2) 81.213(6)	11.9650(3) 73.634(5)	15.7692(11) 71.377(5)	1579.99

Samples of single crystals of **10-14** were activated by heating to 100 °C at 10^{-2} mbar overnight in Schlenk tubes to form the activated, desolvated frameworks **10D-14D**. The samples were back-filled with N_2. The Schlenk was then attached to a N_2 source in the x-ray lab and a small sample of singles crystals from each Schlenk tube was extracted directly into Fomblin oil. As quickly as possible, a single crystal was isolated and mounted onto a mitegen tip and transferred immediately to the N_2 stream on the Rigaku diffractometer. Data collections were then carried out to determine

the structures of the desolvated phases **10D-14D**. The unit cell parameters again were similar to each other which was the first indication of isostructural desolvated phases (*Table 5*).

In **10D-14D**, two symmetry equivalent monodentate carboxylate 2 form bridges that link the originally isolates Ln_2 dimers. Carboxyate 2 is bound to Ce via only O17 in **10-14** but in **10D-14D**, O18 on the same carboxylate group coordinates to the adjacent Ln_2 dimer, creating Ln-carboxylate chains that run down the 100 direction (*Figure 5B*). Once desolvated, all isostructrual **10D-14D** have 1D porosity down the 100 direction.

The main difference observed following structure solution and refinement of the unit cell parameters was the steady decrease in unit cell volume in the isostructural compounds **10D-14D**. This is due to the decrease in size of the central metal Ln(III) ion (*Figure 6*) and is consistent with the lanthanide contraction. A similar effect is seen with other series of isostructural Ln-based MOFs: Combination of 1,3,5-BTB and Ln(III) (where Ln = La-Ho, Y) produces the isostructural MIL-103 series which sees a decreased in a- and c- unit cell parameters that coincides with the lanthanide contraction[10-11]; combination of TATB with Ln (where Ln = Yb, Dy, Er, Y) produces the isostructural PCN-17 series and a decrease in unit cell volume is observed in line with the lanthanide contraction[12].

Table 6: *Calculated void analysis and total accessible volume of **10D-14D**, calculated from single crystal structures using Olex2:*

Ln(HTCPB)	Probe radii down a, b and c-axis			Largest Spherical Void (Å)	Total Accessible Volume (Å^3)		
	a (Å)	b (Å)	c (Å)		Overall	Channel 1	Channel 2
La (10D)	2.0	0.5	0.4	4.6	392.8	202.1	190.7
Ce (11D)	2.0	0.5	0.3	4.4	389.7	207.1	182.5
Pr (12D)	2.0	0.5	0.4	4.6	379.1	195.0	184.1
Nd (13D)	2.0	0.5	0.3	4.4	375.6	194.1	181.5
Sm (14D)	2.0	0.4	0.4	4.4	372.3	195.1	177.2

Void analysis calculated using Olex2 also shows that there is also a decrease in the void space from **10D-14D** (*Table 6*): The overall total accessible volume decreases from 392.8 Å^3 in **10D** to 370.7 Å^3 in **14D**. The respective larger channel 1 and smaller channel 2 are affected proportionally to this, with the total accessible volume of channel 1 reducing from 202.1 Å^3 in **10D** to 195.0 Å^3 in **14D** and channel 2 from 190.7 Å^3 in **10D** to 175.7 Å^3 in **14D**.

As the single structures of the desolvated phase of **10-14** (**10D – 14D**) are isostructural, this implies that desolvation proceeds via the same pathway as shown with **11.** Exposure of **11D** to air causes a transformation to the rehydrated phase **11R**. Samples of single crystals of **10D-14D** were then exposed to air to investigate whether the same conversion occurred, which resulted in complete conversion from **XD** to **XR** (where X=**10-14**) in all cases.

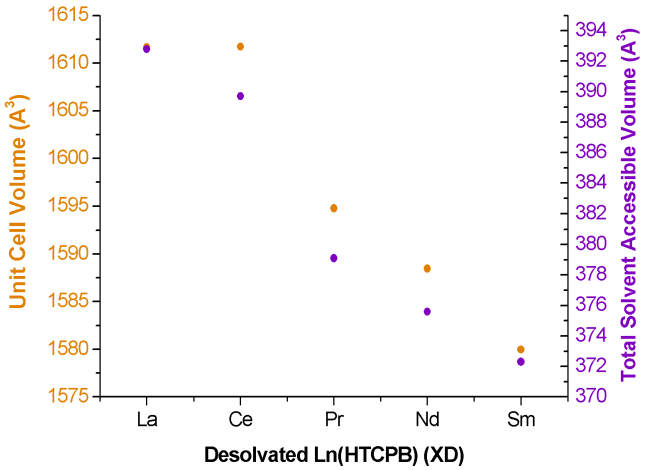

Figure 4: *Decreasing unit cell volume from desolvated La-Sm(HTCPB) (**10D-14D**) following the trend of lanthanide contraction (orange) and decreasing total accessible volume of **10D-14D** alongside unit cell contraction (violet).*

6.3.2.3 Rearranged/Rehydrated Frameworks

Table 7: *Single crystal structure unit cell dimensions for **10R-15R**:*

Ln(HTCPB)	Unit Cell Dimensions			Unit Cell Volume (Å^3)
	a (Å) α (°)	b (Å) β (°)	c (Å) γ (°)	
La (10R)	4.9665(2) 112.792(8)	18.2334(1) 92.366(7)	19.4293(13) 92.678(7)	1616.92
Ce (11R)	5.0714(9) 109.850(9)	18.452(3) 90.950(10)	19.543(4) 94.481(9)	1713.10
Pr (12R)	5.0230(3) 111.965(55)	18.3060(6) 91.924(7)	19.5325(84) 93.140(7)	1650.00
Nd (13R)	4.9745(1) 114.175(8)	18.1990(7) 91.268(6)	19.4455(13) 93.103(7)	1601.79
Sm (14R)	4.9961(2) 113.587(8)	18.0923(7) 91.785(7)	19.4089(13) 93.135(7)	1602.71

Isostructural **11R-14R** following rearrangement of **10D-14D** with exposure to air results in a more relaxed structure with slight channel widening (*Figure 5D*). All have potential porosity down the 100 direction. The channel numbering in **XR** is different to that in **XD** (Where X = Ln); proton movement within the structure between carboxylates has caused the respective ring numbering to

change, leaving four symmetry independent channels (*Figure 5D*). This is discussed in more detail in chapter 5.

Single crystal structure determination of **10D-14D** following exposure to air showed that all isostructural compounds not only have the same desolvated structure, but all act in the same way when exposed to air but converting to **10R-14R**, shown first by the similar unit cell dimensions (*Table 7*) then by single crystal structure determination.

6.3.3 Xylene Separation

As the desolvated phases were shown to be isostructural, the materials were tested for their ability to separate pX and mX. These frameworks have all been shown to be very flexible, so despite the observed decrease in unit cell volume and total accessible volume from **10D-14D**, the materials were expected to take up xylenes as a result of their flexibility.

6.3.3.1 pXmX Selectivity of Ln(HTCPB)

Using the same batch separation procedure as described in chapter 5.2.5, the selectivity of **10D 14D** towards pX/mX was determined (*Table 8*). 50 mg of **10-14** was activated at 100 °C under vacuum overnight in Schlenk tubes to give **10D-14D**. 1 mL of equimolar pX/mX solution was then added to **10D-14D** under N_2 and left for 24 hours after which time the samples were filtered and washed with DCM to remove any surface xylenes. All loaded frameworks were characterised for xylene uptake by CH microanalysis (*Table 10*). The loaded frameworks were then broken down with 1M $NaOH_{(aq)}$ solution and filtered, leaving an aqueous solution of the ligand (Na_4TCPB) and the xylenes. The xylenes were then extracted by washing three times with DCM, dried with $MgSO_4$ and filtered ready for GC analysis. The selectivity (α_{pXmX}) was calculated for each product solution using the equation: $\alpha_{pXmX} = [X_{pX}]/[X_{mX}] / [X_{pX}^{o}]/[X_{mX}^{o}]$ (*Chapter 5.1*):

Table 8: *Selectivity of Ln(HTCPB) towards an equimolar mixture of pX/mX after and 24 hours:*

Ln(HTCPB)	Selectivity (α_{pXmX}), 24 hours
La (10D)	4.48
Ce (11D)	4.55
Pr (12D)	6.36
Nd (13D)	6.20
Sm (14D)	6.11

The pX/mX selectivity was determined after 24 hours and showed an high selectivity of $\alpha_{pXmX} = 4.5$ for **10D** and **11D**, with an increase to even higher values of over 6 with **12D-14D** (*Table 8*). CH microanalysis showed around a 60-68 % loading of pX/mX into the frameworks after 24 hours, similar to the loading of 65 % observed for **11D** in chapter 5.

Table 9: *CH microanalysis of* ***10D-14D*** *loaded with pXmX after 24 hours:*

Ln(HTCPB) 24 hours	Formula	Theory (%)	Found (%)
La (10D.pXmX)	$La(HTCPB)(X)_{0.60}(H_2O)_{0.10}(DCM)_{0.50}$	**C** 59.64 **H** 3.45	**C** 59.64 **H** 3.48
Ce (11D.pXmX)	$Ce(HTCPB)(X)_{0.65}(H_2O)_{0.18}(DCM)_{0.35}$	**C** 59.54 **H** 3.47	**C** 59.54 **H** 3.37
Pr (12D.pXmX)	$Pr(HTCPB)(X)_{0.63}(H_2O)_{0.03}(DCM)_{0.70}$	**C** 58.79 **H** 3.43	**C** 58.79 **H** 3.34
Nd (13D.pXmX)	$Nd(HTCPB)(X)_{0.67}(H_2O)_{0.09}(DCM)_{0.44}$	**C** 59.83 **H** 3.49	**C** 59.83 **H** 2.46
Sm (14D.pXmX)	$Sm(HTCPB)(X)_{0.68}(H_2O)_{0.01}(DCM)_{1.08}$	**C** 56.77 **H** 3.39	**C** 56.77 **H** 3.16

In order to investigate this selectivity, the single crystal structures of pX and mX loaded **10D-14D** were determined for analysis, as was done for **11D** in chapter 5.

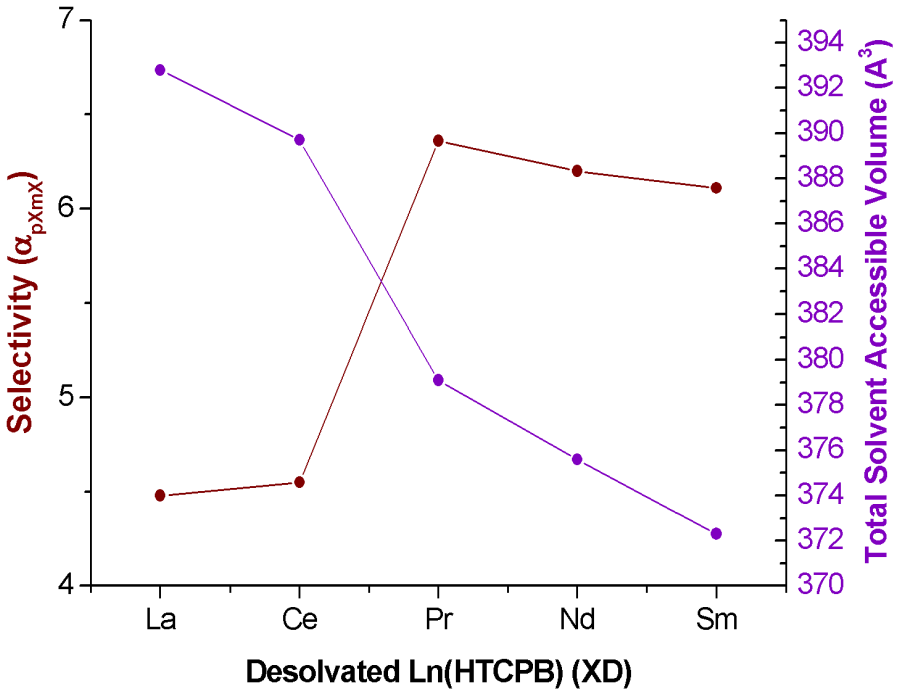

Figure 5: *pX/mX selectivity of* ***10D-14D*** *after 24 hours (brown) against total solvent accessible volume of XD (purple), where X = La-Sm.*

6.3.3.2 Single Crystal Structure Determination of pX and mX loaded Frameworks

A series of single crystal diffraction experiments were carried out to determine the structure of the pX and mX loaded isostructrural frameworks **10D-14D** for comparison with the pX and mX loaded **11D** as discussed in chapter 5; **11P** and **11M** respectively. This was done in order to gain understanding at the molecular level as to how the isomers interact with the host framework in each case and why the different isostructural materials produce different pX/mX selectivities.

Single crystals of **10-14** were activated at 100 °C in a Schlenk tube under a vacuum of 10^{-2} mbar overnight. Following activation the samples were back filled with N_2 and allowed to cool to room temperature after which time, 1 mL of pX (**XP**) and 1 mL of mX (**XM**) were added to the separate samples respectively, where **X** = **10D-14D**. The Schlenk tubes were sealed under N_2 and left for 24 hours before a xylene loaded single crystal was transferred under N_2 directly into fombilin oil, mounted onto a mitegen tip and put directly into a N_2 flow on the goniometer. Single crystal data was collected. Following structure solution and refinement, the same framework atom and ring numbering scheme was used as was done so for all desolvated compounds **10D-14D**.

As described in chapter 4 and 5, **11D** has two distinct channels; the larger channel 1 and the smaller channel 2. For all pX and mX loaded frameworks, the same channels are present albeit with slightly different morphologies which will be discussed later, but the same channel numbering will be used.

Table 10: *Unit cell dimensions of pX (green) and mX (blue) loaded* ***10-14*** *and calculated total accessible volume calculated using Olex2:*

Ln(HTCPB).X	Unit Cell Dimensions			Unit Cell Volume (Å^3)	Total Accessible Volume (Å^3)		
	a (Å) α (°)	b (Å) β (°)	c (Å) γ (°)		Overall	Channel 1	Channel 2
La.pX (10P)	10.1549(5) 89.124(6)	12.6683(6) 79.234(6)	15.7228(11) 68.024(5)	1839.37	657.5	394.4	263.1
Ce.pX (11P)	9.5603(4) 88.455(10)	12.1386(5) 74.417(10)	15.9458(6) 70.233(10)	1673.27	448.9	242.5	206.4
Pr.pX (12P)	9.5660(4) 88.480(6)	12.1457(4) 74.692(5)	15.9184(11) 70.211(5)	1674.50	453.9	246.7	207.2
Nd.pX (13P)	9.5208(2) 88.507(6)	12.1181(3) 74.679(5)	15.8778(11) 70.377(5)	1660.21	445.1	242.1	203.0
Sm.pX (14P)	9.5144 (4) 88.570(6)	12.0813(5) 75.22(5)	15.8641(11) 70.280(5)	1656.03	447.6	244.4	203.2
La.mX (10M)	10.2519(3) 89.609(6)	12.6764(3) 81.143(7)	15.6928(11) 69.124(8)	1880.24	694.6	417.1	277.5
Ce.mX (11M)	9.7441(6) 88.979(2)	12.3318(7) 77.399(2)	15.7737(9) 69.498(2)	1729.02	501.8	283.6	218.2
Pr.mX (12M)	10.110(3) 90.430(9)	12.510(4) 99.570(7)	15.680(4) 110.270(4)	1829.89	643.9	381.8	262.1
Nd.mX (13M)	9.6812(6) 88.977(2)	12.2892(7) 77.463(2)	15.7407(10) 69.750(2)	1711.7	490.5	277.5	213.0
Sm.mX (14M)	9.7513(7) 71.138(2)	18.7501(13) 87.031(2)	22.2553(16) 81.905(2)	3812.1	651.0	381.1	269.9

In all cases, the data shows an overall expansion in the unit cell dimensions and volume with uptake of guests (*Table 10*). The expansion from the empty desolvated frameworks **XD** (**X = 10-14**) is proportional to the size of the guest taken up: The greatest unit cell volume expansion is seen with uptake of mX which has the larger kinetic diameter of 6.4 Å, causing an increase from 1611.7 (**10D**), 1611.7 (**11D**), 1594.8 (**12D**), 1588.5 (**13D**) and 1580.0 (**14D**) Å^3 (*Table 5*) to 1880.2 (**10M**), 1729.0 (**11M**), 1829.9 (**12M**), 1704.0 (**13M**) and 3812.1 (**14M**) Å^3 (*Table 10*). Uptake of pX causes a smaller change, to 1673.3 (**11P**), 1674.5 (**12P**), 1660.2 (**13P**) and 1656.0 (**14P**) Å^3 (*Table 10*), as it is the smaller of the two isomers with a kinetic diameter of 5.8 Å. However, when pX is loaded into **10D**, there is an anomalously large increase in unit cell volume and respective channel 1 and 2 total accessible volumes. Subsequent analysis shows that **10D** has the largest channels of the set; in channel 1 two pX guests enter at a tilt, which forces the channel open further. This is not seen for any of the other pX loaded structures.

Table 11: *Interactions present between guest pX and mX with their host frameworks* ***10P-14P*** *and* ***10M-14M*** *for comparison. Where 2 interactions per X, this indicates 2 symmetrical contacts.*

Interaction	Donor Atom/ Interaction	C-H···π centroid-centroid		C-H···O18		Nº interactions per X†	Shown in Figure
		Length (Å)	Plane-Plane Angle (°)	Length (Å)	Angle (°)		
10P – pX1	H6···π	5.899	141.760	-	-	2	7
10P – pX2	H3···π	5.875	146.457	-	-	2	
10P – pX3	H42··· π	5.176	140.425	-	-	1	
10P – pX3	H42···π	5.565		-	-	1	
10M – mX1	H6···π	5.596	141.581	-	-	1	9
10M – mX1	H6···π	6.316		-	-	1	
10M – mX2	H3···π	5.635	145.072	-	-	1	
10M – mX2	H3···π	6.284		-	-	1	
10M – mX3	H42···π	5.943	139.201	-	-	1	
10M – mX3	H42···π	4.950		-	-	1	
11P –pX1	H3···π	5.658	92.097	-	-	2	Chapter 5
11P – pX2	H44···π	5.561	143.23	-	-	2	
11P – pX2	O18···H20C-C20X	-	-	2.583	146.296	2	
11M – mX1a	H3···π	5.811	93.750	-	-	1	
11M – mX1a	H3···π	6.026		-	-	1	
11M – mX1b	H6···π	6.184	89.067	-	-	1	
11M – mX1b	H6···π	5.961		-	-	1	
11M – mX2	H44···π	5.938	142.140	-	-	1	
11M - mX2	H44···π	4.931		-	-	1	
11M - mX2	O18···H10A-C10X	-	-	3.351	128.200	1	
12P – pX1	H3···π	5.659	92.958	-	-	2	11
12P– pX2	H44···π	5.488	143.098	-	-	2	
12P – pX2	O18···H20C-C20X	-	-	2.608	145.513	2	
12M – mX1	H3···π	6.449	91.062	-	-	1	13
12M – mX1	H6···π	6.036		-	-	1	
12M – mX2	H44···π	5.837	138.615	-	-	1	
12M – mX2	H44···π	4.958		-	-	1	
13P – pX1	H3···π	5.653	92.609	-	-	2	15
13P – pX2	H44···π	5.466	142.351	-	-	2	
13P – pX2	O18···H20C-C20X	-	-	2.558	147.587	2	
13M – mX1	H3···π	5.791	89.512	-	-	1	17
13M – mX1	H3···π	6.011		-	-	1	
13M – mX2	H6···π	5.995	89.157	-	-	1	
13M – mX3	H42···π	4.923	142.343	-	-	1	
13M – mX3	H42···π	5.851		-	-	1	
14P – pX1	H3···π	5.631	92.498	-	-	2	19
14P – pX2	H44···π	5.441	141.777	-	-	2	
14P – pX2	O18···H20C-C20X	-	-	2.566	149.709	2	
14M – mX1	H3···π	5.573	126.126	-	-	1	21
14M – mX2	H3'···π	5.484	114.598	-	-	1	
14M – mX4	H14'···π	5.584	140.095	-	-	1	
14M – mX4	H44···π	5.277	144.956	-	-	1	

†2 interactions implies that 2 symmetrical interactions are formed either side of the central aromatic ring of the xylene guest. Coloured rows represent colour of Ln ion used in figures.

6.3.3.2.1 pX loaded 10D: 10P

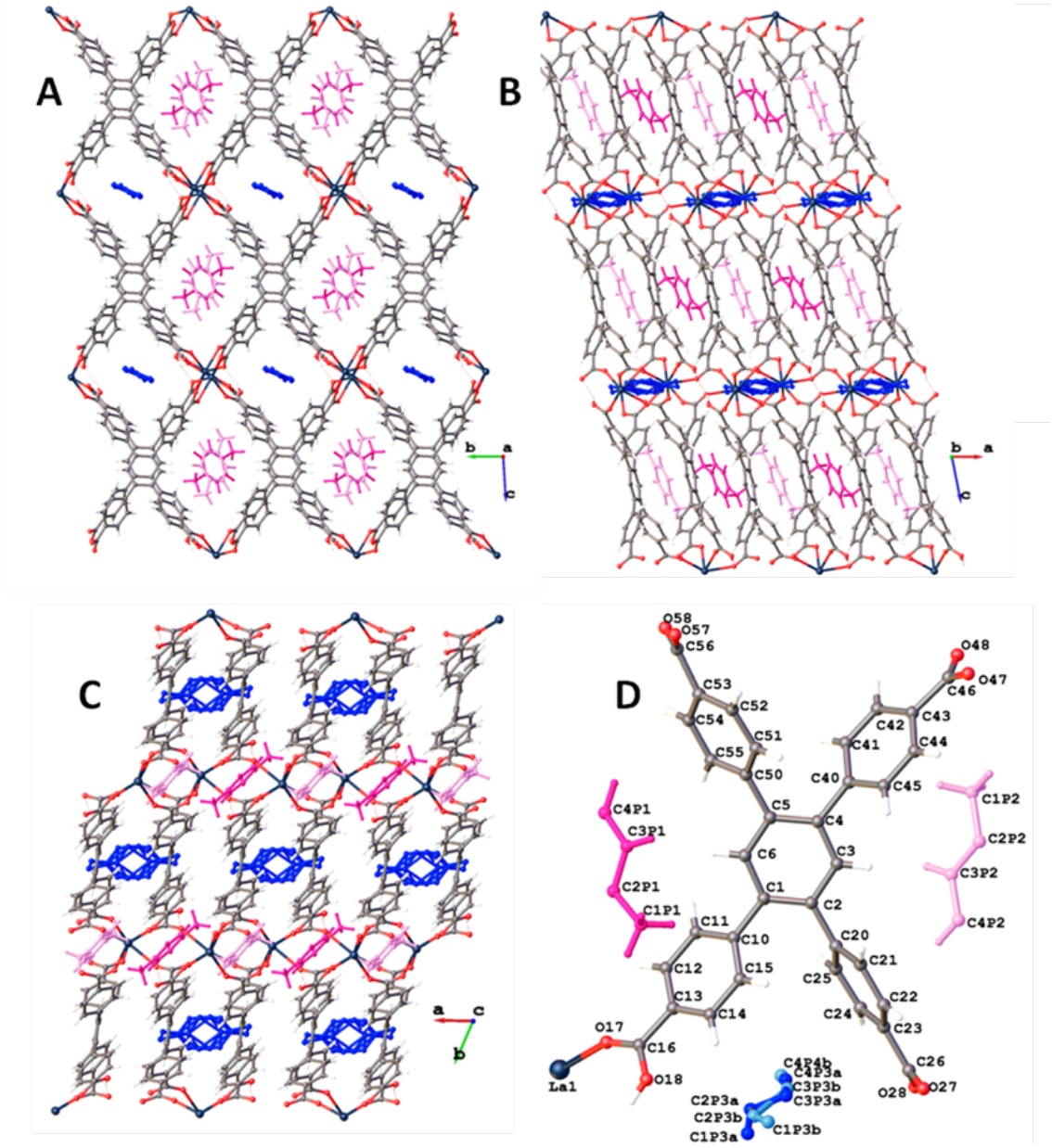

Figure 6: *Single crystal structure of* ***10P****. A: View down 100; B: View down 010; C: View down 001; D: Asymmetric unit with pX1 (pink) and pX2 (pale pink) in channel 1 and disordered pX3 (blue) in channel 2. La (blue), C (grey), O (red), H (white).*

The single crystal of **10P** used had dimensions of 0.12 × 0.09 × 0.08 mm. **10P** contains two sites for pX in channel 1, at each of which, half a pX molecule is found in the asymmetric unit, each refining to 100 % occupancy (pX1 and pX2). In channel 2, two half disordered pX units could be resolved at the same site which on the application of symmetry grew into one full disordered pX molecule (pX3). Each half of the pX disorder refines to 50 %, meaning there is one full half pX molecule in the asymmetric unit of channel 2. Overall, per unit cell, there are 3 pX molecules; 2 in

channel 1 and 1 in channel 2 (*Figure 6D*). The structure has two channels running along the 100 direction; the larger channel 1 housing pX1 and pX2 and the smaller channel 2 containing pX3 (*Figure 6A-C*). This gives **10P** the formula La(HTCPB)·$pX_{1.5}$. This differs from **11P** in that two pX guests are found in channel 1 instead of one, and they both enter at a tilt rather than in line with the channel as does pX in **11P**.

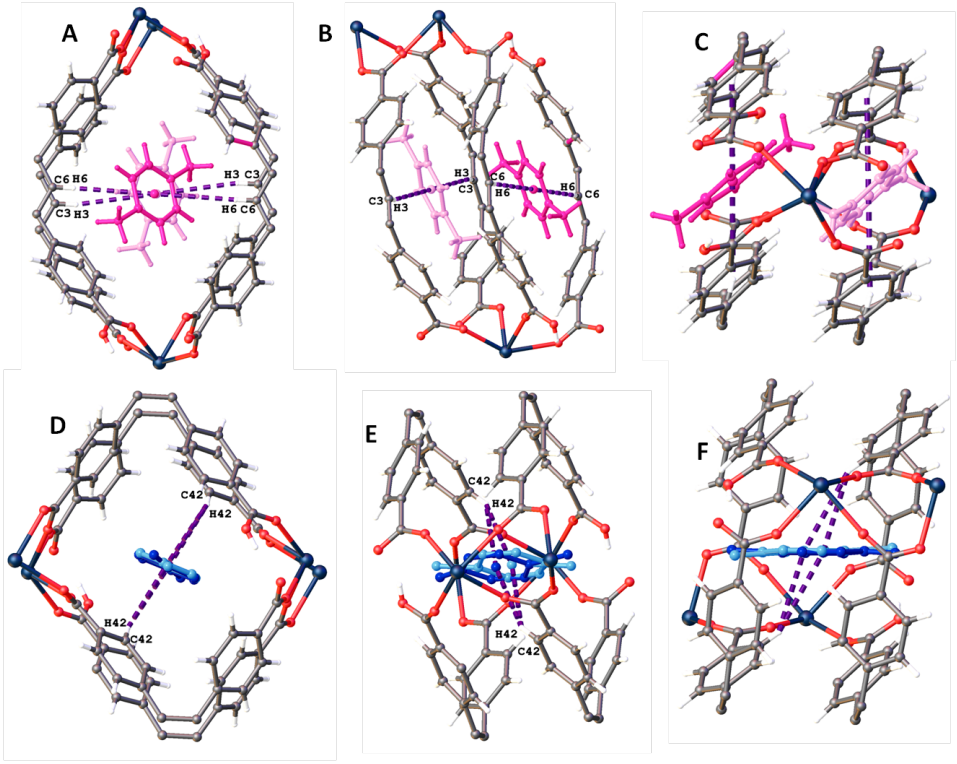

Figure 7: *Intermolecular interactions between pX1 (dark pink) and pX2 (pale pink) in channel 1 and pX3a (dark blue) and pX3b (pale blue) in channel 2 and host framework **10P**. C-H•••π interactions shown in purple. A,D: View down 100; B,E: View down 010; C: View down 001; F: View down plane of guest pX3.*

In channel 1, two symmetrical C6-H6···π interactions of 5.899 Å (centroid-centroid[13]) between the central aromatic ring of the HTCPB ligand and the π-system of pX1 and two symmetrical C3-H3···π interactions of 5.875 Å (centroid-centroid[13]) between the central aromatic ring of the HTCPB ligand and the π-system of pX2 guest anchor the pX guests at these specific locations in the channel (*Table 11, Figure 7A-C*). In contrast to the other pX loaded frameworks, **10P** has two pX guests in channel one, both of which enter at a tilt rather than aligning with the channel direction as seen for **11P-14P**. As a result, the C6-H6···π interactions present between the framework and pX1 and pX2 guests are longer at 5.875 and 5.899 Å respectively and at less optimal angles of 141.760 and 146.457 ° respectively, whereas pX1 in **11P-14P** have C-H···π interaction distances of around 5.6 Å at the more ideal angle of around 90 °.

In channel 2, the central aromatic ring of pX3 lies at a similar position to where pX2 lies in channel 2 of **11P**, with slight lateral disorder along the channel direction. Two asymmetric C42-H42···π interactions of 5.176 Å and 5.565 Å (centroid-centroid[13]) are present between ring 4 of the HTCPB ligand and the π-system of each part of the disorder of the pX3 guest (*Table 11, Figure 7D-F*). This is unlike pX in channel 2 of **11P-14P**, in which two symmetrical host-guest contacts form.

6.3.3.2.2 mX loaded 10D: 10M

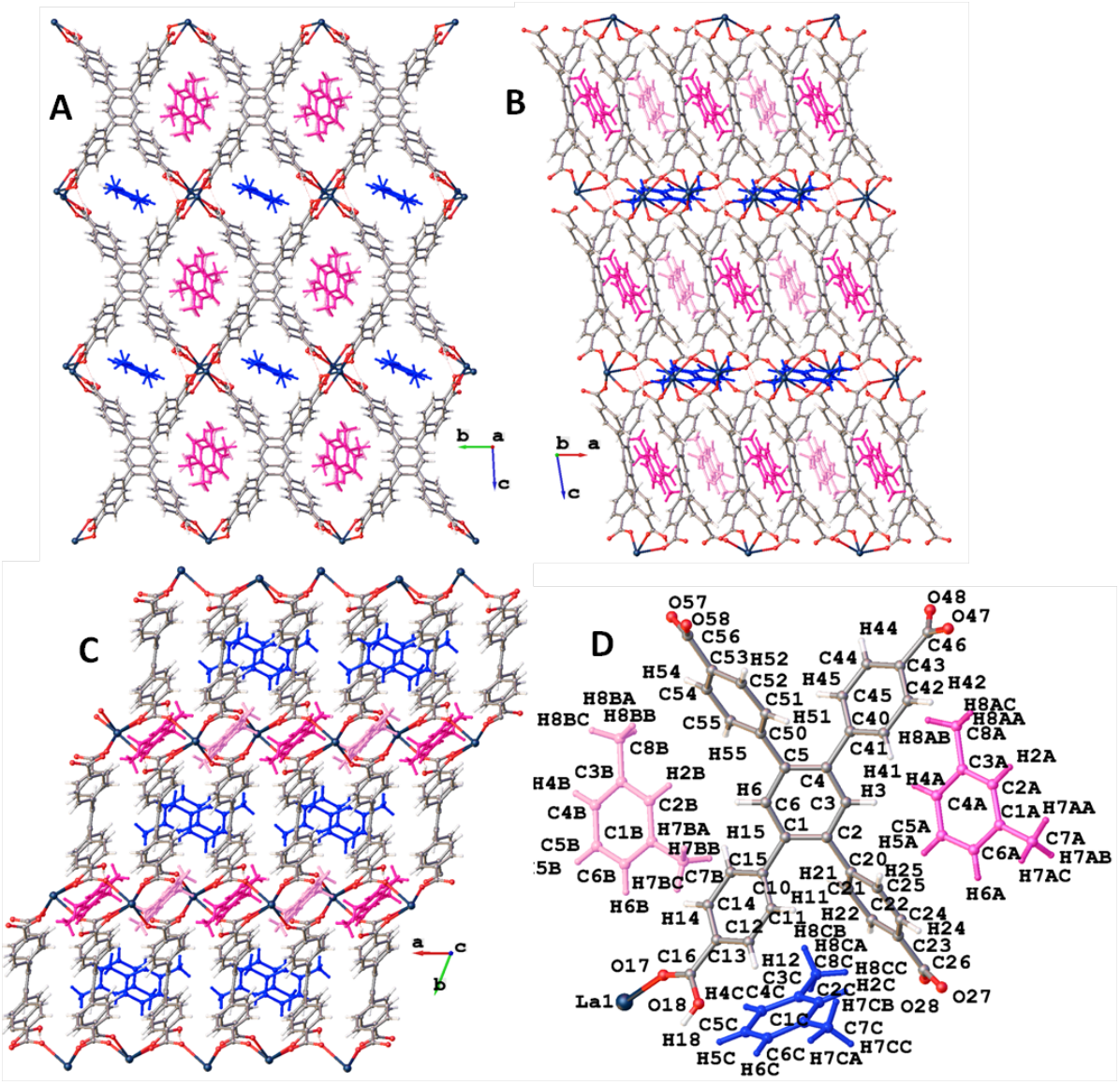

Figure 8: *Single crystal structure of **10M**. A: View down 100; B: View down 010; C: View down 001; D: Asymmetric unit with mX1 (dark pink) and mX2 (pale pink) in channel 1 and pX3 (blue) in channel 2. La (blue), C (grey), O (red), H (white).*

The single crystal of **10M** used had dimensions of 0.96 × 0.15 × 0.069 mm. **10M** contains two disordered sites for mX in channel 1 (mX1 and mX2) each of which is disordered over two positions with itself, but there is no disorder between mX1 and mX2 molecules, unlike mX in channel 1 of **11M-13M**, in which disorder is observed between mX molecules along the channel. Both mX1 and mX2 refine to 100 % occupancy. This differs from **11M** as two mX guests enter channel 1, both at a tilt whereas mX in **11M** channel 1 enters in line with the channel.

In channel 2, mX is disordered over two positions, with the whole molecule refining to 100 % occupancy (mX3). Overall, per unit cell, there are 3 mX molecules; 2 in channel 1 and 1 in channel 2 (Figure 8*D*). The structure has two channels running along the 100 direction; the larger channel 1 housing mX1 and mX2 and the smaller channel 2 containing the disordered mX3 (Figure 8*A-C*). This gives **10M** the formula La(HTCPB)·$mX_{1.5}$.

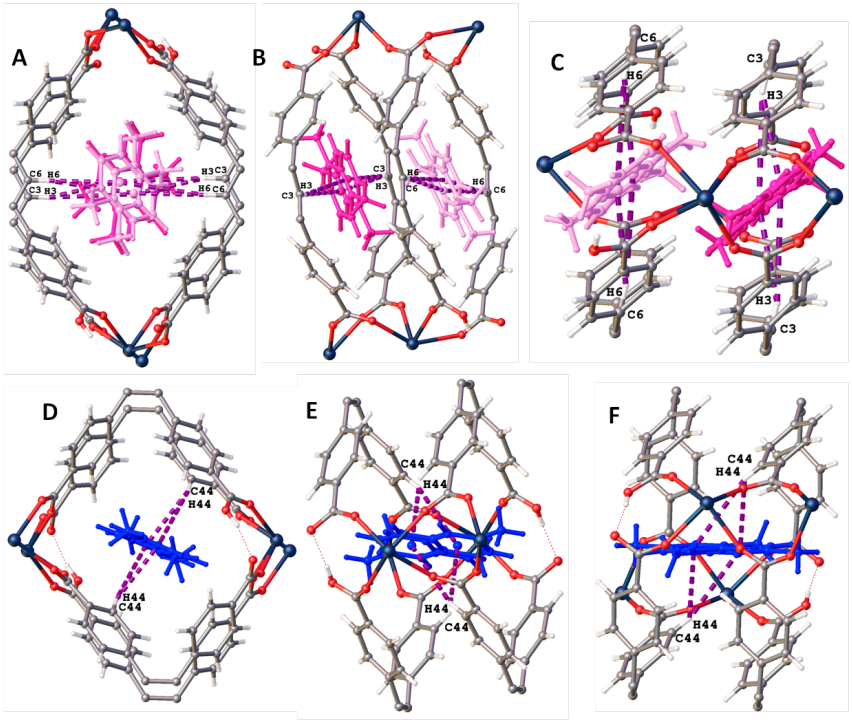

Figure 9: *Intermolecular interactions between mX1 (dark pink) and mX2 (pale pink) in channel 1 and mX3 (dark blue) in channel 2 and host framework* ***10M****. C-H···π interactions shown in purple. A,D: View down 100; B,E: View down 010; C: View down 001; F: View down plane of guest mX3.*

In channel 1, two asymmetric C6-H6···π interactions of 5.596 and Å 6.316 Å (centroid-centroid[13]) between the central aromatic ring of the HTCPB ligand and the π-system of each part of the disorder of mX1, and two asymmetrical C3-H3···π interactions of 5.635 Å and 6.284 Å (centroid-centroid[13]) between the central aromatic ring of the HTCPB ligand and the π-system of each part of the disorder of mX2 anchor the mX guests at these pinch points along the channel (*Table 11, Figure 9A-C*). As the channels in **10M** are larger than those in **11M**, mX enters channel 1 at a tilt

meaning that two mX can fit into the same space that one was found in channel 1 of **11M**, so the continuum of disorder along the channel for mX1 in **11M** is not seen in for mX1 and mX2 in channel 1 of **10M**. In this respect, **10P** and **10M** are similar as two xylene guests are found in each channel 1 and form similar interactions. This is not the case with any of the other pX and mX loaded frameworks (**11P-14P**, **11M-14M**).

In channel 2, the mX guest enters in line with the channel, as does mX2 in channel 2 of **11M-14M** and two asymmetric C42-H42···π interactions of 5.943 Å and 4.950 Å (centroid-centroid[13]) are present between ring 4 of the HTCPB ligand and the π-system of each part of the disorder of the mX3 guest (*Table 11, Figure 9D-F*). Asymmetric interactions are formed as each part of the mX disorder lies off centre compared to pX in the pX loaded frameworks, which lies at the centre of the channel and can form two symmetric interactions.

6.3.3.2.3 pX loaded 12D: 12P

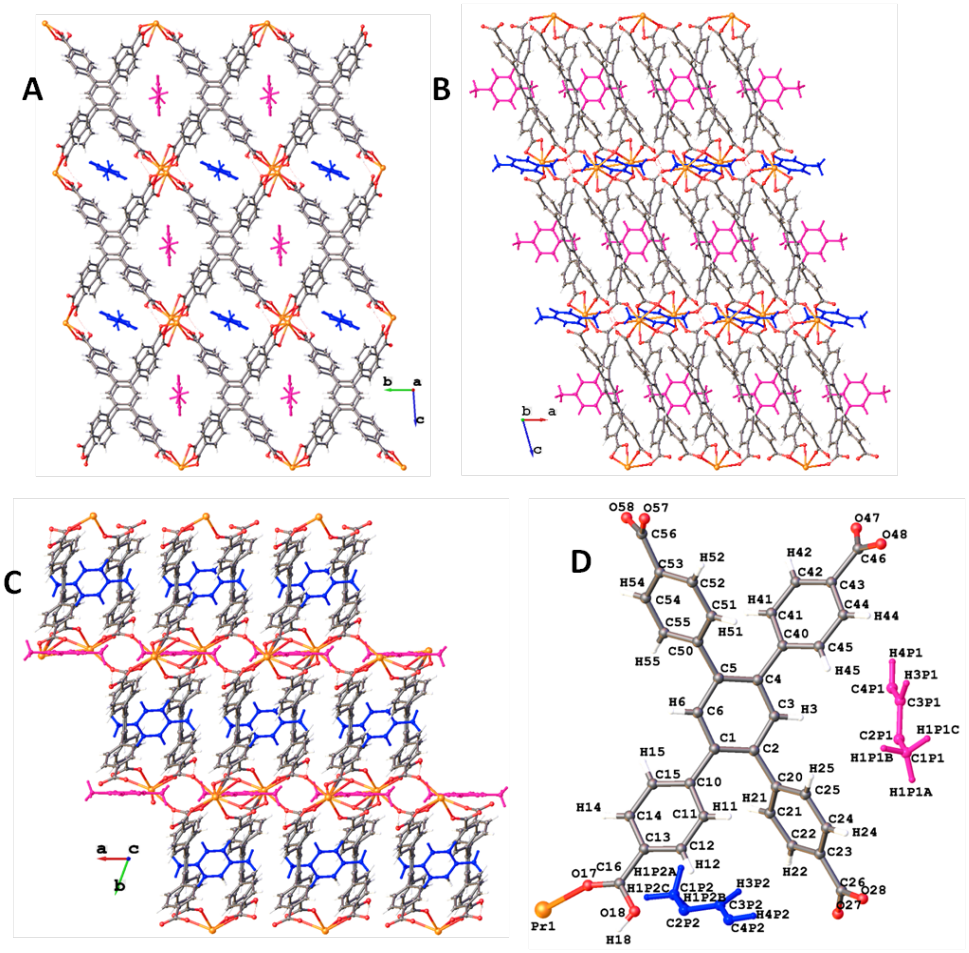

Figure 10: *Single crystal structure of* ***12P****. A: View down 100; B: View down 010; C: View down 001; D: Asymmetric unit with pX1 (pink) in channel 1 and pX2 (blue) in channel 2. Pr (orange), C (grey), O (red), H (white).*

The single crystal of **12P** used had dimensions of 0.06 × 0.05 × 0.03 mm. The asymmetric unit of **12P** contains two half pX molecules both of which refine to 100 % occupancy, one found in each of the two channels: pX1 in channel 1 and pX2 in channel 2. This means that per unit cell there are two whole pX molecules, one per Pr(HTCPB) formula unit (*Figure 10D*). The structure is similar to **11P** as described in chapter 5, with slightly larger unit cell dimensions that the vacant desolvated structure **11D**, due to the inclusion of pX guest. The structure has two channels running along the 100 direction; the larger channel 1 housing pX1 and the smaller channel 2 containing pX2 (*Figure 10A-C*). This gives **12P** the formula Pr(HTCPB)·pX.

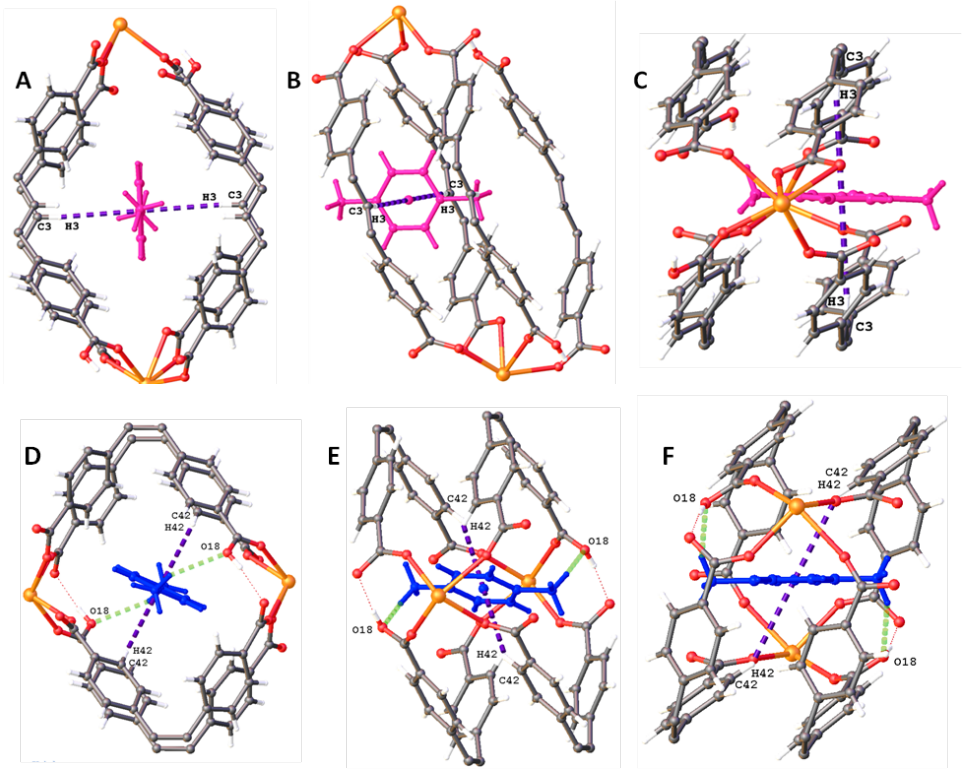

Figure 11: *Intermolecular interactions between pX1 (pink) in channel 1 and pX2 (blue) in channel 2 and host framework* ***12P****. C-H···π interactions shown in purple, C-H···O interactions shown in green. A,D: View down 100; B,E: View down 010; C: View down 001; F: View down plane of guest pX2.*

In channel 1, two symmetrical C3-H3···π interactions of 5.659Å (centroid-centroid[13]) between the central aromatic ring of the HTCPB ligand and the π-system of pX1 guest anchor the pX at specific locations in the channel (*Table 11, Figure 11A-C*). Unlike **10P**, the slightly smaller channel size means that pX enters in line with the channel, forming shorter C-H···π interactions at a more optimal angle of 92.958 °. This is also seen for other pX loaded compounds (**11P**, **13P** and **14P**)

In channel 2, the pX2 guest enters in line with the channel, as does pX2 in channel 2 of **11P-14P** and two symmetric C44-H44···π interactions of 5.488 Å (centroid-centroid[13]) are present between

the central aromatic ring of the HTCPB ligand and the π-system of the pX2 guest (*Table 11, Figure 11D-F*). An O18···H20C-C20X interaction is also present between O18 of the protonated monodentate carboxylate on ring 1 of the HTCPB ligand and the pX2 methyl hydrogens at 2.608 Å. The same C-H···O interaction is observed in pX loaded compounds **11P-14P**. This additional intermolecular host-guest interaction helps to lock the pX guests at specific locations along the channels; an interaction that is not picked up by mX in the mX loaded frameworks.

6.3.3.2.4 mX loaded 12D: 12M

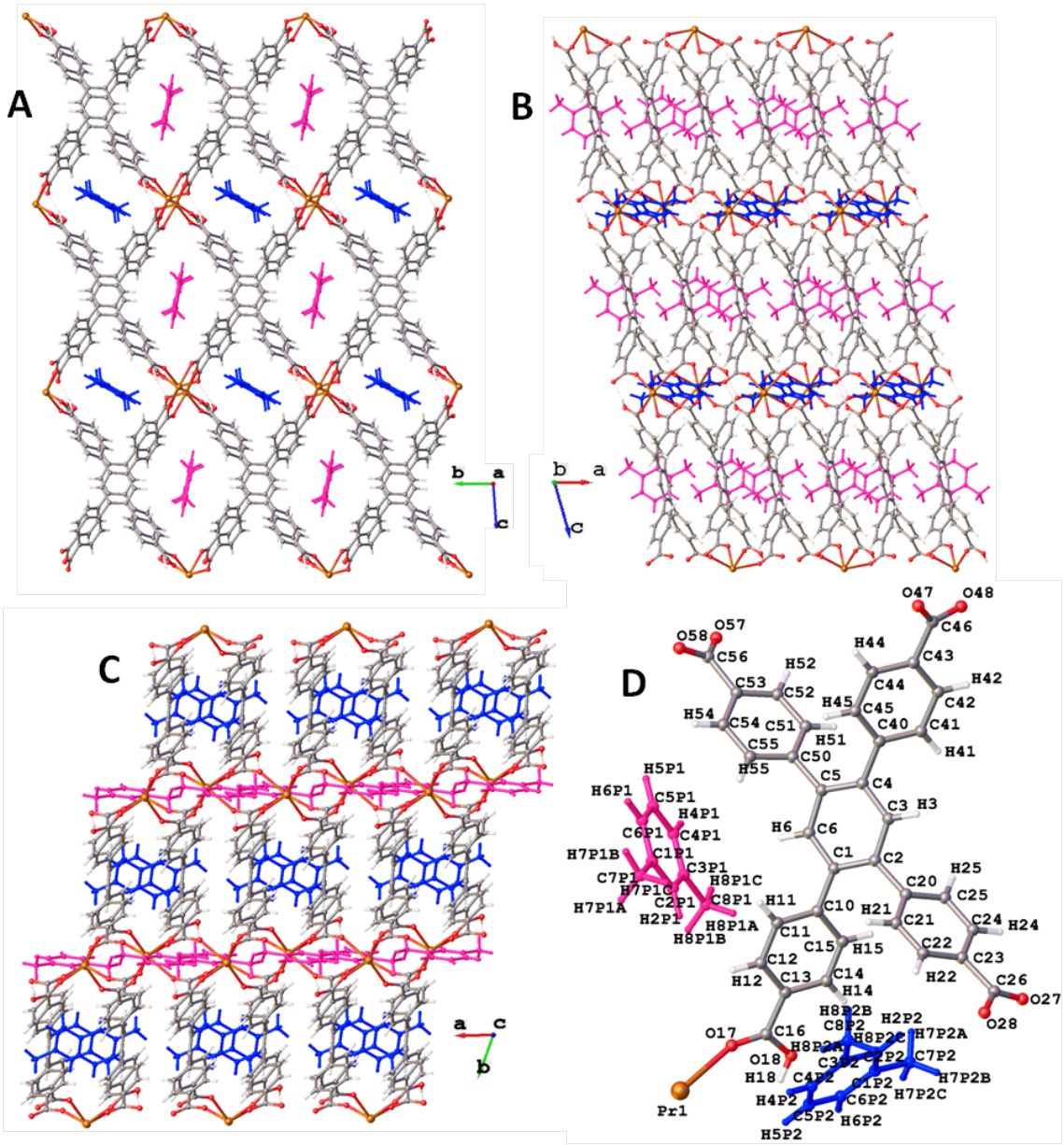

Figure 12: *Single crystal structure of* ***12M****. A: View down 100; B: View down 010; C: View down 001; D: Asymmetric unit with mX1 (pink) in channel 1 and mX2 (blue) in channel 2. Pr (orange), C (grey), O (red), H (white).*

The single crystal of **12M** used had dimensions of 0.069 × 0.046 × 0.036 mm. **12M** contains one disordered site for mX in channel 1 (mX1), found over two positions with the application of symmetry and one mX guest in channel 2 (mX2) which again is disordered over two positions with the application of symmetry. Each mX1 and mX2 refine to 100 % occupancy. Overall, per unit cell, there are 2 mX molecules; 1 in channel 1 and 1 in channel 2 (*Figure 12D*). The structure has two channels running along the 100 direction; the larger channel 1 housing mX1 and the smaller channel 2 containing mX2 (*Figure 12A-C*). This gives **12M** the formula Pr(HTCPB)·mX.

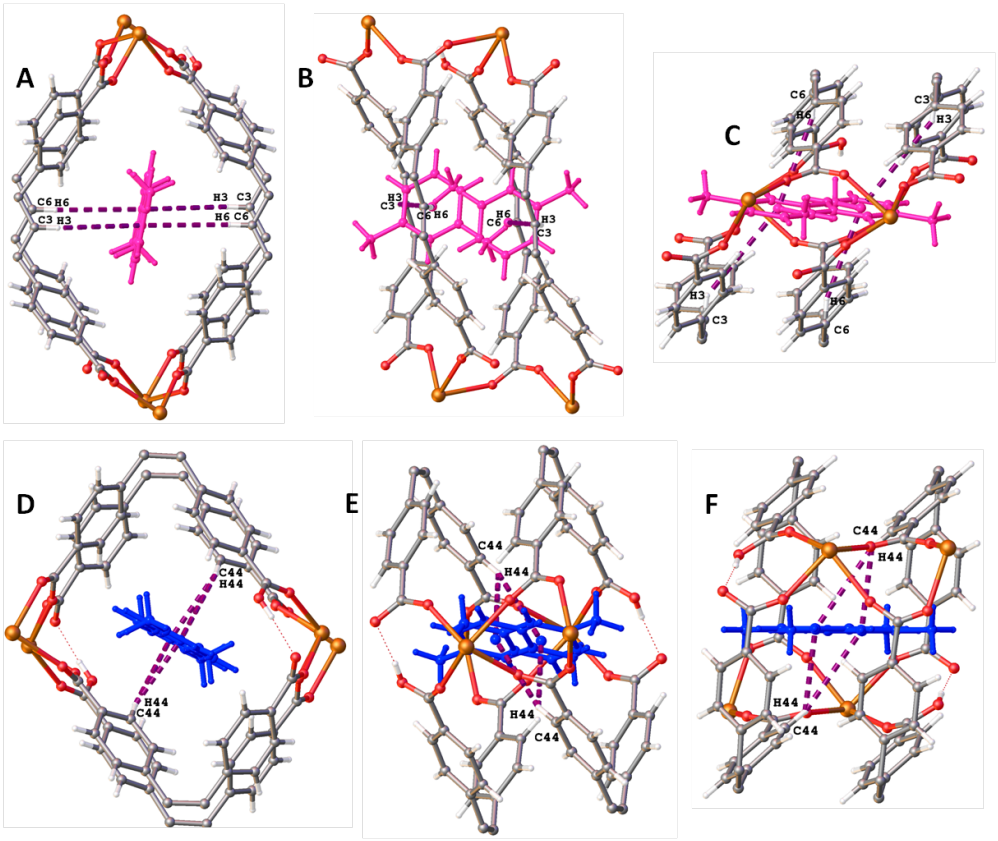

Figure 13: *Intermolecular interactions between mX1 (pink) in channel 1 and mX2 (blue) in channel 2 and host framework* ***12M****. C-H···π interactions shown in purple. A,D: View down 100; B,E: View down 010; C: View down 001; F: View down plane of guest pX2.*

In channel 1 of **12M**, two asymmetric C-H···π interactions form between the central aromatic ring of the HTCPB ligand and each part of the mX1 guest; C3-H3···π at 6.449 Å and C6-H6···π at 4.036 Å (centroid-centroid[13]) (*Table 11***,** *Figure 13A-C*). In channel 2, the mX guest enters in line with the channel, as does mX2 in channel 2 of **11M-14M** and two asymmetric C44-H44···π interactions of 5.837 Å and 4.958 Å (centroid-centroid[13]) are present between ring 4 of the HTCPB ligand and the π-system of each part of the disorder of the mX2 guest (*Table 11***,** *Figure 13D-F*).

6.3.3.2.5 pX loaded 13D: 13M

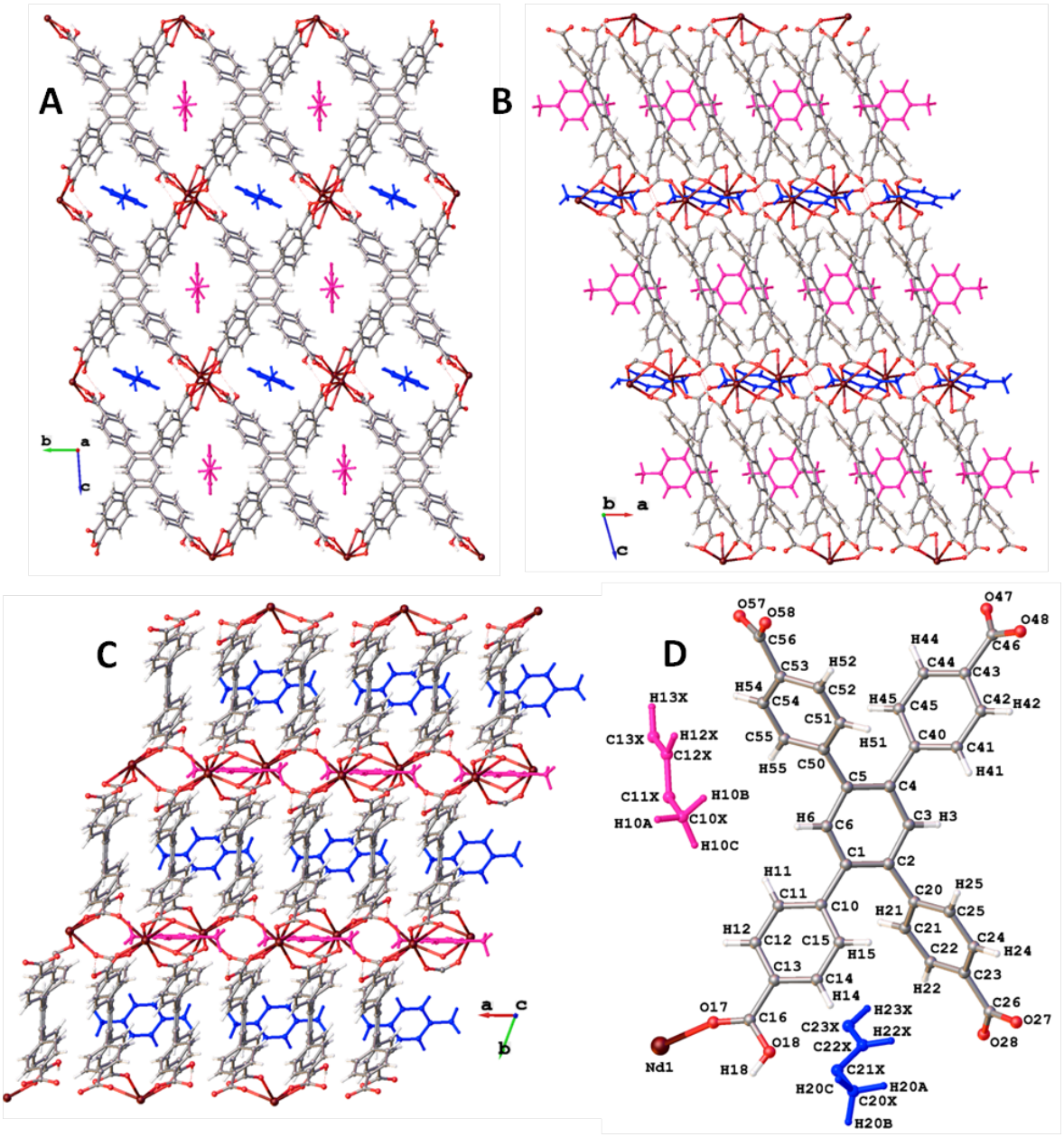

Figure 14: *Single crystal structure of* ***13P****. A: View down 100; B: View down 010; C: View down 001; D: Asymmetric unit with pX1 (pink) in channel 1 and pX2 (blue) in channel 2. Nd (brown), C (grey), O (red), H (white).*

The single crystal of **13P** used had dimensions of 0.08 × 0.05 × 0.03 mm. As in **11P** and **12P**, the asymmetric unit of **13P** contains two half pX molecules both of which refine to 100 % occupancy, one found in each of the two channels: pX1 in channel 1 and pX2 in channel 2. This means that per unit cell there are two whole pX molecules, one per Nd(HTCPB) formula unit (*Figure 14D*). The structure has two channels running along the 100 direction; the larger channel 1 housing pX1 and the smaller channel 2 containing pX2 (*Figure 14A-C*). This gives **13P** the formula Nd(HTCPB)·pX.

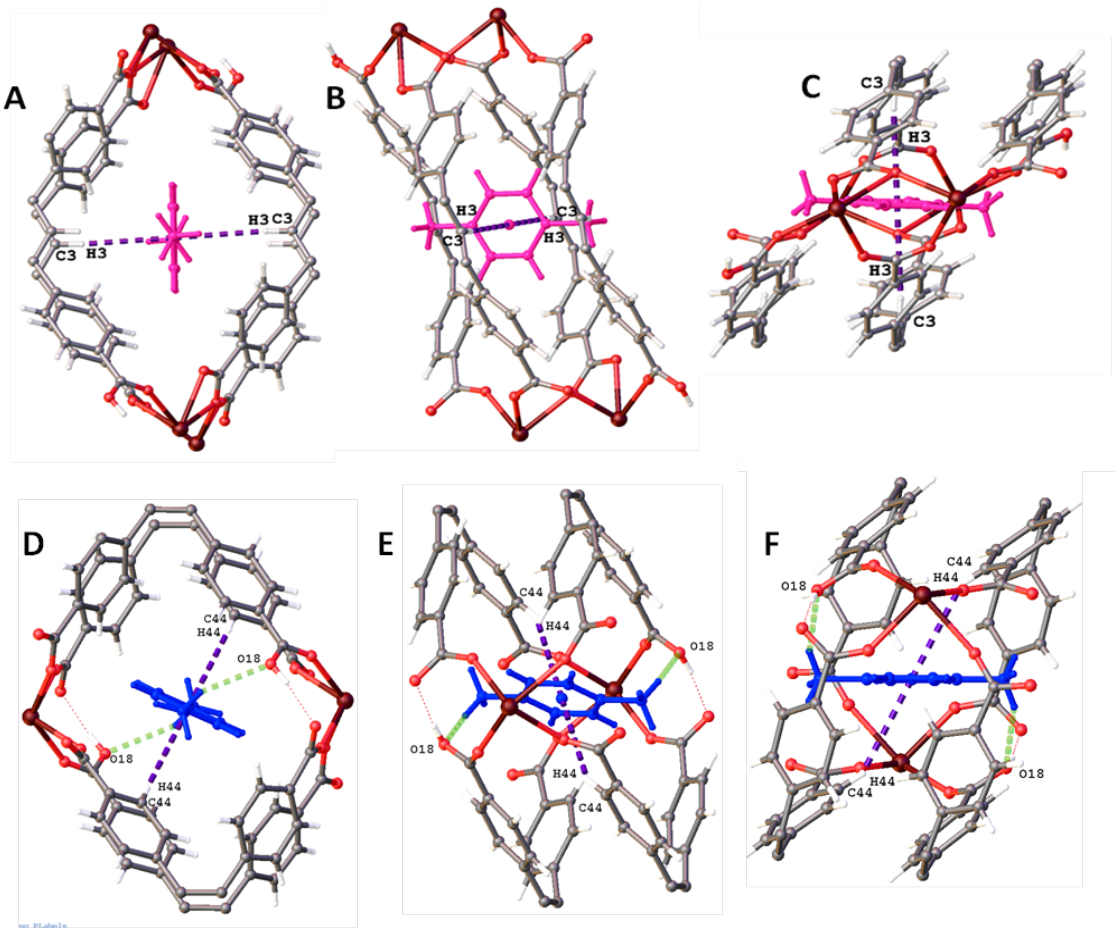

Figure 15: *Intermolecular interactions between pX1 (pink) in channel 1and pX2 (blue) in channel 2 and host framework* ***13P****. C-H···π interactions shown in purple, C-H···O interactions shown in green. A,D: View down 100; B,E: View down 010; C: View down 001; F: View down plane of guest pX2.*

In channel 1, two symmetrical C3-H3···π interactions of 5.653Å (centroid-centroid[13]) at an angle of 92.609 ° between the central aromatic ring of the HTCPB ligand and the π-system of pX1 guest anchor the pX at specific locations in the channel (*Table 11, Figure 15A-C*).

In channel 2, the pX2 guest enters in line with the channel, as does pX2 in channel 2 of **11P-14P** and two symmetric C44-H44···π interactions of 5.466 Å (centroid-centroid[13]) are present between the central aromatic ring of the HTCPB ligand and the π-system of the pX2 guest (*Table 11*). An O18···H20C-C20X interaction is also present between O18 of the protonated monodentate carboxylate on ring 1 of the HTCPB ligand and the pX2 methyl hydrogens at 2.558 Å (*Figure 15*D-F). The same C-H···O interaction is observed in pX loaded compounds **11P-14P**.

6.3.3.2.6 mX loaded 13D: 13M

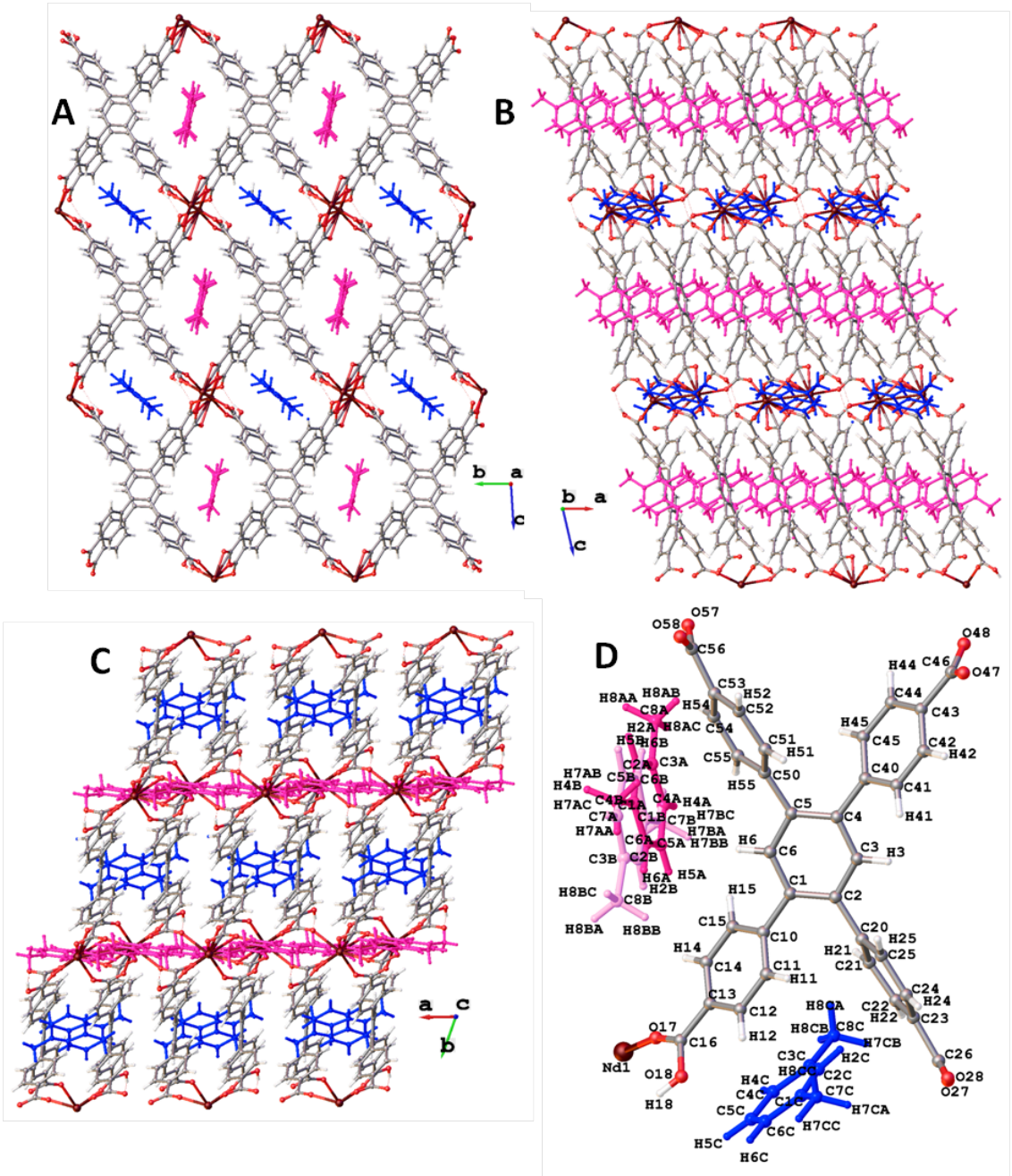

Figure 16: *Single crystal structure of* ***13M****. A: View down 100; B: View down 010; C: View down 001; D: Asymmetric unit with mX1 (dark pink) and mX2 (pale pink) in channel 1 and mX2 (blue) in channel 2. Nd (brown), C (grey), O (red), H (white).*

The single crystal of **13M** used had dimensions of 0.021 × 0.012 × 0.09 mm. **13M** contains two sites for mX in channel 1 (mX1 and mX2) (*Figure 16D*), both of which are present at 50 % occupancy and with the application of symmetry are disordered with each other producing an infinite chain of disordered mX along the channel 1. Guest mX2 is found in channel 2, disordered over two positions present in total at 100 % occupancy. Overall, per unit cell, there are 2 whole mX

molecules; 1 in channel 1 and 1 in channel 2 (*Figure 16D*). The structure has two channels running along the 100 direction; the larger channel 1 housing mX1 and the smaller channel 2 containing mX3 (*Figure 16A-C*). This gives **13M** the formula Nd(HTCPB)·mX.

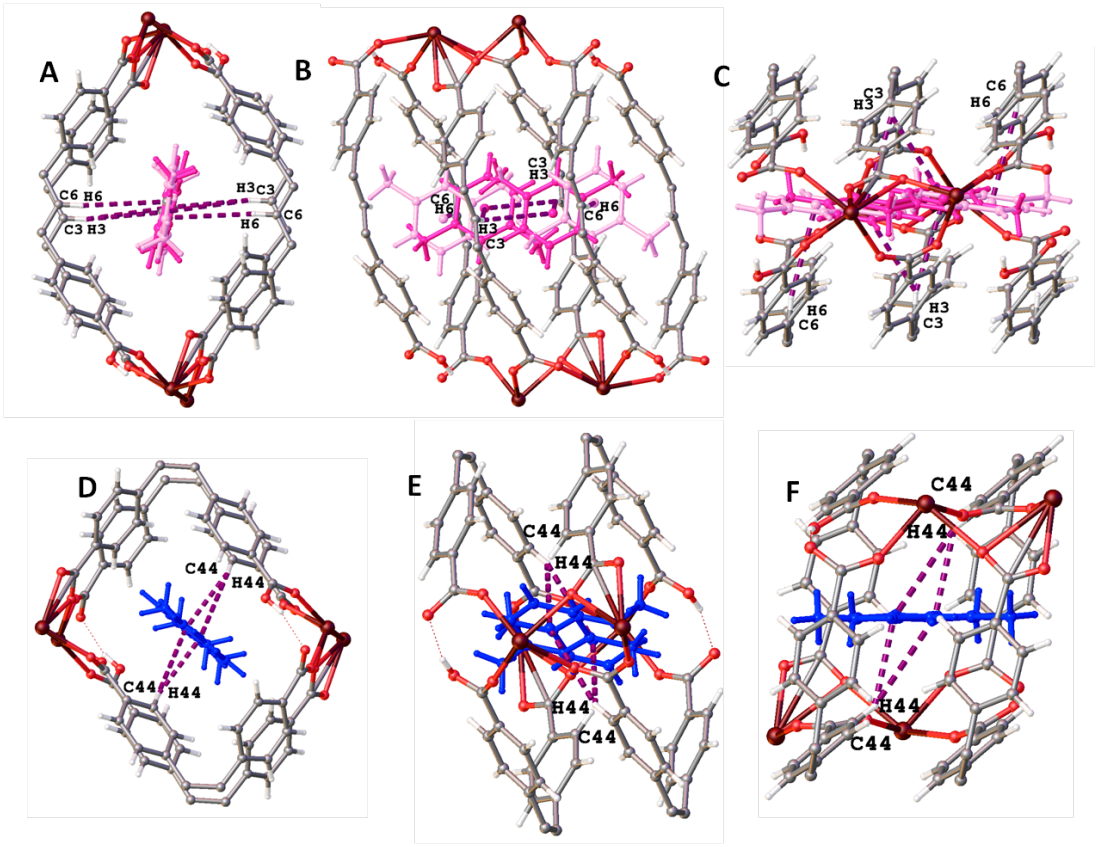

Figure 17: *Intermolecular interactions between mX1 (dark pink) and mX2 (pale pink) in channel 1 and mX3 (dark blue) in channel 2 and host framework* ***13M****. C-H···π interactions shown in purple. A,D: View down 100; B,E: View down 010; C: View down 001; F: View down plane of guest mX3.*

In channel 1 of **13M**, two asymmetric C3-H3···π interactions of 5.791 and 6.011 Å (centroid-centroid[13]) between the central aromatic ring of the HTCPB ligand and the π-system of from, whereas only one C6-H6 ···π interaction forms between mX2 and the framework (*Table 11, Figure 17A-C*). In channel 2, the mX guest enters in line with the channel, as does mX2 in channel 2 of **11M-14M** and two asymmetric C42-H42···π interactions of 4.923 Å and 5.851 Å (centroid-centroid[13]) are present between ring 4 of the HTCPB ligand and the π-system of each part of the disorder of the mX2 guest (*Table 11, Figure 17D-F*).

6.3.3.2.7 pX loaded 14D: 14P

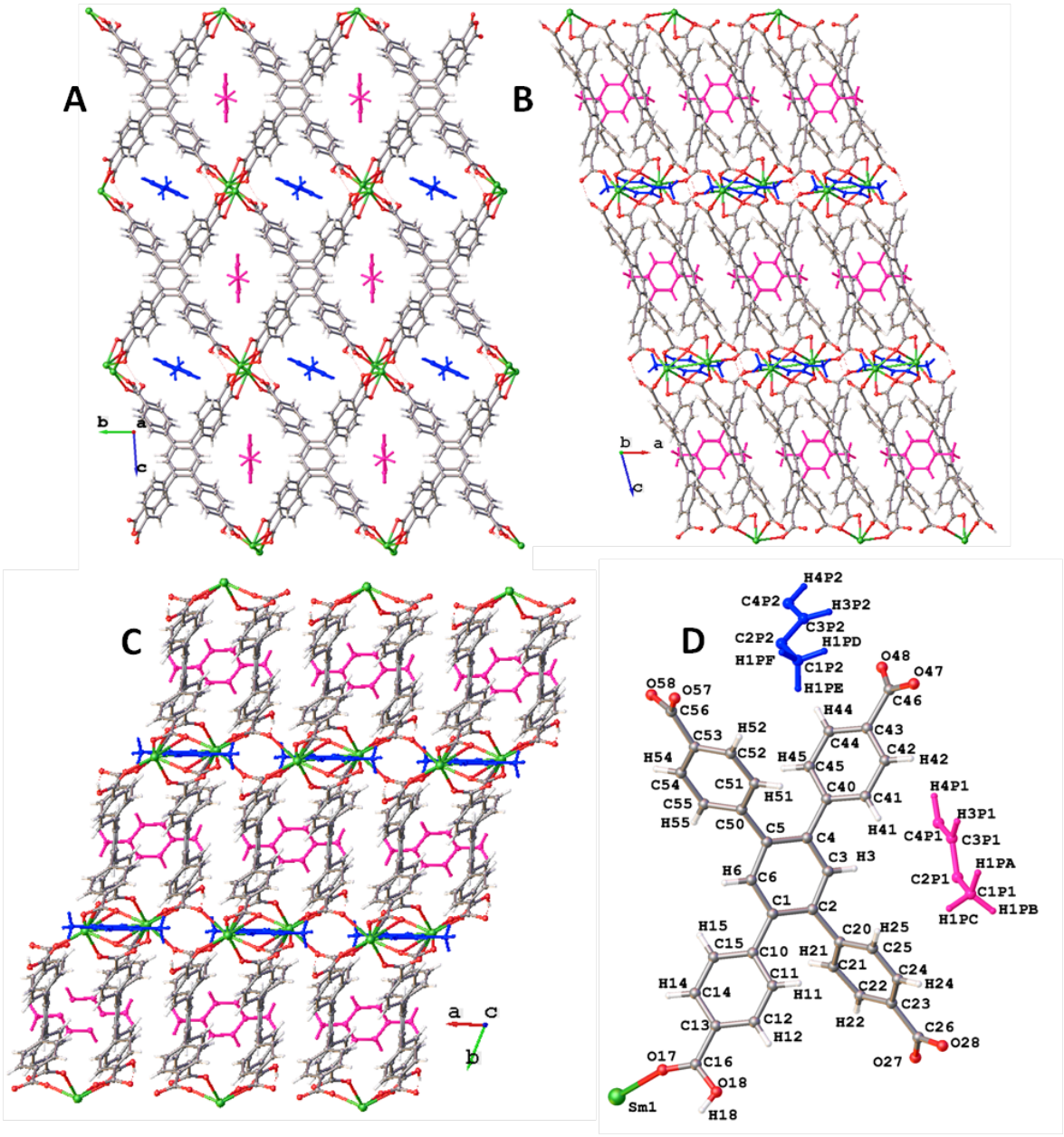

Figure 18: *Single crystal structure of* ***14P****. A: View down 100; B: View down 010; C: View down 001; D: Asymmetric unit with pX1 (pink) in channel 1 and pX2 (blue) in channel 2. Sm (green), C (grey), O (red), H (white).*

The single crystal of **14P** used had dimensions of 0.88 × 0.62 × 0.102 mm. As in **11P, 12P** and **13P**, the asymmetric unit of **14P** contains two half pX molecules both of which refine to 100 % occupancy, one found in each of the two channels: pX1 in channel 1 and pX2 in channel 2. This means that per unit cell there are two whole pX molecules, one per Sm(HTCPB) formula unit (*Figure 18*D). The structure has two channels running along the 100 direction; the larger channel 1

housing pX1 and the smaller channel 2 containing pX2 (*Figure 18A-C*). This gives **14P** the formula Sm(HTCPB)·pX.

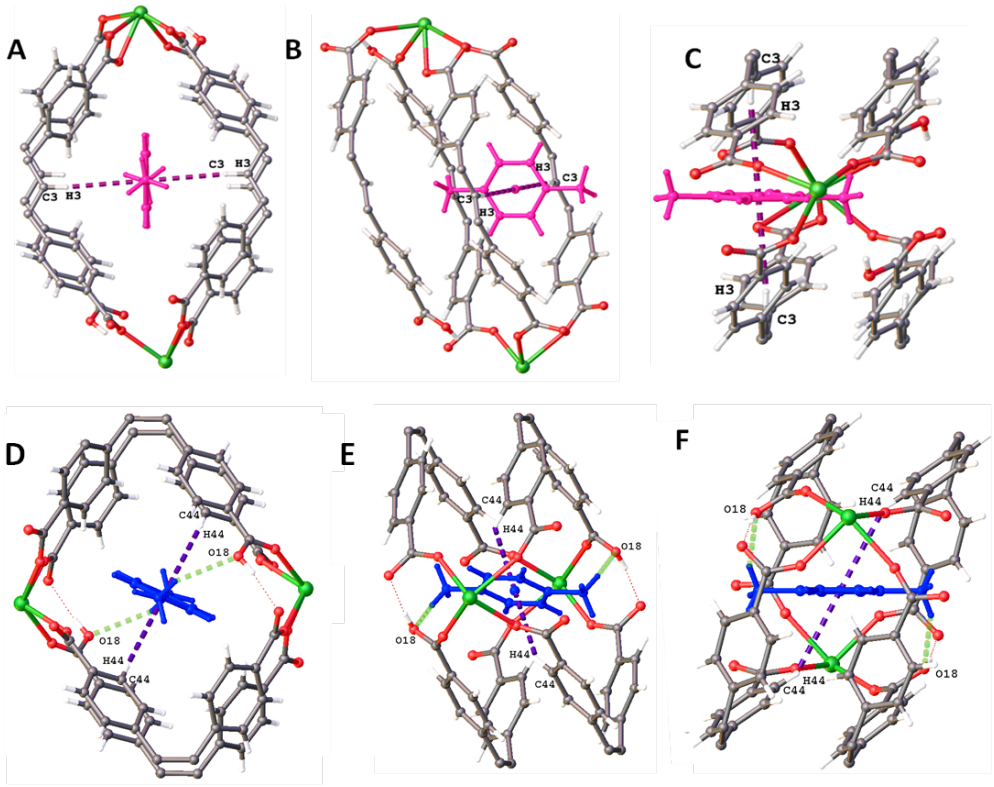

Figure 19: *Intermolecular interactions between pX1 (pink) in channel 1 and pX2 (blue) in channel 2 and host framework **14P**. C H···π interactions shown in purple, C H···O interactions shown in green. A,D: View down 100; B,E: View down 010; C: View down 001; D: View down plane of guest pX2.*

In channel 1 of **14P**, two symmetrical C3-H3···π interactions of 5.631Å (centroid-centroid[13]) at an angle of 92.498 ° between the central aromatic ring of the HTCPB ligand and the π-system of pX1 guest anchor the pX at specific locations in the channel (*Table 11, Figure 19A-C*).

In channel 2, the pX2 guest enters in line with the channel, as does pX2 in channel 2 of **11P-14P** and two symmetric C44-H44···π interactions of 5.441 Å (centroid-centroid[13]) are present between the central aromatic ring of the HTCPB ligand and the π-system of the pX2 guest (*Table 11*). An O18···H20C-C20X interaction is also present between O18 of the protonated monodentate carboxylate on ring 1 of the HTCPB ligand and the pX2 methyl hydrogens at 2.668 Å (*Figure 19D-F*). The same C-H···O interaction is observed in pX loaded compounds **11P-14P**.

6.3.3.2.8 mX loaded 14D: 14M

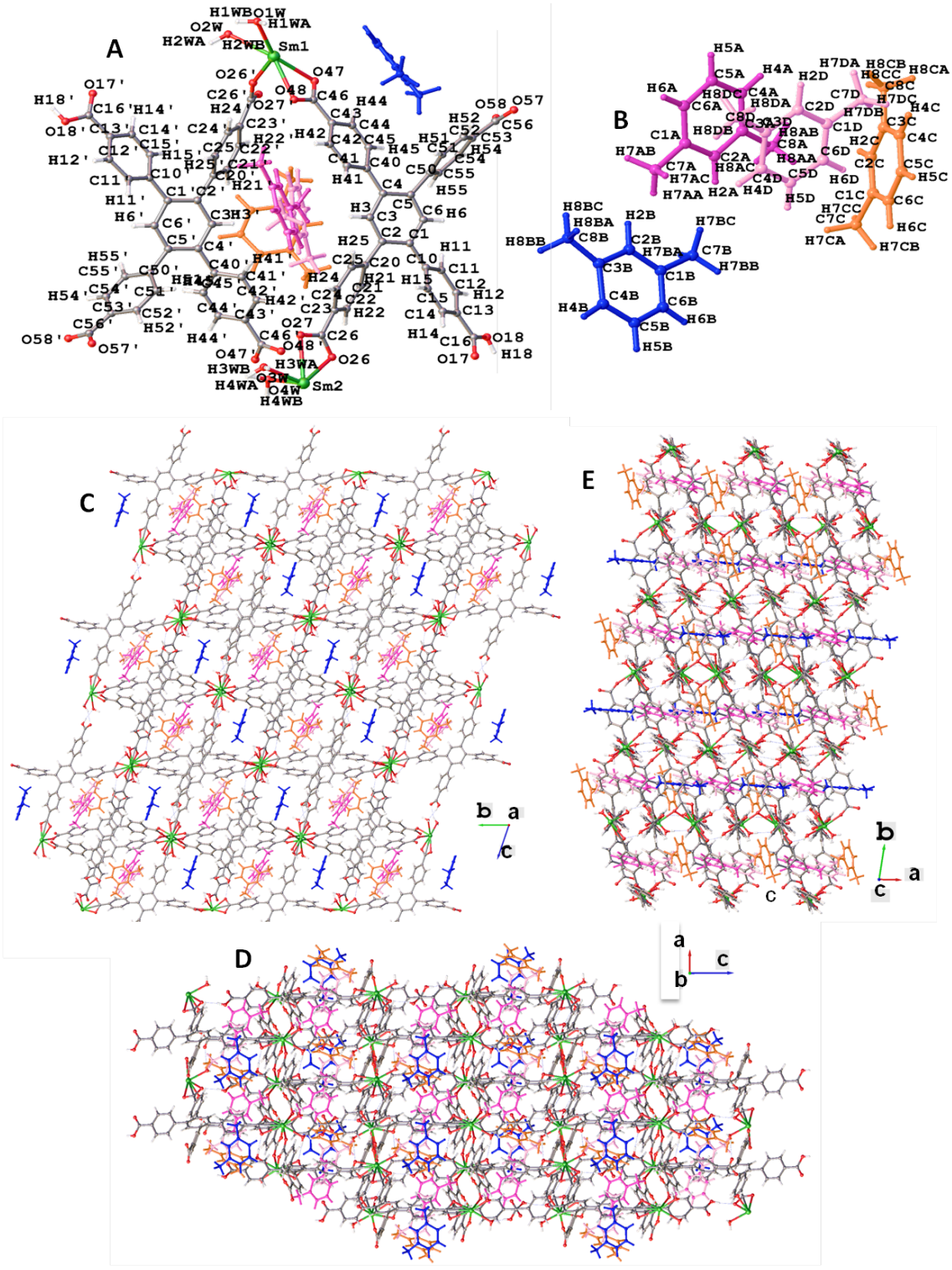

Figure 20: *Single crystal structure of* ***14M****. A: Asymmetric unit with mX1-3 (dark pink, pale pink, orange respectively) in channel 1 and mX4 (blue) in channel 2. HTCPB ligand 1 numbered as normal, HTCPB ligand 2 numbered as 1 with additional ‘’; B: Xylene atom numbering for mX1-4; C: View down 100; D: View down 010; E: View down 001. Sm (green), C (grey), O (red), H (white).*

The single crystal of **14M** used had dimensions of 0.08 × 0.04 × 0.10 mm. **14M** contains two forms of the HTCPB framework (ligand 2 numbered with ') and gives a unit cell around double that of all the other xylene loaded frameworks (*Figure 20A,B, Table 11*). In the unit cell there are two unique Sm metal centres and two unique HTCPB ligands. On one of the HTCPB ligands, ring 1 is detached from Sm leaving a free carboxylate in channel 2. A similar thing is observed in **11S** (discussed in Chapter 4), in which protonated carboxylate 1 becomes detached from Ce and is unable to bind due to the presence of EtOH solvent at the Ce metal centre. In **14M**, the protonated monodentate carboxylate of HTCPB ligand 2 (O17'-C16'-O18'-H18') has become detached and is unable to re-join the Sm metal centre as H_2O has coordinated, preventing carboxylate coordination however carboxylate 1 of HTCPB ligand 1 (Sm-O17-C16-O18-H18) remains coordinated In channel 1 there are three partial mX (mX1-3) guests which altogether refine to 100 % occupancy, leaving 1 mX in channel 1 per unit cell, 0.5 per formula unit. In channel 2, there is 0.5 mX4 guests per unit cell, 0.25 per formula unit, meaning overall there are 1.5 mX guests in **14M** per unit cell, giving the formula $Sm_2(HTCPB)_2(mX)_{1.5}$.

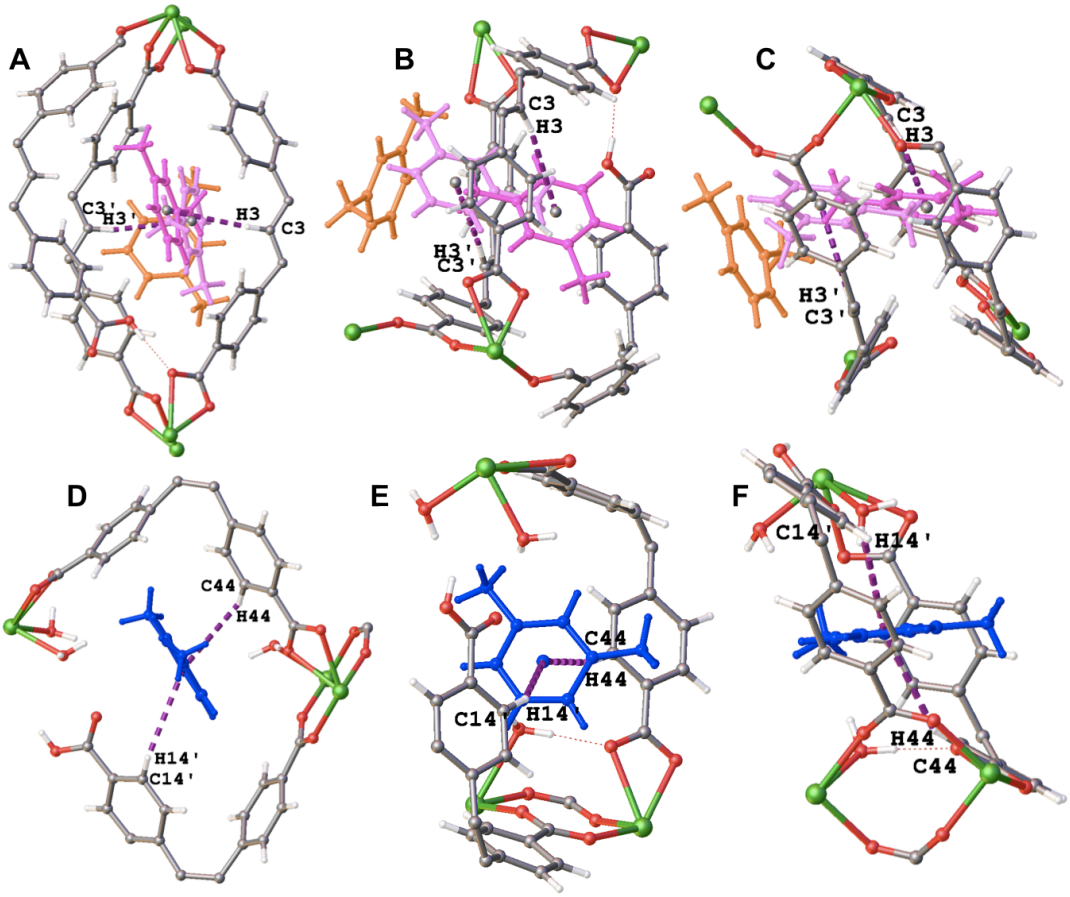

Figure 21: *Intermolecular interactions between mX1 (dark pink) and mX2 (pale pink) in channel 1 (A-C) and mX4 (blue) in channel 2 (D-E) with host framework **14M**. C-H···π interactions are shown in purple. A,D: View down 100; B,E: View down 010; C,F: View down 001.*

In channel 1, three partial mX guests are present, however only mX1 and mX2 interact with the framework as they enter in line with the channel so their central aromatic rings are in a position to form distorted T-shaped C-H···π interactions as seen in the other xylene loaded frameworks. Due to the framework disorder, each mX only picks up one interaction, unlike in the other xylene loaded frameworks in which two interactions are formed either side of the central aromatic ring of the xylene guest. MX1 forms a C3-H3···π interaction with the central aromatic ring of ligand 1 of 5.573 Å (centroid-centroid[13]) and mX2 forms a similar C3'-H3'···π interaction with the central aromatic ring of ligand 2 of 5.484 Å (centroid-centroid[13]) (*Figure 21A-C*, *Table 11*).

In channel 2, mX 4 lies off-centre and forms two asymmetric interactions with the framework. The first interaction is formed from ring 1 of ligand 2 to the central aromatic ring of mX4, with a C14'-H14'···π interaction of 5.584 Å (centroid-centroid[13]) and the second forms to the other side of the aromatic ring of mX4 from ring 4 of ligand 1, with a C44-H44···π interaction of 5.227 Å (centroid-centroid[13]) (*Figure 21D-F*, *Table 11*).

6.3.3.3 Comparison

Analysis of these xylene loaded frameworks highlights the enormous flexibility of the Ln(HTCPB) series of frameworks. Not only can these changes occur without damaging the stability of the structure, but we can observe them using SCXRD, meaning that even the single crystals are extremely stable and can undergo many structural changes and still be able to diffract with enough resolution to determine the single crystal structure.

This study shows that both pX and mX can be taken up by **10D-14D** to produce **10P-14P** and **10M-14M** respectively. Uptake of guest induces an expansion in unit cell volume and total accessible volume to a greater extent with the larger mX guest than pX. PX forms symmetrical C-H···π interactions in channel 1 for **11D-14P** and both C-H···π and C-H···O interactions in channel 2, which holds the pX guests at specific points in the channel, with no disorder observed. The greater expansion in total accessible volume with uptake of mX means that the guest does not fit as well as pX and as a result mX is disordered in both channels of **11M-14M**, which produces more strained and asymmetric C-H···π to form.

10P and **10M** do not fit in with this trend for channel 1. As **10D** has the largest channels, two pX and mX guests enter channel 1 in **10P** and **10M** respectively, both of which form C-H···π interactions with the framework but a much less favourable angle (further from 90 °) than those observed in **11P-14P** and **11M-14M** in which the xylene guests enter in line with the channel direction. However in the smaller channel 2, pX and mX guests enter **10P** and **10M** respectively in

line with the channel and interaction comparable with those in channel 2 of **11P-14P** and **11M-14M** are formed. In **14M**, the structure has changed in that two forms of the framework are present: A xylene loaded **14P** and '**14R**'.

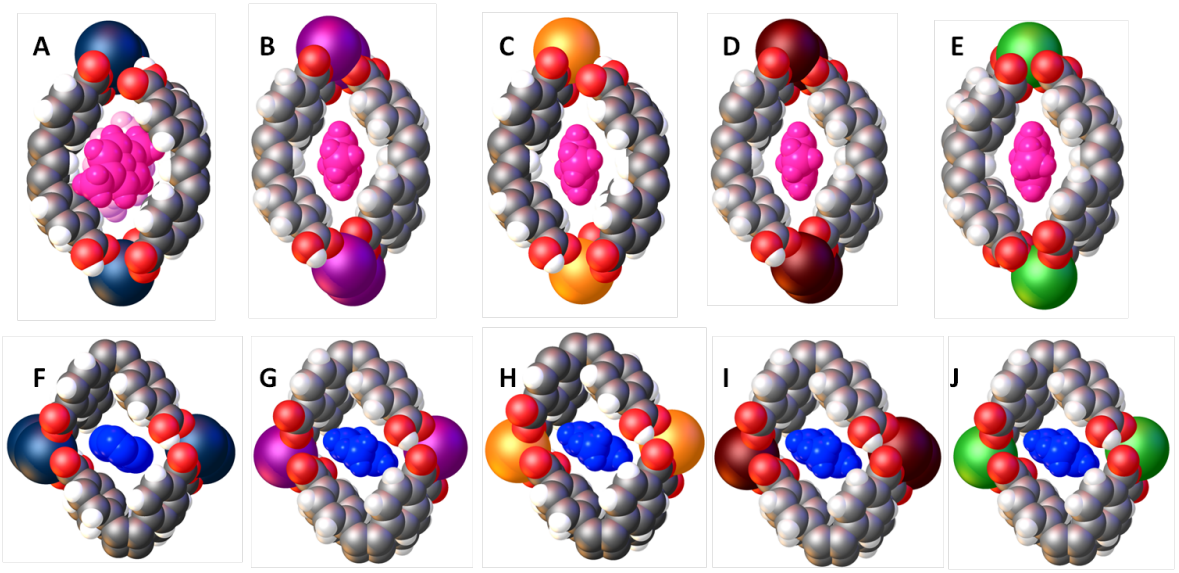

Figure 22: *Spacefill representation of pX loaded frameworks **10P-14P** viewed down the 100 direction. A: pX1 (dark pink) and pX2 (pale pink) in channel 1 of **10P**; B: pX1 (dark pink) in channel 1 of **11P**; C: pX1 (dark pink) in channel 1 of **12P**; D: pX1 (dark pink) in channel 1 of **13P**; E: pX1 (dark pink) in channel 1 of **14P**; F: pX2(blue) in channel 2 of **10P**. H atoms could not be refined on pX2; G: pX2(blue) in channel 2 of **11P**; H: pX2(blue) in channel 2 of **12P**; I: pX2(blue) in channel 2 of **13P**; J: pX2(blue) in channel 2 of **14P**. La (blue), Ce (purple), Pr (orange), Nd (brown), Sm (green), C (grey), O (red), H (white).*

When the pX loaded frameworks are compared to each other and then to the mX loaded frameworks, the orientation, fit and interactions between the guests and host frameworks can provide an explanation for the observed trend in selectivity (*Table 8, Figure 5*).

In channel 1 of the pX loaded frameworks, with the exception of **10P**, all pX guests enter in line with the channel and two symmetrical C-H···π interactions are formed that are very similar in length and angle between the central aromatic ring of the HTCPB ligand from H3, of 5.658, 5.659, 5.653 and 5.631 Å at 92.097, 92.958, 92.609 and 92,498 ° respectively for **11P**, **12P**, **13P** and **14P**. However in **10P** channel 1, the channels are larger and two pX guests are found at a tilt, forming weaker interactions (longer centroid-centroid distance at an angle further from the ideal 90 °) for pX1 and pX2 with the framework. PX1 forms interactions with H6 and pX2 with H3 of 5.875 and 5.899 Å respectively at angles of 146.457 and 141.760 ° (*Figure 22A-E*).

In the smaller channel 2 of all **11P-14P** pX loaded frameworks, pX enters in line with the channel and forms two symmetrical similar strength C-H42/44···π interactions of 5.561, 5.448, 5.466 and 5.441 Å respe4ctively at 143.23, 143.096, 143.351 and 141.777 °. The pX guests in **11P-14P** also

pick up two C-H···O interactions from O18 of the protonated monodentate carboxylate 1 of the HTCPB ligand and the pX methyl groups; one interaction per methyl group; two per pX, of 2.583, 2.608, 2.558 and 2.556 Å respectively with interaction angles of 146.296, 145.513, 147.587 and 149.709 °. These two distinct types of interaction anchor the pX guests at specific locations along the channel in 'pockets' created by the interactions formed. However again in the case of **10P**, the channel 2 is slightly larger and as a result, pX does enter in line with the channel but is slightly disordered along the channel direction. Two asymmetric interactions are picked up by each part of the disorder of 5.176 and 5.565 Å and a plane-plane angle (central HTCPB aromatic ring-pX central aromatic ring) of 140.425 ° (*Figure 22F-J*).

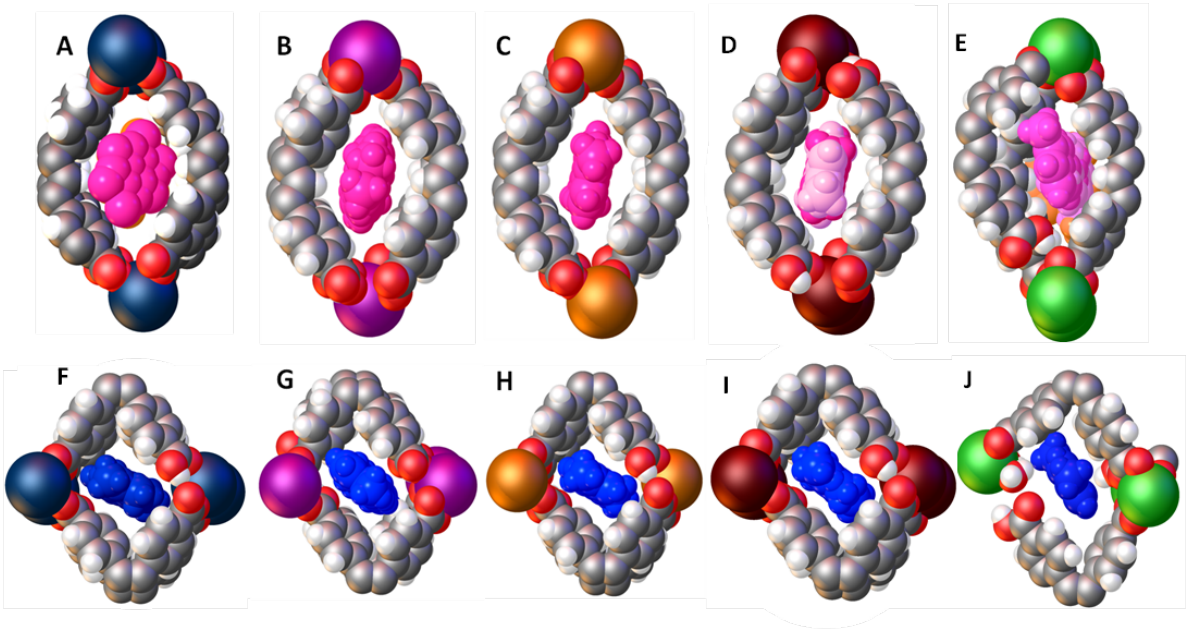

Figure 23: *Spacefill representation of mX loaded frameworks **10M-14M** viewed down the 100 direction. A: mX1 (dark pink) and mX2 (pale pink) in channel 1 of **10M**; B: mX1 (dark pink) in channel 1 of **11M**; C: mX1 (dark pink) in channel 1 of **12M**; D: mX1 (dark pink) in channel 1 of **13M**; E: mX1 (dark pink), mX2 (pale pink) and mX3 (orange) in channel 1 of **14M**; F: mX2(blue) in channel 2 of 1**0M**; G: mX2(blue) in channel 2 of **11P**; H: mX2(blue) in channel 2 of **12P**; I: mX2(blue) in channel 2 of **13M**; J: mX4(blue) in channel 2 of **14M**. La (blue), Ce (purple), Pr (orange), Nd (brown), Sm (green), C (grey), O (red), H (white).*

Compound **10M** has the largest channels and as a result of this, two mX guests (mX1 and mX2) enter channel 1 at a tilt in the same way as two pX enters channel 1 of **10P**. Weaker C-H···π interactions are formed between the host framework and the guest mX molecules: MX1 is disordered over two positions and each part has two asymmetric C6-H6···π interactions of 5.596 and 6.316 Å at an angle of 141.581 ° and mX2 has two asymmetric C3-H3···π interactions of 5.635 and 6.284 Å at 145.072 °. All interactions formed between **10M** and mX1 and mX2 are weaker

than the corresponding C-H···π interactions formed in channel between mX and host frameworks **11M-13M** at a less ideal angle, further from 90 ° as a result of the mX tilt.

In channel 1 of **11M-13M**, one whole mX guest enters in line with the channel for every two mX that enter in **10M**. Stronger C-H···π interactions are picked up between guest mX and host framework at a more ideal angle, closer to 90 °. In **11M** mX1 is disordered over two positions and each part of the disorder forms two asymmetric C-H···π interactions: mX1 forms two C3-H3···π interactions of 5.811 and 6.026 Å at 93.750 ° and mX1 form two asymmetric C6-H6···π interactions of 6.184 and 5.961 Å at 89.067 °. In **12M**, mX1 is disordered over two positions, but in this case, each part picks up two asymmetric C-H···π interactions from different donor atoms either side; C3-H3···π at 6.449 Å and C6-H6··π at 6.036 Å, both at an angle of 91.062 °. In **13M**, mX1 and mX2 are present and disordered with each other along the channel; mX1 forms two asymmetric C3-H3···π interactions of 5.791 and 6.011 Å at 89.512° and mX2 only picks up one C6-H6···π interaction from one side of the mX aromatic ring of 5.995 Å at 89.157°. Despite the fact that the mX guests in channel 1 of **11M-13M** enter in line with the channel as do pX guests in **10P-14P**, the C-H···π interactions formed are longer, more asymmetric and therefore weaker due the enlargement of the channel itself with uptake of the larger mX guest, resulting in a poorer fit and translational disorder along the channel. 11M also has one C-H···O interaction per mX guests in channel 2, similar to those observed between pX and the pX-loaded host frameworks. This may account for the lower selectivity of **11D** compared to **12D-14D** as there is another favourable interaction forming between the mX guest and the framework which is not present in other highly pX selective **12D-14D**.

In **14M**, the framework is disordered over two positions and as a result, three partial mX guests can enter channel 1. In total these guests add up to 100 % occupancy per unit cell, however only mX1 and mX2 enter in line with the channel and are able to pick up C-H···π interactions, whereas mX3 enters perpendicular to the channel direction and does not interact with the framework. Each mX1 and mX2 can only form one interaction to one side of the guest, unlike in all the other xylene loaded frameworks in which two C-H···π interactions form per xylene guest. MX1 forms one C3-H3···π of 5.573 Å at 126 ° and mX2 forms one C3'-H3'···π interaction of 5.484 Å at 114.598 °.

In the smaller channel 2 of all **10M-13M** mX loaded frameworks, mX enters in line with the channel and forms two asymmetrical C44-H44···π interactions in each case, with the exception of **14M**, in which mX4 forms two asymmetric C-H···π interactions, each coming from a different ligand as **14M** is the only framework to have two HTCPB ligands within its asymmetric unit. Ring 1 of HTCPB ligand 2 forms a C14'-H14'···π interaction of 5.584 Å at 140.095 ° and ring 4 of HTCPB ligand 4 forms a C44-H44···π of 5.227 Å at 144.956 °. For **10M-13M** respectively, two asymmetric C44-H44···π interactions form between the host framework and: mX3 in **10M** of

5.493 and 4.950 Å at 139.201 °; mX2 in **11M** of 5.938 and 4.9314 Å at 142.140 °; mX2 in **12M** of 5.837 and 4.958 Å at 138.615 °; mX2 in **13M** of 4.923and 5.851 Å at 142.343 °.

It is clear that mX guest entry into channel 1 of **10M-14M** is more complicated than the more streamlined pX entry into **10P-14P**, resulting in void enlargement, leading to a poorer guest fit and weaker intermolecular host-guest interactions. In channel 2, all pX and mX guests enter their host frameworks in line with the channel, but whereas in **10P-14P**, a combination of symmetrical C-H···π and C-H···O interactions anchor the pX guests at specific locations along the channel, the larger mX guests are unable to fit as well into **10M-14M**, form weaker, asymmetric C-H···π interactions and are unable to form C-H···O interactions due to the orientation of the guest mX.

Analysis of the pX and mX loaded frameworks in this way provides an insight into the trend in pX/mX selectivity observed from **10D-14D**. In all cases, pX is preferred by the framework, hence the high pX/mX selectivity observed. The increase from around α_{pXmX} = 4.5 at **10D** and **11D** to αpXmX = 6 at **12D-14D** can be attributed to the smaller channels, with less disorder and a stronger preference for pX over mX.

6.4 Smaller Ln(III) with H_4TCPB Ligand

Using a similar synthesis to that used for compounds **10-14**, a smaller lanthanide was reacted with the H_4TCPB ligand, and the synthesis product was investigated using single crystal x-ray diffraction. The single crystal structure of **15** was solved and refined using data collected from the Rigaku Rotating Anode Diffractometer at the University of Liverpool. Structure solution and refinement was carried out with the assistance of Dr John Warren.

6.4.1 $Ln_2(HTCPB)_{1.5}$·*guests*

Table 12: *Unit cell dimensions of **15**:*

$Yb_2(TCPB)_{1.5}$ *.guests*	**Unit Cell Dimensions**			**Unit Cell Volume (Å^3)**
	a (Å) **α (°)**	**b (Å)** **β (°)**	**c (Å)** **γ (°)**	
Yb (15)	9.6693(1) 104.968(7)	18.0643(3) 97.656(7)	19.9097(14) 93.485(7)	3313.17

The combination of $Yb(NO_3)_3.6H_2O$ and H_4TCPB produces a framework with a different structure to that observed with the larger lanthanides (**10-14**). The compound crystallise in a triclinic P_{-1} space group creating 3D framework which has the formula $Yb_2(TCPB)(H_2O)(EtOH)\cdot H_2O$ (**15**), (*Table 12*).

Each Yb(III) centre is 8 coordinate and Yb-carboxylate chains run along the c-axis of the structure, which differs from compounds **10-14** in which Ln-carboxylate chains only form after H_2O removal at which point the carboxylate bridge can form between Ln_2 dimers. The structure has channels running along the c-axis with H_2O molecules oriented into the channels.

The asymmetric unit of **15** contains two Yb centres, one and a half HTCPB ligands (HTCPB 1 numbered AX and HTCPB 2 numbered AXL where A = atom type and X = atom number), two coordinated EtOH, two coordinated H_2O and four guest H_2O molecules in the voids of the structure (*Figure 24*).

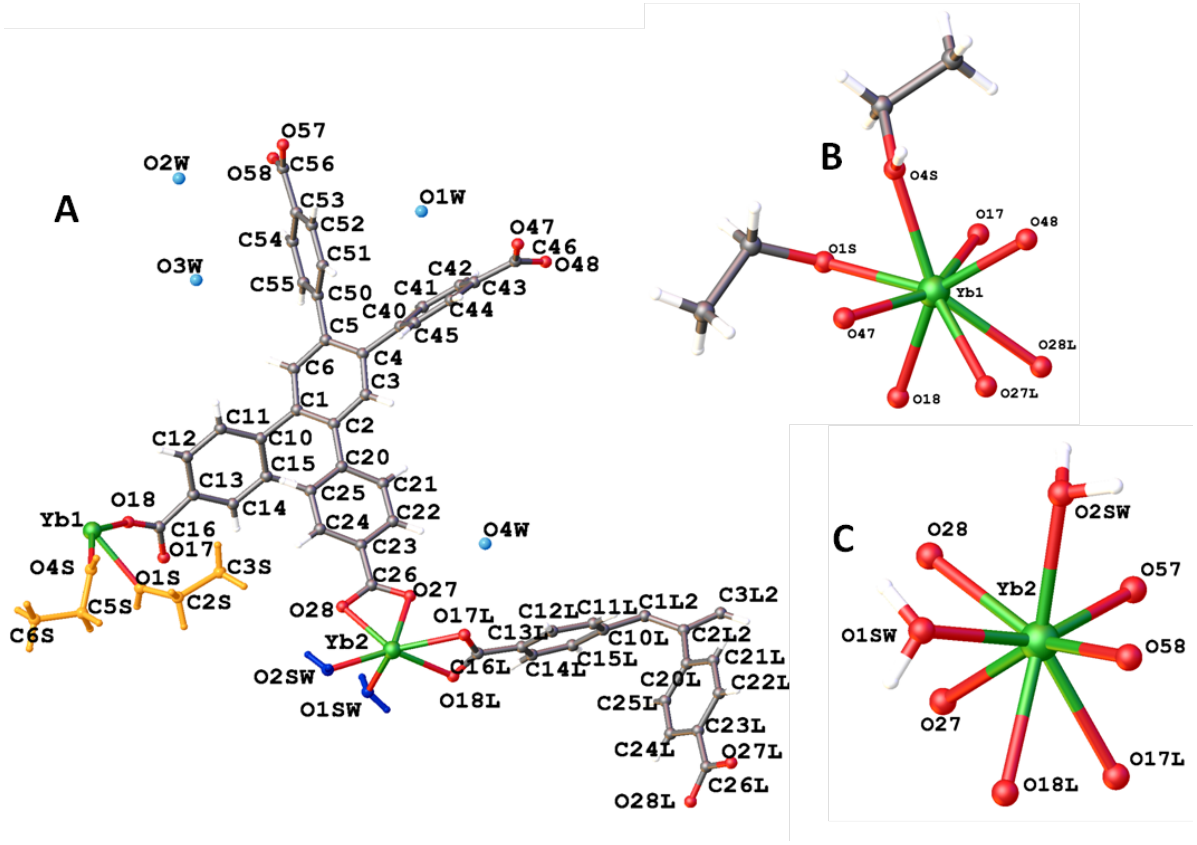

Figure 24: *A: Asymmetric unit in **16** with atom numbering shown. EtOH coordinated to Yb2 (orange), H_2O coordinated to Yb1 (dark blue), Channel H_2O (pale blue); B: Coordination environment of Yb1l C: Coordination environment of Yb2.*

The coordination sphere of Yb1 is filled by six carboxylate oxygens (O47, O48, O17, O18, O27L, O28L) and O from both EtOH molecules (O1S, O4S). Symmetry equivalent Yb1 atoms form Yb-carboxylate chain within the 3D structure of **15**, with Yb metal centres connected by two carboxylate bridges: Within the Yb-carboxylate chain, each Yb1 has carboxylate coordination from

a different ring (ring 1 or 4), of the HTCPB ligand 1 either side of itself, creating the order ···Yb-1-Yb-4-Yb-1-Yb··· 1: Yb-1-Yb = two (Yb1)-O17-C16-O18-(Yb1) and Yb-4-Yb = two (Yb1)-O47-C46-O48-(Yb1) bridges respectively (*Figure 25B*). The carboxylate of HTCPB ligand 2 (O27L, O28L) have bidentate coordination to each Yb1.

The coordination sphere of Yb2 is filled with six carboxylate oxygens (O27, O28, O57, O58, O17L, O18L) and O from both H_2O molecules (O1SW, O2SW). Two symmetry equivalent Yb2 form a Yb_2 dimer within the 3D framework, linked by two (Yb2)-O57-C56-O58-(Yb2) carboxylate bridges. The carboxylate of ring 2 of HTCB ligand 1 (O27, O28) and ring 1 of HTCPB ligand 2 (O17L, O18L) form bidentate coordination to Yb2 (*Figure 25A*).

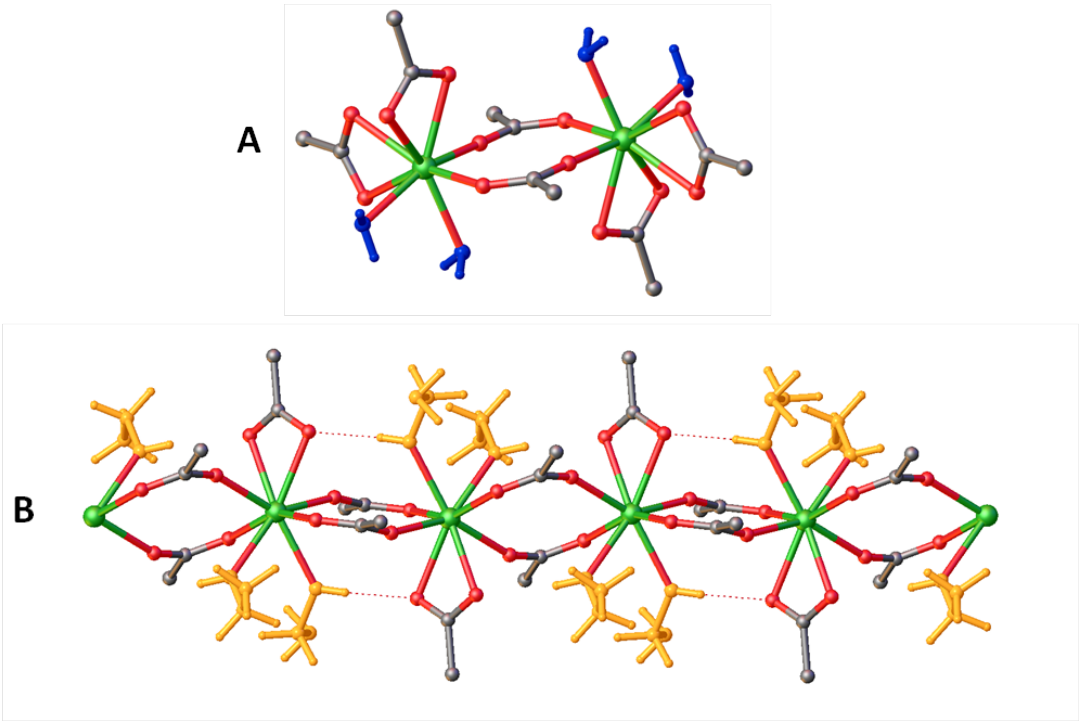

Figure 25: *Yb environments in* ***15****. A: Yb2; B: Yb1. Yb (green), O (red), C (grey), coordinated EtOH (orange), coordinated H_2O (dark blue).*

The structure packs in 3D with channels running down the a-axis, containing guest H_2O molecules (*Figure 26A*). Two distinct channels are present; one housing the coordinated EtOH and H_2O and one guest H_2O and the second housing three guest H_2O molecules. When viewed along the 010 direction, the 'layers' created by Yb1 and Yb2 can be seen, joined via HTCPB coordination (*Figure 26B*).

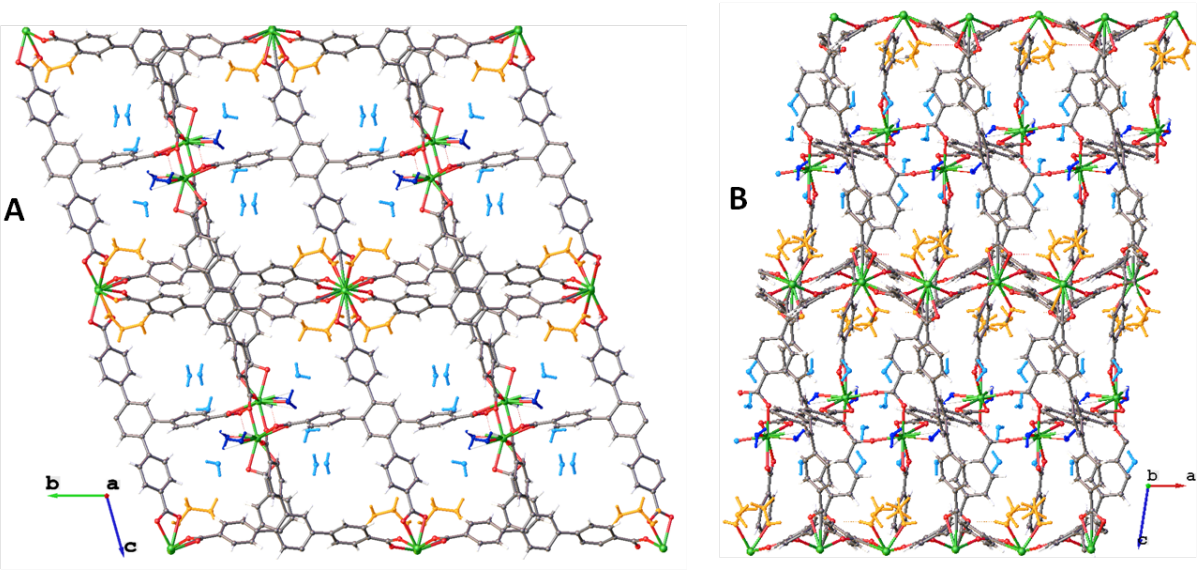

Figure 26: *Packing down A: 100 and B: 010 in* ***15****.*

It is interesting that when smaller lanthanides are used, Ln-carboxylate bridges form in the as-made structures possibly due to the smaller size of the metal centres resulting in closer Ln···Ln distances, meaning carboxylate bridging between Ln centres is easier. When larger lanthanides are used (La-Sm; **10-14**), Ln-carboxylate bridges only form after desolvation, once all solvent has been removed and the structure has shifted to accommodate the formation of such a bridge.

6.5 Conclusions

The combination of $Ln(NO_3)_3$ and the H_4TCPB linker under solvothermal conditions yields a series of isostructural frameworks with the formula Ln(HTCPB), where Ln = La (**10**), Ce (**11**), Pr (**12**), Nd (**13**) and Sm (**14**). Compounds **10-14** are 3D, with carboxylate-bridged, EtOH and H_2O capped Ln_2 dimers connected via mono-protonated HTCPB ligands. After desolvation, the capping EtOH and H_2O solvents are lost and a carboxylate bridge is formed between Ln_2 dimers, creating a Ln-carboxylate chain along the c-axis.

Activation of **10-14** produces the isostructural desolvated frameworks **10D-14D,** which have two channels; a larger channel 1 and a smaller channel 2. As the size of the lanthanide ion (Ln(III)) decreases between La and Sm (**10D-14D**), the unit cell volume and total accessible volume of both channels 1 and 2 decreases in line with the lanthanide contraction: La>Ce>Pr>Nd>Sm.

When exposed to air or moisture, **10D-14D** rearrange to become isostructural **10R-14R**.

Table 13: *Summary of pX and mX loaded Ln(HTCPB) frameworks and their pX/mX selectivity:*

Framework	Formula	pX/mX Selectivity	Interactions
10P	La(HTCPB)pX$_{1.5}$	4.48	2 C-H···π per pX1&2, ch1 2 asym.C-H···π per pX3, ch2
10M	La(HTCPB)mX$_{1.5}$		2 asym. C-H···π per mX1&2, ch1 2 asym. C-H···π per mX3, ch2
11P	Ce(HTCPB)pX	4.55	2 C-H···π per pX1, ch1 2 C-H···π per pX2, ch2 2 C-H···O per pX2, ch2
11M	Ce(HTCPB)mX		2 asym. C-H···π per mX1, ch1 2 asym. C-H···π per mX2, ch2 1 C-H···O per mX2, ch2
12P	Pr(HTCPB)pX	6.36	2 C-H···π per pX1, ch1 2 C-H···π per pX2, ch2 2 C-H···O per pX2, ch2
12M	Pr(HTCPB)mX		2 asym. C-H···π per mX1, ch1 2 asym. C-H···π per mX2, ch2
13P	Nd(HTCPB)pX	6.20	2 C-H···π per pX1, ch1 2 C-H···π per pX2, ch2 2 C-H···O per pX2, ch2
13M	Nd(HTCPB)mX		2 asym. C-H···π per mX1, ch1 1 C-H···π per mX3, ch1 2 asym. C-H···π per mX3, ch2
14P	Sm(HTCPB)pX	6.11	2 C-H···π per pX1, ch1 2 C-H···π per pX2, ch2 2 C-H···O per pX2, ch2
14M	Sm(HTCPB)mX$_{0.75}$		1 C-H···π per pX1&1, ch1 2 asym. C-H···π per mX4, ch2

The pX/mX selectivity of **10D-14D** was measured for comparison with **11D** as discussed in chapter 5. The results show a high selectivity of around $\alpha_{pXmX} = 4.5$ for **10D** and **11D**, increasing to a higher selectivity of above $\alpha_{pXmX} = 6$ for **12D-14D** (*Table 13*). The highest value of $\alpha_{pXmX} = 6.36$ for **12D** is around 50 % higher than any reported zeolite or MOF for batch pX/mX separation. A possible explanation for this trend can be extracted from analysis of the single crystal structures of the pX and mX loaded framework; **10P-14P** and **10M-14M** respectively (*Table 13*). For all pX loaded frameworks, the guest pX molecules are found at similar locations to pX in **11P** as in chapter 5; **12P**, **13P** and **14P**, with the only exception being pX in **10P** in which two pX guests enter in place of 1, both at a tilt. In **10P**, three pX guests are present in the unit cell, two in channel 1 and one in channel 2, whereas only two are present in **11P-14P**, one per channel. As more pX is able to enter channel 1 in **10P**, this may account for the lower selectivity in comparison with **12D-14D**.

For all mX loaded structures, **10M-14M**, inclusion of mX results in a greater channel expansion to that observed with pX inclusion due to the larger size of the guest. In **14M**, the channels have changed significantly as the framework is disordered leaving two unique Sm and HTCPB ligands

in the asymmetric unit. The pX/mX selectivity increase at **12D-14D** can be attributed to the smaller channel sizes presents with smaller lanthanide metal centres. The effects of the size selective channels as discussed for **11D** in chapter 5 are enhanced with the smaller channels and as a result, the intermolecular interactions between guest pX and the host framework **12P-14P** are enhanced, whereas the mX-**11M** intermolecular interactions become less until **14M** at which although mX fits into both channels, only weak or single interactions can form between the host framework and the guests. Only one and a half mX guests are present in total per unit cell of **14M**, compared to two mX guests per unit cell in **11M-13M** and three per unit cell in **10M**. The reduction in the amount of mX able to enter the channels compared to a constant uptake up pX may also contribute to the increasing selectivity across the series. The additional C-H···π interaction in **11M** may account for the lower selectivity of **11D** compared to **12D-14D**.

When smaller lanthanides are combined with the H_4TCPB ligand, a new framework is produced: Yb_2(TCPB)(EtOH)(H_2O)·(H_2O) (**15**). Compound **15** is synthesised as a 3D framework, which already contains Yb-carboxylate chains, connected via HTCPB ligands, with potential porosity, seen in the H_2O-containing channels down the 100 direction, however this has not been measured.

6.6 References

[1] S. Cotton, *Lanthanide and Actinide Chemistry*, John Wiley & Sons, **2007**.

[2] K. Binnemans, *Chem. Rev.* **2009**, *109*, 4283-4374.

[3] J.-C. G. Bunzli, S. V. Eliseeva, *Chem. Sci.* **2013**, *4*, 1939-1949.

[4] J.-P. Bellat, M.-H. S.-Grange, S. Jullian, *Zeolites* **1995**, *15*, 124-130.

[5] M. Guisnet, J.-P. Gilson, *Zeolites for Cleaner Technologies*, Imperial College Press, London, **2002**.

[6] F. Vermoortele, M. Maes, P. Z. Moghadam, M. J. Lennox, F. Ragon, M. Boulhout, S. Biswas, K. G. M. Laurier, I. Beurroies, R. Denoyel, M. Roeffaers, N. Stock, T. Duren, C. Serre, D. E. De Vos, *J. Am. Chem. Soc.* **2011**, *133*, 18526-18529.

[7] O. V. Dolomanov, L. J. Bourhis, R. J. Gildea, J. A. K. Howard, H. Puschmann, *J. Appl. Crystallogr.* **2009**, *42*, 339-341.

[8] L. J. Bourhis, O. V. Dolomanov, R. J. Gildea, J. A. K. Howard, H. Puschmann, *olex2.solve* **2011**.

[9] *IUCr* **2010**, *ChekCell*.

[10] T. Devic, V. Wagner, N. Guillou, A. Vimont, M. Haouas, M. Pascolini, C. Serre, J. Marrot, M. Daturi, F. Taulelle, G. Ferey, *Micropor. Mesopor. Mat.* **2011**, *140*, 25-33.

[11] T. Devic, C. Serre, N. Audebrand, J. Marrot, G. Ferey, *J. Am. Chem. Soc.* **2005**, *127*, 12788-12789.

[12] S. Q. Ma, D. Q. Yuan, X. S. Wang, H. C. Zhou, *Inorg. Chem.* **2009**, *48*, 2072-2077.

[13] S. K. Burley, G. A. Petsko, *Science* **1985**, *229*, 23-28.

6.7 Additional Information

Table 14: *Crystal data and structure refinement parameters* ***10****,* ***10D*** *and* ***10R****:*

Identification code	**MJR0847**	**A00092100_1**	**A00092100_R**
Sample Code	**10**	**10D**	**10R**
Empirical formula	$C_{38}H_{26}LaO_{11.5}$	$C_{34}H_{19}LaO_8$	$C_{34}H_{18}LaO_9$
Formula weight	805.50	694.4	710.14
Temperature/K	100	100	100
Crystal system	triclinic	triclinic	triclinic
Space group	P-1	P-1	P-1
a/Å	10.5437(16)	9.4426(8)	4.9665(2)
b/Å	10.5983(16)	11.9218(10)	18.2334(10)
c/Å	17.026(3)	15.8565(13)	19.4293(13)
α/°	76.090(5)	80.989(6)	112.792(8)
β/°	83.023(4)	73.586(5)	92.366(7)
γ/°	69.992(4)	70.657(5)	92.678(7)
Volume/Å^3	1733.7(5)	1611.7(2)	1616.92(15)
Z	2	2	2
ρcalcmg/mm^3	1.543	1.431	1.459
m/mm^{-1}	1.200	1.373	1.373
F(000)	806.0	688	703
Crystal size/mm^3	0.25 × 0.1 × 0.05	0.06 × 0.05 × 0.05	0.06 × 0.05 × 0.05
2Θ range for data collection	2.4 to 63.34°	5.98 to 52.74°	6.12 to 49.42°
Index ranges	-15 ≤ h ≤ 15, -15 ≤ k ≤ 15, -25 ≤ l ≤ 25	-11 ≤ h ≤ 11, -14 ≤ k ≤ 14, -18 ≤ l ≤ 19	-5 ≤ h ≤ 5, -21 ≤ k ≤ 21, -22 ≤ l ≤ 22
Reflections collected	38498	21366	19273
Independent reflections	11498[R(int) = 0.0906]	6341[R(int) = 0.1402]	5386[R(int) = 0.1543]
Data/restraints/ parameters	11498/3/457	6341/0/389	5386/0/403
Goodness-of-fit on F2	1.052	1.039	1.037
Final R indexes [I>=2σ (I)]	R_1 = 0.0607, wR_2 = 0.1356	R_1 = 0.1253, wR_2 = 0.2949	R_1 = 0.1005, wR_2 = 0.2478
Final R indexes [all data]	R_1 = 0.0804, wR_2 = 0.1490	R_1 = 0.1605, wR_2 = 0.3275	R_1 = 0.1211, wR_2 = 0.2657
Largest diff. peak/hole / e Å^{-3}	2.99/-1.89	5.39/-2.75	3.18/-1.87

Table 15: *Crystal data and structure refinement parameters* ***12****,* ***12D*** *and* ***12R****:*

Identification code	**A00067**	**C00120C1**	**C00164C1**
Sample Code	**12**	**12D**	**12R**
Empirical formula	$C_{37.7}H_{18}O_{11.6}Pr$	$C_{34}H_{19}O_8Pr$	$C_{68}H_{36}O_{18}Pr_2$
Formula weight	797.74	696.4	1422.79
Temperature/K	100.15	100	100
Crystal system	triclinic	triclinic	triclinic
Space group	P-1	P-1	P1
a/Å	10.5353(11)	9.3368(6)	5.022(4)
b/Å	10.5528(14)	11.9277(8)	18.245(19)
c/Å	16.930(2)	15.8081(11)	19.48(2)
α/°	83.0630(10)	81.122(6)	111.94(4)
β/°	76.278(9)	73.804(5)	92.18(4)
γ/°	70.089(6)	71.018(5)	93.078(16)
Volume/Å^3	1717.6(4)	1594.76(19)	1650.00(3)
Z	2	2	1
ρcalcmg/mm^3	1.543	1.45	1.432
m/mm^{-1}	1.481	1.576	1.527
F(000)	792.0	692	706.0
Crystal size/mm^3	0.17 × 0.13 × 0.09	0.12 × 0.15 × 0.06	0.09 × 0.09 × 0.06
2Θ range for data collection	4.7 to 66.2°	6.02 to 52.74°	3.88 to 46.52°
Index ranges	$-16 \le h \le 16$, $-15 \le k \le 16$, $-25 \le l \le 23$	$-11 \le h \le 11$, $-14 \le k \le 14$, $-18 \le l \le 19$	$-5 \le h \le 5$, $-20 \le k \le 20$, $-21 \le l \le 21$
Reflections collected	37457	25667	19309
Independent reflections	11697[R(int) = 0.0943]	6500[R(int) = 0.1604]	8322[R(int) = 0.1334]
Data/restraints/ parameters	11697/0/443	6500/0/389	8322/3/335
Goodness-of-fit on F2	1.098	0.958	1.046
Final R indexes [I>=2σ (I)]	$R_1 = 0.0590$, $wR_2 = 0.1444$	$R_1 = 0.0769$, $wR_2 = 0.1575$	$R_1 = 0.1117$, $wR_2 = 0.2448$
Final R indexes [all data]	$R_1 = 0.0655$, $wR_2 = 0.1503$	$R_1 = 0.1117$, $wR_2 = 0.1729$	$R_1 = 0.1435$, $wR_2 = 0.2836$
Largest diff. peak/hole / e Å^{-3}	3.22/-1.83	2.16/-1.36	1.70/-1.14

Table 16: *Crystal data and structure refinement parameters* ***13****,* ***13D*** *and* ***13R****:*

Identification code	**B00098**	**C00120C1**	**D00104**
Sample Code	13	**13D**	**13R**
Empirical formula	$C_{38}H_{19}NdO_{11.8}$	$C_{34}H_{19}NdO_8$	$C_{34}H_{19.9}NdO_{9.1}$
Formula weight	808.64	699.73	718.8
Temperature/K	100	100	100
Crystal system	triclinic	triclinic	triclinic
Space group	P-1	P-1	P-1
a/Å	10.53780(10)	9.2977(4)	4.97450(10)
b/Å	10.55610(10)	11.9415(5)	18.1990(7)
c/Å	16.8962(11)	15.7797(11)	19.4455(13)
α/°	76.425(5)	81.207(6)	114.174(8)
β/°	83.205(6)	73.748(5)	91.268(6)
γ/°	69.971(5)	71.200(5)	93.103(7)
Volume/Å^3	1715.02(11)	1588.46(15)	1601.79(13)
Z	2	2	2
ρcalcmg/mm^3	1.566	1.463	1.49
m/mm^{-1}	1.578	1.682	1.673
F(000)	803.0	694	714
Crystal size/mm^3	0.226 × 0.147 × 0.047	0.1 × 0.08 × 0.05	0.15 × 0.05 × 0.02
2Θ range for data collection	6.14 to 54.96°	6.04 to 52.74°	6.04 to 52.74°
Index ranges	$-13 \le h \le 13$, $-13 \le k \le 13$, $-17 \le l \le 21$	$-11 \le h \le 11$, $-14 \le k \le 14$, $-19 \le l \le 18$	$-5 \le h \le 6$, $-21 \le k \le 22$, $-24 \le l \le 24$
Reflections collected	30209	27256	28684
Independent reflections	7837[R(int) = 0.0690]	6488[R(int) = 0.1450]	6485[R(int) = 0.1142]
Data/restraints/ parameters	7837/0/442	6488/0/389	6485/0/407
Goodness-of-fit on F2	1.060	0.964	0.982
Final R indexes [I>=2σ (I)]	$R_1 = 0.0542$, $wR_2 = 0.1344$	$R_1 = 0.0681$, $wR_2 = 0.1457$	$R_1 = 0.0643$, $wR_2 = 0.1431$
Final R indexes [all data]	$R_1 = 0.0647$, $wR_2 = 0.1409$	$R_1 = 0.1003$, $wR_2 = 0.1619$	$R_1 = 0.0882$, $wR_2 = 0.1545$
Largest diff. peak/hole / e Å^{-3}	2.86/-1.4	2.19/-2.39	2.64/-1.95

Table 17: *Crystal data and structure refinement parameters* ***14****,* ***14D*** *and* ***14R****:*

Identification code	**B00132C1**	**C00140**	**C00165**
Sample Code	**14**	**14D**	**14R**
Empirical formula	$C_{35}H_{18}O_{11.5}Sm$	$C_{34}H_{19}O_8Sm$	$C_{34}H_{21}O_{9.5}Sm$
Formula weight	772.84	705.84	732.01
Temperature/K	100	100	100
Crystal system	triclinic	triclinic	triclinic
Space group	P-1	P-1	P-1
a/Å	10.5365(2)	9.2318(2)	4.9961(2)
b/Å	10.60220(10)	11.9650(3)	18.0923(7)
c/Å	16.8531(11)	15.7692(11)	19.4089(13)
α/°	76.562(5)	81.213(6)	113.587(8)
β/°	83.482(6)	73.634(5)	91.785(7)
γ/°	69.635(5)	71.377(5)	93.135(7)
Volume/Å^3	1715.56(12)	1579.98(12)	1602.71(14)
Z	2	2	2
ρcalcmg/mm^3	1.496	1.484	1.517
m/mm^{-1}	1.771	1.907	1.886
F(000)	764.0	698	726
Crystal size/mm^3	0.088 × 0.062 × 0.033	0.092 × 0.047 × 0.042	0.12 × 0.07 × 0.06
2Θ range for data collection	6.14 to 54.94°	6.08 to 49.42°	6.02 to 52.74°
Index ranges	$-13 \le h \le 13$, $-13 \le k \le 10$, $-21 \le l \le 21$	$-10 \le h \le 10$, $-14 \le k \le 13$, $-18 \le l \le 18$	$-6 \le h \le 6$, $-22 \le k \le 22$, $-19 \le l \le 24$
Reflections collected	30206	23827	25853
Independent reflections	7824[R(int) = 0.0786]	5361[R(int) = 0.0588]	6542[R(int) = 0.1119]
Data/restraints/ parameters	7824/0/423	5361/0/389	6542/0/399
Goodness-of-fit on F2	1.094	1.037	1.013
Final R indexes [I>=2σ (I)]	$R_1 = 0.0561$, $wR_2 = 0.1504$	$R_1 = 0.0301$, $wR_2 = 0.0706$	$R_1 = 0.0606$, $wR_2 = 0.1279$
Final R indexes [all data]	$R_1 = 0.0695$, $wR_2 = 0.1601$	$R_1 = 0.0356$, $wR_2 = 0.0725$	$R_1 = 0.0793$, $wR_2 = 0.1366$
Largest diff. peak/hole / e Å^{-3}	3.10/-1.29	1.69/-0.99	2.40/-1.73

Table 18: *Crystal data and structure refinement parameters* ***10P***, ***10M***, ***12P*** *and* ***12M****:*

Identification code	**D00105**	**D0068**	**D0067**	**D0071C4**
Sample Code	**10P**	**10M**	**12P**	**12M**
Empirical formula	$C_{45.4}H_{26.3}LaO_8$	$C_{45.8}H_{19}LaO_8$	$C_{42}H_{29}O_8Pr$	$C_{40}H_{26.5}O_8Pr$
Formula weight	838.39	835.75	791.43	776.02
Temperature/K	100	100	100	100(2)
Crystal system	triclinic	triclinic	triclinic	triclinic
Space group	P-1	P-1	P-1	P-1
a/Å	10.1549(5)	10.2519(3)	9.5660(4)	10.014(2)
b/Å	12.6683(6)	12.6764(3)	12.1457(4)	12.396(2)
c/Å	15.7228(11)	15.6928(11)	15.9184(11)	15.776(3)
α/°	89.124(6)	89.609(6)	88.480(6)	89.308(5)
β/°	79.234(6)	81.143(7)	74.692(5)	79.748(6)
γ/°	68.024(5)	69.124(8)	70.211(5)	69.484(5)
Volume/Å^3	1839.37(18)	1880.24(15)	1674.50(15)	1802.1(6)
Z	2	2	2	2
ρcalcmg/mm^3	1.514	1.476	1.57	1.430
m/mm^{-1}	1.218	1.191	1.511	1.402
F(000)	839.0	829.0	796	779.0
Crystal size/mm^3	0.12 × 0.09 × 0.08	0.96 × 0.15 × 0.069	0.06 × 0.05 × 0.03	0.069 × 0.046 × 0.036
2Θ range for data collection	6.14 to 54.98°	6.14 to 46.52°	5.98 to 54.96°	4.42 to 42.08°
Index ranges	-13 ≤ h ≤ 13, -16 ≤ k ≤ 16, -20 ≤ l ≤ 15	-11 ≤ h ≤ 11, -14 ≤ k ≤ 14, -17 ≤ l ≤ 17	-12 ≤ h ≤ 12, -15 ≤ k ≤ 15, -19 ≤ l ≤ 20	-10 ≤ h ≤ 10, -12 ≤ k ≤ 12, -14 ≤ l ≤ 15
Reflections collected	31091	26839	28552	12391
Independent reflections	8425[R(int) = 0.1512]	5384[R(int) = 0.1359]	7666[R(int) = 0.0833]	3725[R(int) = 0.0836]
Data/restraints/ parameters	8425/0/493	5384/0/481	7666/0/481	3725/132/490
Goodness-of-fit on F2	0.979	0.952	1.059	1.058
Final R indexes [I>=2σ (I)]	R_1 = 0.0768, wR_2 = 0.1616	R_1 = 0.0523, wR_2 = 0.1106	R_1 = 0.0489, wR_2 = 0.1126	R_1 = 0.0691, wR_2 = 0.1612
Final R indexes [all data]	R_1 = 0.1123, wR_2 = 0.1793	R_1 = 0.0732, wR_2 = 0.1182	R_1 = 0.0585, wR_2 = 0.1176	R_1 = 0.1150, wR_2 = 0.1918
Largest diff. peak/hole / e Å^{-3}	1.61/-1.45	1.07/-1.01	1.96/-1.60	1.02/-1.48

Table 19: *Crystal data and structure refinement parameters **13P**, **13M**, **14P** and **14M**:*

Identification code	**C00158C2**	**C00161C5**	**C00208P**	**D0070C3**
Sample Code	**13P**	**13M**	**14P**	**14M**
Empirical formula	$C_{42}H_{29}NdO_8$	$C_{42}H_{29}NdO_8$	$C_{42}H_{29}O_8Sm$	$C_{88}H_{71}O_{20}Sm_2$
Formula weight	805.89	805.89	812	1749.15
Temperature/K	100	100(2)	100	100(2)
Crystal system	triclinic	triclinic	triclinic	triclinic
Space group	P-1	P-1	P-1	P-1
a/Å	9.5208(2)	9.6812(6)	9.5144(4)	9.7513(7)
b/Å	12.1181(3)	12.2892(7)	12.0813(5)	18.7501(13)
c/Å	15.8778(11)	15.7406(10)	15.8641(11)	22.2553(16)
α/°	88.507(6)	88.977(2)	88.570(6)	71.138(2)
β/°	74.679(5)	77.463(2)	75.220(5)	87.031(2)
γ/°	70.377(5)	69.750(2)	70.280(5)	81.905(2)
Volume/Å^3	1660.21(13)	1711.72(18)	1656.03(15)	3812.1(5)
Z	2	2	2	2
ρcalcmg/mm^3	1.612	1.564	1.628	1.524
m/mm^{-1}	1.622	1.573	1.831	1.600
F(000)	810	810.0	814	1766.0
Crystal size/mm^3	0.08 × 0.05 × 0.03	0.21 × 0.12 × 0.09	0.88 × 0.62 × 0.102	0.079 × 0.039 × 0.03
2Θ range for data collection	6.02 to 52.74°	4.29 to 56.156°	6 to 52.74°	1.94 to 46.54°
Index ranges	-11 ≤ h ≤ 11, -15 ≤ k ≤ 15, -19 ≤ l ≤ 17	-11 ≤ h ≤ 12, -13 ≤ k ≤ 16, -19 ≤ l ≤ 20	-11 ≤ h ≤ 11, -14 ≤ k ≤ 15, -18 ≤ l ≤ 19	-10 ≤ h ≤ 10, -19 ≤ k ≤ 20, -24 ≤ l ≤ 24
Reflections collected	26768	27051	26641	51227
Independent reflections	6766[R(int) = 0.0794]	8300[R(int) = 0.0901]	6744[R(int) = 0.1165]	10929[R(int) = 0.1575]
Data/restraints/ parameters	6766/0/461	8300/198/542	6744/0/463	10929/88/1077
Goodness-of-fit on F2	1.019	1.012	0.999	1.002
Final R indexes [I>=2σ (I)]	R_1 = 0.0403, wR_2 = 0.0852	R_1 = 0.0500, wR_2 = 0.1020	R_1 = 0.0599, wR_2 = 0.1377	R_1 = 0.0533, wR_2 = 0.0981
Final R indexes [all data]	R_1 = 0.0498, wR_2 = 0.0892	R_1 = 0.0796, wR_2 = 0.1124	R_1 = 0.0703, wR_2 = 0.1436	R_1 = 0.1131, wR_2 = 0.1172
Largest diff. peak/hole / e Å^{-3}	1.24/-1.13	1.57/-2.07	2.11/-2.40	2.25/-1.31

Table 20: *Crystal data and structure refinement parameters for* ***15:***

Identification code	**D00106**
Sample Code	**15**
Empirical formula	$C_{53.8}H_{35.7}O_{18.7}Yb_2$
Formula weight	1327.38
Temperature/K	100
Crystal system	triclinic
Space group	P-1
a/Å	9.66930(10)
b/Å	18.0643(3)
c/Å	19.9097(14)
α/°	104.968(7)
β/°	97.656(7)
γ/°	93.485(7)
Volume/Å^3	3313.2(2)
Z	2
ρcalcmg/mm^3	1.331
m/mm^{-1}	2.864
F(000)	1296.0
Crystal size/mm^3	0.07 × 0.06 × 0.09
2Θ range for data collection	6 to 52.74°
Index ranges	$-11 \leq h \leq 12$, $-22 \leq k \leq 22$, $-23 \leq l \leq 24$
Reflections collected	52845
Independent reflections	13462[R(int) = 0.0567]
Data/restraints/ parameters	13462/6/691
Goodness-of-fit on F2	1.061
Final R indexes [I>=2σ (I)]	$R_1 = 0.0447$, $wR_2 = 0.1229$
Final R indexes [all data]	$R_1 = 0.0550$, $wR_2 = 0.1280$
Largest diff. peak/hole / e Å^{-3}	3.23/-1.08

Chapter 7

Summary and Future Work

7.1 Summary

The aim of this project was to synthesise new, porous, stable 3D Metal-Organic Frameworks with potential applications in separation and storage.

Initial syntheses combining imidazole and carboxylate containing ligands were carried out, as both imidazole and carboxylate ligands individually have been shown to produce robust 3D frameworks. This lead to the production of several coordination compounds (**1-3**, *chapter 3*) which are 2D networks based on metal-carboxylate coordination, with imidazole coordinated as a terminal neutral ligand in all cases. A series of experiments in which the reaction conditions were changed yielded three different frameworks from the same reagents, showing the importance of carefully selected synthesis conditions for the isolation of one desired product (**4-6**, *chapter 3*).

Combination of Co, 1,3,5-BTB and imidazole lead to the formation of a 2D coordination compound containing a novel Co_6 building unit (**7**, *chapter 3*) based on tri-layers of Co-1,3,5-BTB coordination with imidazole coordinated as a capping ligand, hydrogen bonding to adjacent 2D layers. This material was shown to be porous to N_2, CO_2 and CH_4, with the porosity being dependent on the activation method employed, highlighting the importance of investigating all possible activation conditions. Attempts to synthesise similar compounds containing the same Co_6 unit using other N-containing ligands in place of imidazole were unsuccessful and frameworks with individual Co environments were crystallised (**8**, **9**, *chapter 3*), indicating that the hydrogen bonding between 2D layers in **8** plays an important role in structure formation.

Combination of lanthanide salts (La, Ce, Pr, Nd and Sm, **10-15** respectively, *chapter 6*) with the H_4TCPB ligand yielded a series of isostructural 3D frameworks, all of which undergo the same desolvation route, leading to the same isostructural desolvated 3D structure (**10D-14D**). The unit cell parameters of these compounds shrinks in line with the lanthanide contractions and all have been shown to selective to pX over mX.

Ce(HTCPB) (**11**, *chapter 4*) was used to investigate the desolvation process crystallographically: The material can be fully desolvated in the single crystal phase (**11D**) with a partially desolvated stable intermediate also isolated (**11S**). The structure of a rearranged framework was determined following exposure of the material to air (**11R**). All four phases can be isolated in both the single crystal and bulk phases, highlighting the stability of the material. Desolvated Ce(HTCPB) (**11D**, *chapter 5*) was used to selectively sorb xylene and ethylbenzene isomers (pX, mX, oX, EB). The single crystal structures of the C_8-loaded structures were determined and used to explain the selectivity observed, with the high pX/mX and pX/oX selectivities obtained being the key separations under investigation in xylene separation, comparable with the highest values reported for MOF and zeolite materials.

Following on from this, all isostructural Ln(HTCPB) frameworks (**10D-14D**, *chapter 6*) were tested for pX/mX separation and all were shown to be selective to pX over mX. Pr, Nd and Sm(HTCPB) (**12D-14D**) displayed a pX/mX selectivity around 50 % higher than any other material reported to date.

Combination of a smaller lanthanide, Yb, with the same H_4TCPB ligand yielded a different 3D structure, demonstrating that the size of the metal centre is important in structure formation.

7.2 Future Work

The next steps for the lanthanide compounds (**10-14**) would be to scale up the synthesis whilst maintaining phase purity. The high pX selectivity observed could then be used to investigate xylene isomer separation on a larger scale, using chromatography or batch separation with framework regeneration: Currently, the framework is broken down following xylene uptake and the composition of the resulting solution extracted from the framework is measured. For the MOF to be used industrially, MOF regeneration via distillation of xylenes, washing out of the xylenes taken up, or chromatography, would be required.

Another interesting investigation would be to look at potential applications of the stable intermediate of Ce(HTCPB), **11S**. In this thesis, the single crystal structure was determined, however it was not researched any further for this compound or any of the other isostructural Ln(HTCPB) series of compounds. The structure contains a free, non-coordinated carboxylate group within the channels, which may have applications in catalysis. It could also be used in post-synthetic modification experiments, in which the carboxylate group could be reduced or converted to another functional group. This would have many implications in that the fully desolvated material may no longer be equivalent to **11D** and a new structure may be isolated with different applications in separation and storage. Also, the resulting ligand would contain three carboxylate groups and a different fourth group, which would be extremely difficult to synthesise outside of a MOF.

Further investigation into the flexibility of **11D** and **11R** could also be researched: If different guests are loaded into the material, they may have a different effect on the structure isolated.

Finally, if the H_4TCPB ligand itself was modified prior to synthesis, for example, by adding a -Br to one of the pendent phenyl rings, this could lead to the formation of a 3D chiral framework with new interesting properties.